Failure Detection and Battery Management Systems of Lead-Acid Batteries for Micro-Hybrid Vehicles

Von der Fakultät für Elektrotechnik und Informationstechnik
der Rheinisch-Westfälischen Technischen Hochschule Aachen
zur Erlangung des akademischen Grades eines Doktors der
Ingenieurwissenschaften genehmigte Dissertation

vorgelegt von

Master of Science in Engineering
Grzegorz Aleksander Piłatowicz
aus Warschau, Polen

Berichter:
Universitätsprofessor Dr. rer. nat. Dirk Uwe Sauer
Director/Associate Professor Ernst Ferg

Tag der mündlichen Prüfung: 17. Februar 2017

Grzegorz Aleksander Piłatowicz

Failure Detection and Battery Management Systems of Lead-Acid Batteries for Micro-Hybrid Vehicles

Bibliographic information published by the Deutsche Nationalbibliothek
The Deutsche Nationalbibliothek lists this publication in the Deutsche Nationalbibliographie; detailed bibliographic data are available in the Internet at: http://dnb.d-nb.de.

Electronic version
The electronic version is available online on the institutional repository of RWTH Aachen University (https://publications.rwth-aachen.de).

D82 (Diss. RWTH Aachen University, 2017)

AACHENER BEITRÄGE DES ISEA

Vol. 92

Editor:
Univ.-Prof. Dr. ir. Rik W. De Doncker
Director of the Institute for Power Electronics and
Electrical Drives (ISEA), RWTH Aachen University

ISSN 1437-675X

Institut für Stromrichtertechnik und Elektrische Antriebe (ISEA)
Jägerstr. 17/19 • 52066 Aachen • Germany
Tel: +49 (0)241 80-96920
Fax: +49 (0)241 80-92203
post@isea.rwth-aachen.de

Acknowledgments

This thesis was developed during my work as researcher at Institute for Power Electronics and Electrical Drives (ISEA) at RWTH Aachen University.

In the first place, I would like to express my deepest gratitude to my advisor prof. Dirk Uwe Sauer for giving me a chance to conduct my research work at ISEA and start my professional career in the field of battery storage systems. His contagious enthusiasm towards battery storage systems, especially lead-acid batteries helped me a lot to believe in rightness and usefulness of carried out work. In addition, special thanks go to prof. Ernst Ferg for accepting my co-advisor role despite of the long distance, thorough revision of this work and very valuable feedback.

Furthermore, I would like to thank Robert Bosch GmbH for financing conducted investigations. Without it this work would never come to fruition. Professional and target-oriented cooperation with perfect working atmosphere is highly appreciated. Additionally, I am very grateful to renowned representatives of lead-acid battery research community who had always supported me with a valuable advice.

I would also like to take this opportunity to thank my students who worked under my supervision. I am very grateful for their hard work, which highly contributed to development of this thesis.

Special gratitude goes also to all colleagues from ISEA, especially members of lead-acid battery research with whom I had a great honour and pleasure to work. I always appreciated our long discussions, lunch breaks and everything what we were doing together. Without you working at ISEA would never be as rewarding as it was. Additionally, many thanks go to laboratory engineers and administration workers who were always very helpful in solving daily basis problems.

Finally, I would like to thank my loved ones including my parents, my girlfriend Aleksandra and my best friends, who had supported me throughout both my entire education and research work by motivating me and believing in me even when the things did not look promising at all. I will be grateful forever for your support.

Grzegorz Piłatowicz
Founex, September 2017

Contents

1 Motivation

Energy storage systems based on rechargeable batteries are present directly or indirectly in everyday life of most population worldwide. They are used as energy source by consumer electronics, power tools and wireless devices. Many of us cannot imagine living without them. Furthermore, they are also being installed in stationary applications including data centres, hospitals, telecommunication stations, wind and conventional power plants as backup power supplies. Another large part of battery business is occupied by motive branch involving conventional, hybrid and electric vehicles, wheelchairs, e-bikes, fork-lift trucks and golf carts. Their role in moving to a more environmental friendly energy generation and consumption is enormous and should not be underestimated.

Lead-acid batteries (PbA) have been installed in many past and contemporary applications that require installation of the energy source. PbA technology continues to be a key player in future global battery market, which has been consistently growing and it was worth 54 Billion of USD according to [1] in 2013. Moreover, forecasted market growth estimated by the same authors show that it will reach remarkable value of 80 Billion USD by 2020. Due to the enormous investments and research activities the market share in lithium-ion batteries will increase from 31.5% in 2013 up to 40% forecasted for 2020. However, PbA will remain as market leader with 67% and 58°C respectively considering global market share regardless of the application. On the one hand lithium-ion batteries are way superior to PbA technology considering their outstanding specific energy and power density, followed by outstanding cycleability, good rechargeability and efficiency. On the other hand, they are not free from considerable drawbacks, which are: safety related issues, poor performance at low temperatures, high raw material costs and inefficient as well as not economically sustainable recycling in case of cost optimized technologies with lower amount of cobalt and nickel as discussed in [2]. PbA with their very low raw material costs that result in e.g. SLI (starting, lighting, ignition) batteries cheaper than 50 EUR/kWh, robust design, market maturity, good performance at low temperatures and relatively low adverse impact on the environment due to economical recycling with recycle rate up to 97.5% [3][1] makes them an attractive and affordable product. Due to the listed advantages and well developed recycling chain PbA can serve as a technology that could contribute the most to transition from fossil-fuel based to low-emission and sustainable economies regardless of economic development of the particular country or region.

[1] Lead-acid batteries are not only the best recyclable battery technology but also the best recyclable product in the world [2].

Despite of the fact that PbA have been present on the market for over 150 years [4] many aspects of their operation are still partly or little understood. It is because the governing physical laws are a matter of high complexity that also includes multiple cross-relations, which usually can be neglected for a given condition range. Finding reasonable simplifications and useful assumptions for developing solutions, which may significantly reduce environmental footprint of our civilisation, are one of the main motivations standing behind this work.

1.1 Lead-acid batteries as affordable solution for reduction of CO_2 emissions

SLI batteries are the main PbA product being sold worldwide. According to [1] they possessed 64% of overall PbA market share in 2013, whereby industrial and e-bike batteries took 33% and 3% respectively. State-of-the-art automobiles can be divided into three main categories: conventional vehicles with internal combustion engine (ICE) as the only energy and power source for all operation modes, hybrid vehicles with both battery storage system as well as ICE and electric vehicles with solely an electric drivetrain. In all of them the 14 V power net includes a SLI battery that provides energy to all low voltage loads. Hybrid vehicles are characterized by different levels of hybridization that define four main types, namely micro-hybrid (µH) with lowest level of electrification, mild hybrid, full hybrid and plug-in hybrid vehicles. The higher the level of electrification is, the more expensive particular type of hybrid will be. Research presented in this thesis focuses mainly on µH applications with installed PbA SLI battery. They offer the most affordable and accessible solution for lowering overall global CO_2 emissions and consumption of fossil fuels in the passenger transportation sector. Current generation of µH is mainly equipped with automatic start&stop (ASSF) and brake energy regeneration (BER) functionality. Although reduction of the fuel consumption provided by µH is limited, up to 9% as reported by Meissner in [5], it is currently one of the most promising solutions, which can significantly help to reach current global climate goals in the next decade. Two main advantages, which are worth mentioning in this context, are its affordability and low implementation effort[2].

According to the World Bank [6] there were 124 passenger cars per one thousand people in the world by year 2011. It makes approx. 868 million of vehicles for 7 billion of global population, which are being currently driven worldwide. The authors of the referenced report also indicate that total road energy consumption per capita equalled 262 kg of fuel for the whole year leading to a value of 1834 megatons consumed petrol throughout the world. This value is directly proportional to CO_2 emissions mentioned before. If only a manageable 10% fraction of all operated vehicles are µH that provide average fuel savings of 5%, it will lead to enormous savings that cannot be reached by any other solution introduced recently. It is proven by data presented in [7], which indicates that 40% of all newly sold vehicles by 2020 are going to be

[2] Only necessary modifications of the conventional automobile to operate as micro-hybrid vehicle is equipping it with more durable SLI battery, improved starter-generator system and adapted energy management system.

µH. Considering approx. 85 million units [8] of new vehicles that were sold in 2013[3], µH equipped with PbA is the most promising technology that can help to reach current climate goals in comparison to all other relatively expensive solutions and rechargeable battery technologies altogether. This statement emphasizes that lead is not dead as claimed by some authors. PbA technology has high potential for further improvements concerning battery design, further cost reductions and operation strategies. Optimization of the latter one by means of advanced battery management systems (BMS) is the main topic addressed by the presented research.

1.2 Role of the battery management systems in further improvements

The main role of BMS in µH applications is to provide information about the current battery state to the energy management system (EMS). According to this data the EMS decides whether ASSF functionality should stay switched on or rather get turned off. Furthermore, it also determines the time point when the battery should be refreshed, recharged or discharged. Obviously, the more accurate the BMS, the less missed ASSF opportunities and premature engine restarts will occur. Advanced battery diagnostics could also lead to less conservative and more energy saving operation strategies implemented by automotive companies that understandably put the highest priority to vehicle reliability and take always worst cases into account. Even if possible further savings equal to as little as 1% of average fuel consumption, they will result in tremendous additional overall reduction of global CO_2 emissions and usage of non-renewable energy sources as discussed in previous chapter.

BMS used in state-of-the-art and future generations of µH are realized in form of a low-cost electronic battery sensor (EBS) that is attached to the negative pole of a 12 V SLI PbA. It measures terminal voltage, current rate and pole temperature. Limited available computational power and internal memory indicate that developed battery state detection (BSD) algorithms have to be not only highly accurate, fully adaptable to provide precise BSD estimation of considered batteries (regardless whether they are brand new or considerably aged) and robust against measurement as well as modelling noise but also highly simplified. Considering pronounced complexity of PbA technology this requirement makes the development of advanced BSD solutions highly challenging. It cannot be realized by means of pure mathematical solutions, which have been preferred in the past. It is due to the necessary extensive measurement time and resources followed by difficult adaptivity and reduced capability to be properly extrapolated to the current conditions, which have not been investigated during parametrization. Presented work shows how simplified heuristic approaches based on thorough understanding of the considered physical phenomena can be created and implemented in low-cost EBS in a way that allows reaching excellent accuracy in a wide range of operation conditions, which has not been achieved so far. Additionally, discussed results indicate that improving the overall performance of the considered energy storage system does not necessarily have to involve developing a new generation of battery. It

[3] This value grows by approx. 3-4 million of units per a year.

is shown that in many cases employment of smart BMS and EMS does that job well with significantly reduced cost and time necessary for research and development activities.

2 Introduction

The first fully operational PbA was presented by Gaston Plante in the year 1860 [4]. Despite the fact that PbA has already been known and used for more than 150 years, the first fully commercial EBS with the BMS inside for 12 V SLI batteries was introduced only in the year 2003 by Hella [9]. It was due the fact, that until the end of the last century any means of monitoring of the SLI batteries were simply not necessary. The only maintaining of the battery was left to the responsibility of the user himself and solely consisted of refilling of distilled water, which was lost during the operation due to water electrolysis. Automobiles of the past century were characterized by very limited number of installed loads, relatively small maximal required power, no ASSF, no BER and much less safety functionalities such as electronic stability control (ESP). In that time the battery was considered more as an energy buffer used only for starting the vehicle rather than as an active power and energy source, which is the case in the modern conventional and μH vehicles as discussed by Meissner et al. in [10].

The additional ASSF and BER functionality and exponentially growing number of electrical loads that impose an additional stress on the SLI batteries pushed further development of the standard flooded PbA in form of enhanced flooded (EFB) [11] and absorbent glass-mat (AGM) [12] batteries. These, can better handle the more demanding conditions. To further optimize their expected lifetime and reduce warranty costs, a BMS is installed in most of the state-of-the-art automobiles. Together with the EMS, they ensure the correct operation of the battery, cranking capability and reliability of the vehicle. Furthermore, they measure and estimate the impact of ageing on PbA performance and decide if any of the new functionalities should be turned off temporarily or permanently. Additionally, BSD algorithms should be able to provide accurate state estimation regardless of the applied battery technology.

Main parts of the μH specification, which makes accurate BSD particularly challenging, are listed below:

- The battery is never fully charged or discharged.
- Periodical check-ups are not practised.
- There are no long enough and load free rest periods, which allow measuring the fully equilibrated open-circuit voltage as there is always quiescent current flowing.
- Broad ambient temperature range starting from -40 °C up to 115 °C
- Broad considered current range: -1500 A – 200 A

- Different technologies on the market: standard flooded, AGM and EFB

- Narrow target operational SoC range: 90-70 %

- High variation of quality of the commercial batteries available on the market. Even the same products produced by the same manufacturer in the same factory but just a half year apart, may show significantly different performance.

- Not fully standardized labelling of the available PbA. It may happen that a battery with 70 Ah of the nominal capacity on its label after discharging with twenty-hour current rate has got 75 Ah, whereas another product labelled with 80 Ah can show the same actual capacity of 75 Ah.

- High manufacturing tolerances, e.g. typically electrolyte density of a brand-new battery has a tolerance of +/- 0.01 $kg \cdot l^{-1}$, which can mislead the estimated SoC value from open-circuit voltage by approx. +/-4 % at high SoC range. Additionally, filling process of diluted sulfuric acid has also an accuracy of +/-1%, which can extend the given value to +/-7% at SoC of 40% as reported by Meissner et al. in [13].

Accuracy of the state-of-the-art BMS is limited and should be further improved [5]. As it can be concluded from the listed requirements the development of advanced battery management systems is not a trivial task. This topic, namely advances in the field of BSD for PbA in µH applications is the figure of merit of this thesis. Considered subjects are: improvements of the battery terminal voltage prediction under highly dynamic load, state-of-charge (SoC) estimation in rest periods and early internal failure detection as extension of the state-of-health (SoH) estimation algorithms. It was decided to go away from purely mathematical relatively inaccurate approaches and focus on the heuristic solutions that have been described below:

- Battery dynamic response (BDR) estimation using Butler-Volmer equation (BVE) based approach. Its main target is improved cranking capability prediction and estimation of voltage drop in all field relevant conditions. Achieved accuracy is ± 200 mV in cranking conditions, which is approx. two times better than state-of-the-art solutions.

- Fully equilibrated open-circuit voltage (U_{00}) prediction to improve SoC estimation using well-known linear relationship between these two parameters. This approach is based on the results of comprehensive experimental study of the PbA behaviour during rest periods, which has not been fully understood so far. Obtained precision equals ± 5% SoC with a rest period duration of 4h, which is also valid during operation at low temperatures. Stated accuracy is superior in comparison to state-of-the-art algorithms that are in some cases not even able to reach ± 10% SoC when temperature drops below 10 °C.

- Online internal failure detection (IFD) that mainly addresses possible occurrence of internal short-circuits (SCD) during operation. Developed solutions are based on the experimental study of internal short-circuits and sudden capacity loss, which resulted in both early as well as robust IFD.

There are multiple topics regarding advanced BSD algorithms that still require further research, e.g. improved estimation of gassing for more precise Ah counting, technology detection, nominal capacity determination and calculation of acid stratification or dynamic charge acceptance (DCA). However, these topics have not been considered in this work.

Chapters 1 and 2 provide motivation and introduction to the topics addressed in this thesis. Working principle of PbA technology together with fundamentals of BMS and BSD algorithms can be found in chapter 3. Developed algorithms, which significantly improve accuracy of BSD solutions mainly concerning BDR, U_{00} and IFD, have been described in detail in chapters 4, 5 and 6 respectively. Chapter 7 concludes presented work, suggests and prioritize further topics that could be carried out in the future.

3 Battery management systems of lead-acid batteries installed in micro-hybrid vehicles

The main role of BMS in µH applications is a battery monitoring and battery performance prediction under given conditions both realized by BSD algorithms. Although it is known that full integration of BMS within the vehicle power net is the most optimal solution as discussed in [10], car makers usually do not allow BMS to take any direct measures that could be used for increased accuracy of the applied algorithms and improved performance of the whole battery storage system. Good examples are altering current charging strategy to prolong expected battery life or targeted turning on and off any loads to gather extra information for better prediction concerning accuracy, feasibility check and confidence. The main concern is a reduced vehicle reliability that should be guaranteed at any conditions. This means that the BMS can only use information that is available from direct measurements on the battery with excitation originating exclusively from loads originally connected to the power net. Exemplary EBS, which is a hardware platform for BMS functionality in µH is presented in Fig. 1.

Fig. 1. Realization of BMS functionality in µH applications using electronic battery sensor with implemented BSD algorithms (by courtesy of Robert Bosch GmbH).

EBS is mostly based on low-cost fixed-point microcontroller and uses measured battery terminal voltage (U_{batt}), current rate (I_{batt}) and pole temperature (T_{pole}) to perform BSD. The latter parameter is usually recalculated to meaningful battery internal temperature (T_{batt}) by means of applying simplified battery thermal model. An exemplary solution that can be used for this task has already been described by Pilatowicz et al. in [14].

State-of-the-art hardware platforms are characterized by relatively high measurement accuracy as can be seen in [15]. It equals ± 1 mV, ± 1 mA up to 100 mA depending on the given current

measurement range and ± 0.5K for U_{batt}, I_{batt} and T_{pole} respectively. It enormously helps to improve precision of BSD. It is because measurement noise is being always propagated to the output parameters of BMS and reduces confidence (e.g. 10-15 mV of measurement error introduces additional inaccuracy of 1% SoC).

Simplified graphic representation of BMS functionality is depicted in Fig. 2. Even though equipping batteries with special sensors, which could provide information about their internal parameters such as acid density (ρ_{acid}) could provide vital information for BSD as demonstrated in [16], they have not been introduced to the market due to increased cost. It indicates that input parameters of BMS visible in Fig. 2 are the only source of information for battery diagnosis that can be considered in the contemporary and future commercial products.

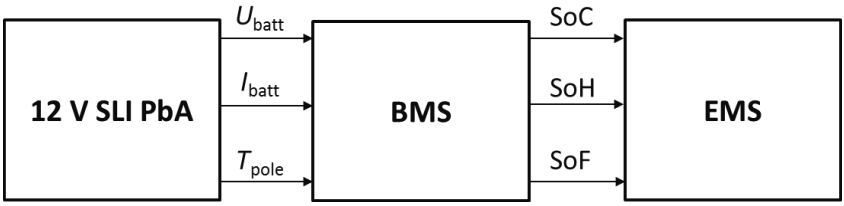

Fig. 2. Simplified graphic representation of BMS functionality in µH applications.

In this chapter, firstly fundamentals of PbA technology are described. They show that development of highly accurate, adaptable and smartly simplified BSD algorithms is only possible when thorough understanding of considered physical phenomena is available. It is due to the pronounced non-linearity and complexity of PbA, which should be well-known to make feasible assumptions. Furthermore, it also helps to develop solutions that extrapolate properly and identify the best operation modes when applied parameters can be adapted in the most effective and precise way. Second part of this chapter focuses on detailed description of the state-of-the-art BSD solutions. It defines introduced SoC, SoH and state-of-function (SoF) signals and shows the most popular existing methods used for estimation of these parameters.

3.1 Fundamentals of lead-acid battery chemistry

The discovery and first concept of lead-acid batteries was presented by Wilhelm Josef Sinsteden in 1854 [17] who observed current flow through lead electrodes located in diluted sulphuric acid. Gaston Plante demonstrated the first working rechargeable lead-acid battery in 1860 [18], which can be considered as birth of this technology. Many different PbA designs have been developed and successfully introduced to the market. They are result of optimization of parameters such as cycleability, available specific energy and power density or significantly reduced water consumption. In this subchapter, the most crucial features of PbA technology are described with the focus on the 12 V SLI batteries.

3.1.1 Working principle and relevant technologies

A generalized one cell layout of a PbA technology is presented in Fig. 3. Active materials of cathode and anode are highly porous PbO_2 and Pb respectively. They are also very often denoted as positive (PAM) and negative active material (NAM) in the literature. Unique feature of the considered system is the fact that the electrolyte (diluted sulphuric acid) does not only provide ion conductivity, which is the case for other chemistries such as lithium-ion batteries, but also takes part in the main reaction.

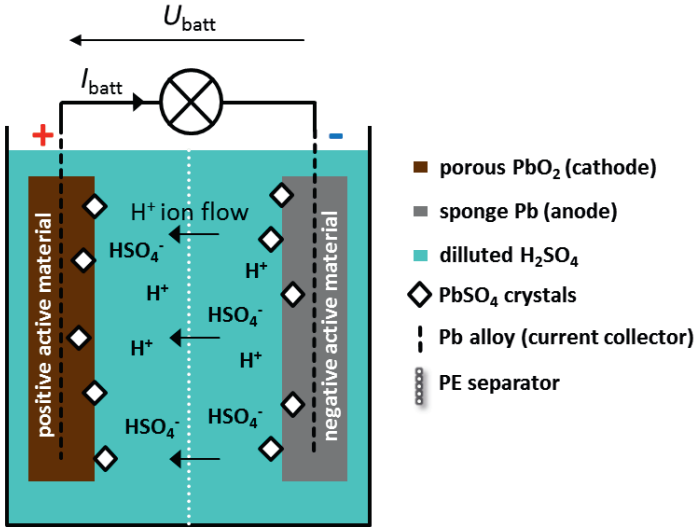

Fig. 3. Generalized one cell layout of $Pb/PbO_2/PbSO4/H_2SO_4/PbSO_4/Pb$ system.

Main reaction of the single electrodes and entire cell has been depicted in (1)-(3).

Negative electrode:

$$Pb + HSO_4^- \xleftrightarrow{\text{charging/discharging}} PbSO_4 + H^+ + 2e^- \tag{1}$$

Positive electrode:

$$PbO_2 + HSO_4^- + 3H^- + 2e^- \xleftrightarrow{\text{charging/discharging}} PbSO_4 + 2H_2O \tag{2}$$

Cell:

$$Pb + PbO_2 + 2H_2SO_4 \xleftrightarrow{\text{charging/discharging}} 2PbSO_4 + 2H_2O \tag{3}$$

It means that ρ_{acid} decreases and increases while the battery is being discharged and charged respectively. Main role of the separator is electrical and mechanical insulation of NAM and PAM from each other, whilst providing excellent ion conductivity and acid diffusion through

the pores. Main reaction involves exchange of two electrons per one lead atom between two active materials. Such chemical process is called redox reaction. It consists of simultaneous reduction and oxidation reactions. During discharging NAM is oxidized and two electrons are removed from each lead atom leading to reaching oxidation number that equals +2. Subsequently, Pb^{2+} ions dissolve into electrolyte where they meet with HSO_4^- ions and precipitate together in form of lead sulphate crystals on the active material. On the positive side two ions removed from NAM provoke splitting of PbO_2 particle into O_2 and Pb^{4+}. The latter one gets reduced to Pb^{2+} and forms $PbSO_4$ compound on the PAM surface. O_2 particle together with H^+ ions get transformed into water molecules, which are also a product of this reaction (see (2)). During charging the same reactions take place but in the opposite direction. This explanation is commonly accepted and called double sulphate theory.

The nominal voltage of a one cell equals conventionally 2 V. It can be described by Nernst equation that determines concentration dependant potential (E_0) of PbA in open-circuit conditions. It has been depicted in (4) and originates from [17].

$$E_0 = 1.931V + \frac{RT}{nF}\left(\ln a^2{}_{HSO_4^-} + \ln a^2{}_{H^+} - \ln a^2{}_{H_2O}\right) \tag{4}$$

Where: R and F are universal gas constant and Faraday constant that equal 8.314 $J \cdot mol^{-1} \cdot K^{-1}$ and 96485 $C \cdot mol^{-1}$. n indicates the number of electrons involved in the main reaction, which equals 2 in this case. T is the temperature in Kelvin and $a_{HSO_4^-}$, a_{H^+}, as well as a_{H_2O} denote chemical activity of HSO_4^-, H^+ and H_2O, which is a dimensionless quantity. The chemical activity of solid materials is constant and that is why Pb and PbO_2 as well as $PbSO_4$ do not play any role in the presented relation.

Theoretically, operation at such high potential, which is significantly above standard potential of the water electrolysis that equals 1.229 V, should cause noticeable thermodynamically unstable operation and immediate loss of considerable amount of water. However, kinetics of these processes (high overvoltage of Pb) on lead electrodes are so slow that resulting gassing rate is relatively low. It is even lower than in case of other technologies based on aqueous electrolytes such as nickel metal-hydride and nickel-cadmium batteries characterized by much smaller nominal voltage of 1.2 V. Still, in brand new SLI batteries gassing effects inflicts self-discharge rate, which equals approx. 3% SoC loss per month at 20 °C [19] and cannot be fully neglected. Water electrolysis is the main side reaction considering PbA technology. It is described by equations (5)-(7) and involves redox reaction resulting in oxygen and hydrogen generation on PAM and NAM respectively. The kinetics of these processes strongly depend on the applied U_{batt} and ambient temperature.

Positive electrode:

$$H_2O \rightarrow \frac{1}{2}O_2 + 2H^+ + 2e^- \tag{5}$$

Negative electrode:

$$2H^+ + 2e^- \rightarrow H_2 \tag{6}$$

Cell:

$$H_2O \rightarrow H_2 + \frac{1}{2}O_2 \tag{7}$$

Commonly accepted approximations [20] say that gassing is tripled and doubled by means of increasing U_{batt} and ambient temperature by 100 mV per cell and 10 °C respectively. Current rate that corresponds to this reaction is denoted as I_{gas} throughout this work.

To impede water consumption and make PbA absolutely maintenance-free valve-regulated lead-acid batteries (VRLA) have been developed. In case of automotive applications their electrolyte is immobilized through an AGM separator, which is not fully saturated to provide gas channels for oxygen evolved at PAM. Stationary battery storage systems also use second possible design of VRLA batteries, which are called gel batteries. They do not use AGM separator but gelled electrolyte (obtained by adding SiO_2) with cracks that have the same function as mentioned gas channels. AGM batteries have been established as SLI batteries due to their lower cost compared to gel technology and higher achievable specific power than flooded as well as gel counterparts. Comparison of further features of these two layouts is illustrated in Fig. 4 assuming same cell and electrode design.

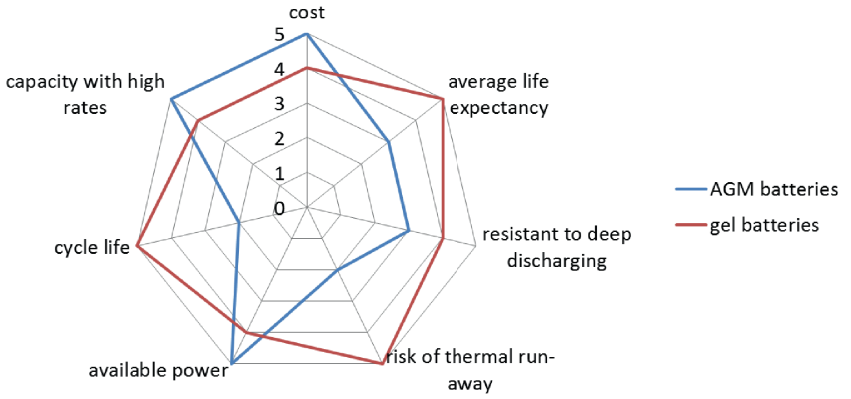

Fig. 4. Comparison between most relevant features of AGM and gel designs concerning commercial VRLA batteries (evaluation based on the authors experience).

On the contrary to traditional vented layout illustrated in Fig. 3, in VRLA batteries part of evolved oxygen is forced to move from PAM to NAM where it gets recombined. They are fully sealed and equipped with safety valve that opens if the inner pressure exceeds a given value, which is usually in the range of 130-210 mBar [21]. It means that even if generated oxygen does not move through gas channels in the separator, it is also able to reach NAM through the top part of the battery. This process has been schematically illustrated in Fig. 5a. It is called closed oxygen cycle (COC) in the further parts of this work. Due to very limited diffusion of O_2 in sulphuric acid recombination processes are negligible in flooded designs. In commercial AGM batteries recombination efficiency is in most cases under normal operation conditions significantly above 90%. Hydrogen evolution is also considerably impeded. It cannot be recombined in any way and determines irreversible water loss of VRLA technology.

Comprehensive description of VRLA design together with all its features can be found in the work of multiple authors [12][22][23][24]. Impeded water loss is not the only advantage of AGM technology.

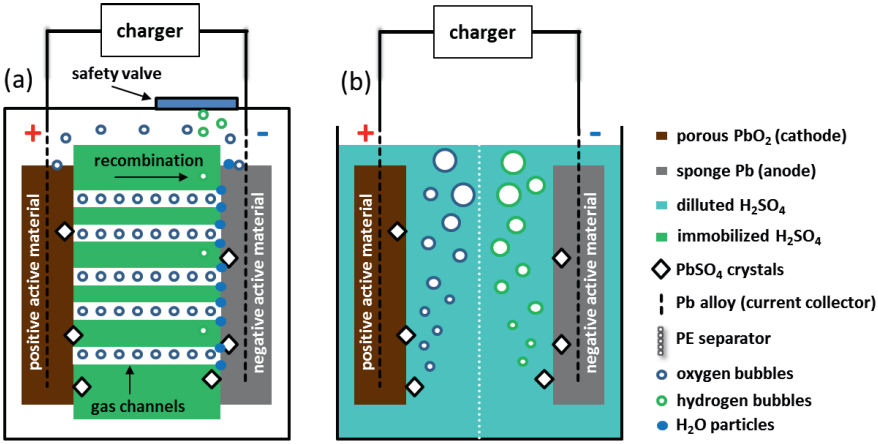

Fig. 5. Schematic illustration of closed oxygen cycle (COC) in sealed AGM batteries (a) that allows recombination of evolved oxygen and vented design (b) where water is released to the environment.

Through increased pressure exerted on PAM and significantly reduced acid stratification they are also more cycleable (more information about ageing mechanisms can be found in chapter (3.1.2). Additionally, distance between PAM and NAM is lower in comparison to traditional designs, which leads to smaller internal resistance (R_i) for the same nominal capacity (C_N). Thus, AGM technology is characterized by higher cold cranking power. Its major drawback is approx. doubled cost that originates from much smaller manufacturing tolerances and complex electrolyte filling process when compared to standard flooded batteries.

The last PbA technology, which is relevant for µH applications, is EFB batteries. They mainly address the issue of significantly increased cost of AGM batteries in comparison to standard

flooded design trying to improve it as much as possible keeping costs low. There is no commonly accepted definition how exactly EFB batteries should be made. However, the most common changes that are introduced to increase their average life expectancy and performance in comparison to standard flooded design are as follows:

- improved design of the electrodes to homogenise current distribution mainly in the vertical direction
- applying additives to active materials and electrolyte that mainly improve DCA[4] (particularly carbon based materials introduced to NAM)
- introduction of passive mixing elements that reduce acid stratification
- pasting special scrim (glass mat retainer covering active mass) sheets on the positive electrode that hinders softening and shedding of PAM

Explanation of all ageing related effects can be found in chapter 3.1.2. Low DCA of PbA refers to limited rechargeability of SLI batteries that cannot accept high amount of energy delivered by BER functionality in a short time. It has been thoroughly studied by Budde-Meiwes et al. [25] and Schaeck et al. [26]. According to results presented by multiple authors [27][28] recent advances in EFB technology make their performance either comparable or even superior to AGM batteries. However, DCA achievable by the state-of-the-art and future commercial PbA battery products will not fulfil the requirements of the car makers due the limitations of the precipitation and dissolution processes. That is the reason why future battery storage systems will consist of multiple battery technologies as presented in [29].

[4] It has to be emphasized that already many additives are being added to both active materials as explained in [18]. In EFB batteries further optimization of their dosage plus addition of entirely new materials is realized.

3.1.2 Ageing phenomena and effects accelerating degradation

To understand failure modes, which limit the achievable performance of PbA technology and lead to reaching application-specific end of life (EoL) definition, ageing phenomena occurring in each PbA should be known. Furthermore, they are also significantly contributing to generation of internal failure mechanisms, which are relevant for online IFD algorithms discussed in Chapter 6. Classification of main ageing effects can be done as follows:

- Corrosion of the positive grid
- Softening and shedding of both active materials
- Sulfation
- Water loss

3.1.2.1 Corrosion

Corrosion of the positive electrode is caused by oxidation of the positive grid, which is usually a lead alloy. It has been described by chemical equation depicted in (8). Additionally, it must be mentioned that also intermediate stage products such as PbO and $PbSO_4$ are considered as corrosion.

$$Pb + 2H_2O \rightarrow PbO_2 + 4H^+ + 4e^- \tag{8}$$

The corrosion products have a higher specific resistance. Additionally, the cross-section area also decreases and therefore the ohmic internal resistance (R_{ohmic}) of the whole battery increases. Furthermore, they these products are more voluminous, which means the plate itself grows over time while being operated in the field. This effect imposes additional mechanical pressure to other components and may also cause losing contact between the grid and PAM, eventually resulting in capacity loss. The rate of corrosion, which is second most pronounced side reaction after water electrolysis, as in case of gassing also grows exponentially with increasing charging voltage and increasing temperature [30][31][32]. A more detailed explanation of this effect can be found in [33]. Exemplary heavily corroded positive plate and a stack of plates withdrawn from 12 V SLI battery are illustrated in Fig. 6.

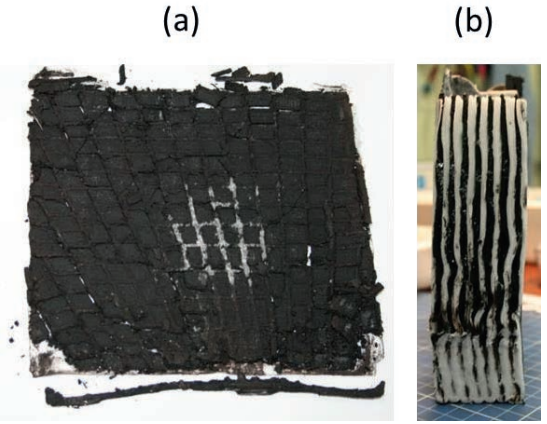

Fig. 6. Heavily corroded positive electrode (a), stack of plates of an AGM battery (b).

Worth mentioning is also the fact that corrosion provides adhesion of the PAM to the grid so that in the new designs it cannot be fully suppressed as demonstrated by Prengaman et al. in [34]. Corrosion cannot be recovered by any means and that is why this effect is categorized as irreversible.

3.1.2.2 Softening and shedding of active materials

Softening and shedding mainly originates from the volume difference between discharge product, $PbSO_4$, and both active materials, namely Pb and PbO_2 for negative and positive electrode respectively. Volume ratio for Pb and $PbSO_4$ equals 1/2.4 and in case of PbO_2 it is 1/1.94, which inflicts a significant "breathing" (expansion and contraction) effect. It must be emphasized that these ratios only occur when the battery is deeply discharged, which is not the case in automotive applications. However, even small cycles that are more field relevant create significant mechanical stress in the active materials. Mentioned stress leads to softening of both active materials. In the worst-case agglomerates of PAM or NAM fall to the bottom of the cell and thus cannot take part in the main reaction anymore. This phenomenon is called shedding. Even though the volume ratio of PAM is smaller than for NAM, the positive electrode suffers considerably more from the softening and shedding phenomenon than the negative electrode as explained in [22]. This can be explained by much higher flexibility of lead in comparison to lead dioxide structure, which means that NAM can be compressed more easily during discharging.

Fig. 7 presents positive plate extracted from a heavily cycled flooded battery. The softened and dislodged active material is clearly visible. It can be assumed that with deeper and more cycles imposed a higher resulting rate of battery ageing occurs. More information about these phenomena together with production and operation parameters, which influence their rate in commercial applications, can be found in [33]. Modelling solutions based on the experimental measurements and mechanical Woehler curve approach have been described in [14]. The lost

active material cannot be recovered by any means, which is the reason why this effect is as in case of corrosion considered as irreversible.

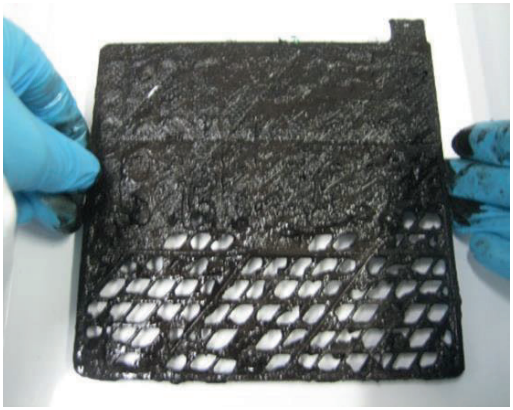

Fig. 7. Exemplary positive electrode that suffered from considerable softening and shedding of active material.

3.1.2.3 Sulfation

It is well known that sulfation is the main failure mode of the state-of-the-art 12V SLI batteries. Sulfation refers to an accumulation of hardly dissolvable $PbSO_4$, which cannot be recharged by means of the operation charging strategy. Because of this it is considered as loss of active material causing an increase of internal resistance and capacity loss. Nevertheless, it can be partially or fully recovered by means of targeted intensive refresh charging strategies as demonstrated in [35][36], which are also being used in automotive applications as demonstrated in [37]. It must be distinguished between sulfation and conversion of the active material into lead sulfate. The latter one stands for the standard reaction that occurs while discharging PbA batteries and cannot be considered as ageing effect itself. This issue has been explained in detail in [38].

The main reason for the occurrence of sulfation in PbA, which are used in μH applications, is their operation in high-rate partial state-of-charge (HRPSoC) regime and recrystallization phenomena that cause the growth of lead sulfate crystals to form, which cannot be dissolved anymore using a standard charging routine. It means that once the $PbSO_4$ crystals reach a certain size and loose contact with the rest of active material, only a part of them can be converted back under application specified charging procedure. Large part of $PbSO_4$ remains in an irreversible form and tend to grow even further during subsequent cycles, which is a cause of performance degradation. An additional effect that considerably accelerates sulfation is acid stratification. It is caused by the fact that the electrolyte, diluted sulfuric acid, also takes part in the main reaction, which means that HSO_4^- ions are consumed while discharging and generated while charging. More concentrated acid is heavier than less concentrated one, so that the former one falls down due to gravity to the bottom of the cell as demonstrated in Fig. 8.

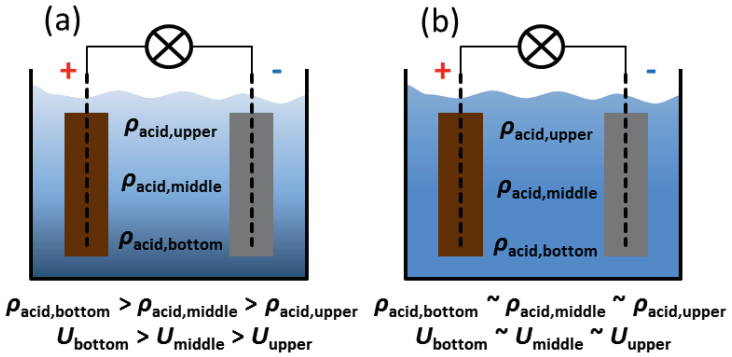

Fig. 8. Schematic and simplified illustration of acid stratification: (a) highly stratified cell, (b) equilibrated cell. $\rho_{acid,i}$ and U_i correspond to acid density and potential of considered level of the system.

Such state inflicts differential discharging and charging of the bottom and upper part of electrodes respectively. Furthermore, exchange currents occurring during rest periods, which are provoked by vertical potential gradient, contribute to further growing of the inhomogeneous SoC distribution. The lower average SoC of a given area is the higher its sulfation rate becomes. This explains why mostly lower parts of the stratified cells suffer from this ageing effect as demonstrated in [39].

Another phenomenon, namely diffusion is counteracting the effect of gravity and homogenise the electrolyte back again. However, its rate is relatively small and large time constants are needed to reach a fully homogenized state. For example, full discharging of 12 V SLI battery with a current rate equal to four times the twenty-hour rate ($I_{20} = C_N/20$) and subsequent full charging with $5I_{20}$ with maximal voltage of 14.7 V may cause a significant gradient of acid density between the upper and bottom part of a SLI battery of 0.2 kg·l^{-1} [5]. The time constant of the homogenization process via diffusion at 25 °C from such a state equals approximately one week and can vary with a cell design. The diffusion is being characterized by the exponential temperature dependency, which means that at lower temperatures its rate is considerably smaller. Acid stratification is mainly present in standard flooded and EFB designs. However, AGM batteries are also affected by this effect, but in much less extent as reported in [41] and [42]. In their case, it has just got different characteristics, namely its rate is noticeably smaller than for other technologies and it is more permanent. It means that once it is established it will most likely be present until the end of life of the battery [22]. More information about measuring and consequences of acid stratification can be found in [39], [43], [44] and [45].

[5] Acid density of fully charged and fully discharged standardized 12 V SLI PbA equals approx. 1.28 kg·l^{-1} and 1.06 kg·l^{-1}[40], which indicates $\Delta\rho_{acid}$ of 0.22 kg·l^{-1} between these two states.

Fig. 9 presents the size of $PbSO_4$ crystals in the SLI battery directly after failure in the field, in three different states. The battery has suffered from a significant amount of sulfation because the $PbSO_4$ crystal sizes are much higher than 10µm, whilst for a new battery operated in upper SoC their range usually does not exceed 1µm. Another important factor that significantly increases the rate of sulfation is the duration of rest periods with small quiescent currents, especially at elevated temperatures. The longer the rest periods and the higher the temperature is, the bigger lead sulfate crystals will grow.

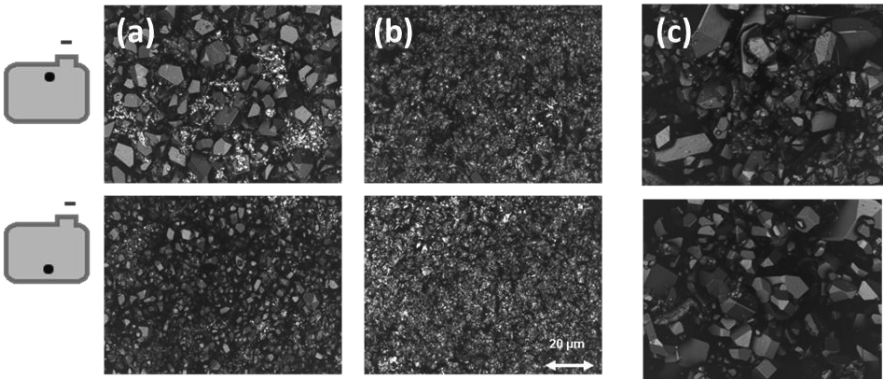

Fig. 9. Laser microscope pictures of the negative plates extracted from SLI standard flooded battery: (a) fully discharged state, (b) fully charged state, (c) plates withdrawn from a field aged battery directly after failed cranking. Upper and lower pictures correspond to NAM observed in the top and bottom of the plate respectively. (by courtesy of ISEA, RWTH Aachen University)

It has to be noted that in automotive applications in most cases the negative electrode suffers much more from sulfation than the positive one. The exact reason is not clear but it is believed to be caused by the much larger pore size of the NAM, namely 5-10 µm in comparison to less than 2 µm in case of PAM [39]. Another explanation lays is the approximately 70 times higher double-layer capacity of PAM [46], which means that NAM is being much more cycled than PAM because much higher average faradic current is flowing through it. Additionally, NAM has got higher self-discharge rate. Factor 2-5 higher than PAM has already been reported in the literature [47].

3.1.2.4 Water loss

In the 1980's and 1990's water loss was not considered as an issue in SLI lead-acid batteries. It was due to the widely-accepted practice of the regular refilling of water, which was a standard for many years. However, introduction of the absolutely maintenance-free batteries, particularly AGM, flooded and EFB designs changed this situation dramatically. For AGM a refill is impossible and even more standard flooded and EFB batteries do not have an option to access the internal parts of the battery without damaging of the housing so that water cannot be refilled

anymore[6]. This is the reason why nowadays it is considered as an irreversible ageing effect. The consequences of too high water loss are increase the plate's grid corrosion rates [17] and thereby increases the self-discharge rate (sulfation) due to higher acid density. Additionally, in case of AGM batteries there is a considerable risk of dry spots occurrence, which will cause a capacity loss especially in the middle of the plate. This is because of complex filling process of the AGM separator [48] and heat generation [20] due to lower acid concentration in the middle of the electrode. Therefore, active material may lose its contact to the acid in these areas. Another failure mode worth mentioning is a consequence of excessive water loss is the drying out of the upper part of both electrodes (including lugs and upper plate areas) caused by too low electrolyte level. This results in significant capacity and performance deterioration, which is mostly associated to standard flooded and EFB batteries. Additionally, in some cases such extensive degradation leads to premature cell or battery failure

According to Pavlov [18] significant gassing of PAM and NAM starts to occur at SoC above 70% and 95% SoC respectively. These values are valid for charging at relatively low rates. At this state battery current that flows into gassing slowly increases with simultaneous decrease of current rate that is consumed by main reaction. It indicates that during extended overcharging and after reaching of a physical fully charged state all measured I_{batt} is consumed by side reactions. If the gassing current is known, which can be obtained either by direct measurement in a mentioned conditions or estimation provided by BMS, lost water during operation is calculated using Faraday laws of electrolysis available as analytical equation in (9). It describes relationship between electric charge and resulting water mass consumed by water electrolysis.

$$m_{\mathrm{H_2O}} = \frac{Q_{\mathrm{gas}} M_{\mathrm{H_2O}}}{nF} \tag{9}$$

Where: m_{H2O} is amount of lost water in grams; Q_{gas} denotes energy in C that is converted into gassing. M_{H2O} is the molar mass of water equal to 18.3 g·mol^{-1}. Presented relation can be directly used to estimate decrease of water in electrolyte of a one cell[7] assuming that water lost through diffusion can be neglected. For a complete water consumption of a 12 V SLI battery this value must by multiplied by 6 as this number of cells is connected in series. It must be noted that in case of the AGM batteries water loss means only the water vapour that has been released to the surroundings via safety valve or through possible leakages in the housing. It means that the calculation of the water consumption using (9) is not possible. The biggest part of gas evolved during operation is recombined thanks to the presence of COC. Modelling of water loss and its necessary parameters has already been described in [17] and [31]. Even though state-of-the-art SLI batteries are absolutely antimony free, which indicates that their gassing current rate should not vastly increase during operation as demonstrated in [49], still a moderate growth should be expected. This is due to

[6] This statement is not valid for automobiles that are being driven in Asia, especially in Japan where refilling of water is a common practice during every year inspection. However, Japanese battery makers are currently making decisive steps, which will lead to adaptation of the European standard housings also in Japan soon.

[7] Density of water equals 1 kg·l^{-1}.

presence of impurities that cannot be completely avoided. They cause reduction of hydrogen overvoltage and increase the current rate that flows into gassing as explained in [50].

3.1.3 Design of 12 V starter batteries

The overall design of the SLI PbA did not change within the last fifty years. Since 1960s a standard 12 V layout with six lead-acid cells connected in series remained unchanged [10] and it is still being used by most of the automotive industry. Even though the exponentially growing number of electrical loads within the last decades and introduction of μH functionality imposed additional technical requirements, the battery itself retained its classical appearance and internal build-up. However, the mentioned new requirements were a leading driver for some significant technological improvements. The most of them concerning performance have already been explained in the previous chapters. Concerning housing worth mentioning is development of double-lid technology, which avoids acid leakage while tilting or even turning the battery upside-down for a short time. Fig. 10 presents the classical prismatic layout of 12 V SLI battery. It should be mentioned that also cylindrical designs [12] with spirally wound electrodes are known. However, they have not been widely adapted due to their unavoidable volume loss between cells and further losses imposed by housing arrangements required by national and international standards.

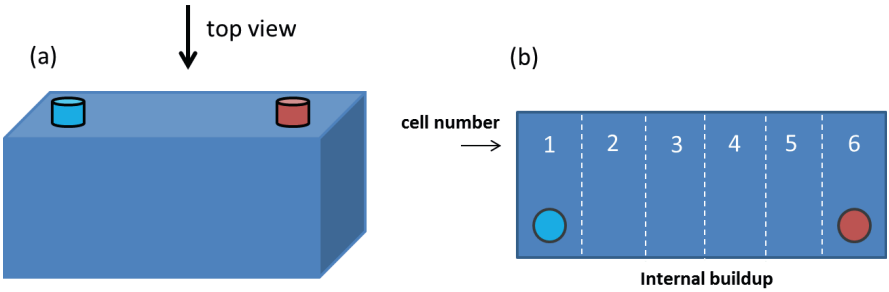

Fig. 10. Simplified graphical illustration of classical layout of the 12 V SLI battery: (a) front side, (b) top view.

In case of AGM batteries six cells are completely sealed so that COC can operate efficiently. Flooded and EFB batteries are vented, which means that each cell is connected to a main gas canal that ends up on both sides of the battery.

Fig. 11 depicts a simplified internal build-up of the classical design of a 12 V SLI battery. Cells are separated from each other by a dividing wall, which is usually made from polypropylene (PP), as well as the other parts of the housing. Each cell has got its own diluted sulfuric acid reservoir, which is not exchanged between cells. Furthermore, in case of AGM batteries the immobilized electrolyte cannot be exchanged between two different AGM separators even when they are in the same cell. Single cells are not accessible from the outside of the battery so that the only measurable voltage is the one of six cells connected in series. The standardized capacity of one plate equals 8 Ah (same height), which means that multiple plates must be connected in parallel to obtain higher capacities. It must be noted that this value is just an average and can noticeably vary from one plate design to another. The connection between cells, which is not directly visible in Fig. 11, can be found in Fig.

13. A schematic illustration of the positive electrode put into polyethylene (PE) separator pocket can be found in Fig. 12. It provides ionic conductivity and protects it from possible electric short-circuits. Such configuration refers to standard flooded and EFB batteries. For the negative electrode, the grid and plate design may vary but the general concept usually stays the same. Mentioned higher capacity, which is usually greater than 40 Ah for conventional and hybrid automotive applications, is realized by installing a higher number of alternately positioned positive and negative plates into stacks.

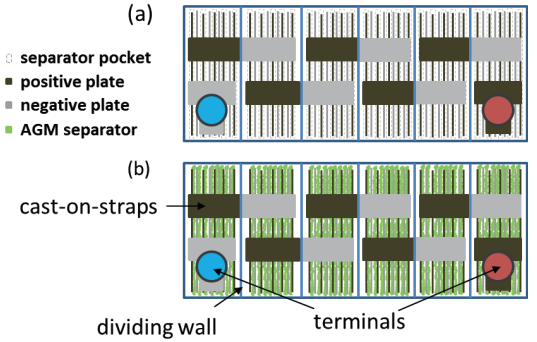

Fig. 11. Simplified internal build-up of 12 V SLI battery: (a) flooded and EFB design, (b) AGM design. Green colour of AGM separator has been chosen only for better visualization purposes.

Equation (10) presents a rule of thumb for calculating the number of both positive and negative plates in each stack (n_{plates}).

$$n_{\text{plates}} = \frac{C_{\text{N}}}{10} + 1 \tag{10}$$

Both electrodes are designed as thin flat plates, which provide a relatively low R_{ohmic} and therefore high specific power density. In order to compensate for corrosion positive grids are usually thicker. For SLI batteries their thickness typically lies in range of 1.2 – 1.8 mm, whereby negative plates are 1.0 – 1.4 mm thick. According to Pavlov [18] usually there is one negative plate more in each stack, which means that for 70 Ah battery there will be 8 positive and 9 negative electrodes in each cell. The main reason for this is increased discharge time with cold cranking current, which is directly linked to increased amount of NAM per cell [49]. This parameter is of high importance for SLI batteries.

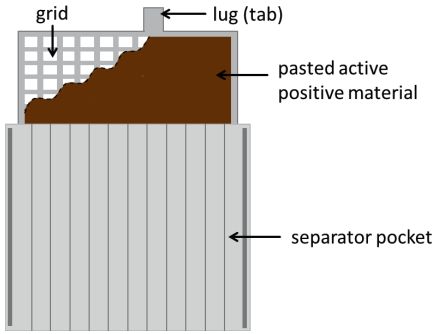

Fig. 12. Schematic illustration of the positive electrode design, which is typical for SLI batteries. Each installed positive plate is fully covered by the separator pocket and connected to the stack via cast-on-straps.

Parallel connection of flat plates is realized by so called cast-on-straps (COS), which are firstly brought on the lugs of either the positive or negative electrodes within one stack in liquid form during manufacturing and subsequently solidifies by cooling. A schematic drawing of their layout can be found in Fig. 13.

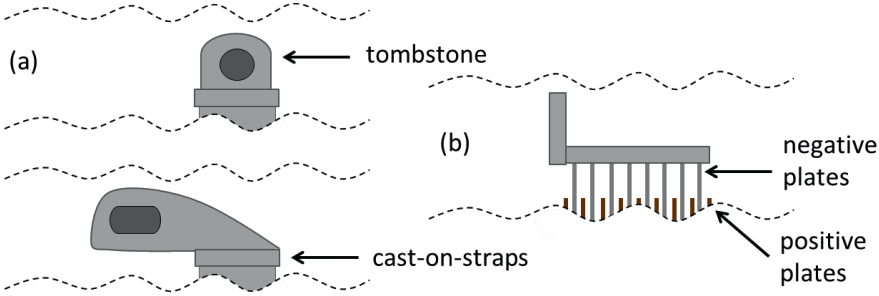

Fig. 13. Realization of the parallel connection in the stack of plates: (a) standard designs of COS, (b) side view of the stack with the alternatively positioned positive and negative electrodes.

COS of the positive and negative electrodes from different cells are being welded together, which provides electrical contact between cells and realizes series connection between them. Flat plates can be manufactured in different technologies. The most relevant ones are expanded, gravity cast, concast (continuous casting) and punched grids. More information about their features can be found in [18].

In the following section the concept of battery state detection methods with special emphasis on µH applications is presented. It briefly describes the requirements, state-of-the-art solutions

and actual challenges. Furthermore, most commonly used signal definitions describing battery state have been also elucidated.

3.2 Battery state detection algorithms

The functionality of BMS installed in μH applications focuses mostly only on pure battery monitoring, and it is realized by BSD algorithms. It means that the BMS do not have access to the EMS of the vehicle and cannot trigger any action even if it could be beneficial concerning the increase of the expected life or improvement of actual performance. In many stationary battery storage systems, this is also the case [51]. However, installations where BMS controls charging and discharging process as well as triggers refresh or equalization charging are also known [52][53][54]. Intensive refreshing charging that involves overcharging at high voltage level during extended time of several hours is only realizable in facilities with multiple string battery storage system or diesel generator. Operating in such conditions also allows performing periodical capacity check-ups, which are an enormous help for algorithms based on adaptation approaches. In case of μH applications with single 12 V SLI battery such measures cannot be carried out so that development of smart and accurate adaptation approaches is one of the most important and challenging requirement that must be faced by software developers.

Mentioned adaptivity is only one out of several targets that must be at least partly fulfilled by every state detection algorithm. Other possible targets consider:

- Accurate estimation of considered parameter that describes state of the battery in wide range of possible operation conditions.

- Simplicity (lack of complex mathematical operations) and relatively low amount of required dedicated internal memory, which makes it suitable for implementation in a low-cost EBS.

- Adaptivity, which provides high accuracy not only for new batteries but also for aged ones. Additionally, it should also be able to perform plausibility check and avoid adaptation when current results are not feasible.

- Scalability, which allows easy scaling of given approach to different battery sizes, types and technologies. Compatibility with products produced by various manufacturers is also crucial.

- Simplified calibration, which is not resource and time intensive.

- Numerical stability and robustness against measurement and modelling noise.

- Ability to estimate expected current error range. This represents crucial information for BMS. During operation, it is of high importance for safety critical functions, which mostly involve worst case calculation.

This subchapter provides detailed explanation of the state-of-the-art BSD solutions and discusses how they could be improved in a way that could significantly help to optimize operation and efficiency of each μH vehicle.

3.2.1 Generalized structure and definition of state defining signals

Generalized structure and implementation of BSD has been depicted in Fig. 14: the graphical illustration indicates division of BSD algorithms into four main categorizes:

- Core algorithms estimate considered state signals either continuously or in a fixed time intervals.

- Supporting algorithms are opportunity related solutions, which recalibrate or compensate inaccuracies of core algorithms if a given operation mode that can deliver additional information about actual battery state is detected. Good examples are extended rest periods or long driving phases with constant overcharging. Additionally, supporting algorithms are also approaches that extract further battery parameters from the input signals of EBS. R_i is such a parameter that can be obtained by means of passive electrochemical impedance spectroscopy (EIS) described in [55], which is performed using available current ripple originating from loads installed in the vehicle.

- Auxiliary algorithms are considered as additional functionality that complements classical functions of BSD. Examples are IFD solutions as well as all approaches that predict acid stratification, short-term and long-term DCA.

- Adaptation algorithms make sure that parameters of other algorithms get updated to the actual ageing progress of the given battery. Their implementation is necessary to keep low level of error throughout the whole battery life. In case of exchanging of failed OEM (original equipment) battery with a new one they also try to detect its technology and size to scale other approaches properly.

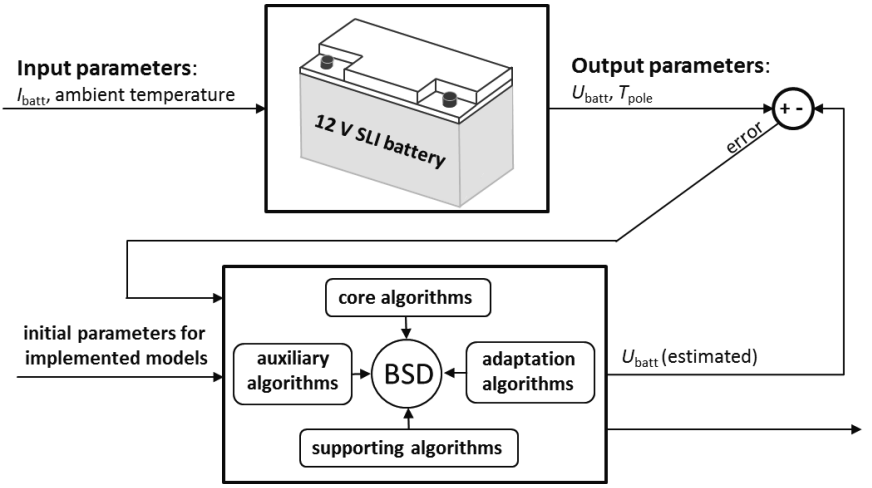

Fig. 14. Generalized structure and implementation of BSD.

3.2.1.1 State-of-charge

SoC is a fuel gauge of a battery, which defines how much charge is available for the user or all connected loads at a given time point. It can be specified as relation between actual capacity and capacity of a fully charged battery, which has been depicted in (11).

$$\mathrm{SoC} = \frac{\text{actual capacity}}{\text{capacity at a fully charged state}} \tag{11}$$

The term DoD, which is also widely used in the literature, denotes depths-of-discharge and equals 1 – SoC. At a first glance relation (11) seems to be clear and easy implementable. However, both of used capacities strongly depend on the current operation conditions, such as discharge current rate, temperature, battery health and short-term history. Pilatowicz et al. [14] described commonly used factors that lead to change of available actual capacity of 0.6% per 1 K and its reduction to approx. 55% C_N when discharge rate increases from nominal I_{20} to $20I_{20}$. Additionally, actual progress of ageing and the fact that most of brand new batteries are oversized up to 10% of C_N (difference between actual and rated capacity) further increase the complexity of SoC estimation. These issues have been thoroughly discussed by Sauer [56] and Jossen [22]. In this work term SoC is always related to C_N provided by the manufacturer, which should be reachable under nominal conditions. They refer to discharging at 25 °C with I_{20} until U_{batt} reaches 10.5V with preceding full charging according to EN norm 50342-1 [57], which suggests charging at 25°C with $5I_{20}$ and given maximal U_{batt} for 24 h that is the overall time of the whole charging procedure. In BMS of µH applications also two other definitions are commonly used. All of them have been illustrated in Fig. 15.

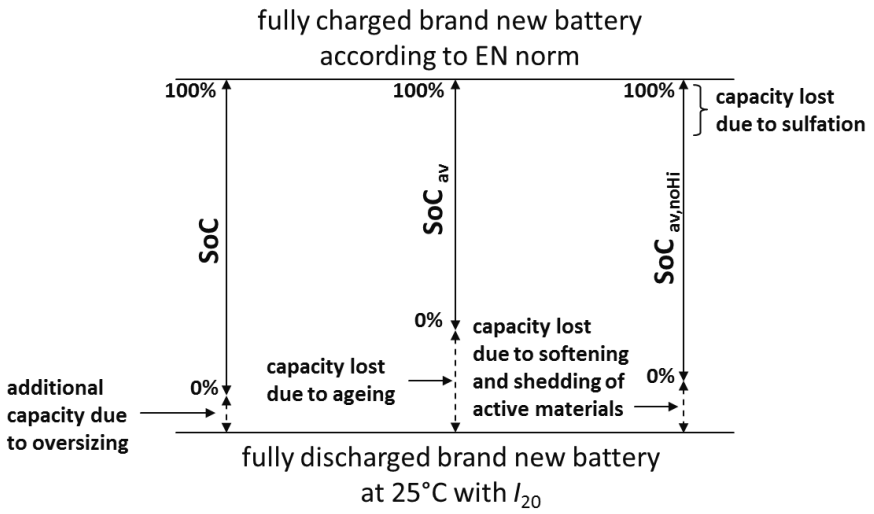

Fig. 15. SoC definitions commonly used in µH applications.

The first newly introduced definition, SoC_{av}, considers the capacity loss caused by ageing. The second one, $SoC_{av,noHi}$, also reduces the operation range due to ageing. However, it also distinguishes whether the capacity was lost due to reversible sulfation or irreversible softening and shedding of active materials. Only the latter one is limiting available SoC range. This is due to the HRPSoC regime used in uH applications that is related to operation at partial SoC, which is most often set to 80% in the considered case. Applying SoC_{av} triggers constant discharging to a new 80% level when additional capacity loss is detected. Using $SoC_{av,noHi}$ hinders it and helps prolonging battery life, which otherwise would much faster deteriorate due to increased sulfation induced by operation at lower SoC concerning real physical state of the battery.

3.2.1.2 State-of-health

The SoH is a crucial parameter concerning long-term condition of the battery. In most cases, it is specified as relation between C_N and actual capacity measured under nominal conditions, which has been shown in (12).

$$\mathrm{SoH} = \frac{\text{available capacity of fully charged battery measured at nom. conditions}}{\text{rated capacity provided by manufacturer}} \tag{12}$$

In case of µH applications factor that decides whether given SLI battery reached EoL directly corresponds to its cranking capability at low temperatures. Usually, it is assumed that failed cranking occurs with high probability when SoH lies in range of 0.4-0.5 leading to taking 0.5 as a worst-case threshold. This definition has been adapted and used throughout this work. It is because of direct dependency of developed models and their parameters to the actual value of capacity. Nevertheless, battery parameter that is directly correlated with cranking capability

should be linked to its R_i rather than available capacity. As it was the case with SoC, R_i can be also defined in multiple ways as explained by Pilatowicz et al. in [58]. The most often applied definition uses its purely ohmic contribution only. It corresponds to limited electron and ion conductivities of current collectors, active materials, terminals, connectors and electrolyte. Due to current rate and temperature dependency of R_{ohmic} it is normalized to 100% SoC and 25 °C, which has been denoted as $R_{0,25}$. Current value of $R_{0,25}$ is compared with the one typical for a brand-new battery as depicted in (13). If the relation indicates that actual $R_{0,25}$ is doubled than EoL is reached.

$$\mathrm{SoH}_{R_i} = \frac{R_{0,25}(t)}{R_{0,25}(t=0)} \tag{13}$$

Despite of the fact that definitions presented above describe battery long-term condition in a relatively good way, estimation or measuring of both R_i and actual capacity values is considered as challenging in a practical applications, especially in µH vehicles. This is the reason why very simplified methods are being used. The simplest one considers the time in operation meaning that regardless of the current state the battery is always exchanged after given time interval of several years. Counted time can be also weighted with the current operation conditions leading to shorter or longer expected life e.g. operation at elevated temperatures over an extended time usually significantly accelerates the battery ageing.

Another parameter which can be also categorized as SoH related signal is an IFD flag. It informs EMS if the battery state regardless of ageing can be assumed as acceptable considering possible occurrence of internal failure mechanisms. They are related to internal short circuits and sudden connection/capacity loss, which can significantly deteriorate battery performance either in short or long period. Development of novel solutions concerning this issue have been explained in chapter 6.

3.2.1.3 State-of-function

SoF signals usually refer to calculation of the available power in given conditions and under a given load profile. In case of µH vehicles it is most often directly associated with cranking current profile, shown in Fig. 16. Voltage drop imposed by maximal current rate during cranking denoted as $I_{crank,max}$ decides if ICE is going to be successfully restarted. If a resulting U_{batt} drops below a particular value lying in range of 7-8 V, successful cranking cannot be guaranteed anymore. It is due to minimal operation voltage of electronic control unit of ICE that controls fuel injection during starting. Schaeck et al. [26] introduced a minimal voltage specification at different phases applied for cranking capability estimation in case of warm cranking imposed by ASSF functionality. It provides two different voltage limits, the first one refers to minimal voltage caused by $I_{crank,max}$ and the second one corresponds to voltage level during the rest of the cranking profile. Mentioned voltage limits are 8 and 9.5 V respectively.

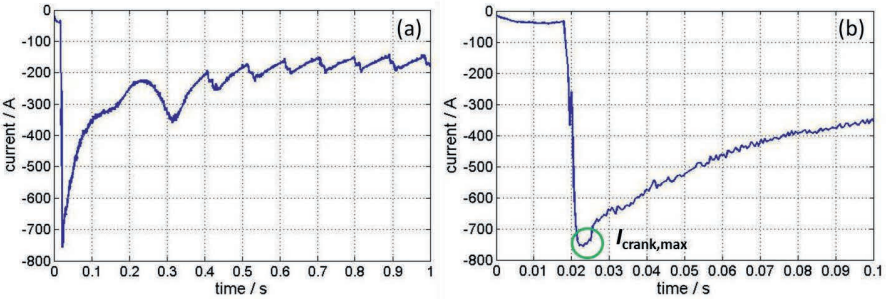

Fig. 16. Exemplary cranking current profile measured in the vehicle: (a) full duration of a cranking event; (b) zoomed first 100ms of cranking that highlights inrush current with its maximal value denoted as $I_{crank,max}$.

They impose implementation of two different SoF signals continuously estimated by BMS that could be called SoF_{V1} and SoF_{V2}. Information provided by these signals gives EMS a feedback about any risk of failed cranking assuming different scenarios. Examples are listed below:

- Cranking capability if the temperature drops to a level of -18 °C, which is called cold cranking capability.

- Cranking capability in case of airport scenario. This considers constant parking of the vehicle for 4-6 weeks, which is called long term cranking capability. Usually after such extended rest period SoC of the battery is reduced approximately by 25% due to presence of quiescent loads.

- Cranking capability after typical overnight parking phase. This is called short-term cranking capability.

- Warm cranking (or recranking) capability in case of µH vehicles with ASSF functionality. It very often considers pre-discharging phase with various current rates (up to 100 A). Two realizations are common, namely constant SoF estimation when the engine is already turned off and so called stop-enable variant. The latter one is used to decide during driving whether ASSF can stay switched on.

Based on this information the EMS can actively reduce the current load on the battery or set more intensive charging regime, which will ensure the cranking capability and reliability of the vehicle. Furthermore, EMS could theoretically inform the driver about the possible violation of the cranking capability. However, this functionality is rather unwanted and rarely implemented by the car makers so that the EMS has in most cases to fully care for the reliability of the vehicle. If BMS reports violation of the given limits, EMS can decide to crank the engine even before the end of idling period so that the trip can be safely continued.

Other known SoF definitions are rather used in different applications such as electric vehicles. In most cases, they impose calculation of maximal available time with given power or maximal power in a given time that can be accessed by the driver in certain conditions. However, they are not relevant for μH applications and have not been considered in this work.

3.2.2 Overview over the state-of-the-art solutions

BMS and battery monitoring of PbA has been a topic of numerous works presented by multiple researchers e.g. [22][53][54][55][59][60]. Many of the known approaches are relatively universal and can be applied for BSD regardless of the considered application or even used battery technology. However, deep and thorough understanding of application and its specification is necessary to develop highly accurate BSD algorithms e.g. implementing full charge detector in application where battery is never fully charged is not meaningful. Furthermore, each battery technology has its own exceptional features that must be known to avoid accumulation of unwanted errors. Good examples are hysteresis behaviour of NiMH batteries described in detail by Thele et al. [61] or very flat relationship between U_{00} and SoC of lithium-ion batteries with lithium-iron-phosphate cathode [62]. Overview over BSD algorithms relevant for μH applications with PbA technology has been provided in Table I, Table II and Fig. 19, following categorization presented in Fig. 14.

Methods used for SoC estimation are described in Table I. Most of them have been already elucidated in detail by Piller et al. and Meissner et al. in [63] and [13]. Their accuracy strongly depends on proper adaptation, which has been only partly discussed by the authors. It can be efficiently performed only in certain conditions. This statement has been emphasized by Budde-Meiwes et al. in [64], who showed that behaviour of PbA strongly depends on parameters such as short-term history, existence of acid stratification or actual charge or discharge current rate. Detailed explanation of EIS methodology used by the authors of [64] can be found in [40][65][66][67]. It is based on evaluation of the complex impedance that is obtained by means of division of inputted AC current and resulting answer in form of AC voltage. It can be carried out in form of one or multiple frequency measurement.

Most often applied adaptation algorithms, which can be employed for this task, are based on Kalman filter [68][69][70], self-adapting characteristic maps [55] or simple fitting approaches. The latter ones can be realized with or without storing of the historical data. An example of an approach that does not require any dedicated memory is recursive least-square algorithm [62].

Accurate SoH estimation is the most challenging task in μH applications. It is because of a narrow operation window at high SoCs and lack of full charging as well as full discharging. Simple observation of low sampled U_{batt} during discharging with low to moderate current rate in this range does not provide sufficient information about available capacity as schematically demonstrated in Fig. 17.

Cat.	Method	Comments
Core algorithms	I_{batt} integration (Ah counting)	Needs to be frequently recalibrated using supporting algorithms due to measurement errors, integration errors and presence of side reactions.
	Dynamic observer realized as linear model, look-up table or artificial neural network	It observes battery behaviour during operation with highly dynamic load profile. It requires extensive parametrization or reference measurements for each considered battery, which hardly ever consider all possible operation modes and conditions.
Supporting algorithms	Linear relationship between U_{00} and SoC	Direct measurement of U_{00} in the field conditions is not possible, especially at low temperatures. Extensive relaxation behaviour of PbA with charge short-term history should be considered as well as the impact of quiescent current. Additionally, ageing considerably impacts modelled linear relationship, which should be adapted for best results.
	Full discharge/charge detection	Full charging hardly ever happens in the field conditions, especially under HRPSoC regime typical for µH applications. Getting closer to full discharged state brings a risk of failed cranking that must be avoided.
	Estimation of I_{gas}	Significantly reduces necessary frequency of Ah counting recalibration. It is strongly influenced by ageing and requires adaptation
	Estimation of acid stratification	Helps reducing error imposed by acid stratification resulting in increased U_{batt} that mainly falsifies U_{00} estimation. However, known solutions require too high computational power for implementation in EBS.
	Electrochemical Impedance spectroscopy (EIS)	It is realized as passive EIS only. It means that only frequencies can be used, which are already included in the measured current profile. In most cases, only high frequency ($1 < f < 500$ Hz) excitation is available indicating that low frequency behaviour cannot be observed using this method.

Table I. Overview over SoC estimation methods relevant for µH applications.

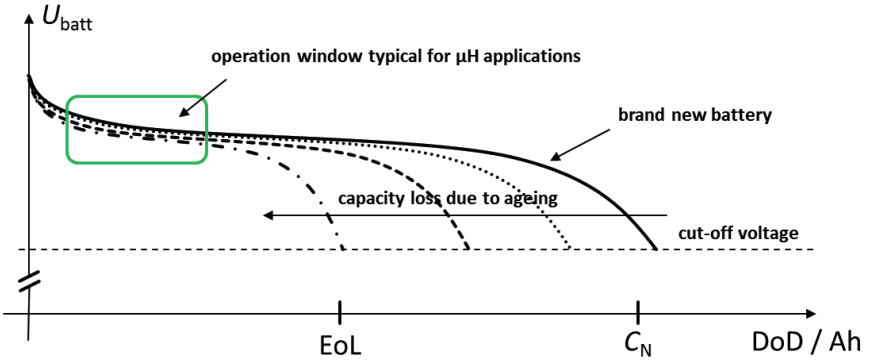

Fig. 17. Schematic illustration of voltage profiles, which are obtained by discharging PbA with increasing progress of ageing under nominal conditions.

SoH estimation algorithms, which are used in state-of-the-art solutions are described in Table II. Mentioned rain flow cycle counting algorithm has already been described by Meissner et al. in [10]. It counts cycles experienced by the battery, which can be further used for estimation of the battery stress. To increase accuracy weighting of the counted cycles with the current operation conditions such as current rate, average SoC or temperature is necessary. Exemplary weighting methods and derived factors of detected cycles or cumulative Ah throughput can be found in the work of Pilatowicz et al. [14] and Schiffer et al. [31]. Main disadvantage of this method is lack of any link to the current actual state of particular SLI battery, which can lead to unacceptable error in case when undetected exchange of battery occurs or battery characterized by entirely different performance than the one determined during parametrization is installed. It may happen not only for different battery products but also for the same battery size, type and technology, which has been manufactured in different manufacturing site or batch. Mentioned supporting methods partly address this issue, but their accuracy is limited due to pronounced non-linearity of PbA and extensive necessary parametrization routines, which are hardly ever carried out for all considered conditions. Because of many assumptions that need to be made, expected improvements of accuracy are in some cases not satisfactory. On the one hand Huet et al. [71] showed that conductance measured by an external device (applying EIS methodology) can provide useful information to detect potential batteries with internal defect. On the other hand, after thorough discussion, one of his main conclusions was the fact that the only accurate method of quantitative assessing SoH is deliberate discharging or performing capacity check-ups. Presented discussion indicates that currently there is no known simple and relatively universal method of SoH estimation that could deliver precise information (with accuracy better than ± 15-20% C_N) about SoH of the battery.

Prediction or estimation of SoF signals is most often performed using an electrical model. Depending on the chosen implementation and particular parameter, which has to be calculated, it is usually a modification of the generic equivalent electrical circuit (EEC) presented in Fig. 18. Its main advantage over the other methodologies is its universality. It can be very easily

adapted to simulate other battery technologies with the given accuracy and without major changes of the model structure. However, it requires appropriate testing equipment unless smart adaptive algorithms are introduced as explained by Waag in [72], e.g. EIS measuring device or battery tester and sufficient number of new batteries for calibration tests.

Cat.	Method	Comments
Core algorithms	Cycle counting (e.g. rainflow counting algorithm)	Demands extensive parametrization of each considered battery. Accurate estimation requires knowing of number of cycles until EoL as well as impact factors such as DoD, temperature, current rate, charging strategy and battery technology. This approach also does not consider a possible refresh charging.
Supporting algorithms	Observation of relationship between SoC and R_{ohmic}, which alters with ageing	For accurate estimation reaching low SoC is necessary. However, it may hardly ever occur in the field conditions (frequent driving).
	Long-term SoC observation	Capacity loss due to sulfation can be observed if SoC continues to drop (U_{00}) despite of highly positive Ah throughput and low temperature (e.g. operation in winter).
	Comparison of the U_{00} with the charge/discharge observer	In case when U_{00} is high but the voltage during discharging continues to drop as if the battery was nearly fully discharged, it indicates capacity loss due to softening of PAM. On the contrary, very low charging current as if the battery was fully charged and relatively low U_{00}, indicates capacity loss due to sulfation.
	Observation of the battery voltage during charging	Increasing sulfation causes earlier reaching of the constant voltage phase during charging. The accuracy of this approach is limited due to other factors that should be considered such as short-term history and current rate. This method requires also extensive parametrization measurements.
	EIS measurements	As in case of SoC it is only realizable in µH applications as passive EIS in the range of high frequencies. Known approaches are rather qualitative than quantitative.

Table II. Overview over SoH estimation methods relevant for µH applications.

Discussion about physical meaning of each element and necessary parametrization efforts can be found in [73][74][75][76][77][78][79][80]. The main aim of the quoted research was a

development of offline models for computer aided engineering and gaining better understanding of PbA behaviour. This is the reason why time and equipment intensive measurements are acceptable. However, in case of BMS much more simplified approaches are more common. Blanke et al. [66] introduced EEC model with one series resistance and only one RC element for cranking capability prediction. Generally, the longer considered time range is and the more operation conditions have to be considered the more RC elements are necessary for accurate SoF estimation.

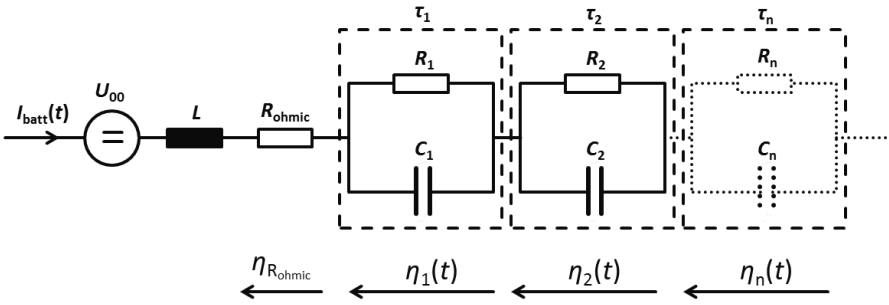

Fig. 18. Generic EEC (modified Randle's equivalent circuit [81]) applied for the simulation and modelling of electrochemical storage systems with arbitrary number of RC elements (time constants).

In most cases much of used EEC elements are fully empirical and their values originate from fitting of discharge and charge pulses. It indicates that taking a new battery type requires each time new parametrization that covers all operation conditions. SoF estimation has been schematically illustrated in Fig. 19.

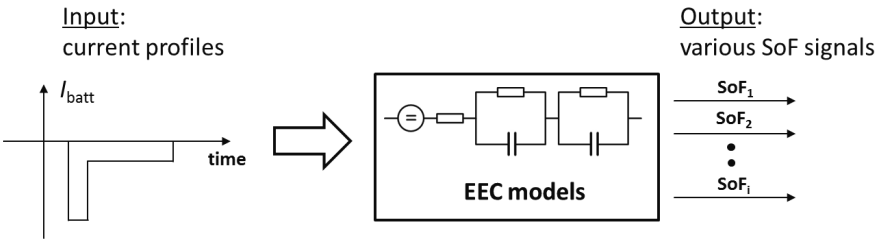

Fig. 19. Schematic visualization of SoF determination principle.

In case of SoF that correspond to cranking capability not only a proper EEC model has to be applied but also supporting algorithms that detect last $I_{crank,max}$ and adapt used current profile. As it is the case of SoC and SoH algorithms the most challenging target is the proper and accurate adaptation of the applied model. The more parameters are implemented the more complex and resource demanding it becomes. Waag et al. [72] presented a promising and

relatively easy to implement approach for available power prediction of lithium-ion batteries together with novel adaptation technique [82]. However, in case of PbA technology assumed symmetry between charge and discharge reaction cannot be applied. It is due to significantly different behaviour of PbA caused by side reactions and considerable inhomogeneities that must be taken into account.

3.2.3 Current challenges and possible advances

Current challenges in BSD for μH applications can be divided into the following targets:

- Improved SoF estimation related to cranking capability regardless of the current operation conditions and short-term history, which will result in accuracy below state-of-the art level of ± 400 mV. This should be valid for both considered cases, namely cold and warm cranking capability prediction.

- SoC estimation with accuracy that lies in range of at least ± 5% for all operating conditions, especially low temperatures. Currently, standard solutions are characterized by error above ± 10% SoC especially at temperatures below 10 °C.

- Reliable and adaptable SoH estimation with precision of at least ± 10% C_N.

- Long term DCA prediction, which will allow precise calculation of time that is needed to recharge the battery to a target average SoC, whereby the accuracy should be in the range of minutes. It is crucial for implementation of less conservative operation strategies that will allow higher usage of the battery and better fuel economy. Moreover, this will result in reduced CO_2 emissions in vehicles. Currently, operating with lower average SoC than 80% is hardly ever implemented due to increased risk of deep discharging. Such algorithm could efficiently help to address this issue.

- Simple and accurate estimation of acid stratification that could contribute to improved precision of all considered SoC, SoH and SoF algorithms.

- Technology and battery size detection in case of detected battery exchange.

- Reliable internal failure detection that could avoid instabilities in the power net and contribute to increased reliability of each μH vehicle considering current and future generations.

- Calculation of reliable and quantitative confidence intervals or quality factors of each state signal, which should be outputted together with estimated values. They are of high importance for EMS, which should know what are the realistic actual worst-case conditions.

All the listed issues should be solved in the most adaptable way leading to high precision for both brand new and aged batteries. Necessary parametrization efforts should be reduced to

absolute minimum. In ideal case SoC, SoH and SoF estimation should take place after observation of battery behaviour excited with short dynamic profile. Additionally, approaches that are based on passive EIS are suggested to be at least partly removed and exchanged with other methods. They use measured current ripple, which is considered as unwanted by car makers. Situation when a given load, which generates current ripple with a certain frequency range, is exchanged with ripple free solution would reduce accuracy and therefore should be avoided.

Further part of this work presents three approaches, which show how improved SoF and SoC estimation as well as internal failure detection can be achieved without implementation of complex and resource intensive algorithms. They also indicate significant advantages, which originate from physico-chemical background of the developed solutions. These are:

- Improved adaptivity resulting from known nature of the modelled phenomena and their characteristics.

- Reliable extrapolation to wide range of various operation conditions and reduced parametrization effort.

- Physical meaning of the adapted parameters, which can be used not only for original goal but also for calculation of other relevant parameters.

- Making feasible assumptions and simplifications that do not reduce validity of considered algorithms.

- Understanding of expected errors and their origins.

- Feasible plausibility check, which means that outputted state signals can be better self-diagnosed. Therefore, they can be treated with higher confidence.

4 Butler-Volmer equation based approach for dynamic voltage drop estimation

In this chapter an approach which can accurately determine the battery's dynamic response (BDR) has been developed. It is responsible for the estimation of the critical SoF parameters for the vehicle operation, such as short-term or long-term, warm and cold cranking capability. Especially for µH vehicles, where a wrong warm cranking capability prediction could lead to a vehicle breakdown in the middle of the traffic, these parameters are of high importance. Developed method is based on the well-known Butler-Volmer equation (BVE) that describes kinetics of electrode processes. It is specially optimized to be implemented in EBS, which is currently being installed in most the micro-hybrids and many higher class conventional vehicles. This chapter consists of both the theoretical description of the applied methodology and validation. The focus lays on the correct calibration, reduction of the parameters which have to be adapted during operation, scalability for the different battery sizes and technologies and smart integration with other components of the BMS.

4.1 Butler-Volmer Equation

PbA voltage response or overvoltage caused by the external current flow can be described by the following equation:

$$U_{\text{batt}} - U_{00} = \eta = \eta_{\text{ohmic}} + \eta_{\text{act}} + \eta_{\text{con}} + \eta_{\text{cry}} \tag{14}$$

where: η_{ohmic} is overvoltage caused by R_{ohmic} of the system; η_{act} is an activation overvoltage, which is related to the charge-transfer processes that occur in the active material/electrolyte interface; η_{con} corresponds to sum of the concentration related diffusion, migration and convection overvoltages; η_{cry} is a sum of crystallization and nucleation overvoltage.

The main scope of this research is modelling of η_{act} of the negative electrode, employing the Butler-Volmer equation, which after η_{ohmic} plays a key role in cranking capability prediction. For the sake of simplicity and validity with the applied equivalent electrical circuit approach it will be represented as the charge-transfer resistance (R_{ct}) in the further parts of this work, whereby R_{ct} can be divided into $R_{\text{ct,NAM}}$ (negative electrode) and $R_{\text{ct,PAM}}$ (positive electrode). Since in most cases it cannot be measured separately from the R_{ohmic} (or η_{ohmic}), the ohmic behaviour of the PbA has been analysed as well. This was necessary for the development of evaluation techniques, which can accurately extract the R_{ct} from the overall measured resistance e.g. obtained from a pulse tests in DC domain. Other mentioned overvoltages were neglected. Description of their behaviour and possible modelling approaches can be found in the work of Thele in [67]. At this point, it must be noted that an accurate BDR estimation using just R_{ohmic} and $R_{\text{ct,NAM}}$ is only valid for high current pulses in the range of tens of milliseconds. For pulses

up to several seconds $R_{ct,PAM}$ has to be taken into consideration as well. Calculation of BDR for longer time periods requires implementation of further resistances, which can be associated to the previously mentioned concentration and crystallization phenomena.

The Butler-Volmer equation (15), was published in [83]. It describes rate of the electrochemical processes expressed as the electrical current rate which occurs directly in the active material/electrolyte interface. In this context, the term velocity has to be understood as the number of moles per second of the active materials which are taking part in the electrochemical reaction. The first and second exponential term correspond to the anodic (positive currents) and the cathodic (negative currents) reaction respectively. In case of the PbA it can be used for modeling not only the kinetics of the charge-transfer phenomena but also the gassing (water electrolysis) reaction as presented in [84].

$$i = f(\eta_{\text{act}}) = i_0 \left\{ \exp\left[\frac{\alpha n F}{RT}\eta_{\text{act}}\right] - \exp\left[-\frac{(1-\alpha)nF}{RT}\eta_{\text{act}}\right] \right\} \tag{15}$$

where: i is an overall current rate, which is imposed by the given activation overvoltage, η_{act}; α is a symmetry factor between discharging and charging states, which are very often called in the literature cathodic and anodic respectively; i_0 is an exchange current, which can be also expressed as the multiplication of the specific exchange current density (i_0') which is a physical parameter of the system and the available active surface area (A) for the electrochemical reaction (16).

$$i_0 = i'_0 * A \tag{16}$$

In case of the PbA, negative electrode consists of highly porous lead as an active material. Main reaction during discharging can be described as depicted in (1). Charging is described by the same reaction but in an opposite direction. In case of lack of the concentration limitations (enough available reaction reagents, namely Pb^{2+} and HSO_4^- ions) and negligible impact of crystallization or deposition phenomena, the only effect which causes appearance of the overvoltage is the dissolution process. It is followed by the diffusion of the Pb^{2+} and SO_4^{2-} ions to the place where deposition of lead ions to lead sulfate takes place. These processes are treated together in this study. They are being modelled by the provided implementation of the BVE (15). The number of the electrons, n, involved in electrochemical reaction equals two.

Fig. 20a), b) and c) show three current-overvoltage plots obtained from BVE. Each one depicts the impact of varying one of three available parameters, namely α, i_0 and n. Additionally, Fig. 20c illustrates the influence of the temperature without varying of the mentioned parameters.

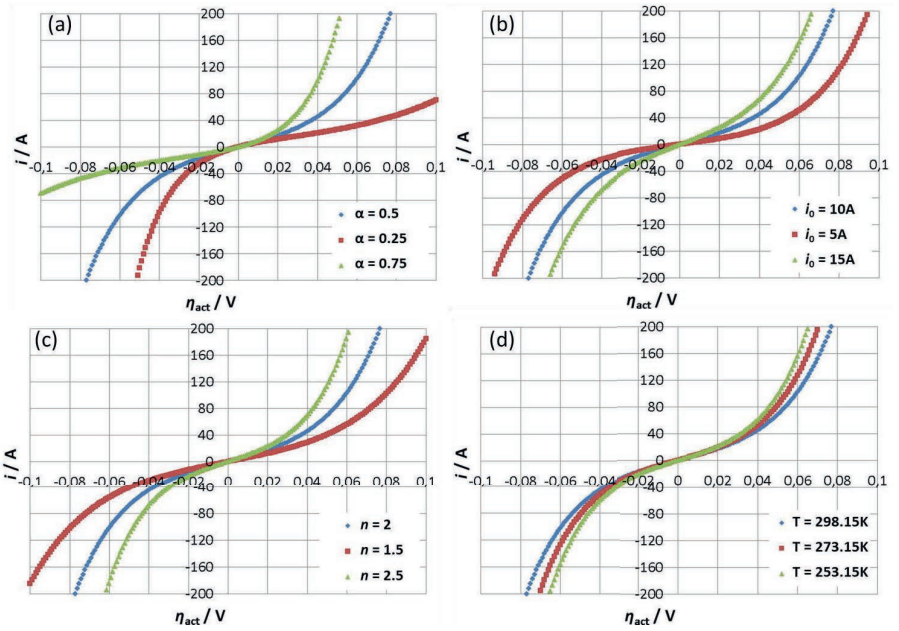

Fig. 20. Overall current rate obtained from BVE (14) by means of varying different parameters (if not mentioned otherwise $i_0 = 10$ A, $\alpha = 0.5$, $n = 2$ and T = 298.15 K): (a) α; (b) i_0; (c) n; (d) T. Presented characteristics are related to one-cell system.

Slight decrease of the charge-transfer resistance, especially for the low current rates can be noticed from the given characteristics. It is caused by the reduction of the temperature voltage (U_T), which is specified as presented in (17) and equals approx. 26 mV for the temperature of 25 °C (298.15 K).

$$U_T = \frac{RT}{F} \tag{17}$$

The following statements can be derived from the attached graphs:

- In case of the same or very similar kinetics of both charging and discharging reactions, the symmetry factor (α) equals 0.5. In this case the resulting current-overvoltage relation can be assumed as the same. A good example of such an electrochemical storage system is the lithium-ion battery as demonstrated by Waag et al. in [85]. However, PbA are very non-linear energy sources and their α parameter lies in the range of 0.2-0.3 as reported in [86] and [40].

- Reducing or increasing the symmetry factor (α) causes a significant increase of R_{ct} in direction of charging and discharging respectively. It can be observed as a much higher η_{act} resulting from the same current rate.

- Increasing or decreasing of the exchange current rate (i_0) causes a symmetrical decreasing and increasing of the η_{act} respectively. It has to be noted that the resulting current-overvoltage curves are changed in the same manner throughout the whole considered current range.

- Changing of the number of electrons involved in the electrochemical reactions causes an effect like varying the i_0 parameter. However, it can be noticed that the low current range is not influenced in the same manner as the high current range. It can be concluded that fully empirical modification of the n parameter can increase the accuracy of the model, especially in the high current range.

To obtain a previously mentioned charge-transfer resistance (R_{ct}), which will be used for the further modelling, implementation and analysis, the BVE from (15) has to be differentiated as presented in (18).

$$\boldsymbol{R_{ct}^{-1} = \frac{di}{d\eta_{act}} = i_0 \frac{nF}{RT}\left\{\alpha \exp\left[\frac{\alpha n F \eta_{act}}{RT}\right] + (1-\alpha)\exp\left[-\frac{(1-\alpha) n F \eta_{act}}{RT}\right]\right\}} \tag{18}$$

Fig. 21 illustrates the R_{ct} as a function of the overall current rate. The chosen visualization shows the impact of the same parameter variation as illustrated in Fig. 20. Additional details concerning the theory of BVE and its application in the modelling of the generalized electrode kinetics of the arbitrary electrochemical systems can be found in the work of Erdey-Gruz [87] and Bode [88].

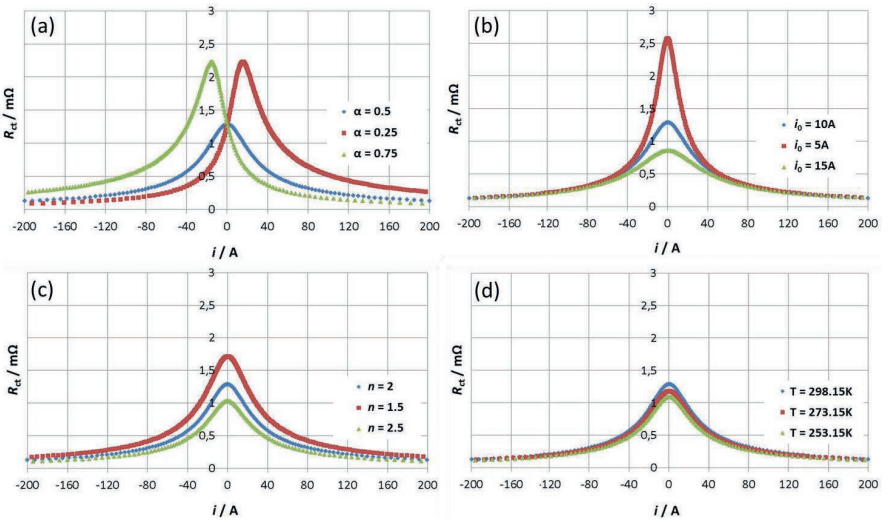

Fig. 21. R_{ct} obtained from BVE (15) by means of varying different parameters (if not mentioned otherwise $i_0 = 10$A, $\alpha = 0.5$, $n = 2$ and T = 298.15 K): (a) α; (b) i_0; (c) n; (d) T. Presented characteristics are related to one-cell system.

If either the high current range or the low current range is considered as the focus of interest, the BVE shown in (15) can be simplified. For higher discharging current range the resulting overvoltage must fulfil the condition from (19). Then, BVE can be represented just by one exponential term, which has been presented in (20) and illustrated in Fig. 22.

$$\eta_{\mathrm{act}} \gg \frac{RT}{nF} \tag{19}$$

$$\begin{aligned} i = f(\eta_{\mathrm{act}}) &= i_0 \left[exp\left(\frac{\alpha nF\eta_{\mathrm{act}}}{RT} \right) \right], \nabla i > 0 \\ i = f(\eta_{\mathrm{act}}) &= i_0 \left\{ exp\left[-\frac{(1-\alpha)nF\eta_{\mathrm{act}}}{RT} \right] \right\}, \nabla i < 0 \end{aligned} \tag{20}$$

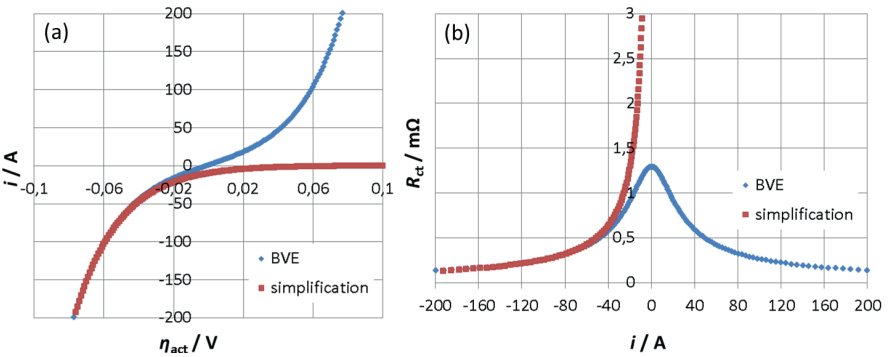

Fig. 22. Simplification of BVE for high discharge current rates (20) (i_0 = 10 A, α = 0.5, n = 2 and T = 298.15K): (a) current-voltage characteristics, (b) relationship between current rate and resulting R_{ct}. Presented characteristics are related to one-cell system.

Equation (15) can be further simplified to the form depicted in (21), which is widely known as Tafel equation and originates from the work of Julius Tafel [89].

$$\eta_{\mathrm{act}} = a + b \lg i \tag{21}$$

where: a is an empirical parameter that corresponds to the activation energy of the used materials and considered processes; b is called Tafel slope and decides about the inclination of the resulting characteristic. It is very often employed for the analysis of gassing processes as presented in [20].

If the considered current rate is relatively small so that the activation overvoltage fulfils the relation from (22), BVE can be simplified to the form depicted in (23) and illustrated in Fig. 23. Simplifications presented in (20) and (23) can be very helpful for a simplified analysis of the considered processes or for the implementation of the BVE in a BMS that is realized on a microcontroller with limited computational power and internal storage.

$$\eta_{act} \ll \frac{RT}{nF} \tag{22}$$

$$\begin{aligned} i &= \frac{i_0 nF}{RT}\eta_{act}, \nabla i > 0 \\ i &= -\frac{i_0 nF}{RT}\eta_{act}, \nabla i < 0 \end{aligned} \tag{23}$$

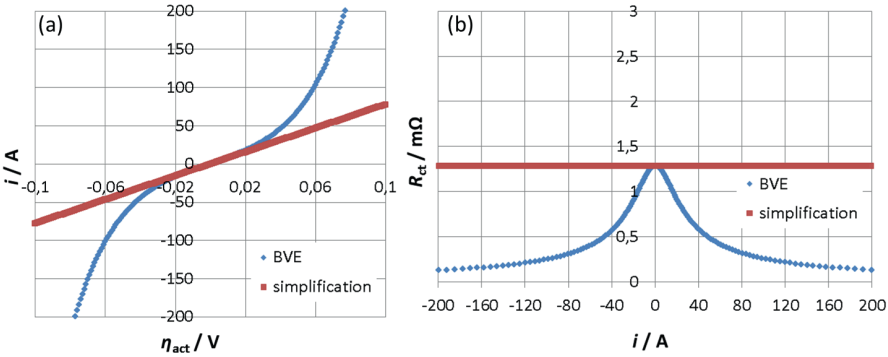

Fig. 23. Simplification of BVE for low discharge current rates (23) (i_0 = 10 A, α = 0.5, n `= 2 and T = 298.15K): (a) current-voltage characteristics, (b) relationship between current rate and resulting R_{ct}. Presented characteristics are related to one-cell system.

Due to the fact, that temperature and SoC strongly influence the speed of the electrochemical processes occurring in PbA, it is widely known that for a good accuracy of each electrical model also these parameters should be considered. Expected influences of temperature and SoC on the i_0 have already been published by Champlin et al. [90] and can be observed in qualitative manner in Fig. 24.

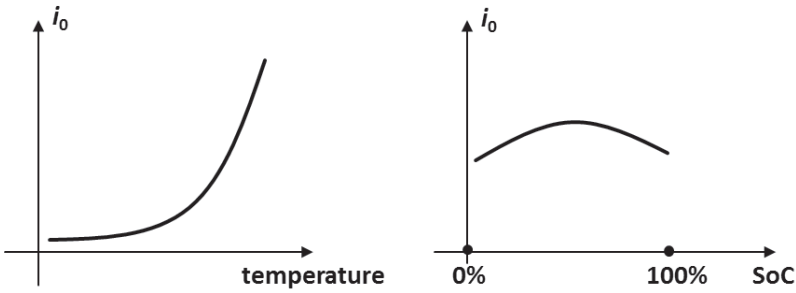

Fig. 24. i_0 parameter as the function of the temperature and SoC.

Temperature dependency results from the widely-known Arrhenius law [91], which can be briefly summarized as doubling of the electrochemical reaction's speed per increase of ten

degrees in Kelvin scale. Impact of SoC can be explained by means of the available number of sites for the electrochemical reaction to take place (3). When the battery is at high SoCs the charge component of BVE tends to zero because the amount of available $PbSO_4$ sites goes to zero (charging and discharging or anodic and cathodic ionic current must be equal in equilibrium). Similarly, the same process occurs when the battery approaches the range of low SoCs (limited number of Pb sites). Measured values are shown and discussed in Chapter 4.3. Shukla [92] and Hariprakash et al. [93] obtained R_{ct} characteristics that originate from the same behaviour of parameter i_0.

4.2 Electrical model of the negative electrode

This subchapter briefly explains dynamic modelling of PbA technology using EEC approach and smart implementation of BVE as a core of the electrical model developed for the estimation of the NAM overvoltage.

4.2.1 Dynamic modelling of lead-acid batteries

Adaptation of generic EEC battery model depicted in Fig. 18 for PbA has been shown in Fig. 25. All presented elements have been directly associated to physical phenomena, which they model.

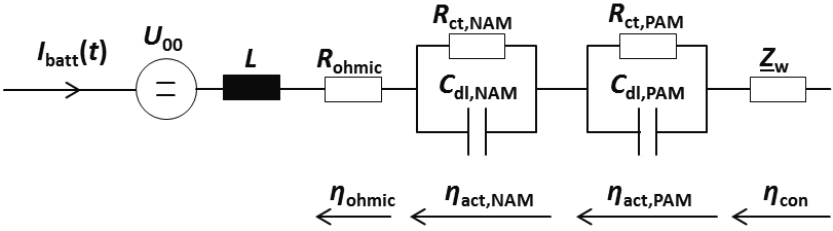

Fig. 25. Adaptation of generic EEC model for simulation of PbAs dynamic behaviour.

Additional elements which have not been explained yet are $C_{dl,NAM}$ and $C_{dl,PAM}$ as well as L and $\underline{Z}_w$. The first both capacities refer to double-layer capacity of NAM and PAM respectively. Parameter L describes the inductance of the internal parts and poles of PbA which is mostly notable in a high frequency range. In case of SLI lead-acid batteries which are in the scope of this work its impact can be neglected, due to its relatively low value which typically lies in the range of several hundreds of nH. $\underline{Z}_w$ describes concentration related effects. It can be modelled by the means of the Warburg impedance, which has been described in detail in the work of Mauracher et al. [75]. Modelling of the concentration phenomena is not in the scope of this work and will be neglected in the further analysis.

Fig. 26 depicts a correlation between the model from Fig. 25 and the impedance spectra measured using the EIS method. As it was mentioned before the influence of the inductance is clearly visible in the high frequency area, where the imaginary part of the complex impedance is positive. The ohmic resistance can be directly associated with the minimum value of the real

part of the complex impedance measured in the whole considered frequency range. The first and second visible semi-circles correspond to the charge-transfer resistance connected in parallel with the double-layer capacitance of the negative and positive electrode respectively. The last, low frequency range shows the impact of the concentration related effects and is neglected in this work.

Complex impedance of the model presented in the Fig. 25 can be analytically described by (24), whereas parameter $\underline{Z}_w$ has been neglected.

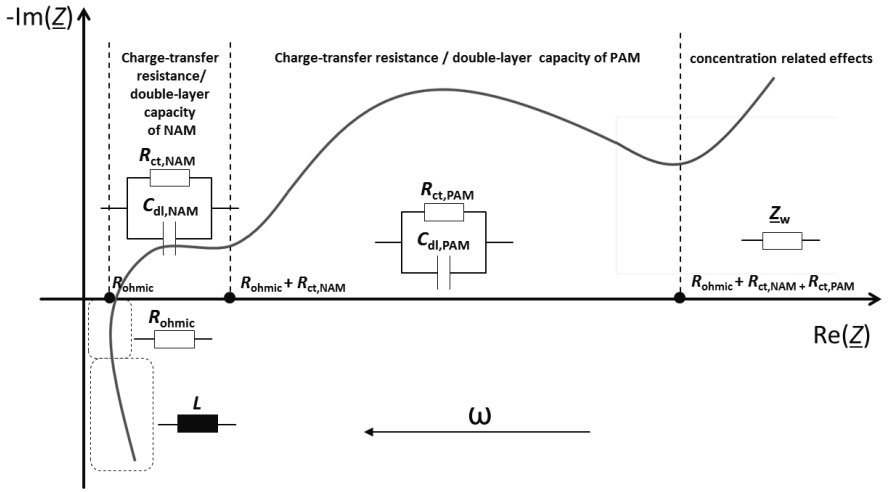

Fig. 26. Correlation between employed EEC of PbA based on Randle's theory and EIS test results represented by the Nyquist graph.

$$\underline{\boldsymbol{Z}} = \mathrm{Re}(\underline{\boldsymbol{Z}}) + \boldsymbol{j}\mathrm{Im}(\underline{\boldsymbol{Z}}) \tag{24}$$
$$= \boldsymbol{j\omega L} + \boldsymbol{R}_{\mathrm{ohmic}} + \frac{\boldsymbol{R}_{\mathrm{ct,NAM}}}{(\boldsymbol{j\omega})^{\xi_1}\boldsymbol{R}_{\mathrm{ct,NAM}}\boldsymbol{C}_{\mathrm{dl,NAM}} + \boldsymbol{1}}$$
$$+ \frac{\boldsymbol{R}_{\mathrm{ct,PAM}}}{(\boldsymbol{j\omega})^{\xi_2}\boldsymbol{R}_{\mathrm{ct,PAM}}\boldsymbol{C}_{\mathrm{dl,PAM}} + \boldsymbol{1}}$$

Parameters ξ_1 and ξ_2, which have not been described yet, are depression factors and will be explained later in this chapter. A RC element with additional depression factor will be called ZARC element in the further analysis.

Values of all elements presented in the model in Fig. 25 can be obtained by employing any non-linear fitting algorithm, e.g. least mean-square based one, and fitting of the obtained EIS measurement results in the relation shown in (24). Resulting parameters are only valid for the given working point, which consists of a superimposed DC current rate, SoC, SoH and internal temperature of the battery under test (BUT). Due to this reason and high non-linearity of the PbA, a measurement procedure that consists of many working points mainly related to the

application is necessary for having a good accuracy in the range of the considered conditions. Depression factors model the non-ideal capacitive behaviour of the double-layer capacitance. Their value is typically in a range from 0 up to 1, whereas an ideal capacitor is represented by ξ that equals one. ZARC element cannot be directly modelled in DC domain and can be only approximated by a specific number of pure RC elements connected in series (same approach as illustrated in Fig. 18). Because of that Thele in [67] investigated different values of depression factors and their impact on the accuracy of the model represented just by single RC elements without any additional parts in DC domain. He concluded that for ξ higher than 0.8 simulation with single RC elements provides satisfactory results. For values from 0.6 up to 0.8 and less than 0.6 an empirical employment of respectively 3 RC and 5 RC elements was necessary.

Fig. 27 presents the measurement results of a BDR test performed on a 74 Ah flooded battery equipped with standard hydrogen electrode (see Fig. 29), which was subjected to a discharge current pulse of -200 A. It clearly shows the validity of the chosen EEC.

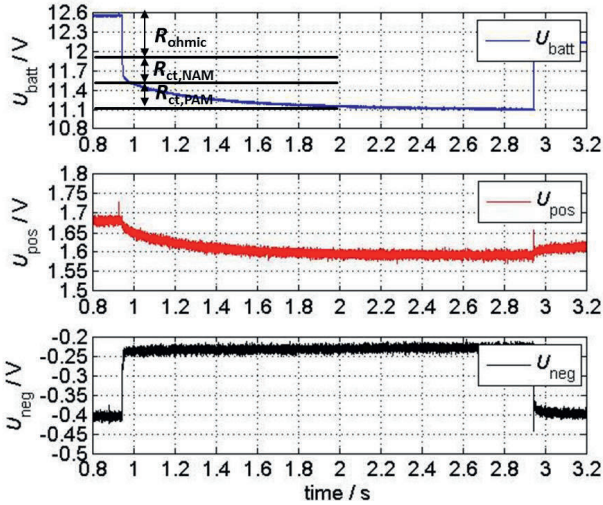

Fig. 27.Pulse test results performed on 74 Ah standard flooded battery conditioned to 70% SoC and 25 °C. Induced discharging current rate equals 200 A. U_{pos} and U_{neg} mean the potentials of the positive and negative electrode respectively (voltages measured using standard hydrogen electrode provided by Gaskatel GmbH).

4.2.2 Adaptation of Butler-Volmer equation for simulation of negative electrode

The dynamic behaviour of NAM can be modelled by employing the simplified electrical equivalent circuit, which has already been presented in Fig. 25. After simplification, the model takes the form of a simple RC element, which is depicted in Fig. 28.

Kirchev et al [80] and Kowal [65] derived a model with 2 RC elements connected in series, whereas the first one is related to the mentioned charge-transfer and non-faradic double-layer

processes and the second one corresponds to additional overvoltage caused by ion transfer through adsorption layer formed by the expander[8] molecules.

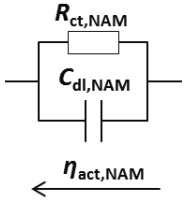

Fig. 28. Equivalent electrical circuit of NAM.

Furthermore, additional adsorption effects of hydrogen ions have also been considered. They form the third RC element, which can mainly be observed at very low frequencies. At this point it must be noted that these effects can only be measured by means of half-cell EIS measurement. To perform such a test additional hardware and intrusion in the interiors of the battery is necessary. Due to these requirements, it cannot be practiced in the field but exclusively in a laboratory environment. Highly dynamic modelling of the negative electrode in a high current range, which is in the scope of this work, considers only time constants in the range of milliseconds. This fact together with the complexity of the low frequency phenomena and their noticeable appearance only during long pulses with relatively small DC currents resulted in the employment of a model with one RC element, i.e. the impact of low frequencies has been neglected.

Half-cell EIS measurements have been carried out to prove the validity of the assumption saying that the first semicircle (Fig. 26) of the impedance spectra measured on the SLI lead-acid battery can be directly associated to NAM. Furthermore, these measurements also showed if this assumption can be used for the parameterization of the model presented in Fig. 28. The resulting impedance spectra are shown in Fig. 25 and Fig. 26. Schematic representation of the used test setup has been illustrated in Fig. 29. During the EIS measurements voltage of the whole battery, positive and negative electrode (U_{batt}, U_{pos} and U_{neg} in Fig. 29) was logged and used for the calculation of the complex impedances of each channel. Battery tester and EIS measurement unit used in this test was Digatron BNT 200-018-4ME and EIS-Meter, whereby the latter one was developed at ISEA [66].

Fig. 30 and Fig. 31 (own study) clearly show that regardless of the conditions and superimposed DC current rate the measured first semi-circle can be directly associated to the negative electrode, which proves previously mentioned assumptions. Furthermore, at discharge current rates above $20I_{20}$, which are relevant for most of the SoF estimation algorithms, low frequency

[8] Term „expander“ refers to the additives which are added to the negative active material. More information about their role in the system can be found in [18].

semi-circles are not visible anymore. Therefore, the validity of all simplifying steps mentioned earlier is proven.

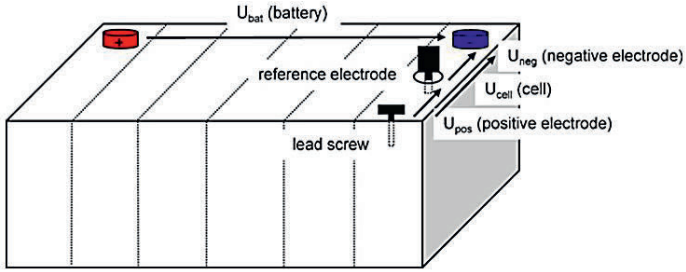

Fig. 29. Test setup for the EIS measurements of the positive and negative half-cell [64]. Used reference electrode was a standard hydrogen electrode provided by Gaskatel GmbH.

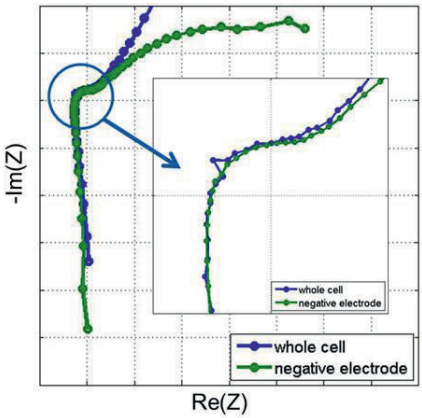

Fig. 30. Comparison of the impedance spectra of the whole cell and negative electrode measured on a 70 Ah AGM battery conditioned to 90% SoC and 25 °C. Superimposed DC current equals zero. Complex impedance of the single cell was obtained by dividing of the obtained impedance by the number of cells, which in case of SLI batteries equals six.

For better understanding of the chosen approach, it has to be emphasized that the $R_{ct,NAM}$, which is being calculated using the BVE, corresponds to the faradaic processes and therefore steady-state response of the negative electrode. It means that the overall overvoltage caused by R_{ohmic} and $R_{ct,NAM}$ for the given discharge current rate will be fully visible only after the time corresponding to at least three four time constants. It is due to the presence of the double-layer capacity (Fig. 28), which is being charged in this time and reduces the current that flows directly through the charge-transfer resistance. In stationary state the double-layer capacity is fully

charged or discharged and can be assumed as a brake in the circuit, where no current is flowing and $I_{batt} = I_{Rohmic} = I_{Rct,NAM}$ (Fig. 25).

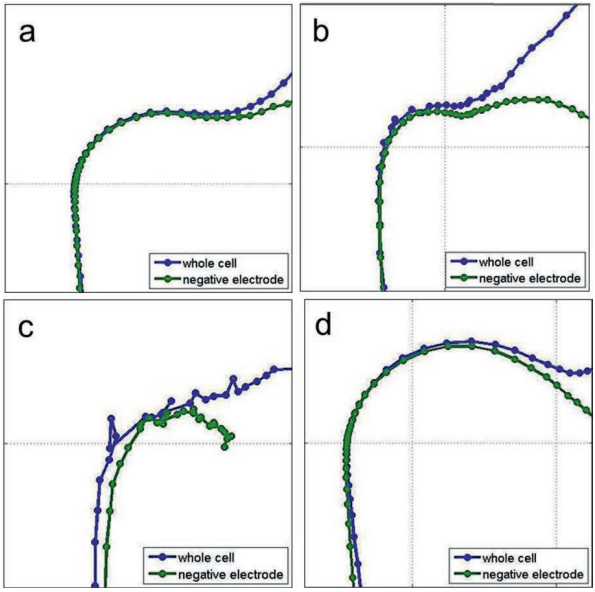

Fig. 31.Comparison of the impedance spectra of the whole cell and negative electrode measured on a 70 Ah AGM battery: (a) 90% SoC, 0 °C, no superimposed DC current; (b) 70% SoC, 25 °C, superimposed DC current of $-I_{20}$; (c) 70% SoC, 25 °C, superimposed DC current of $-20I_{20}$; (d) 70% SoC, 0 °C, superimposed DC current of $2I_{20}$.

Schematic visualization of the possible model implementation is presented in Fig. 32. It has to be emphasized that $C_{dl,NAM}$ shown in the picture corresponds to the effective double-layer capacity (25). Furthermore, in order to get an output, which is valid for the whole 12 V SLI battery and not just for one cell the values of the double-layer capacity and output activation overvoltage ($\eta_{act,NAM}$) have to be multiplied by six.

$$\boldsymbol{C}_{\mathrm{eff,NAM}} = \frac{\mathbf{1}}{\left(\boldsymbol{R}_{\mathrm{ct,NAM}} \cdot \boldsymbol{C}_{\mathrm{dl,NAM}}\right)^{-\frac{\mathbf{1}}{\xi_1}} \cdot \boldsymbol{R}_{\mathrm{ct,NAM}}} \tag{25}$$

After carrying out of the parameterization tests and fitting routines it was concluded that the parameters α and n of the BVE can be kept constant without significantly decreasing the accuracy of the model. With these assumptions, the employed form of BVE can be rewritten to the form depicted in (26). It must be noted that i_0 is additionally strongly influenced by the remaining capacity of the given battery as well. This issue will be addressed in the further part of this study.

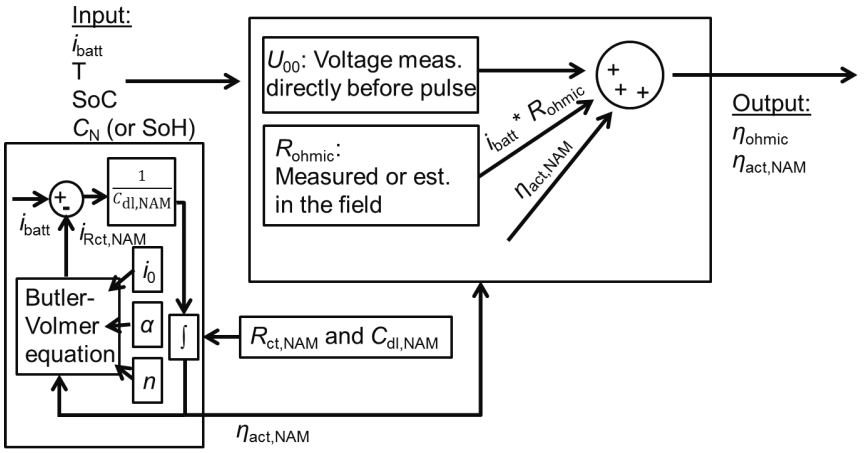

Fig. 32. Schematic representation of the developed electrical model of NAM. Characteristics of BVE is SoC, temperature and C_N (SoH) dependent. Used $C_{dl,NAM}$ values and their dependencies come directly from the performed EIS parameterization tests described in chapter 4.3.

$$i = f(\eta_{act}) = i_0(\mathrm{T,SoC,SoH})\left\{\exp\left[\frac{\alpha n F \eta_{act}}{RT}\right] - \exp\left[-\frac{(1-\alpha) n F \eta_{act}}{RT}\right]\right\} \tag{26}$$

Concentration limitations cannot be neglected in the following cases:

- Severely aged battery
- Very low temperatures (relatively slow diffusion of the ions in the solution)
- Relatively long discharging phase in the range of several seconds with current rate above 200 times of the nominal twenty-hour rate (SLI batteries)
- Very low SoCs (highly depleted electrolyte)

In these conditions, there are not enough reactants (1) for the reaction to take place with the speed induced by the flowing current. Thus, an additional voltage drop or resistance increase will appear during the measurement. To increase the validity of BVE so that the model can accurately predict BDR even in such conditions, additional concentration related terms as presented in (27) must be included.

$$\begin{aligned} i_{batt} = f(\eta_{act}) = i_0(\mathrm{T,SoC,SoH})\Bigg\{&\left(\frac{c_{HSO_4^-}}{c^0_{SO_4^{2-}}}\right)^{\gamma_{HSO_4^-}} \exp\left[\frac{\alpha n F \eta_{act}}{RT}\right] \\ &- \left(\frac{c_{Pb^{2+}}}{c^0_{Pb^{2+}}}\right)^{\gamma_{Pb^{2+}}} \exp\left[-\frac{(1-\alpha) n F \eta_{act}}{RT}\right]\Bigg\} \end{aligned} \tag{27}$$

where: c^0_{HSO42-} and c^0_{Pb2+} correspond to the equilibrium concentrations of the HSO_4^- and Pb^{2+} ions in the pores of the active material respectively; c_{SO42-} and $cPb2+$ are current concentrations of the HSO_4^- ions Pb^{2+} ions in the pores of active material respectively; γ_{HSO42-} and γ_{Pb2+} are empirical coefficients which can be given a constant value of 1.5 as reported by Thele in [67]. Typically, for the SLI batteries under discharge conditions, terms with Pb^{2+} ions can be neglected.

Calculation of introduced concentration terms can be realized by an additional mass transport and $PbSO_4$ solubility model that considers spatial resolution of the modelled battery. An example of such an implementation can be found in [67]. However, relatively high computational power and storage space demand makes it not suitable for the implementation in the BMS that is the main scope of this study. Visualization of the discussed phenomena can be observed in Fig. 33.

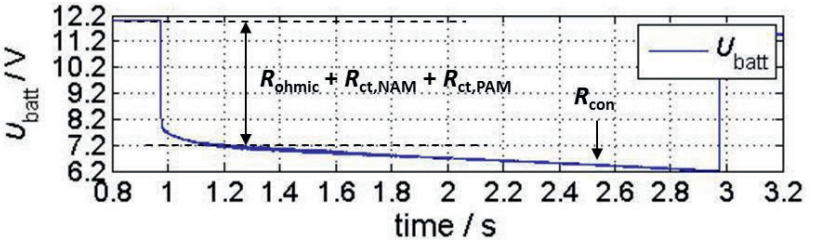

Fig. 33. Pulse test results performed on a 74 Ah flooded battery conditioned to 25 °C and 20% SoC. The battery under test was subjected to a 700 A pulse.

4.2.3 Implementation in BMS

BMS are usually implemented on a hardware platform with the given initial parameterization. For the accurate estimation of a voltage response of the battery subjected to a given load profiles it is necessary to know the method and accuracy of the ohmic internal resistance measurement. It usually happens that R_{ohmic} delivered by the BMS is not a pure internal resistance but it consists of some unwanted parts of the other resistance contributions. In order to get a pure R_{ohmic} the hardware has to be able to measure voltage and current rate with a very high sampling frequency of at least 2 kHz. It should be chosen in a way that the resulting value corresponds to at least 1 kHz resistance obtained from the EIS measurement as explained by Pilatowicz et al. [58]. This issue has been presented in Fig. 34.

It can be assumed that pure R_{ohmic} contribution corresponds to the minimum value of the real part of the measured impedance spectra at the given conditions (28). In most cases for SLI batteries it is located around the 1 kHz frequency. If the considered frequency is smaller than 1 kHz as it is most commonly the case in the field, the obtained resistance will include an additional part of the $R_{ct,NAM}$. However, even higher frequencies are necessary for the measurements at low SoCs and deep temperatures as presented in [66].

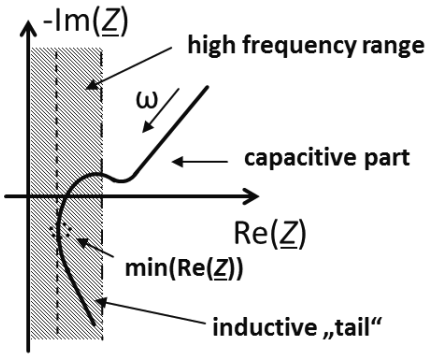

Fig. 34. Schematic representation of the impedance spectrum measured at high frequencies.

$$\boldsymbol{R_{\text{ohmic}} = \min(\text{Re}(\underline{Z}))} \tag{28}$$

Due to the fact, that $R_{\text{ct,NAM}}$ and R_{ohmic} are nearly always measured together (limited sampling frequency of the used low-cost hardware) and in the end their sum has to be valid for reaching the very high accuracy, the values calculated by the developed model have to be empirically corrected so that the relation from (29) is fulfilled. Otherwise, additional error will be introduced and accuracy of the BMS will automatically be noticeably reduced.

$$\boldsymbol{R_{\text{dynamic}} = (R_{\text{ohmic}} + \Delta R) + (R_{\text{ct,NAM}} - \Delta R)} \tag{29}$$

The developed algorithms can be implemented on a platform, which allows measurement of the internal resistance that corresponds to a maximal frequency smaller than 1 kHz. In such case, empirical correction is necessary. This can be realized by adjustments of parameter α and i_0 of the employed BVE (26).

Another important issue regards the fact that accurate prediction of the cranking capability or maximal voltage drop caused by inrush currents does not require the simulation of entire dynamic behaviour of NAM. Thus, considerable simplifications can be applied. Usually, minimal voltage (U_{crank}) occurs after time interval of several milliseconds counted from the beginning of a cranking event (see Fig. 16) and corresponds to stationary overvoltage involving R_{ohmic} and $R_{\text{ct,NAM}}$. It means that this calculation does not require implementation of $C_{\text{dl,NAM}}$, which can be neglected (Fig. 35). This assumption is valid for a wide range of field conditions, especially for operation at low temperatures. However, it is possible that a noticeable deviation emerges between predicted and measured voltage while operating at elevated temperatures. This refers to a much higher expected value of NAM time constant typical for these conditions, which could lead to extended transient period resulting in overestimation of U_{min}. This situation is even more likely if battery size significantly exceeds 60 Ah, which indicates even higher value of time constant.

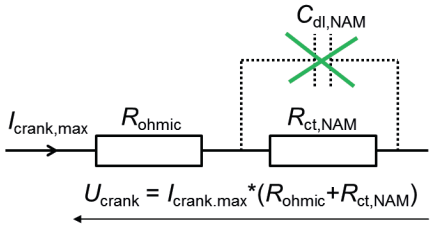

Fig. 35. Simplification of the applied battery equivalent circuit: neglecting of $C_{dl,NAM}$ and focusing on the calculation of the stationary voltage drop caused by modelled $R_{ct,NAM}$.

PAM is characterized by 70 times higher time constant than NAM as explained in [46], which means that it can be also fully neglected for cranking capability prediction. Exemplary separation of dynamic response between NAM and PAM has been depicted in Fig. 36.

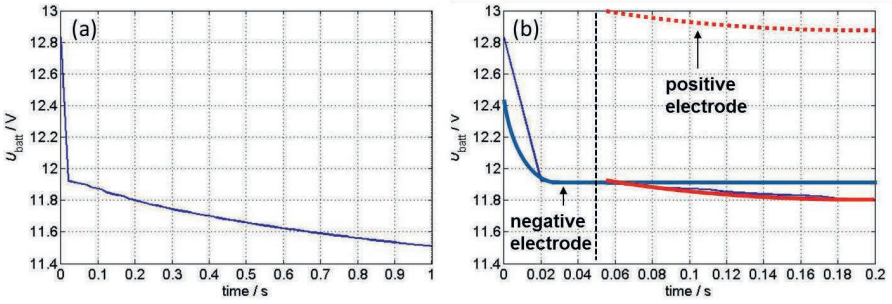

Fig. 36. Exemplary separation of the dynamic response between the negative and positive electrode, 74 Ah flooded battery conditioned to 25 °C and 90% SoC, 200 A discharge pulse: (a) battery voltage during the whole one second pulse; (b) separation of the overvoltage caused by charge-transfer resistance of the negative and positive electrode.

4.3 Calibration methodology and results of validation

Developed model can be parametrized and validated by means of both EIS methodology and discharging pulses. However, the former approach provides small-signal resistance, which is a derivative of overvoltage over current (18). It cannot be directly compared with the large-signal resistance obtained from the test results in DC domain. The difference between these two resistances has been illustrated in Fig. 37.

Presented current-voltage characteristics show clearly that at small current rates the difference between small and large-signal resistance is negligible. However, at high current rates it must be taken into account. The effect of this is graphically presented in Fig. 38.

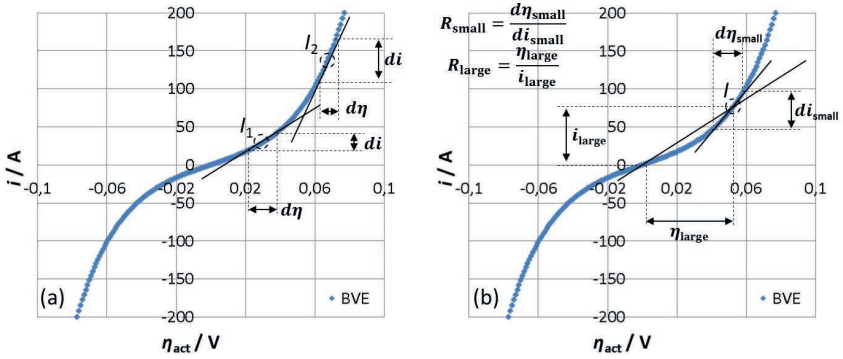

Fig. 37. Difference between small-signal and large-signal resistance: (a) extraction of the small-signal resistance from the two different working points; (b) comparison of the small-signal and large-signal resistance for two different working points.

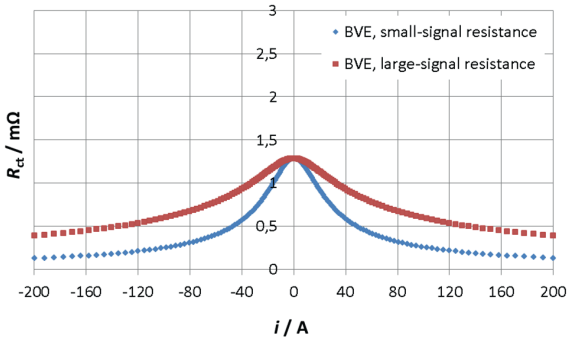

Fig. 38. Direct comparison of the small and large-signal resistance resulting from BVE (15) (i_0 = 10 A, α = 0.5, n = 2 and T = 298.15K).

The large-signal resistance can be automatically calculated from the small-signal resistance. This operation can be done by applying the relation from

(30).

$$\eta_{act} = \int R_{small}(I_{DC}) \cdot dI_{DC}$$
$$R_{large} = \frac{\eta_{act}}{I_{DC}} \tag{30}$$

4.3.1 Calibration measurements

A final calibration of the developed model has been performed using EIS methodology with supporting discharge pulses that have been imposed after collecting impedance spectra. It is

due to main limitation of EIS tests with superimposed DC currents related to violation of quasi-stationarity when BUT gets discharged more than 5% DoD. This means that at high current rates only very few high frequencies can be measured in the available measurement time, leading to lack of information related to the first semi-circle that corresponds to $R_{ct,NAM}$. Working ranges that have been considered during parametrization of three specimens, namely 74 Ah standard flooded, 60 Ah AGM and 44 Ah standard flooded battery have been listed below:

- Temperatures: -20 – 50 °C
- SoCs: 20 – 90%
- EIS with superimposed DC current rates: 0, ± 0.5I_{20}, ± I_{20}, ± 2I_{20}, ± 4I_{20}, ± 10I_{20}, ± 20I_{20}
- Discharge pulses: 50, 100, 150, 200 A (maximal current rate of the applied tester)

As previously mentioned it was found that the only parameter, which has to be modelled as variable is i_0. Other parameters of BVE have been kept constant throughout the whole parametrization. Main fitting condition of i_0 that had to be fulfilled was a minimum value of error between resulting $R_{ct,NAM}$ from BVE and measured $R_{ct,NAM}$ from impedance spectra for discharging currents. Fig. 39 presents large-signal resistances obtained from BVE fitted for different SoC at temperature of 25 °C. Fitting results have been divided into two ranges. The first one corresponds to currents typical for cranking events and the second one refers to discharging phases during a trip. The latter ones are usually present in the modern µH vehicles.

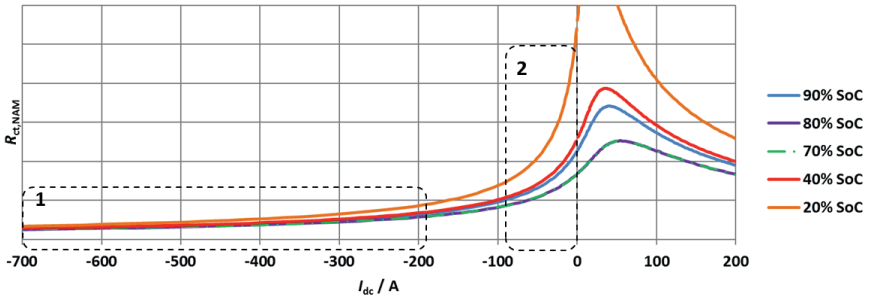

Fig. 39. Impact of SoC on the large-signal resistances obtained from the fitting of the BVE, 74 Ah standard flooded battery conditioned to 25 °C. Current ranges typical for: (1) cranking events; (2) discharging phases during a trip (ASSF).

This relation shows clearly that SoC is hardly influencing the *R*ct,NAM in the current range typical for cranking events. For -700 A current rate the difference between 40% SoC and 80% SoC equals 50 uΩ. This value corresponds to 35 mV estimation error of the voltage drop. Furthermore, employing minimal current rate of -200 A gives an expected maximal absolute error of 40 mV (0.2 mΩ). These values lead to a conclusion that the influence of SoC can be

neglected if such a limited accuracy can be accepted. This statement is valid for lower temperatures as well.

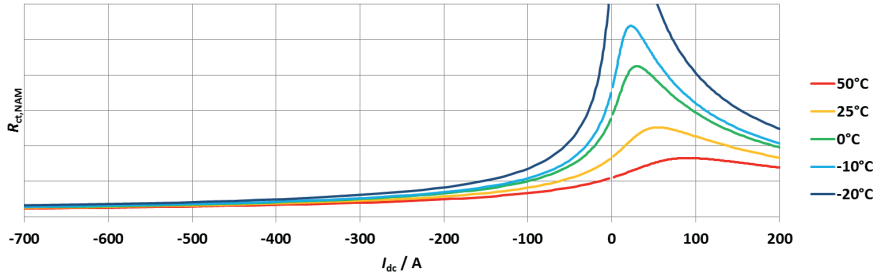

Fig. 40. Impact of temperature on the large-signal resistances obtained from fitting of BVE, 74 Ah standard flooded battery conditioned to 80% SoC.

Fig. 40 illustrates the impact of the temperature on the fitting results. As expected, it strongly influences the behaviour of resulted large-signal resistance in the 2nd current range. Neglecting the impact of the temperature for the current rate of -700 A (0.1 mΩ) can lead to the maximal expected absolute error of 70 mV. In case of -200 A and -50 A this value rises to the level of 120 mV (0.6 mΩ) and 110 mV (2.2 mΩ) respectively. Neglecting of BVE together with its dependencies and taking the constant value of Rct,NAM measured at 80% SoC, 25 °C and -700 A for cranking current rates and -100 A for additional discharging phases imposed by ASSF leads to the error of 250 mV and 150 mV respectively. Obtained errors correspond to neglecting certain dependencies only. In the field conditions their value will significantly increase due to modelling and measurement noise as well as other effects involving varying short-term history and pronounced inhomogenities of PbA technology.

4.3.2 Scalability analysis

Scalability is an important factor, especially for implementation of the algorithms such as the BVE in BMS. It provides a feeling and shows if the parameters obtained from the calibration measurement could be scaled and directly used for the diagnostics and modelling of batteries of different sizes. In case of the SLI batteries the chosen scaling factors can be C_N or remaining capacity (C_{rem}). According to Thele [67], i_0 can be linearly scaled with C_{rem} for the batteries of different size but the same design, technology and manufacturer. This statement has been verified in this section. Furthermore, scalability for other technologies, designs and manufacturers was analysed. Examination of scalability was performed on the batteries described in Table III. It involved EIS testing at varying SoCs and temperature of 25 °C. i_0 values has been extracted by means of fitting of the employed BVE to the measurement results described in the previous chapter.

Number	Battery
1	74 Ah standard flooded, manufacturer A
2	60 Ah AGM, manufacturer A
3	44 Ah standard flooded, manufacturer A
4	60 Ah standard flooded, manufacturer A
5	95 Ah standard flooded, manufacturer A
6	60 Ah EFB, manufacturer A
7	60 Ah standard flooded, manufacturer B
8	70 Ah standard flooded, manufacturer B
9	80 Ah standard flooded, manufacturer B
10	70 Ah AGM, manufacturer C
11	60 Ah EFB, manufacturer D

Table III. List of batteries tested for scalability analysis.

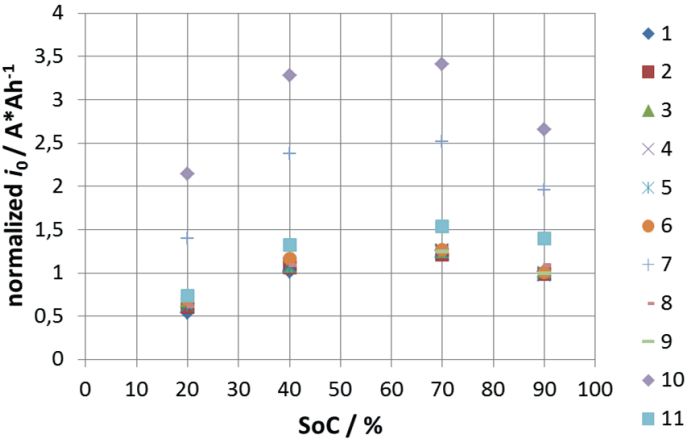

Fig. 41. Scalability of investigated batteries. i_0 has been linearly scaled using C_{rem}. All measurements have been carried out at 25 °C. Presented values have been normalized with i_0 obtained from evaluation of test data originating from tested battery no. 1 conditioned to 25°C and 90% SoC.

From Fig. 41 eight out of eleven analysed batteries behave in very similar way and can be characterized by similar values, whereby two of them can be considered as not scalable due to their much higher values of parameter i_0. BUT no. 11 can be classified as scalable or hardly scalable in comparison to the eight easily scalable batteries. Batteries number 7 and 10 are not scalable with data originating from other batteries and are characterized by significantly higher values of the i_0 parameter in the whole considered range. This means that the charge-transfer resistance obtained from BVE with these values will be noticeably lower than in case of the other batteries. Summarizing, the obtained relations could be treated as standard or worst-case implementation, which will not lead to voltage drop estimation error that could cause any failure. A good example of such a case is negative cranking capability prediction (failed cranking) for a battery which eventually will manage to start a vehicle. According to the presented results this statement is valid regardless of the applied battery manufacturer, type and technology. Observed lack of scalability for limited number of batteries could be explained by means of oversizing of negative electrodes by battery manufacturers, as already reported by Garche et al. in [94]. It must be emphasized that for the considered case the applied scaling factor was C_{rem}, which assumes that both electrodes are scaled in similar way. In case NAM is oversized and PAM limits C_{rem}, much higher values of i_0 (higher A) should be measurable as it was the case in presented analysis. Lower size of NAM would result in reduced C_{rem}. For a more accurate statistical analysis more batteries should be tested and analysed, particularly AGM and EFB batteries of different manufacturers, designs and sizes.

4.3.3 Validation with pulse tests

The main task of the developed model is to predict the dynamic response of the negative electrode. To validate a series pulse tests were carried out. The only and most important requirement is a reliable ohmic internal resistance measurement technique prior the pulse tests. In this way, this resistance value can be subtracted from the obtained overall dynamic resistance. Additional prerequisite is the employment of equipment with relatively high sampling rate that allows measurement of time constants in range of several milliseconds. This is usually the case of negative electrode discharged with high current rates.

Fig. 42 presents a schematic visualization of the implemented testing procedure. It can be noticed that special emphasis has been put into the investigation of the impact of different short-term histories, which are neglected by the model. Before imposing of each pulse R_{ohmic} estimation using EIS measurement without any superimposed DC current was carried out. Determination of the resulting $R_{ct,NAM}$ was conducted in two steps. In the first step the overall R_i of the battery was calculated by dividing measured voltage drop by the current rate. Used voltage drop refers to voltage difference between U_{batt} registered before the pulse and after 4 time constants corresponding to the negative electrode (Fig. 25). The value of the used time constant has been obtained from the parametrization tests. Because it is smaller for very high currents, two different values have been used for 200 and 700 A pulses (20-40 and 10-20ms respectively). The second calculation step consisted of subtraction of R_{ohmic} measured using EIS methodology from the R_i obtained from the first step, which resulted in obtaining final $R_{ct,NAM}$ value.

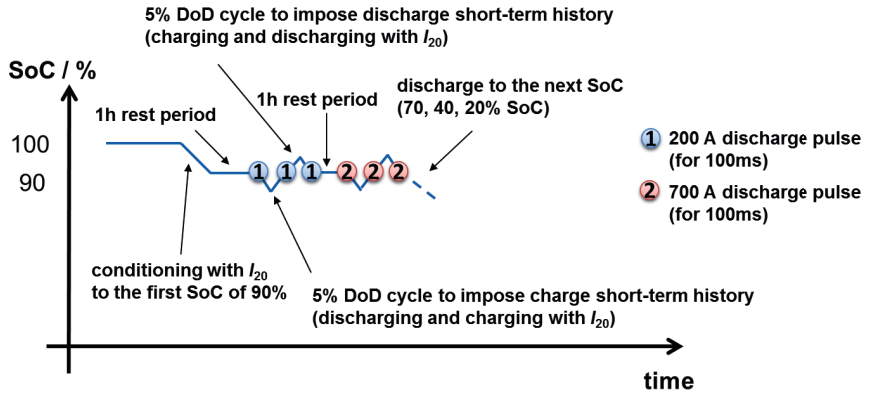

Fig. 42. Schematic representation of the carried-out validation pulse test. The first three pulses are characterized by the current rate of 200 A while the last three by a current rate of 700 A. Detailed description of the used testing protocol can be found in chapter 9.3.1.

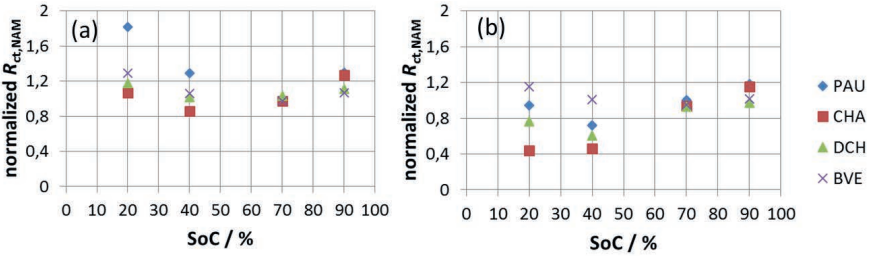

Fig. 43. Results of discharge pulse tests with different short-term history performed on 74 Ah standard flooded battery conditioned to 25 °C: (a) 200 A; (b) 700 A. Presented values have been normalized to measurement point obtained at 70% SoC (PAU).

Fig. 43 depicts the comparison between the $R_{ct,NAM}$ estimated by the model and obtained from the pulse tests. Very good correlation can be observed, especially for all results obtained at 70 and 90% SoC. At the low SoC scattering of the ohmic internal resistance and generally not fully reproducible behaviour of flooded PbA, makes the evaluation of measured data a challenging task. This can be indirectly noted from the increasing variation of the values resulted from pulses with different short-term histories. Presented results indicate that the best match is achieved with the pulses that were preceded by discharging. This statement can be linked with the specification of the calibration tests, where the parameters are mainly extracted from EIS measurements performed during discharging.

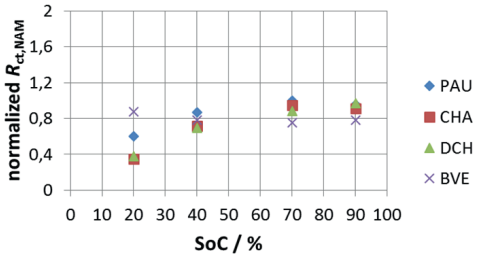

Fig. 44. Results of 700 A discharge pulse tests with different short-term history performed on 44 Ah standard flooded battery conditioned to 25 °C. Presented values have been normalized to measurement point obtained at 70% SoC (PAU).

Fig. 44 illustrates pulse tests result of the 44 Ah standard flooded battery. It has to be noted that -700 A current rate is much higher than the cold cranking current printed on the label of the tested battery that equals 440 A. This explains relatively high deviation of the model in the low SoC range. It can be linked to the additional diffusion overvoltage that influenced the test results. Nevertheless, good correlation between the estimated and measured $R_{ct,NAM}$ in the high SoC range has been recorded.

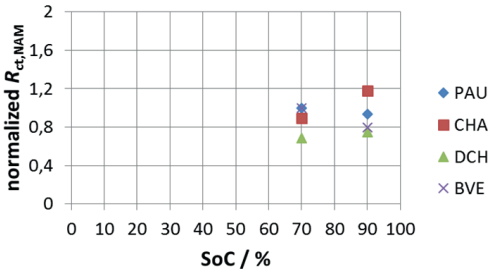

Fig. 45. Results of 200 A discharge pulse tests with different short-term history performed on 60 Ah AGM battery conditioned to -20 °C. Presented values have been normalized to measurement point obtained at 70% SoC (PAU).

Test results recorded from the pulse tests with 60 Ah AGM battery at -20 °C has been presented in Fig. 45. Even higher scattering of results for different short-term histories is clearly visible in comparison to the case of 25 °C (Fig. 43). Furthermore, yet again better correlation of the $R_{ct,NAM}$ predicted using the developed model and measurement results with discharge short-term history can be clearly seen. This fact does not have to be necessary considered as the disadvantage of the implemented solution. It is because of the additional discharge phases imposed by ASSF, which at least for cranking capability prediction always inflict short-term discharge history. An additional error of the conducted scalability procedure can be observed in the Fig. 46. It can be noticed that the estimated values of $R_{ct,NAM}$ in the whole considered SoC range are smaller than measurement results. It is due to the higher estimated value of i_0 from a

parameter set obtained after scaling (chapter 4.3.2) that resulted from the initial fitting of BVE to the parametrization test results of the considered battery type.

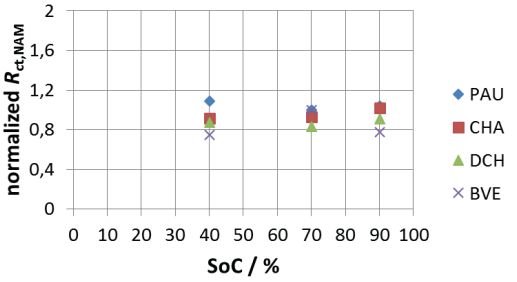

Fig. 46. Results of 200 A discharge pulse tests with different short-term history performed on 60 Ah AGM battery conditioned to 0 °C. Presented values have been normalized to measurement point obtained at 70% SoC (PAU).

Average absolute value of error resulted from the comparison of all performed pulse tests equalled approximately 0.2 mΩ and 0.1 mΩ in case of 200 A and 700 A discharge pulses respectively. It leads to respective expected voltage drop prediction error of 40 mV and 70 mV, which can be considered as an acceptable result for the target application, namely BMS for µH vehicles. If all short-term histories (charge, discharge and rest period) are considered, mentioned errors must be doubled due to increased error reported for validation pulses imposed after charging and extensive time at rest.

4.3.4 Validation with synthetic driving profile

Pulse tests described in the previous chapters provide a good insight into the accuracy of the developed model considering different conditions and short-term histories. However, these tests are rather static, which means that the battery is not being tested in a reasonable dynamic regime as it is the case in the field. Direct vehicle tests could be an option but their main disadvantage is a high variety of many parameters from one test to another, which cannot be avoided. It means that a trip with the same velocity profile, temperature profile, rest periods, etc. is hardly possible to reproduce. Due to this, a synthetic driving profile has been developed. It is designed to be carried out using laboratory equipment including programmable battery tester, climate chamber and arbitrary internal resistance measurement technique, which in this case was realized by additional short EIS measurements. The test consists of a conditioning routine and five days of simulated driving. Table IV presents an overview of carried out tests and types of batteries.

battery	Initial SoC [%]	T [°C]
74 Ah standard flooded	80, 60, 40	10, -10
60 Ah AGM	80, 60, 40	35, 10, -10
44 Ah standard flooded	80, 60, 40	10, -10

Table IV. Testing conditions and batteries used for validation with synthetic driving profile.

Fig. 47 shows voltage and current profile measured during validation test with synthetic driving profile at 10 °C performed using 74 Ah standard flooded battery with initial SoC of 80%. Developed test consists of seven different phases, which has been highlighted on the voltage curve. They can be described as follows (detailed description of applied testing protocol can be found in chapter 9.3.2):

1) Three initial cycles carried out at 25 °C that consist of discharging with I_{20} until battery voltage of 10.5 V is reached and subsequent charging for 24 hours with $5I_{20}$ and 16 V (14.7 V in case of AGM batteries) constant voltage phase. They are finished with rest period of 18 hours, which is necessary for temperature setup (in this case 10 °C) and subsequent discharging with I_{20} to target initial SoC (in this case 80%).

2) First day of urban driving that comprises 2 hours of dynamic driving profile which imitates driving with ASSF and 22 hours of rest period with key-off load.

3) Second day of driving which simulates a relatively long trip on a motorway, which ends up with short urban driving phase. It is succeeded by a long relaxation phase with key-off load.

4) Further day of urban driving that consists of slight changes in comparison to the first one. They will be described later.

5) Additional day of urban driving with minor changes. As the in the case of 4) it will be described later.

6) Last day of driving with deep discharge phases.

7) Full charging for 24 hours with $5I_{20}$ and constant voltage phase set to 16.0 V (14.7 V in case of AGM batteries). In this phase the ambient temperature equals 25 °C.

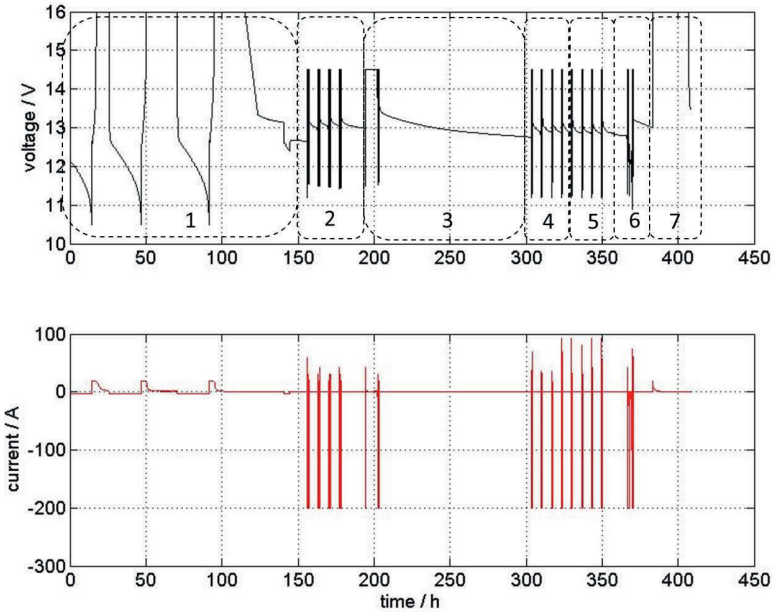

Fig. 47. Voltage and current curves measured during validation test with synthetic driving profile. Tested specimen is 74 Ah standard flooded battery conditioned to 10 °C. Initial SoC equals 80%.

Multiple internal resistance measurements had been carried out within the synthetic driving profile, so that a relatively accurate calculation of the resulting $R_{ct,NAM}$ could be performed. The main target of phase 2 is the validation of the developed model with the same currents while the SoC is gradually increasing. Phase 3 focuses on the validation after field relevant intensive charging. Additionally, an extra relaxation phase of 100 hours has been added. Phase 4 and 5 aim to check if the current dependency modelled by the parameterized BVE for varying currents is well matched. The last driving phase provides information about the battery behaviour during and after extensive discharging, so that also in this case the developed model could be validated. As it can be seen from the description above almost all relevant conditions have been covered by the performed tests with synthetic driving profile.

The accuracy of the developed model has been calculated using double step evaluation routine illustrated in Fig. 48 and (31). It assumes that the polarization of the positive electrode can be fully neglected up to 20 ms (maximal sample rate of the used battery tester) of the BDR. Furthermore, it allows neglecting of the U_{00} (see Fig. 25) in the procedure that could be the source of further errors. The first step is the compensation of the overvoltage from $R_{ct,NAM}$ (estimated) and R_{ohmic} (measured) at the end of the stop phase and directly before the cranking event. The second step uses the voltage calculated in the first step and predicts voltage drop from the imposed inrush cranking current in the given relative short time range. Subsequently,

the calculated voltage has been compared with the measured one and error in mV has been obtained.

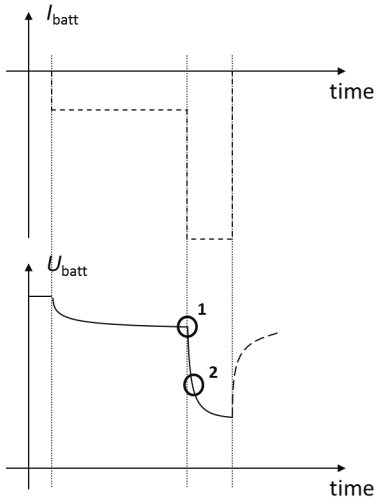

Fig. 48. Working principle of the double step evaluation technique.

$$\begin{aligned} \boldsymbol{U_1(t_1)} &= \boldsymbol{U}_{\text{batt}}\boldsymbol{(t_1)} - \boldsymbol{\eta}_{\text{act,NAM}}\boldsymbol{(I_1)} - \boldsymbol{\eta}_{\text{ohm}}\boldsymbol{(I_1)} \\ \boldsymbol{U_2(t_2)} &= \boldsymbol{U_1(t_1)} + \boldsymbol{\eta}_{\text{act,NAM}}\boldsymbol{(I_2)} + \boldsymbol{\eta}_{\text{ohm}}\boldsymbol{(I_2)} \\ \boldsymbol{U}_{\text{error}}\boldsymbol{(t_2)} &= \boldsymbol{U}_{\text{batt}}\boldsymbol{(t_2)} - \boldsymbol{U_2(t_2)} \end{aligned} \tag{31}$$

Within the whole test using synthetic driving profile there are 102 ASSF phases (referring to stop-start functionality), which have been used for the determination of the maximum and average absolute error of the developed approach. It should be noted that one calculated point corresponds to accumulated error of the model for high discharge current (inrush current during cranking) and medium discharge current simulating idling in front of traffic lights (engine is switched off and the whole power demand is covered by the battery). Applied inrush current of 200 A refers to the hardware limit of the battery testing setup. Discharge current during idling phases was varying in range of $4I_{20}$ up to $40I_{20}$ and 10 A up to 80 A. This considers that operating with both normalized and not normalized currents has been considered. It was also assumed that R_{ohmic} is independent from the current rate and short-term history, which is not always the case. It had to be considered for proper interpretation of the results.

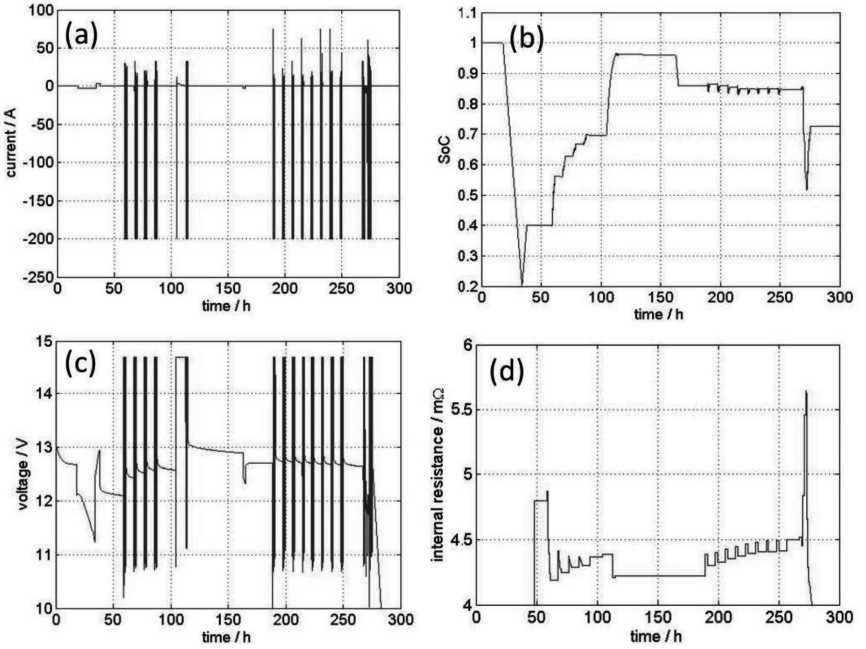

Fig. 49. Measurement results obtained from validation test with synthetic driving profile. Tested battery is 60 Ah AGM battery conditioned to -10 °C. Initial SoC equals 40%: (a) current profile, (b) SoC, (c) voltage profile, (d) R_{ohmic} measured with EIS meter.

Fig. 49 shows measurement results of a 60 Ah AGM battery subjected to proposed validation test with synthetic driving profile. Because tested battery was not a brand-new sample, there are no 3 full initialization cycles at the beginning of the test as it is the case for Fig. 47. Further difference is the initial SoC, which equals 40% and 80% for the results presented in Fig. 49 and Fig. 47 respectively. Applied test profile enforces all relevant working conditions for modern automobiles including various short-term histories. Resulting voltage drop estimation error for all cranking pulses can be seen in Fig. 50. Visible scattering is a result of discontinuously measured R_{ohmic} and modelling noise that do not consider various short-term histories as well as other undesired factors.

The measured average absolute voltage error for all considered working points and batteries caused by inaccuracy of both modelled $R_{ct,NAM}$ and measured R_{ohmic} was in range of 20-50 mV. It refers to cranking events with 200 A and corresponds to 0.1-0.25 mΩ. Linear extrapolation of the given deviation of resistance to a current rate of 700 A provides 70-175 mV of expected error, which is noticeable lower than ± 400 mV typical for state-of-the-art algorithms. Maximal error did not exceed a value of ± 100 mV in most cases. Together with results of static pulse tests presented in chapter 4.3.3 they both prove the high accuracy of the developed approach. Obtained high precision is valid for a wide spectrum of conditions, which are typical for automotive applications, especially state-of-the-art µH vehicles.

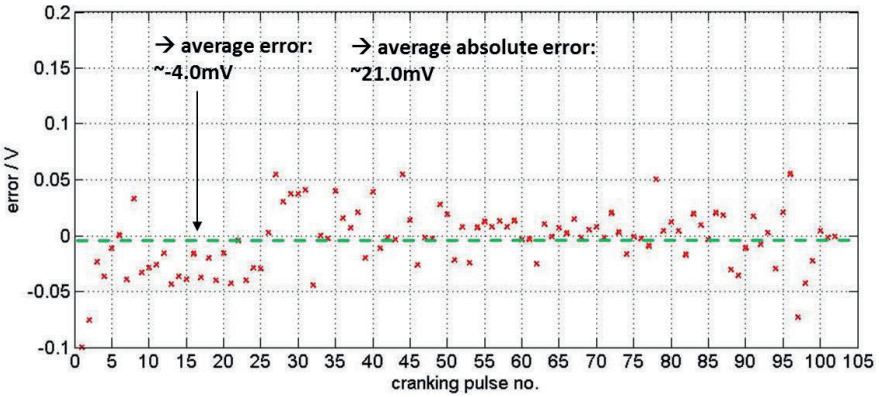

Fig. 50. Voltage drop estimation error obtained using double step evaluation technique (Fig. 48). It refers to cranking phases with $I_{crank,max}$ of 200 A and time interval of 20 ms. Presented data is a result of analysis of validation test with synthetic driving profile performed on 60 Ah AGM battery conditioned to -10 °C. Initial SoC equals 40%

4.4 Further potentials of the developed approach

One of the main advantages of the developed model is its possible application as a supporting tool for SoH estimation in BMS. It is because the i_0 parameter of the modelled BVE is strongly influenced by remaining active surface of the battery. Therefore, it should be directly proportional to the remaining capacity of the given battery, which is commonly used for the calculation of SoH. Measurement results that support these statements are presented in Fig. 51 and originate from the work of Pilatowicz et al. [14]. It should be noted that solutions presented in this work refer only to the state of NAM. It means that they are only valid for SoH that is determined by the state of the negative electrode, which is the case for all applications working in HRPSoC regime including concerned µH applications.

Authors in [14] cycled BUT with shallow DoD of 5% (with upper SoC limit of 80%), which indicates that main failure mode was rather sulfation of NAM than softening and shedding of PAM. Increasing DoD significantly reduces observed increase of $R_{ct,NAM}$ with capacity loss as depicted in Fig. 52. Linear increase of the $R_{ct,NAM}$ during cycling with 50% DoD was hardly noticeable. Its increase equals approximately 5%. Lower cycle depths of 10% resulted in much higher increase of charge-transfer resistance, namely 20% at EoL conditions. Presented results lead to the following conclusion. The lower the DoD of the cycles, the higher the increase of $R_{ct,NAM}$ at the end of life will be. Further investigation is needed to check if cycles with low DoD in range of 1-5%, which are typical for state-of-the-art µH vehicles, always cause proportional increase of charge-transfer resistance. Observed behaviour can be explained by the fact that deep cycles cause fast and severe deterioration of PAM. NAM is also affected but in a significantly less pronounced and slower way. It means that most of C_{loss} indicated in Fig. 52b refers to PAM.

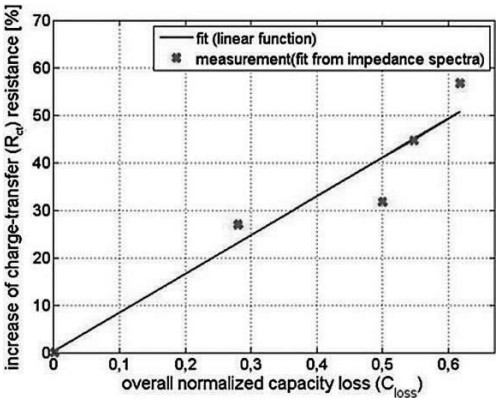

Fig. 51. Proportional increase of the charge-transfer resistance with the capacity loss [14].

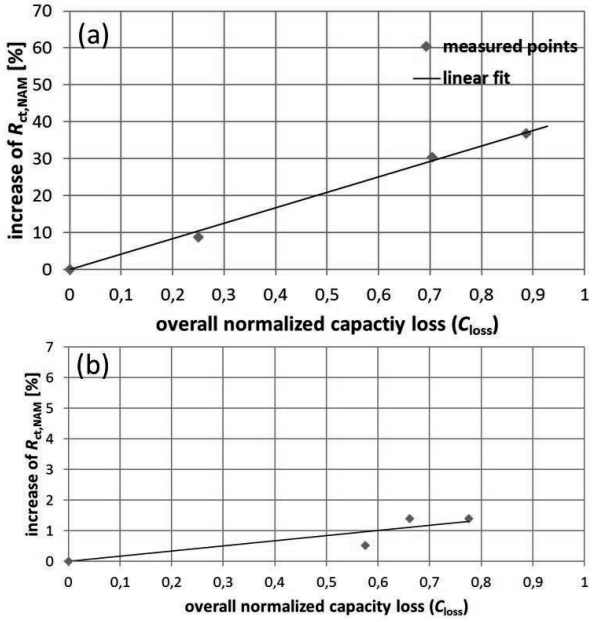

Fig. 52. Correlation between $R_{ct,NAM}$ and capacity loss (C_{loss}) during cycling of a 60 Ah EFB battery at 25 °C with: (a) 10% DoD; (b) 50% DoD. C_{loss} has been normalized to 25 °C and I_{20} discharge current rate.

Knowing SoH related to NAM provides not only information about remaining life of the battery. It also gives an opportunity to trigger refresh charging in micro-hybrid vehicles when they are necessary. Schaeck et al. in [37] mentioned a time interval between two succeeding refresh charging that corresponds to reaching 6 charge turnovers. On the one hand, such

definition is easily implementable in EMS, but, on the other hand it is not optimal. Too frequent overcharging causes increased corrosion of the grid, active material shedding and water loss, whereby to seldom refreshing may induce formation of hard sulfation that cannot be recovered even by means of refresh charging that is limited by field conditions. Accurate adaptation of the developed model and determination of sulfation level of NAM using i_0 addresses this issue and offers an opportunity to trigger refresh charging in the most optimal conditions leading to prolonged battery life and reduction of manufacturer's warranty costs.

Furthermore, time constant which can be obtained from the developed model (Fig. 28) can be used for the estimation of the SoH as well. Huet concluded in his study [71] that the more aged the battery is, the smaller the resulting time constant will be. However, it has to be emphasized that the time constant has to be extracted from the measurement results carried out at the same conditions. Otherwise, obtained results can lead to many misinterpretations.

4.5 Summary

The topic of the BDR estimation is not a novel subject. Many researchers and engineers have already been working on this issue and reported obtained results in several publications, e.g. [13], [14], [66], [95], [96] and [97]. They used many simplifications, which are acceptable for the standard BMS solutions and requirements. As a state-of-the-art solution a linearization of the summed ohmic and charge-transfer resistance of the negative electrode can be considered, which in fact can be acceptable in a very high discharge current range with current rate higher than 200 A. It is due to the relatively flat current dependency of the charge-transfer resistance in this range, which can be observed in the data presented in 4.3.1. However, if the BDR of the battery must be calculated during ASSF phases as well, when the current rate is usually not higher than -20 A, this assumption can be a source of a relatively high error. Additionally, the requirements of the car makers are becoming more and more strict, which makes it necessary to develop more complex and accurate approaches as the one presented in this work. Therefore, described novel solutions can be considered as a further step in the development of advanced battery management systems. Together with the ongoing research and development activities that are focused on making much better long-living lead-acid batteries, they can provide environmentally friendly and costly-attractive solutions not only for SLI but for other applications as well.

Developed electrical model of the negative electrode that is based on Butler-Volmer equation considers all most relevant parameters, namely temperature, SoC, current rate and remaining (nominal) capacity. It estimates charge-transfer resistance of the negative electrode and calculates voltage drop of NAM using given discharge current value. Described model is fully scalable for different battery manufacturers, sizes and types. Presented parametrization and validation tests provided enough evidence to state that it successfully covers whole operation range of µH applications. Achieved significantly reduced complexity (operation with just one variable) indicates high potential for accurate adaptation in the field. It can be realized using either passive impedance spectroscopy or battery response to frequent loads such as indicators and windscreen wipers. The latter one requires measurement of input signals with high

sampling frequency at least during first 100 ms of discharge pulse. Achieved accuracy with known R_{ohmic} equals ± 200 mV or ± 300 mV as a worst case (for cranking current rate of -700 A), which can be considered as an excellent result concerning well-known high complexity of PbA. The same approach can be used to create a model of positive electrode resistance, which may together with the already presented approach also lead to a comprehensive and highly accurate voltage response estimator not only in range of milliseconds but also seconds.

5 Open-circuit voltage prediction

SoC estimation is an important part of each BMS. An accurate SoC prediction is necessary to prolong the service life of a PbA and ensure the required reliability of the vehicle. It is also crucial concerning further reduction of warranty costs caused by inappropriate operation triggered by inaccurate or lack of BMS e.g. allowing deep discharging and extensive sulfation. These issues are mostly pronounced in case of state-of-the-art μH vehicles characterized by increased battery stress. Such factors like: additional cycling, lower average SoC during operation and bigger risk of under discharge play a fundamental role. For these reasons, precise SoC estimation is of high importance.

Currently most often applied SoC calculation method in the field involves battery current integration. It is characterized by relatively good short-term accuracy. However, with time the estimation error grows due to the measurement and integration errors followed by presence of side reactions that do not contribute to the charging process but consume a part of the integrated battery current. From this point, the current integration has to be periodically recalibrated with the correct SoC value obtained using different method. A widely-used approach to deliver its value involves its direct dependency from U_{00}. However, measuring fully equilibrated U_{00} in the field is very difficult or even not possible at all. Even during parking phases quiescent current ($I_{quiescent}$) is always flowing and battery internal temperature in most cases significantly differs from room temperature. Additionally, extended relaxation of the battery voltage takes place and it cannot be neglected as well. These factors should be compensated that makes an accurate U_{00} estimation a challenging task. This statement is proven by the fact that state-of-the-art solutions are characterized by low level of accuracy, especially at low temperatures with errors up to ± 10% SoC (value based on the authors experience).

The main aim of this section was to gain a better understanding of PbA relaxation behaviour and development of accurate U_{00} estimation algorithms that can be directly implemented in a BMS. The mentioned relaxation refers to battery voltage recovery during rest periods. It was found that it is strongly dependent on short-term charge or discharge history, whereby the former one is mostly present under field conditions and the latter one is typical for most of standard laboratory tests. Preceding charging imposes higher overvoltage and longer overall duration of relaxation, which should be considered. Additionally, low temperatures that can occur in the field make this process extremely slow (duration of relaxation is significantly higher than available practical rest time in the considered application). Overall relaxation duration in the range of hundreds of hours has been measured. This work reveals influences of the operation conditions on the relaxation, opens a discussion about the possible physical reasons standing behind them and shows how the observed effects can be modelled using an approach characterized by low complexity and very limited usage of memory. First section of

this chapter explains the relation between U_{00} and SoC as well as conditions, which should be considered for accurate estimation of the later one in the field. Subsequently, results of experimental investigation of the relaxation behaviour are shown and discussed in detail. A novel double-layer gel-crystal model of the positive electrode is presented that provides a comprehensive physical explanation of the observed effects and is a basis for the development of online U_{00} prediction algorithms presented in the last part of this chapter.

5.1 Open-circuit voltage and its dependencies

Direct and almost linear relationship between U_{00} and SoC is well-known. It is related to the fact that not only active material on the plates but also electrolyte takes part in the main reaction. Therefore, its density (ρ_{acid}) decreases while discharging and increases while charging, which makes it proportional to SoC. Furthermore, generalized state of active material on both electrodes does not influence U_{00}. Thus, only ρ_{acid} as explained by Sauer [17] and illustrated in (32) determines U_{00}.

$$\boldsymbol{U_{00} = 6 \cdot (1.922804 + 0.147519 \cdot \log m + 0.063651 \cdot \log^2 m + 0.073772 \cdot \log^3 m + 0.033612 \cdot \log^4 m)} \tag{32}$$

m is the molality that expresses an amount of H_2SO_4 in moles dissolved in a given mass of a solvent in kg. Thus, the unit of molality is mole·kg^{-1}. m is a temperature independent quantity describing U_{00}, which is preferable for generalized description. However, temperature dependent ρ_{acid}, is more often used in the practical applications and calculations. It is because it is much easier measurable in the field. Characteristic tables with equivalent values of m and ρ_{acid} (at 25 °C) can be found in [88]. A broadly used linear approximation of (32) presented in (33) originates from [19] and involves ρ_{acid}. It is valid for any 12 V PbA conditioned to room temperature.

$$\boldsymbol{U_{00} = 6 \cdot (\rho_{\text{acid}} + 0.84)} \tag{33}$$

It must be mentioned that depending on the amount and type of electrolyte additives, the coefficient introduced in (33) may vary, e.g. it increases with higher H_3PO_4 content as discussed by Meissner in [98]. It is usually in range between 0.84 and 0.86. The temperature dependency of U_{00} equals 1.38 mV·K^{-1} for 12 V battery [17]. Graphical illustration of the described relations from (32) and (33) can be found in Fig. 53.

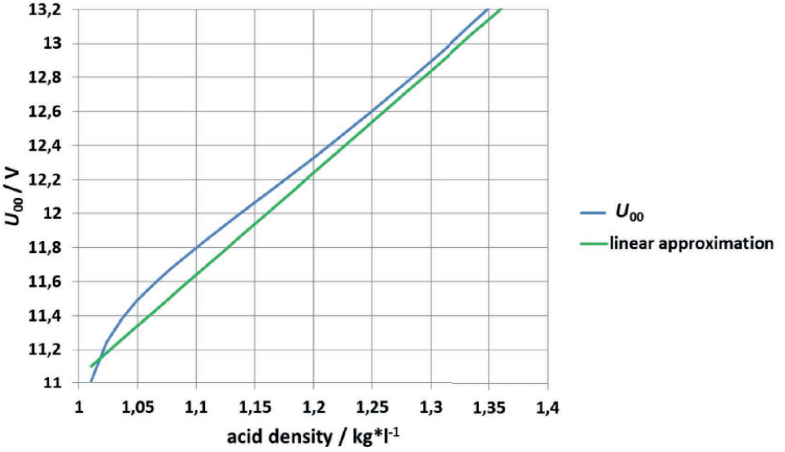

Fig. 53. Comparison between U_{00} obtained using (32) and linear approximation from (33).

Further consideration of the fact that U_{00} only depends on ρ_{acid} and it is fully independent from the state of the electrodes leads to the following conclusion. Extreme oversizing of the acid reservoir could lead to negligible change of U_{00} with SoC, which in this case is directly linked to limiting amount of active material on the plates taking part in the main reaction. However, using higher than necessary volume of electrolyte has been practiced for prolonging of the estimated lifetime mainly in the stationary applications, where battery weight and volume is not a decisive factor. In the automotive applications, these parameters are mostly of high importance. In most cases, there is less available capacity in acid than active material on the plates making it capacity limiting[9].

According to [40] ρ_{acid} for a fully charged and fully discharged 12 V SLI standard flooded battery conditioned to 25 °C equals 1.28 and 1.06 kg·l^{-1} respectively. AGM batteries are characterized by slightly increased maximal acid density (approx. 1.3 kg·l^{-1}) due to even overall acid volume filled into each cell. Applying described assumptions result in the straightforward and easily implementable relation between U_{00} and SoC presented in Fig. 54. It is of high significance for low-cost BMS solutions. It can be clearly seen that a change of 10% SoC can be associated to 100-150 mV U_{00} variation. It shows that resolution and measurement accuracy of the state-of-the-art voltage sensors is sufficient for an accurate SoC estimation from the obtained U_{00} voltage.

[9] Some battery manufacturers oversize one of the electrodes so that generalized declaration, which one limits available capacity, is not possible.

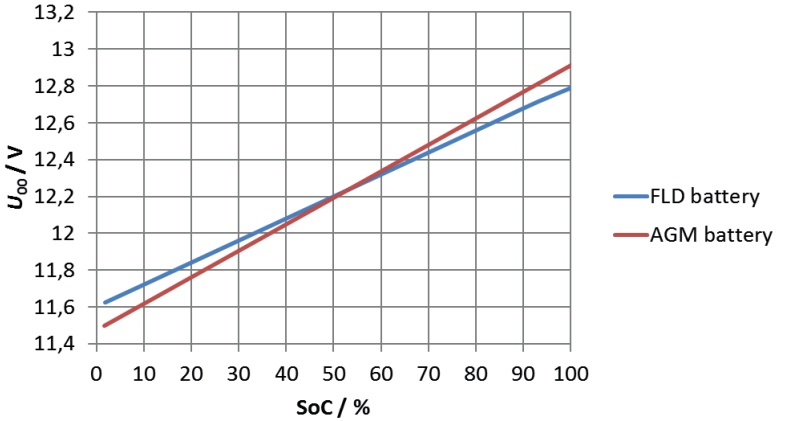

Fig. 54. Simplified and exemplary relation between U_{00} and SoC (U_{00} characteristic curve) for AGM and standard flooded battery. Presented results are valid for 12 V SLI PbA operated at 25 °C and conditioned with I_{20}.

Although relation between SoC and U_{00} can be very accurately approximated by linear function and used in the field, following issues must be mentioned for the proper understanding of the accuracy of this approach:

- There is no universal U_{00} characteristic curve valid for every 12 V SLI PbA. Each battery manufacturer freely designs its product causing considerable variation between ρ_{acid} at fully charged and discharged state respectively. It makes clear that reaching high accuracy requires special parameterization measurement for each type of battery. Not doing so for low accuracy solutions should not cause higher increase of expected error than ± 10% SoC.

- Brand new batteries are not fully formed in most cases. It means that in the first months of operation residual basic sulfates are still present on the electrodes. They are being gradually formed into PbO_2 and Pb for PAM and NAM respectively. In this process sulfate ions SO_4^{2-} are released into electrolyte and its density grows leading to direct shift of the characteristic curve towards higher values. This issue can be addressed by special preconditioning before each U_{00} parameterization test. An example of such procedure is constant overcharging at elevated temperature for a week.

- According to Meissner et al. [13] the variation of maximum ρ_{acid} in the manufacturing process equals ± 0.01 kg·l^{-1} or ± 60 mV referring to U_{00}. Furthermore, not only variation of ρ_{acid} impacts the value of U_{00} at different SoCs but also the electrolyte volume. Its filling process is characterized by considerable scattering as well. It shows that even if a parametrized U_{00} characteristic curve is available, still an error of 4-7 % may occur due to high manufacturing tolerances. Production of 12 V SLI are not expected to be more precise in the future (on this specific step) because otherwise low price, which is

the main advantage of PbA, increases considerable leading to loss of market segment competitiveness.

- Ageing effects and water electrolysis cause shifting of U_{00} characteristic curve towards higher (gassing and corrosion) and lower (sulfation) values as demonstrated in [10]. To address this, issue a smart adaptation algorithms adjusting implemented and parametrized U_{00} characteristic curve during operation may be of a fundamental importance. However, this task is highly challenging and had not yet been solved at the time point when this work was carried out.

- U_{00} directly depends on ρ_{acid}, which is located in the electrolyte/active material interface and not in the bulk electrolyte. It means that any horizontal or vertical concentration gradient (acid stratification) will cause imprecise U_{00} readings.

All the mentioned aspects have been graphically illustrated in Fig. 55.

The focus of this work is to develop a more accurate estimation of U_{00} in field-related operation conditions specific for µH applications. The focus of presented study was put exclusively on the relaxation behaviour and on the estimation of the true value of U_{00}. This means that some issues mentioned above, like obtaining correct U_{00} characteristic curve regardless of manufacturing tolerances and battery type or adaptation of such curve with ageing, have not been directly concerned. However, it must be emphasized that they are crucial for specification of the final accuracy concerning SoC estimation and cannot be neglected.

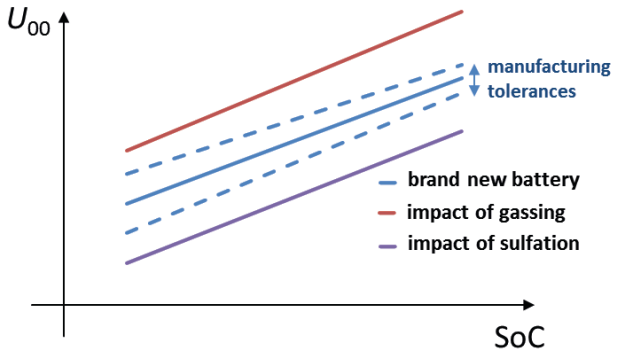

Fig. 55. Schematic illustration showing how manufacturing tolerances and ageing impact U_{00} characteristic curve.

5.2 Relaxation behaviour with charge and discharge short-term history

Majority of research that has been carried out in the field focuses almost exclusively on relaxation behaviour with discharge short-term history. However, in case of µH applications the battery is in most cases being charged before turning off the engine (accumulated amount of charge is positive). It means that before the rest period occurs the battery is in most cases

charged rather than discharged considering Ah counting with I_{batt} during a single trip. According to the present understanding of the working principles and occurring phenomena in PbA chemistry, voltage regeneration during rest periods preceded by charging and discharging should be relatively similar. However, it is not the case as exemplarily shown in Fig. 56.

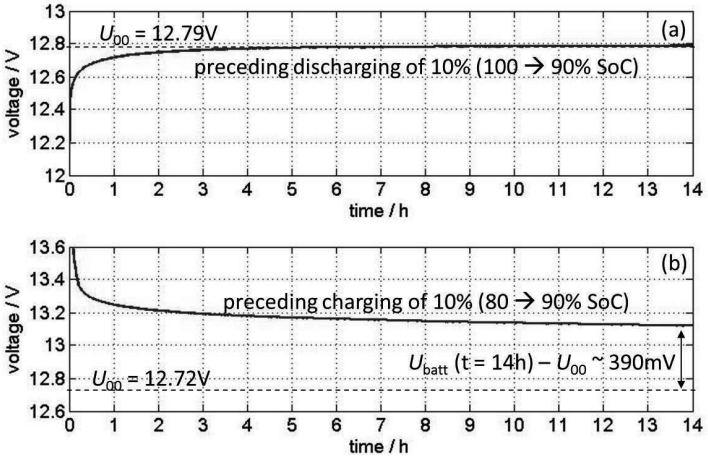

Fig. 56. Measured relaxation behaviour without $I_{quiescent}$ of a 74 Ah standard flooded battery conditioned to -20 °C and 90% SoC with preceding pure (a) discharging and (b) charging short-term history. Charging and discharging current rate equalled I_{20}. Relaxation tests have been performed on the same battery type and batch but their ageing state was different (see Fig. 55), explaining difference in the value of U_{00}.

Impact of acid stratification can be neglected in this case. It is due to low current rate and low amount of discharged and charged amp-hours (Q_{cha}) preceding discussed relaxation behaviour with different short-term histories. Fig. 56 clearly shows that deviation between battery terminal voltage (U_{batt}) and U_{00} after several hours at rest can be as high as 390 mV. It can be directly associated to inacceptable SoC estimation error (in considered applications) exceeding 30%. Furthermore, measurement results presented in this study and further analysis revealed that observed effects can be linked to additional physical phenomenon. It was found that it cannot be characterized by any hysteresis model (see [61] where a hysteresis model for nickel metal hydride batteries was explained in detail), which was suggested by Steffens in [59], who used two different U_{00} characteristic curves for SoC estimation considering both discharge and charge short-term histories. Observed voltage decay during rest periods preceded by charging in comparison to discharging short-term history is much slower. It vanishes only when an equilibrated U_{00} is reached as presented in Fig. 57 (self-discharge can be neglected in this case due to low temperature of -20 °C). Obviously, the use of an empirical approach not linked in any way with the processes occurring in the PbA can be useful to achieve reasonable results. However, they will be valid only for limited range of operating conditions (mostly high temperatures), which is their main disadvantage. Accurate estimation of the SoC using U_{00}

characteristic curve requires knowledge of U_{00}. Even though that statistically average operation of a passenger µH vehicle in Europe clearly shows that it is being driven for less than two hours per day [99] and the remaining 22 hours are rest periods, length of the relaxation processes imposing additional overvoltage is even higher than the available time at rest, especially at low temperatures as depicted in Fig. 57.

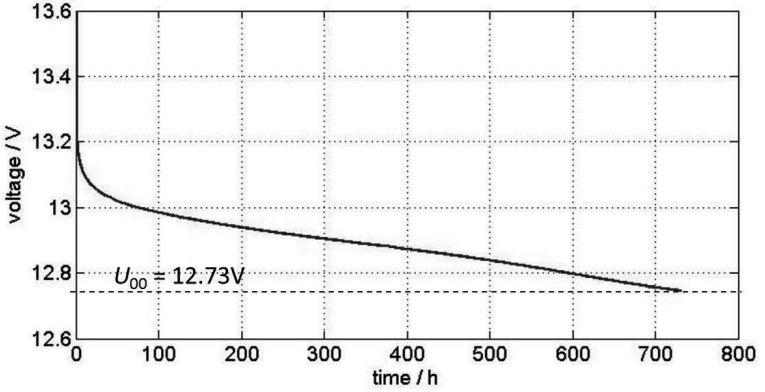

Fig. 57. Relaxation behaviour of 74 Ah standard flooded battery conditioned to 90% SoC, -20 °C with I_{20} recorded without $I_{quiescent}$. Superimposed charge short-term history equals Q_{cha} = 3% DoD.

Furthermore, even when the engine is switched off there is always $I_{quiescent}$ current flowing. It is usually in the range of 10-20 mA and refers to vehicle deadlock or anti-theft systems, electronic clock, environmental friendly restarting function of the engine and other electronic devices, which go into sleep mode. Due to the pronounced non-linearity of PbA, the battery overall internal resistance ($R_{overall}$) while discharging with $I_{quiescent}$ is in Ω range, which may result in additional overvoltage even higher than 100 mV causing SoC deviation as high as 10% and above that. U_{batt} during relaxation after discharging can be analytically described as depicted in (34).

$$\boldsymbol{U}_{\mathrm{batt}} = \boldsymbol{U_{00}} + \boldsymbol{\eta}_{\mathrm{act}} + \boldsymbol{\eta}_{\mathrm{strat}} + \boldsymbol{\eta}_{\mathrm{con}} + \boldsymbol{\eta}_{\mathrm{quiescent}} + \boldsymbol{\eta}_{\mathrm{SD}} + \boldsymbol{\eta}_{\mathrm{solid}} \tag{34}$$

It has been assumed that η_{act} fully vanishes in a time not longer than one hour[10]. η_{strat} refers to overvoltage caused by acid stratification, which is relevant for standard flooded and EFB batteries. Electrolyte of AGM batteries is immobilized in the AGM separator, which significantly impedes its generation. According to experience of the author η_{strat} cannot be fully neglected for moving vehicles in the field related conditions. Mixing of the electrolyte caused

[10] Due to pronounced non-linearity of PbA and considerable increase of given time constants for low size batteries and operation at low temperatures as low as -40 °C, one-hour margin was applied. It can be considered as worst case valid for all conditions.

by acceleration and deceleration of the vehicle is not sufficient to equalize acid density gradients within the battery without additional passive modifications or active mixing systems. $\eta_{quiescent}$ is a quiescent overvoltage, which is a direct consequence of $I_{quiescent}$. η_{SD} emphasizes the need of self-discharge consideration if the vehicle is resting for a long time at elevated temperatures. It can be understood as additional overvoltage or rather $\Delta U_{00} = U_{00}$(t = current interruption) – U_{00}(t = end of relaxation) related to the difference between battery state at the beginning and the end of relaxation. The average self-discharge rate of state-of-the-art PbA equals approx. 3% SoC per a month at 20 °C [19] and according to Arrhenius equation it is reduced by factor two every temperature decrease of 10 °C [20]. η_{solid} corresponds to additional solid-state effects, which have been observed throughout this study. They are explained by developed novel double-layer gel-crystal model (see chapter 5.4). The developed model provides good extrapolation ability, which is necessary for further improvement of U_{00} estimation accuracy, mostly relevant for operation at low temperatures. η_{solid} and residual η_{con} (overvoltage from concentration gradients between the pores of the active material and bulk electrolyte) still present after 1h of relaxation are treated together and called η_{relax} in the further part of this work.

5.3 Experimental study and identified relations

In order to investigate relaxation behaviour of 12 V SLI PbA in conditions relevant to μH applications a comprehensive experimental study was conducted. It considered all parameters that were identified as potentially influential. They can be found in Table V.

Investigated parameter	Phase	Section
impact of the current rate and maximum voltage	charging before relaxation	-
impact of the current ripple	charging before relaxation	-
impact of Q_{cha} imposed by preceding charging (short-term history with positive Ah balance)	short-term history before relaxation	5.3.3
impact of charging strategy (EN and field relevant charging)	charging before relaxation	5.3.3
additional discharge pulses and discharge behaviour after uncompleted relaxation	during and after relaxation	5.3.7
half-cell measurements	during relaxation	5.3.1
EIS tests	during relaxation	-
impact of temperature	during relaxation	5.3.2
impact of $I_{quiescent}$ (direct influence on relaxation, which shall not be mistaken with $\eta_{quiescent}$)	during relaxation	5.3.5
impact of SoC	during relaxation	5.3.4
impact of ageing	during relaxation	5.3.6

Table V. Specification of the carried out comprehensive experimental study of relaxation behaviour with charge short-term history.

For the sake of performing a reproducible and systematic study each battery was conditioned and tested using the same standardized relaxation test (SRT). SRTs specification has been depicted in Fig. 58 (detailed specification can be found in chapter 9.3.3).

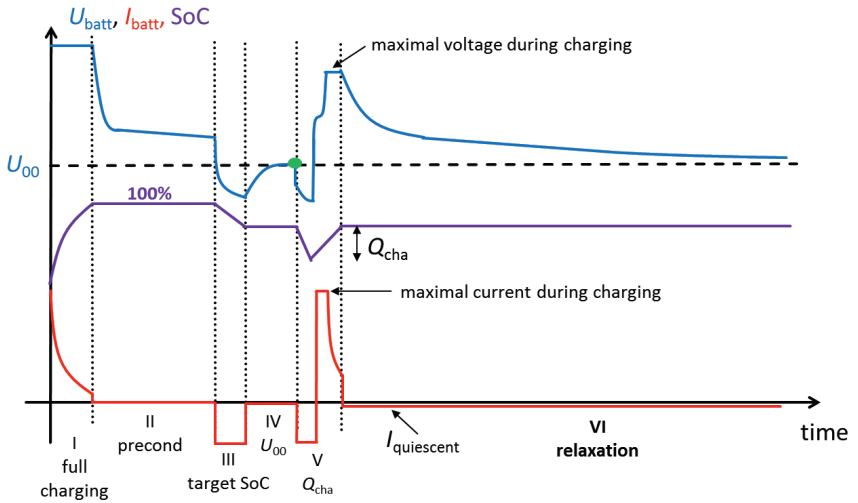

Fig. 58. Specification of standard relaxation test (SRT). SRT has been divided into six phases, which are: (I) full charging, (II) preconditioning comprising destratification, damping of relaxation originating from full charging and temperature setup, (III) conditioning to the target SoC by discharging with I_{20}, (IV) collecting of the reference U_{00} (fully equilibrated) at the end of the rest period with purely discharge short-term history, (V) imposing a given Q_{cha}, (VI) observation of the relaxation behaviour.

SRT has been designed in a way that significantly reduces expected generation of acid stratification. In the field-related specification of the concerned µH applications PbA experiences a very shallow micro- cycling that hardly ever exceeds 5% and remains below 1% of DoD in most cases, which justifies chosen the Q_{cha} values. Furthermore, in the well-known testing procedures such as Japanese SBA S0101 test [100], dynamic pulse cycling test [39] and in the micro-hybrid test that is the part of coming European 50342-6 norm [101] it is also the case. Due to these reasons in the majority of carried out tests Q_{cha} was not higher than 5%. Thus, acid stratification can be fully neglected even while testing EFB and standard flooded batteries. It has to be added that acid stratification is also present in AGM batteries. However, it has got entirely different characteristics, it is rather permanent and does not get homogenized by diffusion or gassing. Direct cause for this issue has been explained in [22]. It is related to low-cost AGM separators broadly used in the commercial products. They are characterized by limited surface area and increased average pore size that provoke generation of vertical acid concentration gradients. Nevertheless, acid stratification of AGM batteries is significantly smaller than for standard flooded and EFB batteries and that is the reason why it was neglected in the presented work.

In the following part of this subchapter only parameters, which considerably influence relaxation behaviour of PbA have been discussed. It was found that factors describing charging routine do not influence subsequent relaxation processes in any way. This statement is valid for

all aspects mentioned in Table V besides Q_{cha}. It has to be mentioned that an indirect impact of charging strategy regardless of its parameters was also reported. It refers more to other phenomena and not to the charging itself. This was observed in other three cases:

- Cycling with high current rates causes generation of significant acid stratification, which leads to premature termination of relaxation. In this case obtained reference U_{00} ($U_{00,ref}$) is falsified by additional η_{strat}, which fades away together with η_{relax}. This process leads to artificially accelerated relaxation with less η_{relax}.

- Applying intensive and periodically executed charging strategy for extended amount of time, e.g. increasing maximal voltage from 14.5 V up to 16 V. This behaviour is only valid for very first relaxation after a mentioned change was employed and causes a temporary decrease of expected relaxation time (t_{relax}) and η_{relax}.

- Operating a battery after long rest period (where $t_{relax} >> 2$ weeks), which causes a temporary long relaxation and increase of η_{relax}.

Further analysis revealed that testing of relaxation behaviour using EIS methodology is not feasible. It is due to the violation of one of the main requirements that have to be fulfilled, namely stationarity. It emphasizes the need to keep the internal state of tested specimen in unchanged state, which is not the case for any measured relaxation curve. After current interruption battery state continuously change concerning relaxation related effects, which indicates clear violation of stationarity. It means that generalized internal state of the battery after one hour and e.g. two hours of relaxation is entirely different. This is because long expected duration of relaxation inflicts the necessity to record EIS sweeps up to very low frequencies. Evaluation of EIS spectra where high and low frequency impedance correspond to battery at different states is not feasible. Thus, analysis of test results obtained using EIS cannot lead to any reasonable conclusion.

For the sake of clarity, better understanding and comparison with the other test results all presented original voltage curves have been modified in such a way that $U_{00,ref}$ for each considered evaluation or investigated relaxation parameter is constant and provided. It means that the whole recorded profiles have been shifted so that $U_{00,ref}$ of the given test equals chosen global $U_{00,ref}$. It means that in case when there are two different voltage curves recorded during relaxation and the difference between their $U_{00,ref}$ is e.g. 20 mV, an offset of exactly the same value has been added or subtracted from one of them in this specific case. It was necessary due to the significant U_{00} deviation between batteries and tests, which mostly originated from different ageing progress of various tested specimens.

5.3.1 Half-cell measurements

Multiple SRTs with logging of half-cell potentials have been performed to check if extended relaxation and higher η_{relax} typical for charge short-term history can be associated to one particular electrode or both. All tests have been carried out using 74 Ah standard flooded battery equipped with Hydroflex reversible hydrogen reference electrode manufactured by Gaskatel

GmbH and lead screw attached to the positive cast-on-straps of the narrowest cell with negative terminal (see Fig. 29). It is a reliable and proven technique that allows long lasting in-situ measurements of half-cells.

Fig. 59 presents U_{batt} and half-cell potentials recorded during SRT performed on a 74 Ah standard flooded battery conditioned to -10 °C and excited with Q_{cha} = 5% DoD. The results shared that almost whole η_{relax} can be assigned to PAM. Potential of NAM in case of relaxation with both short-term charge and discharge history reaches a stationary or fully equilibrated state in less than 1 h. Other tests performed at various conditions including temperatures in range of -20-25 °C and different values of Q_{cha} starting from 1 up to 10% DoD showed exactly the same behaviour, and therefore are not reported in this work. It is believed that observed effects are caused by further phenomena that have not been investigated so far. Their explanation can be found in chapter 5.2.

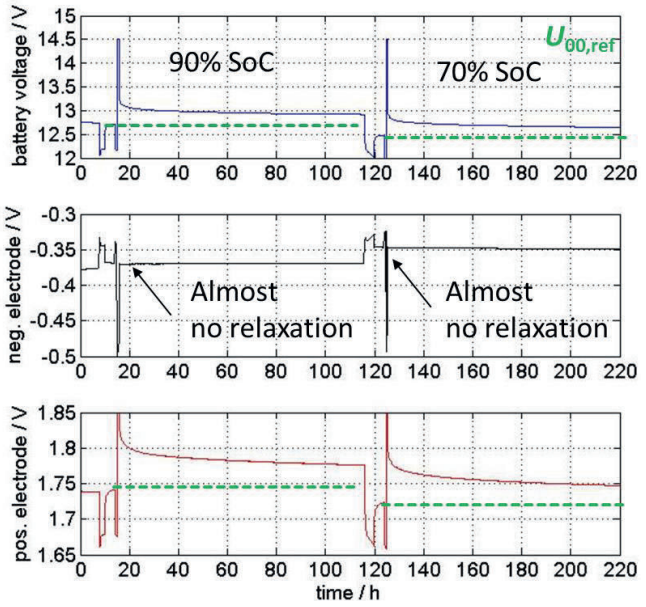

Fig. 59. Half-cell measurement results performed on a 74 Ah standard flooded battery conditioned to -10 °C and subjected to SRT. Imposed Q_{cha} equals 5% DoD. It was applied for testing at both considered SoC, namely 90 and 70%.

Although the time constant of PAM is approx. 70 times higher than the one of NAM as explained in [46], it is still in range of seconds rather than a hundred of hours as shown in Fig. 59. This observation clearly indicates that there must be an additional mechanism, which imposes shown behaviour.

5.3.2 Temperature

Temperature very strongly influences relaxation behaviour. It is due to well-known exponential temperature dependency of both chemical and electrochemical reaction kinetics taking part in each electrochemical energy storage system. In order to observe the course of U_{batt} during rest periods imposed with charge short-term history and obtain a quantitative relation between t_{relax} and temperature, multiple SRTs at relatively wide temperature range have been carried out. Resulting relation between these two parameters concerning relaxation without $I_{quiescent}$ has been illustrated in Fig. 60.

It was found that t_{relax} gets doubled with the temperature decrease of approx. 15 °C. Worth mentioning is also the order of magnitude of the observed relaxation behaviour. Relatively scarce charging, which increases SoC of tested specimen by 1% introduced considerable η_{relax} that needed an extended time to fully decay. Furthermore, at -20 °C relaxation lasted longer than a week. Extrapolation of the obtained relation to -40 °C, which is possible in the cold northern European countries, leads to t_{relax} that is as high as 634 h (circa 26 days). This value corresponds to relatively high value of time constant representing observed phenomena.

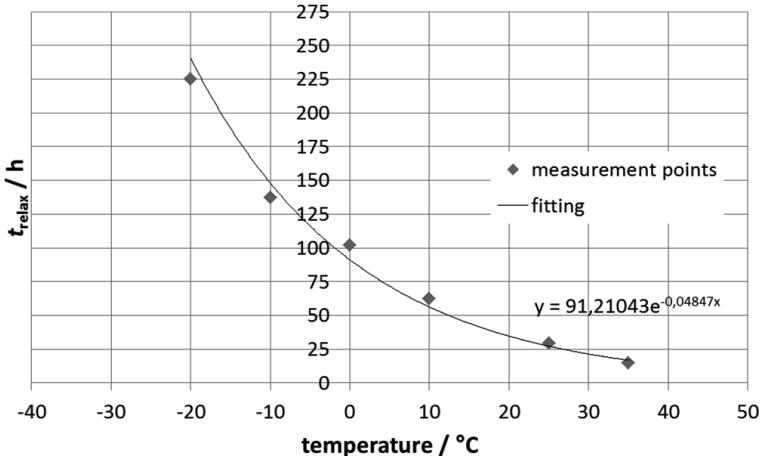

Fig. 60. Relationship between temperature and t_{relax} originating from 74 Ah standard flooded battery subjected to SRT at various temperatures. Other testing conditions are: 90% SoC, Q_{cha} = 1% DoD, $I_{quiescent}$ = 0.

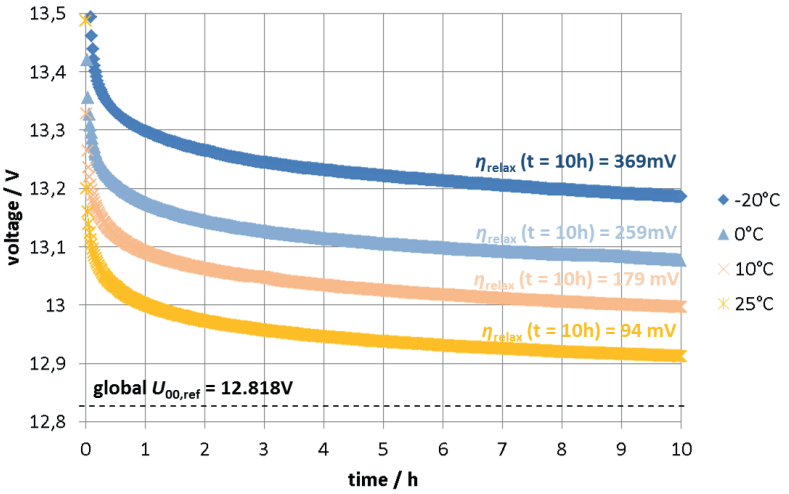

Fig. 61. Battery terminal voltage recorded during first 10 h of relaxation of 74 Ah standard flooded battery subjected to SRT at various temperatures. BUT was conditioned to: 90% SoC, Q_{cha} = 3% DoD and $I_{quiescent}$ = 0.

Fig. 61 depicts U_{batt} during first 10 h of relaxation measured at different temperatures. It is clearly visible that the lower the temperature is the longer the relaxation lasts and also the higher expected η_{relax} becomes. Presented test data shows that even at 25 °C significant η_{relax} after 10h of relaxation is still available. The shape of recorded relaxation curves is very similar. In the first hour of rest period a sharp voltage drop can be observed. It can be associated to η_{ohmic}, η_{act} and partly to η_{con}. In the further part of relaxation U_{batt} gets gradually flatter until it reaches a stable and nearly linear decrease rate as it has been demonstrated in Fig. 57.

5.3.3 Charge short-term history

Over the course of carried out experimental investigations it was found that cumulative number of amp-hours injected into PbA (called Q_{cha} in this work) is the only parameter of charge short-term history, which influences the relaxation behaviour. Other factors such as current rate or maximal voltage during charging do not considerably alter relaxation behaviour. Cumulative amp-hours refer to the fact that interruptions of charging with both short discharging and resting periods before relaxation do not influence the following relaxation in any significant way. Such operation is more relevant to the field, where each µH vehicle is almost never constantly (without interruptions) charged during driving.

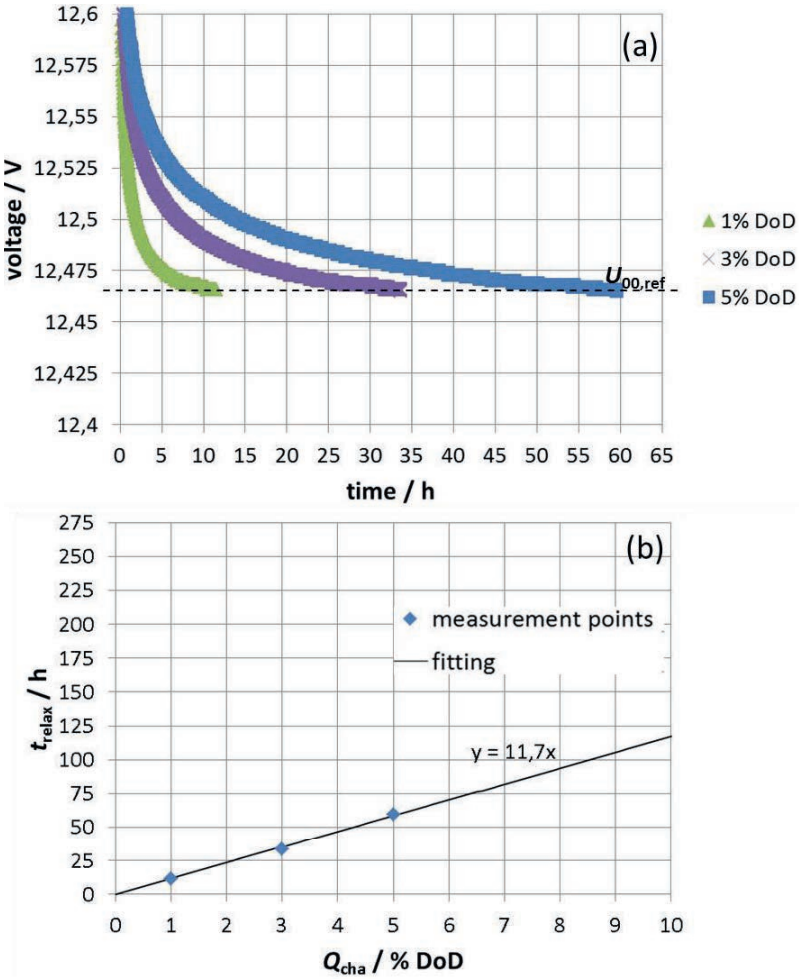

Fig. 62. Investigation of relaxation behaviour with varying Q_{cha}. Presented data originates from SRT carried out on a brand new 74 Ah standard flooded battery conditioned to 80% SoC and 25 °C, $I_{quiescent}$ = 0: (a) original relaxation curves, (b) relation between t_{relax} and Q_{cha}.

For the sake of simplicity and on the contrary to the results presented in chapters 5.3.2, 5.3.4 and 5.3.5, the data shown in this part is related to the brand new battery that has not reached a stationary field-relevant state considering relaxation behaviour. It is due to the additional saturation effect that appears after a few months in the field and significantly changes the initial relaxation characteristics. This topic has been described in detail in chapter 5.3.6.

Fig. 62 shows relaxation behaviour of 74 Ah standard flooded battery subjected to SRT and excited with different values of Q_{cha}. From the presented test results it can be concluded that expected t_{relax} is directly proportional to Q_{cha} and can be modelled applying simple linear function. It is also the case for modelling of η_{relax} as demonstrated in Fig. 63.

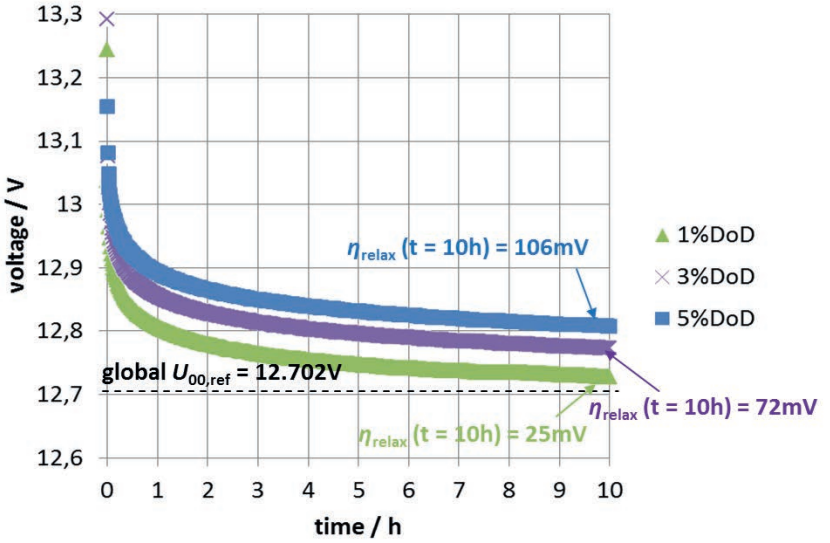

Fig. 63. Battery voltage recorded during first 10 h of relaxation of a brand new 74 Ah standard flooded battery subjected to SRT. Tested specimen was conditioned to: 90% SoC, 25 °C and $I_{quiescent} = 0$.

Until this point Q_{cha} was calculated using pure amp-hour counting so that a question arises if observed relaxation behaviour is being generated in the same way by both main reaction and side reactions. To analyse this aspect overcharging test presented in Fig. 64 has been conducted. Over the course of described test tested specimen gets continuously more charged indicating that in the last charging stages nearly whole charging current flows into side reactions (mainly into gassing). It can be clearly seen by comparing first two with the last two relaxation curves that are characterized by almost no relaxation

Fig. 65 presents all relaxation curves collected from overcharging test depicted in Fig. 64. First short charging routine (denoted as 1), which is the most field relevant among other ones, was not able to bring tested battery to a fully charged state. It is indicated by the relatively low U_{batt} at the end of relaxation period signalizing U_{00} lower than expected value at fully charge state. Full physical charging was firstly achieved by second charging strategy, which originates from [57]. It imposed high η_{relax} present for the whole duration of considered rest period. Further charging of battery regardless of the used methodology caused a negligible relaxation, which was characterized by lower η_{relax} and t_{relax}.

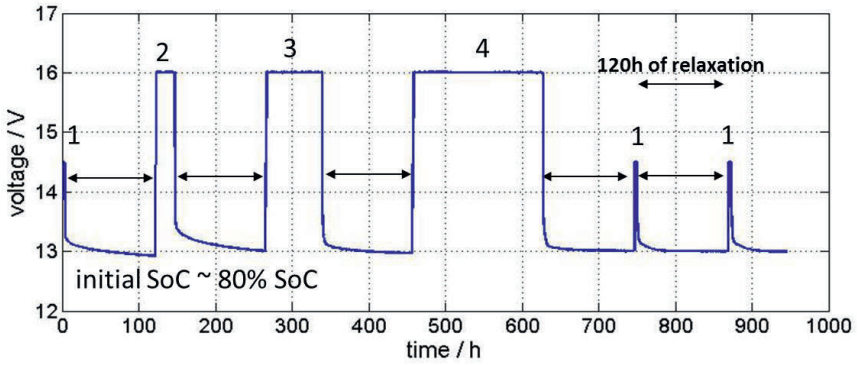

Fig. 64. Specification of an overcharging test designed to investigate whether gassing generates the same amount of relaxation as the main reaction. Tested specimen was a 74 Ah standard flooded battery conditioned to 25 °C with initial SoC of approx. 80% SoC. Testing procedure consists of 120 h long relaxation phases with $I_{quiescent} = 0$ and various charging strategies: (1) $5I_{20}$, 14.5 V for 3 h, (2) $5I_{20}$, 16 V for 24 h, (3) $5I_{20}$, 16 V for 72 h (4) $5I_{20}$, 16 V for 168h.

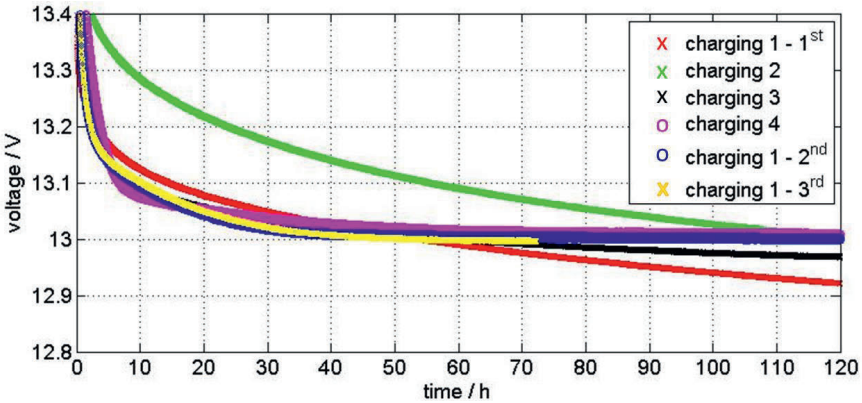

Fig. 65. Relaxation curves extracted from overcharging test described in Fig. 64.

Significantly increased value of U_{00} was also observed at the end of the test. It was caused by considerable water loss resulting from extensive overcharging. It can be recognized from high U_{batt} visible already at the end of charging with 4th technique. This statement was further proven by means of ρ_{acid} measurement performed after the test, which showed a value of 1.33 kg·l^{-1} that corresponds to clear change in the density. Employing (33) and measured ρ_{acid} provides U_{00} value of 13.02 V, which fully matches with the presented test results. It can be concluded that current, which flows into side reactions, does not inflict any changes of relaxation behaviour. Continuous overcharging causes quicker drop of U_{batt} directly after imposing current

interruption. Subsequently, U_{batt} stabilizes very fast at level close to U_{00} and behaves as if $Q_{cha} = 0$.

Summarizing, Q_{cha} has got a decisive impact on the relaxation behaviour of PbA as it is also the case for temperature. Q_{cha} considers only amp-hours that are consumed by main reaction, which means that energy consumed by side reactions does not have any considerable impact on the relaxation. Furthermore, other parameters of charging procedure such as maximum voltage and charging current rate does not directly influence relaxation behaviour as well. Good example of significance of Q_{cha} is the following calculation of the expected t_{relax} at low temperatures. Direct linear relation between t_{relax} and Q_{cha} together with data presented in Fig. 60 results in expected t_{relax} of 2250 h at -20 °C and with Q_{cha} of 10% DoD (if there is no $I_{quiescent}$). This value is equivalent to 3 months of rest period that is required for full completion of the relaxation processes, which is hardly ever available in the field conditions.

5.3.4 State-of-charge

µH vehicles are operate in a narrow SoC window, which could suggest that investigation of SoC dependence of the relaxation behaviour is not necessary. However, in the field it is possible to have conditions where SoC decreases to a level as low as 50% due to heavy traffic or extended standing time as reported by Budde-Meiwes et al. in [102]. Obviously, main target of SoC estimation using U_{00} characteristic curve is to predict SoC without knowing its value before. It means that theoretically SoC should be treated as fully unknown parameter. Nevertheless, any information about current range of actual value of SoC can significantly improve U_{00} estimation accuracy as explained in this subchapter.

t_{relax} shows a linear SoC dependency in the considered SoC range as it has been presented in Fig. 66. The higher the SoC is the longer relaxation lasts. Nonetheless, it was also found from other test results, which has not been shown, that in SoC range below 50% SoC expected t_{relax} may increase back again. However, operation at such low SoCs is not relevant for µH applications and that is why this range was neglected in the further consideration.

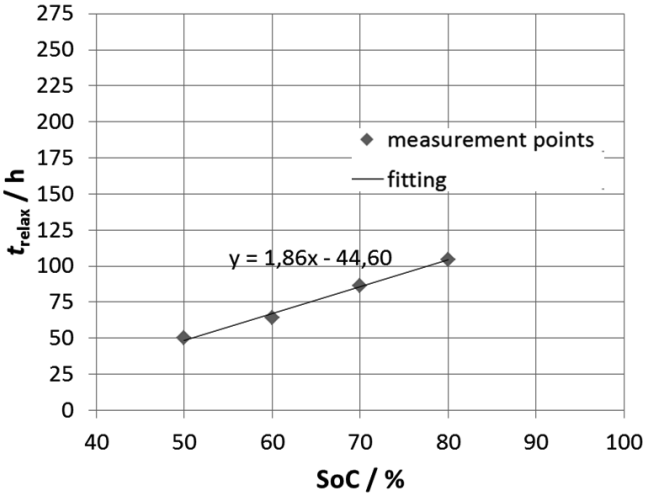

Fig. 66. SoC dependency of t_{relax} extracted from SRT performed on 74 Ah standard flooded battery conditioned to 25 °C and excited with Q_{cha} = 5% DoD, $I_{quiescent}$ = 0.

U_{batt} measured during relaxation periods with different SoC have been depicted in Fig. 67. In comparison with temperature and Q_{cha}, SoC influence relaxation behaviour of PbA in less pronounced way. Doubling of expected duration of relaxation appears when SoC increases by nearly 50%. It has to be emphasized that such SoC jumps hardly ever occur in the field. This observation is vital for the development of U_{00} estimation algorithms because expected SoC recalibration or correction should not exceed ± 5% in most cases. This range does not impose a significant modelling noise according to the presented relations.

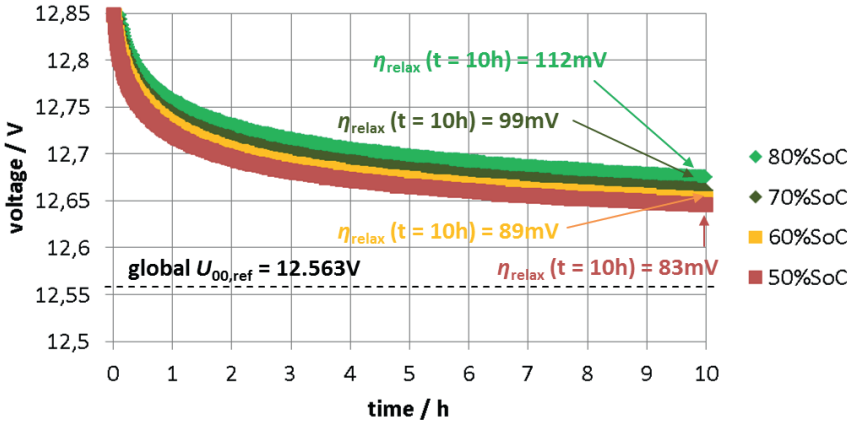

Fig. 67. Battery voltage recorded during first 10 h of relaxation of 74 Ah standard flooded battery subjected to SRT. BUT was conditioned to 25 °C and excited with Q_{cha} = 5% DoD, $I_{quiescent}$ = 0.

Presented findings indicate that development of universal model, which is able to predict whole relaxation behaviour or relaxation parameters, is not possible without knowing at least rough estimation of SoC value. Operating with just rough estimation should not be a problem for a highly adaptable solution, which can readapt itself within the first few hours of relaxation. Such algorithm has a much higher potential for delivering an accurate value of estimated U_{00}.

5.3.5 Quiescent current

Considerations involved in the introduction of this chapter indicated that rest periods in the state-of-the-art µH vehicles are never fully free of some current. $I_{quiescent}$ refers to ignition-off state that causes not only an additional voltage drop (denoted as $\eta_{quiescent}$ and described in chapter 5.2) but also alters relaxation behaviour. Accurate estimation of η_{relax} and U_{00} requires consideration of $I_{quiescent}$ as an independent parameter as it also strongly influences other effects and causes cross relations. Relationships presented in chapters 5.3.2, 5.3.3 and 5.3.4 are only valid for pure open-circuit conditions. On the one hand they can be used for gaining better understanding, planning laboratory tests and evaluating their results. On the other hand they cannot be used for online U_{00} estimation in the field. All tests presented in this chapter have been carried out using battery testers manufactured by Digatron Power Electronics GmbH equipped with either 100A or 200 A, 18 V channels. Their current setting accuracy for the considered very low current rates is much lower than desired ± mA. That is why before each test started every channel had been checked by means of measuring the deviation between set current in the program and real $I_{quiescent}$ flowing through battery with a precise laboratory multimeter. Obtained current offsets were subsequently used to adjust set value in the program in order to be sure that a desired value of $I_{quiescent}$ is being used.

Fig. 68 presents relaxation curves with and without $I_{quiescent}$ recorded from SRT performed on 74 Ah standard flooded batteries conditioned to different operation conditions. Even though that the considered current rate is relatively small and lies in range of mA, it very strongly impacts relaxation behaviour of PbA. This observation refers to both shape of U_{batt} during relaxation and expected value of t_{relax}.

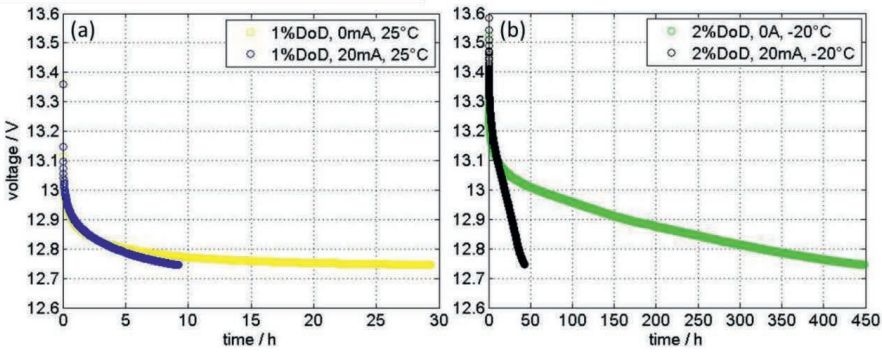

Fig. 68. Comparison of relaxation behaviour with and without $I_{quiescent}$ of 20 mA imposed during relaxation phases of SRT performed on 74 Ah standard flooded battery. (a) Tested specimen conditioned to 25 °C, 90% SoC and excited with Q_{cha} of 1% DoD, (b) Battery conditioned to -20 °C, 90% SoC and excited with Q_{cha} that equals 2% DoD.

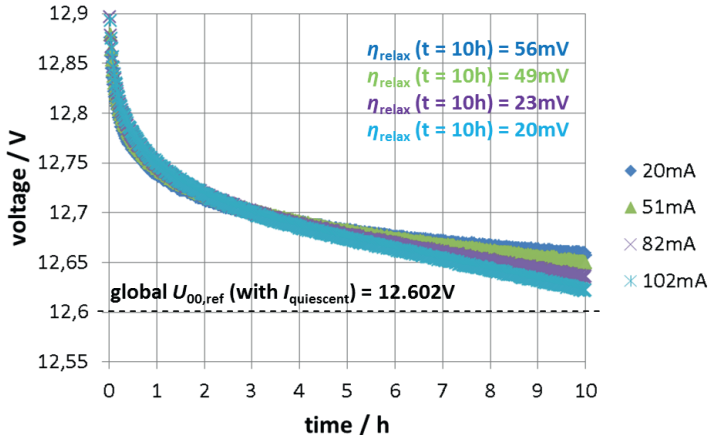

Fig. 69. Battery terminal voltage recorded during first 10 h of relaxation originating from SRT with varying $I_{quiescent}$. Tested specimen was 60 Ah AGM battery. BUT was conditioned to 90% SoC, 25 °C and excited with Q_{cha} = 5% DoD.

The latter one got reduced by factor 10.5 in case of relaxation at low temperatures as illustrated in Fig. 68b, whereby at 25 °C resulted reduction of t_{relax} was 3.3. These results illustrate

mentioned cross relations that are caused by $I_{quiescent}$. Furthermore, the impact of $I_{quiescent}$ on U_{batt} profile for higher Q_{cha} values appears mainly after 4th hour of relaxation as illustrated in Fig. 69. The lower Q_{cha} is the faster an increased slope of U_{batt} will get visible. On the one hand $I_{quiescent}$ makes U_{00} estimation relatively easier because it reduces expected duration of relaxation and η_{relax}. On the other hand, $I_{quiescent}$ during long rest periods significantly discharges the battery so that an accurate prediction of U_{00} should also involve compensation of the discharged energy. Eventually, 100 h of relaxation with $I_{quiescent}$ of 20 mA will result in ΔU_{00} at the end of relaxation that equals 2 Ah (3.33% SoC for 60 Ah battery).

5.3.6 Impact of ageing

The overall efforts in the presented study indicated that relaxation behaviour not only depends on the operation conditions (see chapters 5.3.2-5.3.5) but also on ageing state. It was observed that impact of ageing is only related to relaxation with charge short-term history, which is the main scope of this work. Evidence supporting this statement has been depicted in Fig. 70. Even though that ageing of these batteries was caused by deep cycling (continuous testing using SRT procedure with varying parameters mentioned in Table V) and extensive overcharging that are rare for batteries operated in µH vehicles. The results showed that the expected duration of relaxation and the corresponding overvoltage after a certain time of rest increase.

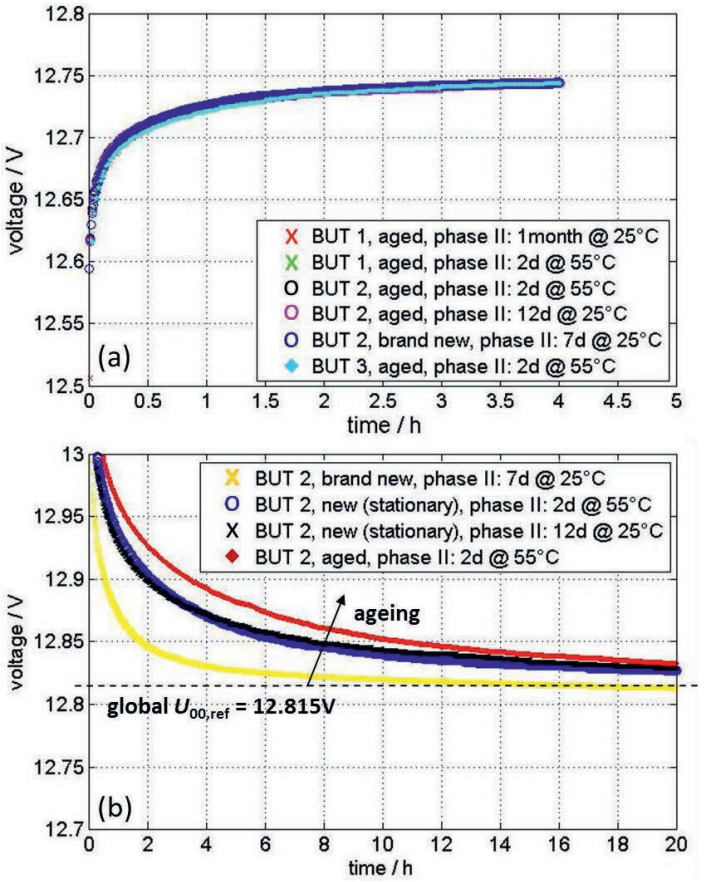

Fig. 70. Influence of ageing on relaxation behaviour. SRT results of 74 Ah standard flooded batteries conditioned to 25 °C and 90% SoC, $I_{quiescent} = 0$. (a) U_{batt} recorded during phase III (see Fig. 58), (b) relaxation behaviour excited with $Q_{cha} = 1\%$ DoD. Brand new battery was subjected to three initialization full cycles before SRT started.

Fig. 70b demonstrates how the voltage curves recorded during relaxation change with the progress of ageing. Battery denoted as a brand new one was subjected to three initialization full cycles before the test, whereas an aged battery was cycled more than 10 times before the presented test was carried out. The brand new battery (yellow curve) has reached $U_{00,ref}$ value relatively fast (in time below 20h) with overvoltage after 4h at test below 2% SoC equivalent. If compared to aged battery (red curve), these parameters significantly increased. Presented results also signalize that identified effects cannot be associated to preconditioning procedure. Discussed behaviour is only related to the ageing itself as depicted in Fig. 70b. Clearly, no significant difference occurred between relaxation measured after storing BUT for 12 days and 2 days at the temperature of 25 and 55 °C respectively.

It can be concluded that at the beginning of battery life relaxation with short-term charging history is relatively fast, which means that expected t_{relax} and η_{relax} regardless of the given conditions will be low. Afterwards, it sharply increases and reaches a stationary state after some certain amount of time in the field. This period of time should not exceed a few months. As battery ages, further gradual increase of t_{relax} and η_{relax} is expected. Depending on the increase of self-discharge rate, environmental and operation conditions it should reach a maximum after certain time and start decreasing back again due to increased self-discharge.

In order to gain better understanding of the mentioned phenomena, special run-in relaxation test (RIRT) has been developed and carried out. It consists of relaxation check-ups, synthetic driving profile, parking with $I_{quiescent}$ = 20 mA and motorway driving periods. It has been illustrated in Fig. 71 and explained in detail in Table VI.

phase	description	explanation
1	check-up of the relaxation behaviour at 90% SoC, 25 °C, Q_{cha} = 1% DoD and $I_{quiescent}$ = 0	see phase III, IV, V of SRT (Fig. 58)
2	5 days of synthetic driving profile (emulation of ASSF and BER functionality)	1) discharging with $4I_{20}$ for 5 min. 2) quasi-cranking pulse with 100 A for 10 sec. 3) charging with $5I_{20}$ and 14.5 V for 5 min. 4) repetition of steps 1-3 for 6 times 5) 11h of rest period with $I_{quiescent}$ = 20 mA 6) repetition of steps 1-5 for 10 times
3	long parking phase	rest period for 2 days with $I_{quiescent}$ = -20 mA
4	motorway driving	Charging with $5I_{20}$ and 14.5 V for 3 h followed by 66 h of rest period without $I_{quiescent}$ employed for destratification and removal of residual relaxation.

Table VI. Detailed description of the developed RIRT testing procedure.

For the sake of better visualization only four relaxation check-ups have been presented, whereby the whole tests lasted for more than 4 months delivering altogether 11 check-ups for evaluation. Recorded relaxation curves are depicted in Fig. 72. They show the same behaviour as it was the case in Fig. 70, which further proves existence of run-in effects inflicting relatively swift transition between relaxation behaviour typical for brand new and stabilized batteries.

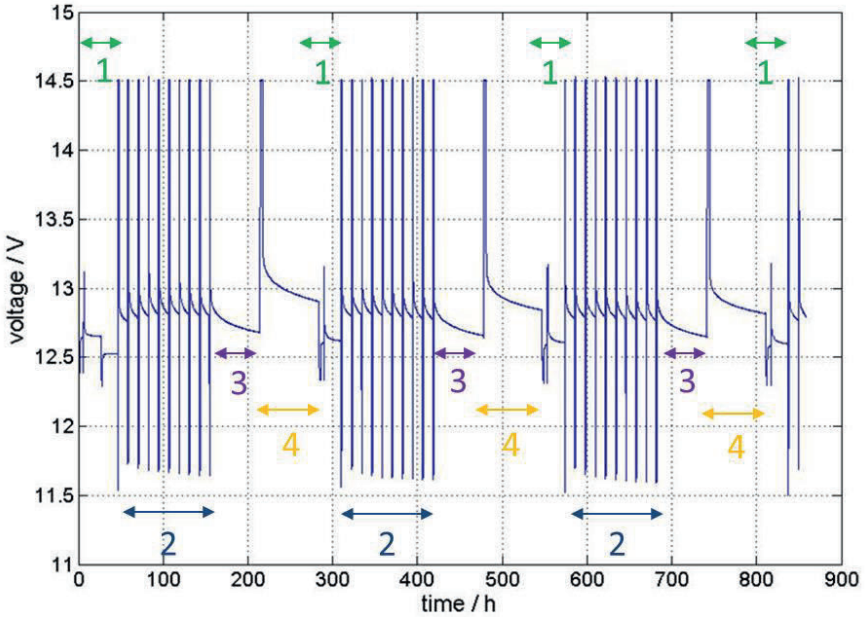

Fig. 71. Schematic representation of the developed run-in relaxation test (RIRT) performed using brand new 74 Ah standard flooded battery conditioned to 25 °C. Initial SoC equals 90% SoC. Before testing started BUT was subjected to three initializing full cycles and preconditioned according to phase II and III of SRT. Detailed explanation of each phase can be found in Table VI.

For a new battery, the state of PAM influences extended relaxation. According the presented test results it was significantly different when compared to 1-2 months in the field and cannot be neglected for proper testing of PbA characteristics, which in any way include evaluation of relaxation behaviour. As the result of all carried out tests it has been assumed that all extracted relationships between relaxation parameters and operation conditions are directly applicable for batteries at any age.

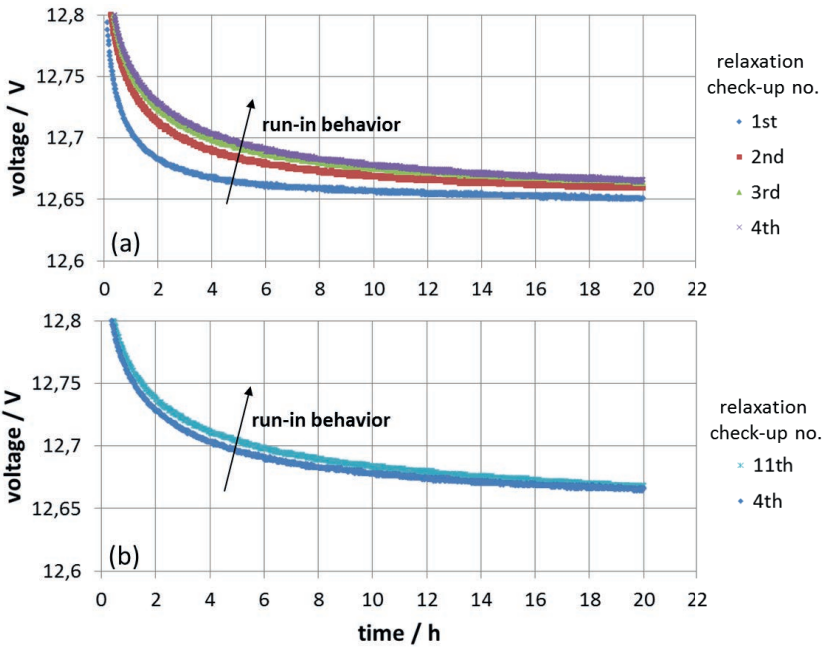

Fig. 72. Evolution of relaxation behaviour within RIRT performed on 74 Ah standard flooded battery conditioned to 25% SoC, 90% SoC and excited with Q_{cha} = 1% DoD, $I_{quiescent}$ = 0. (a) comparison of the first four relaxation check-ups with significant change, (b) gradual increase of relaxation parameters in the following part of the test .

The only exception is Q_{cha} relationship, which is considerably influenced by ageing. It refers only to observed η_{relax} as demonstrated in Fig. 73. Presence of $I_{quiescent}$ caused perturbation of linear relation between t_{relax} and Q_{cha}. It is related to gradual discharge of tested battery during relatively long relaxation phases that inflict considerable reduction of real $U_{00,ref}$. This process has not been considered as already described in chapter 5.3.3. Presented results point out that ageing causes saturation of the reachable η_{relax} at a given conditions in a considered Q_{cha} range of 0-10% DoD. Observation of these two parameters could be used for improving accuracy of SoH prediction considering state of PAM or adjustment of any relaxation model with the known SoH value. However, confirmation of this statement requires conducting further studies and validation tests that has not been in the scope of this thesis. Nevertheless, these aspects are not in the scope of this work and have not been investigated. Discussion about possible mechanisms, which inflict observed saturation of η_{relax} can be found in chapter 5.4.

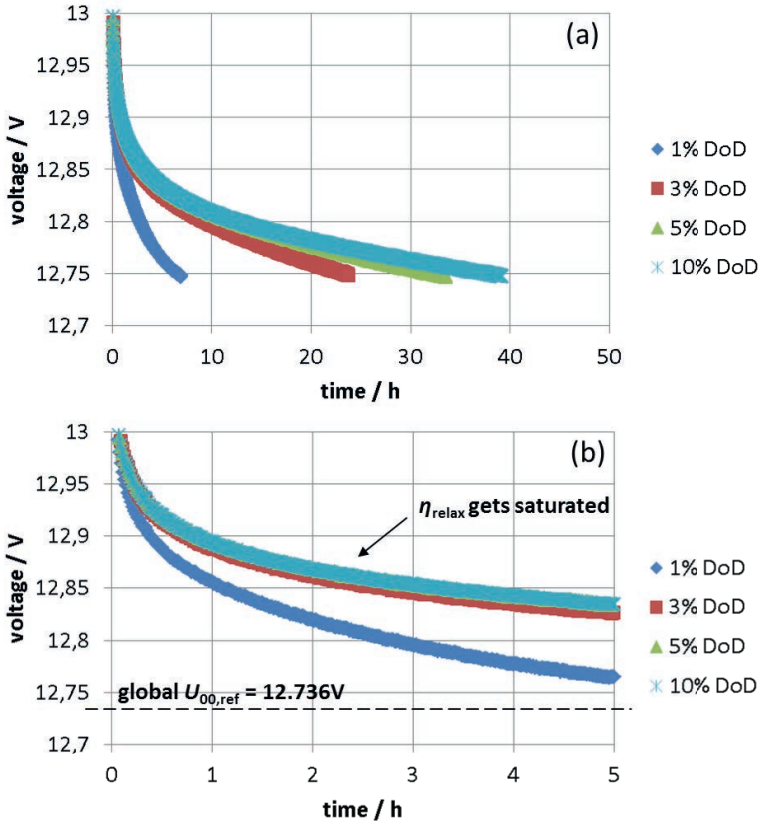

Fig. 73. Relaxation behaviour altered by progressed ageing demonstrated using SRT results performed on 60 Ah AGM battery conditioned to 90% SoC, 25 °C and excited with Q_{cha} = 1% DoD, $I_{quiescent}$ = 20 mA: (a) duration of whole relaxation, which shows that t_{relax} increases as it was the case for brand new batteries, (b) first 5 h of relaxation, where saturation of η_{relax} gets visible.

Measurement results presented in this subchapter clearly indicate that ageing or reaching a stabilized stationary state cannot be neglected for a proper modelling and prediction of relaxation behaviour. Observed transition between brand new and stationary state concerning relaxation behaviour has been called run-in effect. At the time point when the battery reaches stabilized state, saturation phenomena does not change significantly in short-term anymore. It means that using parameters for a new but already stabilized battery should provide a relatively accurate U_{00} estimation according to the understanding resulted from the carried out study. Long-term adjustment of parameters could be realized by smart adaptation algorithms.

Following section focuses on studying whether the relaxation parameters, η_{relax} and t_{relax} are visible during the following discharging of the battery. Because in most cases the duration of

rest periods is not long enough to reach steady-state with U_{batt} decay caused entirely by self-discharge, it is of high importance to know whether subsequent discharging can deliver information for recalibration of the U_{00} estimation algorithm (e.g. due to further progress of ageing). Second aspect that has been addressed is the possibility to readjust the current value of Q_{cha} (provided by Ah counting), which is crucial for the final long-term accuracy. After an unfinished relaxation, the Q_{cha} cannot be set back to 0 in all cases. Finally, carried out tests are answering the question if a deliberate discharging of the battery in order to remove or significantly reduce relaxation behaviour after charge short-term history is feasible and what are the most vital parameters.

5.3.7 Discharging after unfinished relaxation

Discharging during rest periods or relaxation phases (as they are called in this work) is highly possible according to the specification of µH applications. Among others it frequently happens that cooling fan attached to the cooler is still operating even when the engine is switched off by the driver. This situation is likely when the vehicle is being driven for a long time in traffic at elevated temperatures. Furthermore, comfort functionalities such as seat heating or entertainment systems can be also used during idling. Turning on any extra load means an additional discharging period for a battery at rest. Additionally, in the future generations of µH vehicles it will be possible to access remotely vehicle power net using a mobile phone. This new functionality also involves switching on and off of auxiliary systems that discharge battery during relaxation as well. This emphasizes field relevance of periodical discharging during rest periods and indicates the necessity to investigate its influence on the relaxation behaviour. Another aspect which is worth mentioning is analysing if extended relaxation behaviour with short-term charge history can be removed by means of targeted short discharging.

Impact of discharging phases on relaxation behaviour has been examined using modified SRT. It was adjusted in a way that allows analysing which conditions have to be fulfilled to fully remove relaxation behaviour typical for cumulated charge short-term history. This has the goal to switch to purely diffusive relaxation present after discharging. Introduced modification of SRT consists of additional discharging pulse directly after phase V (see Fig. 58). Exemplary U_{batt} profile recorded during testing of a 74 Ah standard flooded battery can be found in Fig. 74.

It is clearly visible that additional discharging with less discharged amp-hours than charged ones does not lead to full removal of the observed relaxation behaviour “from above” that is typical to charge short-term history. When number of discharged amp-hours during relaxation (Q_{dch}) is smaller than Q_{cha}, U_{batt} jumps back to a relatively high voltage level and continues relaxing “from above”. Only in case of Q_{dch} that is higher or equal Q_{cha} purely diffusive relaxation “from below” was observed.

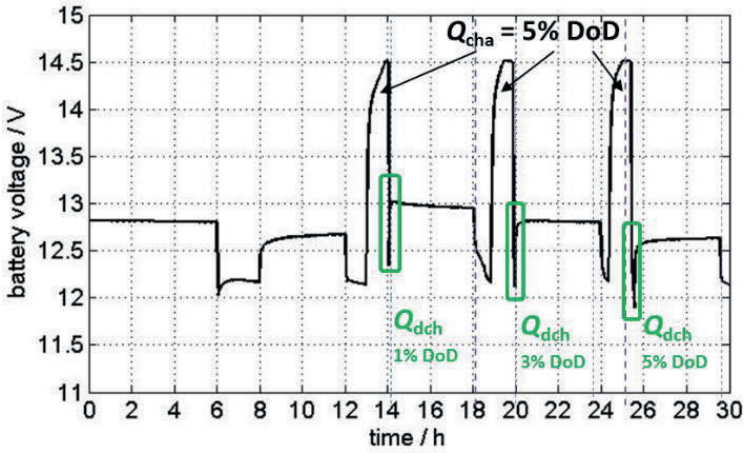

Fig. 74. Influence of additional discharging pulses on relaxation behaviour. Modified SRT results performed on 74 Ah standard flooded battery conditioned to -10 °C, 90% SoC and excited with Q_{cha} = 5% DoD, $I_{quiescent}$ = 0. Discharging pulse rate equals $20I_{20}$.

Further investigation revealed that this effect does not depend on discharging current rate or any parameter of preceding charging. It explains why the presence of $I_{quiescent}$ significantly reduces the duration of relaxation. However, in case of intensive charging with high value of Q_{cha} full removal of relaxation still requires an extended relaxation time due to relatively low value of $I_{quiescent}$ (mostly below 20 mA).

Time point when discharge pulse is imposed is the only further factor, which reduces the amount of necessary Q_{dch} needed to remove η_{relax}. As it could be expected from previous considerations the later a discharge pulse occurs, the less Q_{dch} is needed to fully remove relaxation "from above". Relations presented in 5.3.3 are also valid for the present investigation. Lower temperature and higher SoC cause significantly higher values of η_{relax}, which has been depicted in Fig. 44. In case of testing at -20 °C and with Q_{dch} = 5% DoD, resulting η_{relax} was noticeable due to insufficient resting time to reach $U_{00,ref}$.

Further test was carried out to see if identified effects are related to ρ_{acid} in the pores of active material or rather to direct changes in PbO_2 structure itself. If the former one is true, exciting relaxation with $Q_{cha} > 5\%$ and followed by discharging with $Q_{dch} = 5\%$ should fully remove relaxation behaviour typical for charge short-term history. This condition is true if capacity of the electrolyte in the pores of PAM does not exceed a value of 5% C_N. In this case, highly concentrated acid in the pores (decisive for U_{00} (see (33)) generated during charging should be fully consumed by discharging reaction as explained in (3).

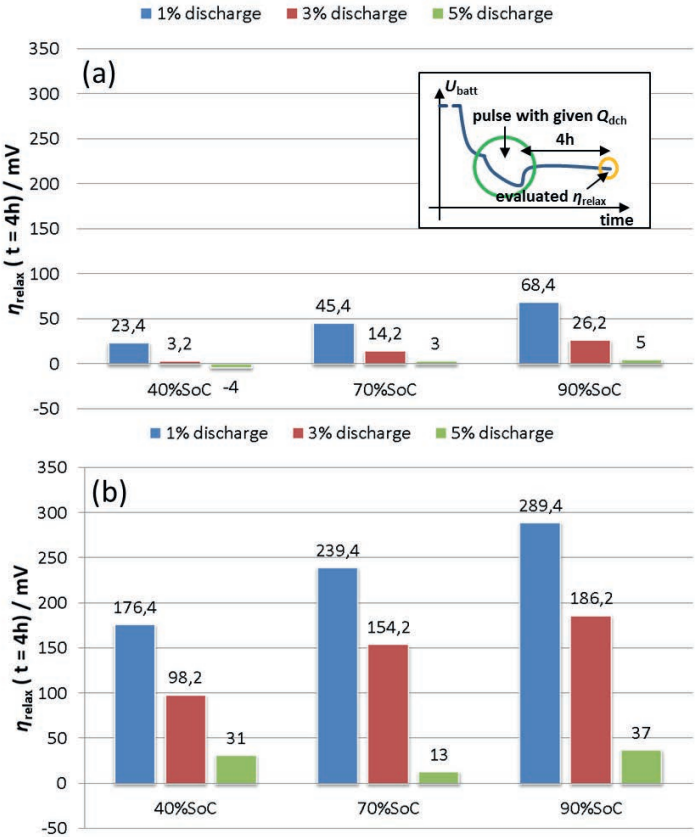

Fig. 75. Residual η_{relax} measured during SRT with additional discharge pulses. Each pulse is characterized by varying value of Q_{dch} followed by 4 h of rest period. Presented η_{relax} was collected at the end of this quiescent phase. Tested specimen is 74 Ah standard flooded battery conditioned to (a) 25 °C as well as (b) -10 °C and excited with Q_{cha} = 5% DoD, $I_{quiescent}$ = 0. Deviation of $U_{00,ref}$ between pulses with different Q_{dch} was compensated with the assumption that 1% SoC = 11 mV.

As demonstrated in Fig. 76 measured relaxation behaviour with charge short-term history cannot be explained using an argument of high ρ_{acid} in the pores. Relaxation excited with Q_{cha} of 20% DoD was only removable with the same amount of Q_{dch}. Thus, it can be concluded that observed phenomena fully refer to changes of active material taking place on its surface. Additional test was carried out to provide additional evidence that could further support this statement. It involved manual shaking of the battery for at least one minute during relaxation (swift movement of the battery upwards and downwards and sliding it leftwards and rightwards) to provoke forced mixing of electrolyte in the pores. Obviously, testing in such conditions is also relevant for practical applications because every 12 V SLI battery experiences mechanical

vibrations in the field. As it is clearly visible in Fig. 77 there is no difference between relaxation behaviour with and without forced mixing of the electrolyte, which is a further proof for the discussed hypothesis.

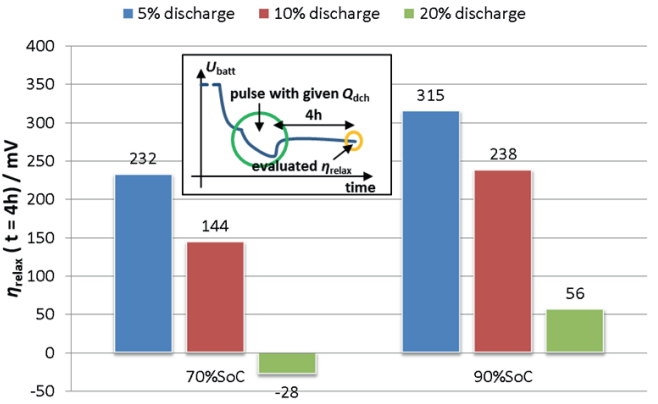

Fig. 76. Residual η_{relax} measured during SRT with additional discharge pulses. Each pulse is characterized by varying value of Q_{dch} followed by 4 h of rest period. Presented η_{relax} was collected at the end of this quiescent phase. Tested specimen is 74 Ah standard flooded battery conditioned to -10 °C and excited with Q_{cha} = 20% DoD, $I_{quiescent}$ = 0. Deviation of $U_{00,ref}$ between pulses with different Q_{dch} was compensated with the assumption that 1% SoC = 11 mV.

Expected duration of relaxation is significantly higher than available time at rest in the field. Therefore, this issue has to be considered, especially for analysing operation conditions that could be used for accurate adaptation of any U_{00} estimation model.

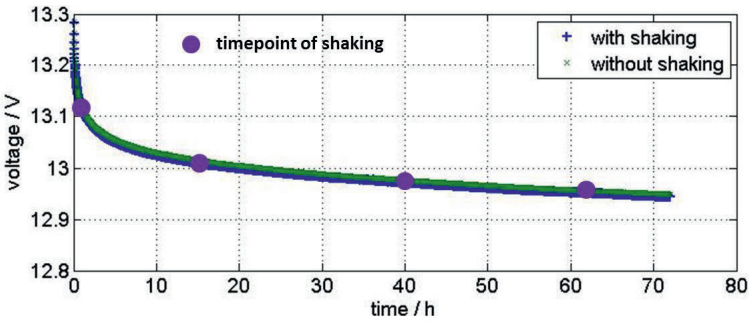

Fig. 77. Impact of manual shaking on the relaxation behaviour recorded during SRT performed using a 74 Ah standard flooded battery conditioned to 25 °C, 90% SoC and excited with Q_{cha} = 3% DoD, $I_{quiescent}$ = 0.

Worth mentioning is also the fact that each BMS not only estimates the value of SoC but also calculates signals called state-of-function (SoF). This term describes all parameters, which are being calculated for power or cranking capability prediction. Their accuracy should be as high as possible due to safety related aspects and reliability of the vehicle meaning that knowing η_{relax} could provide improvements in voltage drop prediction during cranking or any other relevant discharging phase. Observed effects are also crucial for every offline model used for computer aided engineering considering prediction of the expected voltage level of power net.

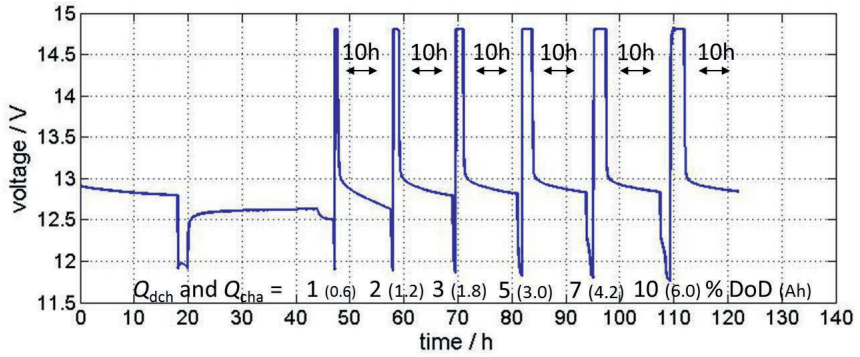

Fig. 78. Battery terminal voltage recorded during investigation of discharging behaviour of a 60 Ah AGM battery using SRT with unfinished relaxation excited with varying Q_{cha}, Q_{dch} and $I_{quiescent}$ = 20 mA. Tested battery was conditioned to 90% SoC and -20 °C.

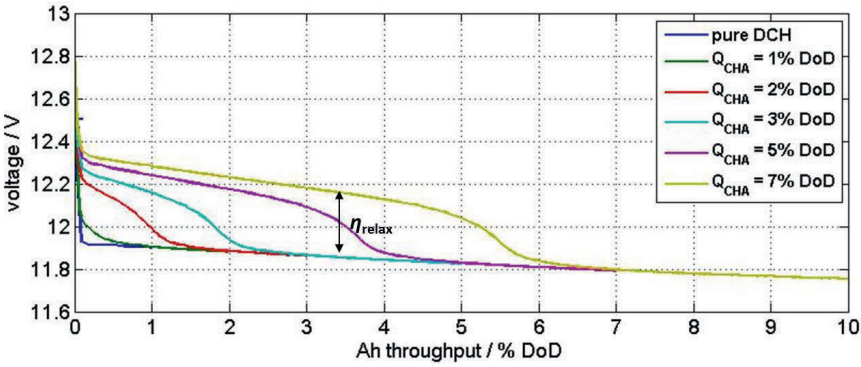

Fig. 79. Discharging curves extracted from SRT, which has been executed with varying Q_{cha} and performed on 60 Ah AGM battery conditioned to 90% SoC and -20 °C, $I_{quiescent}$ = 20 mA. Discharging current rate equals I_{20}. 1% Q_{cha} curve means discharging that started after exiting relaxation with Q_{cha} = 1% DoD and subsequent 10 h of relaxation. Constant value of 0.33% DoD should be added to the presented discharge profiles. It corresponds to Q_{dch} that was discharged during relaxation with $I_{quiescent}$.

A better understanding related to the impact of η_{relax} on the following discharging behaviour was the main motivation of the further study. To analyse the discharging behaviour with unfinished relaxation characterized by charge short-term history 60 Ah AGM batteries were subjected to a SRT testing procedure with different Q_{cha} and fixed t_{relax} of 10 h as shown in Fig. 78. Q_{dch} imposed after each 10 h at rest equals Q_{cha} to the prevent significant SoC decrease throughout the whole test.

Fig. 79 depicts all discharging curves recorded during SRT with the battery conditioned to -20 °C. As it was the case in discharge pulse investigation discussed at the beginning of this subchapter (see Fig. 75), η_{relax} can be fully removed only when amount of charged amp-hours that excited relaxation with charge short-term history is equal to the number of discharged amp-hours ($Q_{cha} = Q_{dch}$).

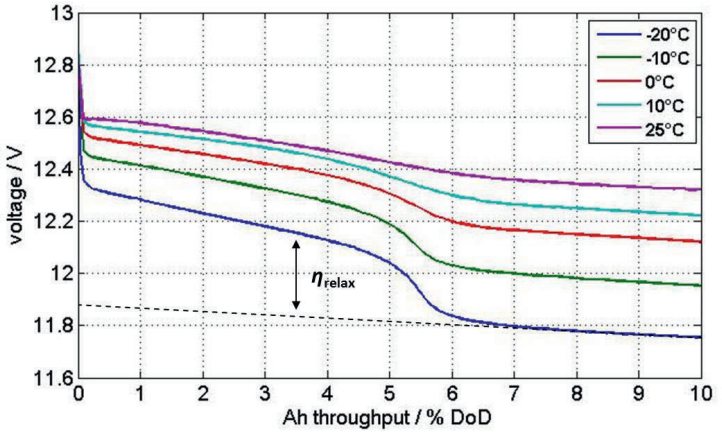

Fig. 80. Voltage curves recorded during discharging after unfinished relaxation excited with Q_{cha} = 7% DoD and followed by short rest period of 10 h with $I_{quiescent}$ = 20 mA. Test data originates from SRT performed on 60 Ah AGM battery conditioned to 90% SoC and various temperatures. Discharging current rate equals I_{20}.

Reported maximal η_{relax} is in the range of 400 mV, which fully complies with the data presented in Fig. 61 and signalizes a possibility of direct implementation of the presented relations for estimation of additional overvoltage during discharging. Full removal of η_{relax} that did not fade away during preceding relaxation is being signalized by a characteristic voltage step or voltage dip (e.g. visible in Fig. 80 between Ah throughput between 5 and 6 % DoD). From this time point U_{batt} behaves as if no charge short-term history was available. This type of behaviour was also observed during previous investigations. It was found that increasing temperature significantly decreases magnitude of the observed η_{relax} during discharging phases, which has been illustrated in Fig. 80. Furthermore, discharging behaviour observed while enforcing discharging phase at a different time points during relaxation also comply with the understanding and knowledge gathered from the previous tests. As demonstrated in Fig. 81 the

later a discharging phase occurs or the more progressed relaxation is the less η_{relax} and time until characteristic voltage step emerges is needed.

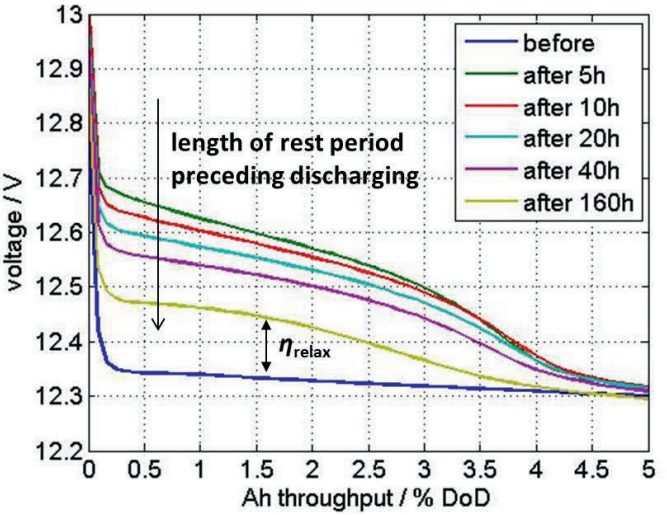

Fig. 81. Voltage curves recorded during discharging after unfinished relaxation excited with Q_{cha} = 5% DoD and followed by rest periods with various duration, whereby $I_{quiescent}$ = 0. Presented test data originates from SRT performed on 60 Ah AGM battery conditioned to 90% SoC and 0 °C. Discharging current rate equals I_{20}.

Further experimental investigation was carried out to provide additional evidence that observed altered discharging behaviour is caused by presence of η_{relax} originating from unfinished relaxation rather than other effects. Testing was conducted using slightly modified SRT presented in Fig. 78 and the same specimen conditioned to even conditions. The only change is introduction of additional 10-minute-long rest periods during last discharging (Q_{dch} = 10% DoD) phase. Resulting U_{batt} profile has been depicted in Fig. 82. If identified effects were related rather to changing value of $R_{overall}$, U_{batt} recorded during short rest periods imposed whilst discharging would not show a characteristic voltage step. However, the opposite behaviour was recorded, which is a further proof that η_{relax} does not only refer to relaxation phases but also stays present in the following discharging events. Nevertheless, as it is visible in Fig. 82b $R_{overall}$ increases slightly after emergence of characteristic voltage step as well. The difference between voltage drop before and after voltage step in case of $R_{overall}$ and quasi U_{00} (voltage measured at the end of 10-minute-long rest period) equals approx. 100 mV and 200 mV respectively. Thus, the latter one is determinant.

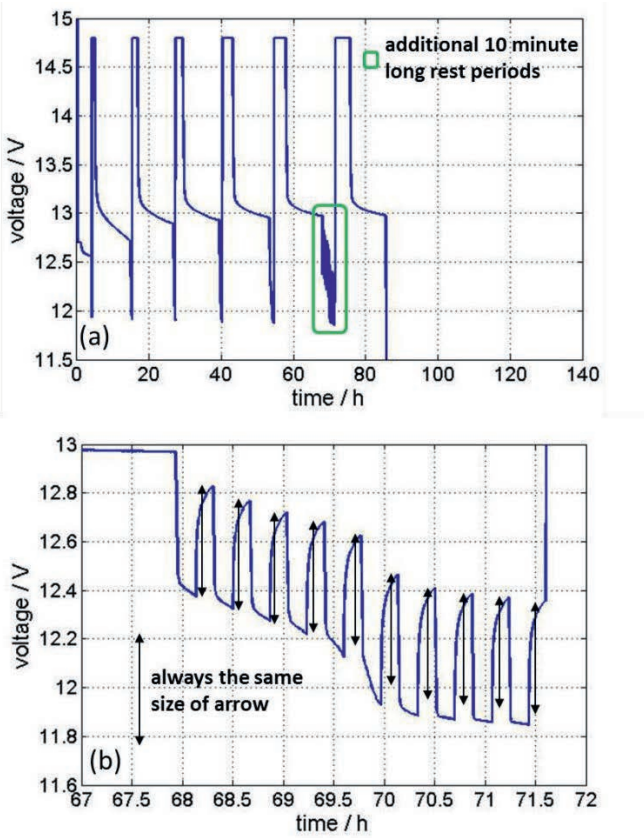

Fig. 82. Battery terminal voltage recorded during SRT with additional rest periods incorporated in the last discharging phase (after Q_{cha} = 7% DoD). Tested specimen was a 60 Ah AGM battery conditioned to 90% SoC, -20 °C and excited with Q_{cha} = 1, 2, 3, 5, 7, 10 % DoD (this order), $I_{quiescent}$ = 20 mA. (a) overview over the whole test, (b) zoomed last discharge phase.

Discussion presented in this chapter highlighted the fact that studied relaxation behaviour and its characteristic parameters are not only relevant to rest periods but are also important during following discharging phases. Although modelling of discharging behaviour is not in a scope of this work, gained understanding can be used for further improvements of other parameter that are being calculated by BMS, e.g. SoF signals.

5.3.8 Summary of all observed dependencies

Results of the comprehensive experimental study concerning relaxation behaviour of PbA have been presented and thoroughly discussed in chapters 5.3.1-5.3.7. It was found that the studied behaviour is highly complex and interdependent, which makes building of any model a

challenging task. Nevertheless, gained deep understanding concerning both quantitative and qualitative relationships, makes it possible. It should be added that feasible assumptions, which can be used for the development of simplified BMS solutions, were determined over the course of carried out tests as well. Their main goal is to reduce the complexity in a way that still allows achieving a good accuracy of U_{00} and t_{relax} estimation for operation conditions typical for µH applications.

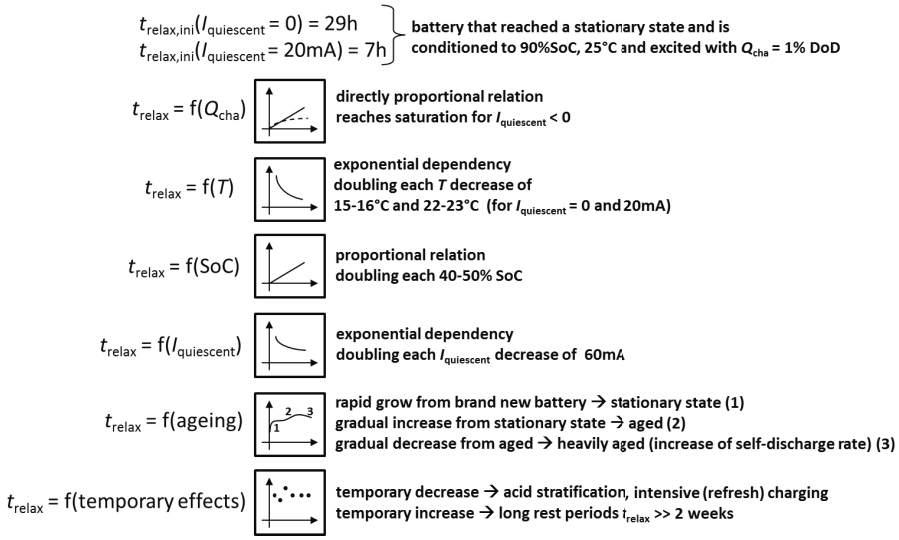

Fig. 83. Schematic representation of all identified effects and corresponding factors that considerably influence relaxation behaviour.

Fig. 83 presents an overview of all extracted dependencies concerning calculation of t_{relax}. It can be estimated using initial or standardized value ($t_{relax,ini}$), which is scaled with given factors that consider different operation conditions. Main advantage of this approach is its universality. It can be used for an accurate prediction of relaxation time of every battery type at any state. $t_{relax,ini}$ can be easily obtained from a simplified calibration test for relaxation (SCTR). An example of such testing procedure has been depicted in Fig. 84. If the tested battery before the measurement was at relatively high SoC (U_{batt} at room temperature > 12.6 V), it can be carried out without any modifications (like introduction of the extended rest period after 1st charging due to high number of Q_{cha}). Otherwise, prior to the beginning the battery should be fully charged and preconditioned in the same way as used for SRT. It is due to the risk of generation of too high acid stratification and residual relaxation during the first charging. The main disadvantage of this method is a fact that this is an empirical method, which may lead to significant error if considered battery behaves differently. This may be caused by either presence or increase in dosage of additives in PAM or significantly increased self-discharge rate.

Suggested SCTR consists of three relaxation events at standardized conditions with $I_{quiescent} = 0$, which show if the battery have already reached a stationary state and provide a stable value of $t_{relax,ini}$. As a practical rule $t_{relax,ini}$ extracted from the last repetition can be divided by four in order to get a stationary value, which refers to $I_{quiescent} = 20$ mA. First relaxation check-up usually deviates from stationary reproducible state as it was discussed before and pointed out in Fig. 83. In this case it was caused by relatively long rest period before BUT was subjected to SCTR. If $t_{relax,ini}$ is known, extracted scaling factors that cover all field relevant conditions are directly applicable for final estimation of t_{relax}. It has to be noted that the main disadvantage of presented scaling technique is the fact that the more current operation conditions deviate from standardized ones the higher estimation error is expected. Analogically to t_{relax}, the same approach for estimation of η_{relax} can be derived as well.

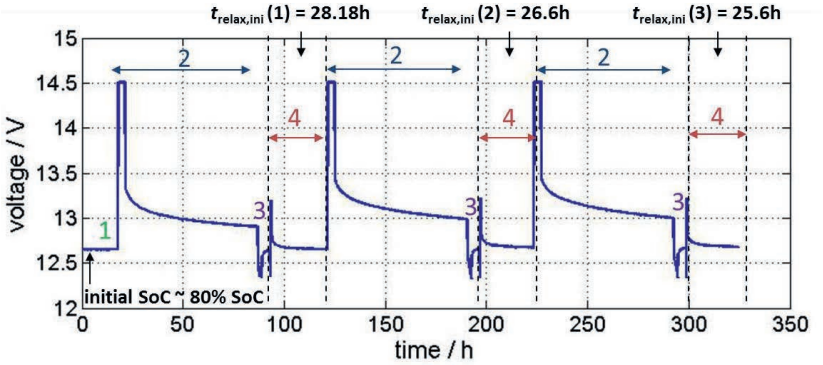

Fig. 84. Specification of SCTR using an example of measurement data obtained from testing of 95Ah standard flooded battery conditioned to 25 °C, $I_{quiescent} = 0$. Presented test has been divided into four phases, which are repeated 3 times: (1) temperature setup to 25 °C, (2) charging with $5I_{20}$, 14.5 V for 3 h followed by 66 h rest period employed for destratification and removal of residual relaxation, (3) discharging with I_{20} to target SoC of 90% and waiting for 4 h to obtain $U_{00,ref}$, (4) relaxation phase excited with I_{20} and $Q_{cha} = 1\%$ DoD until $U_{batt} = U_{00,ref} + 11$ mV.

Thorough understanding together with qualitative and quantitative relations, which have been found over the course of presented experimental study, are a solid basis for the development of U_{00} semi-empirical estimation algorithms. They explain in detail all parameters that have to be taken into account and other factors that can be neglected. Furthermore, η_{relax} that causes significant deviation between U_{batt} and U_{00} in relaxation phases does not disappear during followed discharge phase as presented and discussed in 5.3.7. This information can be used for both smart adaptation of any U_{00} estimation model and improving electrical models that are applied for calculation of SoF signals. Investigated relaxation behaviour alters with ageing as showed in chapter 5.3.6. Presented results indicate that mechanisms occurring while battery ages need to be taken into account to provide high accuracy considering modelling of relaxation

throughout whole battery life. Observed saturation behaviour discussed in chapter 5.3.6 could be also used for this task.

5.4 Double-layer gel-crystal model of the positive electrode

5.4.1 Structural changes of the positive electrode during operation

Comprehensive experimental study described in the previous sections delivered a full overview of the possible parameter dependencies of PbA relaxation behaviour. One of the most crucial findings indicates that all observed relaxation effects can be directly linked to the positive electrode. Furthermore, all qualitative and quantitative relationships, which are relevant for µH applications, have been identified and extracted. Still the most important question has not been answered yet, which can be formulated as follows: What are the physical causes of observed phenomena and how do they relate to the observed trends. Characteristics and relevant features of PAM have been studied in detail to provide the most feasible explanation and extensive discussion and can be found in multiple publications of renowned researchers and engineers e.g. [18][20][22][88][103]. It is believed that extended relaxation phases observed after either charge period or operation with positive balance of amp-hours are caused by phenomena, which alter internal structure of PAM, especially at the active material/electrolyte interface. This statement has been already explained in chapter 5.3.3 and further experimentally examined in chapter 5.3.7. Considered mechanisms are measurable as decisive contribution to η_{relax} that has been already introduced in (34) as η_{solid}. It corresponds only to relaxation with charge short-term history involving significantly higher η_{relax} in comparison to voltage recovery after discharging. Accurate modelling of η_{solid} is the key to improved U_{00} estimation algorithms, which are able to work efficiently not only in the conditions used in parameterization measurements, but also far beyond them.

It is well-known that PAM is characterized by a certain non-stoichiometry. Lead dioxide (most often described as stoichiometric PbO_2) obtained either chemically or electrochemically always comprises some distortions in its molecular structure and takes the form of $PbO_{2-\delta}$, as introduced by Meissner in [104]or $PbO_{2-x}(OH)_y$ as suggested by Pavlov in [18]. The parameters δ, x and y refer to the mentioned non-stoichiometry.

Furthermore, there are two different types of PbO_2, namely rhombic α-PbO_2 and tetragonal β-PbO_2, which are described by various electrochemical activity and physical as well as electrical features. They both appear in commercial PbA during operation and have to be taken into account. Pavlov in [18] presented non-stoichiometry of all mentioned forms of PbO_2 obtained using different methods and proved that there is no such thing as fixed stoichiometric chemical composition of PbO_2. It will change in the course of battery life depending on short-term and long-term history. For the sake of clarity distorted form of PbO_2 will be called $PbO(OH)_2$ from now on. The described non-stoichiometry is directly linked to the incorporation of the hydrogen, hydrogen species or OH^- ions into PAM, which will be addressed as hydration in the further part of this work. Mentioned changes in the positive active material has been already observed by multiple authors, e.g. [105][106][107][108][109][110] and discussed mainly in terms of its impact on the battery failure mode or expected life. Kirchev et al. [78]

derived chemical equations, which analytically explain how PAM gets hydrated and dehydrated during charging (oxidation of $PbSO_4$) and following rest periods respectively. They have been illustrated in (35).

Monahov et al. [111] and Pavlov et al. [107][109] claimed that hydrated PAM cannot be found by means of X-ray diffraction. If this statement is correct, their findings provide a strong evidence of the existence of $PbO(OH)_2$ because X-Ray methodology allows analysing and detection of crystalline material exclusively. It signalizes that $PbO(OH)_2$ is an amorphous, non-crystalline material characterized by lack of symmetry or correlation in particle structure that is typical for crystals.

$$
\begin{aligned}
&PbSO_4 \Leftrightarrow Pb^{2+} + SO_4^{2-} \\
&Pb^{2+} \rightarrow Pb^{4+} + 2e^- \\
&Pb^{4+} + 4H_2O \rightarrow Pb(OH)_4 + 4H^+ \\
&Pb(OH)_4 \xrightarrow{\text{hydration}} PbO(OH)_2 + H_2O \\
&PbO(OH)_2 \xrightarrow{\text{dehydration}} PbO_2 + H_2O
\end{aligned}
\tag{35}
$$

According to Pavlov et al. [112], obtained scanning electron microscope (SEM) pictures additionally show that hydrated active material form gel zones with drop-like or spherical particles. They dehydrate with time and reform themselves into crystalline back again. This process has been illustrated in Fig. 85.

It has been assumed that changes in the active material appear mostly directly on its surface as mentioned at the beginning of this chapter, which is proven by transmission electron microscope (TEM) micrographs of PbO_2 particles presented in [109] and depicted in Fig. 86. Blurred areas in Fig. 86d illustrate PbO2 particle extracted from PAM of PbA, directly signalize existence of an electron beam transparent hydrated zones. They are mostly accumulated close to active material/electrolyte interface, which fully complies with the findings presented in chapter 5.3. Furthermore, authors of [113] also found that heating up of the probes under microscope increases areas of the dark spots. Thus, the gel zones get dehydrated (bounded water evaporates) faster and turn back into crystalline.

Another experimental investigation presented in [109] further proves mentioned statements. It focused on evaluation of diffraction peak area during overcharging and following rest periods. High and low peak values found during rest periods and overcharging respectively directly link forming of gel zones with the concerned relaxation behaviour. Presented evidence clearly show that the surface of PAM changes significantly during operation. According to the own results presented in chapter 5.3 and mentioned publications of multiple authors it has been assumed that considered processes can be directly linked to formation of the hydrated zones (or hydration layer).

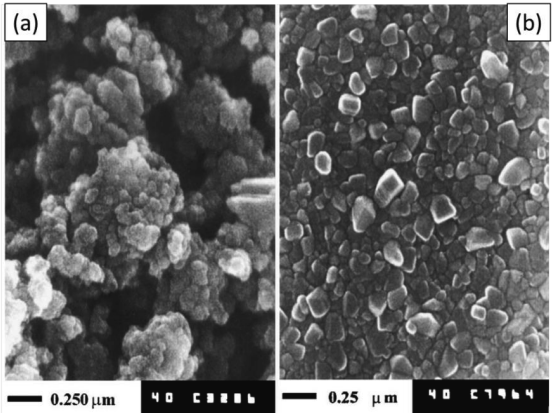

Fig. 85. SEM pictures of PbO_2 particles obtained by Pavlov et al. [112]: (a) Ions of the solution contribute to the growth of gel zones that are visible as spherical or drop-like particles, (b) Growth of the crystalline areas at the expense of gel zones.

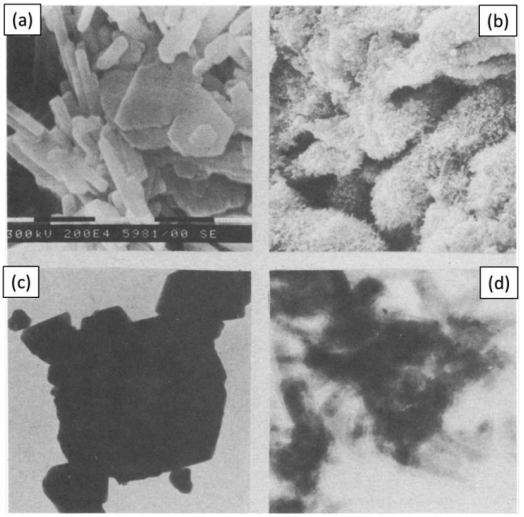

Fig. 86. SEM (a and b) and TEM (c and d) micrographs originating from [109] of chemically obtained PbO_2 as well as PAM extracted from PbA respectively. The former one can be assumed as highly crystalline material.

Charging increases hydration of the positive electrode, whereby rest periods reduce it. However, until this point it has not been discussed how it influences measured potential of PAM or how η_{solid} is being generated. This question has already been answered by Atlung and Pohl [114][115]. They discussed behaviour of not-stoichiometric metal oxides concerning

equilibrated state in aqueous electrolytes and derived corresponding analytic expressions for electrode potential (ε). Equation resulting from their work that describes relation between ε and distortion factor x has been depicted in (36).

$$\boldsymbol{\varepsilon = const. + \frac{RT}{F}(\ln a_{H^+} - 2.1 \ln x)} \tag{36}$$

If a_{H+} is assumed as constant and x equals 0.01, resulting η_{solid} for 298.15 K (25 °C) amounts to 124 mV. It has to be noted that this value is not directly transferable to commercial PbA because of expected inhomogeneous distribution of gel zones with different x factors on the electrode surface, which in the end will result in generation of a mixed potential. However, it shows clearly that distortion shifts electrode potential towards higher values. This finding fully complies with relaxation behaviour observed in all available test data. Potential shift has been also mentioned by Pavlov et al. [113], who directly linked it to water that enters PbO_2 particles. Meissner in [104] added that the shape of the particles also influences equilibrium potential of PAM. The more spherical particles are the higher ε will be. It has been graphically illustrated in Fig. 87. This consideration is fully coherent with SEM pictures presented in Fig. 85 (hydrated layers are characterized by more spherical shape than crystalline material) and together with other explanation described in this chapter provides a solid evidence for the determined concept.

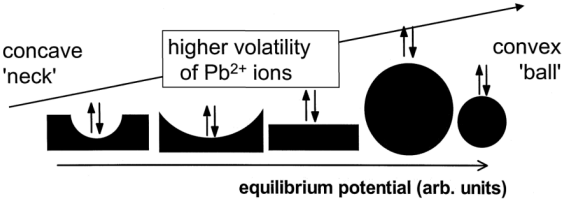

Fig. 87. Impact of electrode surface on the expected equilibrium potential (arbitrary units) according to [104].

5.4.2 Introduction into gel-crystal system concept

Extensive evidence was presented in the introduction of this chapter, which proves that assumed changes in PAM during operation take place. It was also shown that they are mainly concentrated on PAM surface, which is in direct contact with the electrolyte and decides about the current value of equilibrated U_{00}.

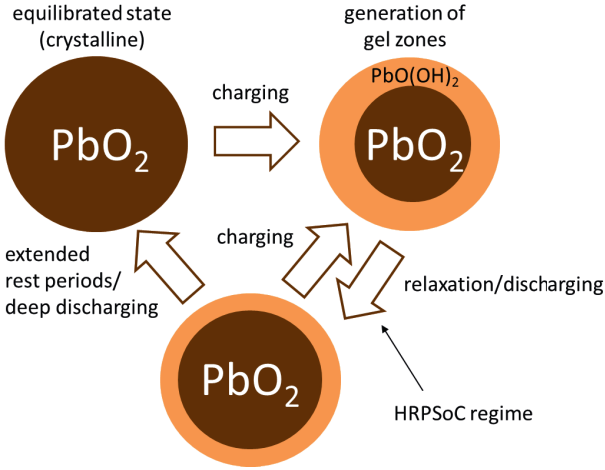

Fig. 88. One particle phenomenological gel-crystal model that explains processes occurring in PAM during operation. For the sake of simplicity formation of $PbSO_4$ has been neglected.

Changes of the lead dioxide are removed during rest periods or discharging because distorted or hydrated PAM turns back into crystalline or is discharged respectively. These processes can be illustrated using a one particle phenomenological model presented in Fig. 88. Nevertheless, present understanding has a few discrepancies with the findings available in the literature. They have been listed and discussed below:

- In order to obtain a sharp and representative micrograph using nearly any known technique each probe has to be firstly extracted from a battery or test cell and subsequently washed and dried before it can be put under the microscope. Therefore, it should be expected that a considerable part of gel zones gets lost during preparation, which highly influence PbA relaxation behaviour. Additionally, generated η_{solid} fades away relatively fast at room temperature according to the carried out experimental study, which suggests the necessity of freezing of the probes directly after current interruption. Such sample preparation was most probably not the case concerning decisive majority of the available micrographs. It means that pictures and recordings presented in the literature do not show exact state of PAM that could be directly linked with the freshly charged battery. Hence sample preparation influences interpretation.

- Carried out relaxation tests with commercial batteries conditioned to 25°C provided t_{relax} in range of at least several hours, whereby measurement results performed on test cells presented in the literature (see [107]) are rather in the region of minutes or even seconds [116].

- Kirchev et al. [78] showed an EEC model of PbA, which includes an RC element associated to gel layer. In this work, amorphous material is characterized by time constant in the range of milliseconds. On the one hand, it provides good electron transfer through hydrated layer, but, on the other hand it does not explain why experimentally obtained t_{relax} is much higher.

- It was found by Pavlov et al. [117], who used XRD technique, that overcharging at high SoC cause a significant decrease of crystallinity, which can be mainly linked to gassing, whereas an opposite relation considering relaxation behaviour in such operation mode was found in the investigation described in chapter 5.3.3.

- Pavlov et al. [107][113] explained that there is an equilibrium between crystalline and gel zones, where always approx. 30% of PAM is hydrated. It means that if the positive electrode is immersed in the sulfuric acid some of its part will be always amorphous regardless of the short-term history.

Known publications and current theories do not address some of the relationships identified in the presented work. Examples are the impact of ageing, SoC, temperature or $I_{quiescent}$ in context of relaxation behaviour. They are of high significance for practical applications and commercial batteries and cannot be neglected. Issues listed above show that the well-known gel-crystal model depicted in Fig. 88 does not fully explain observed complexity. That is the reason why a novel complemented double-layer gel-crystal model has been developed and described in chapter 5.4.3. It is based on the work of Kordes [118], who found that hydrated layers or gel zones consist of both softly and hardly bounded water. The first one fully evaporates at the temperature above 90 °C, which is slightly above the maximal operation temperature of SLI batteries operated in µH applications. The second one leaves PbO_2 at the temperature of 200 °C. Weakly and tightly bound OH^- groups has been also mentioned by Pavlov and co-worker in [107]. These finding indicate that considered gel layer has to be understood as inhomogeneous and dynamic.

5.4.3 Double-layer gel-crystal model and explanation of the identified relations

Findings described in chapter 5.4.2 signalize that hydrated layer located on PAM surface represented by one particle model consists of both weakly and tightly bound water or OH^- groups. It means that a gel zone can be split into two parts, soft and hard layer respectively. The former one can be associated to observed relaxation behaviour with charge short-term history (see chapter 5.3.3). The latter one together with composition of crystalline PbO_2 changes during battery life and explains observed impact of ageing (see chapter 5.3.6). Soft layer may fully vanish or recrystallize during relaxation, whereas hard layer is always present. Developed comprehensive one particle model of PAM that is being supported by previously described

theories can be found in Fig. 89. It schematically illustrates derived double-layer gel-crystal model (DLGCM).

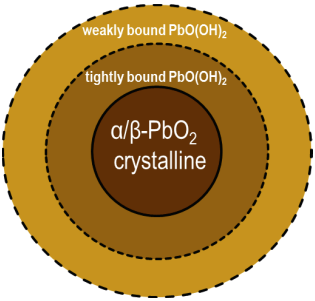

Fig. 89. Schematic visualization of one particle double-layer gel-crystal model of PAM.

Presented visualization indicates that particle core consists of fully crystalline PbO_2 material that consists of both forms of PAM namely α- and β-PbO_2. At the beginning of each SLI battery life when soaking and formation are carried out, their ratio equals nearly 1:1. It is due to the fact that this processes are usually conducted in electrolyte with ρ_{acid} as low as 1.15 $kg \cdot l^{-1}$, which promotes formation of α-PbO_2. β-PbO_2 is being generated mostly in more concentrated acid. Pavlov in [18] explained that this ratio is needed to obtain a battery with a long expected life and high capacity. SLI batteries are being operated after formation in µH applications rather at high SoC and therefore also at high ρ_{acid}. Constant operation at ρ_{acid}, which is significantly higher than 1.2 $kg \cdot l^{-1}$, imposes transformation of α-PbO_2 into β-PbO_2, especially at the surface of PAM. This process has been illustrated in Fig. 90 and already discussed by multiple researchers e.g. [118][119][120][121].

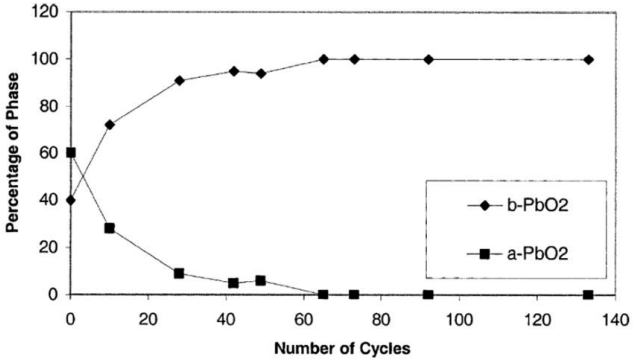

Fig. 90. Composition of PAM recorded during 100% DoD cycling performed on 40 Ah AGM batteries. Presented tests results originate from the work of Ball et al. [119].

Considering DLGCM these phenomena can be adapted in a way depicted in Fig. 91. Described behaviour fully explains impact of ageing and saturation behaviour observed within the course of carried out experimental study described in chapter 5.3.

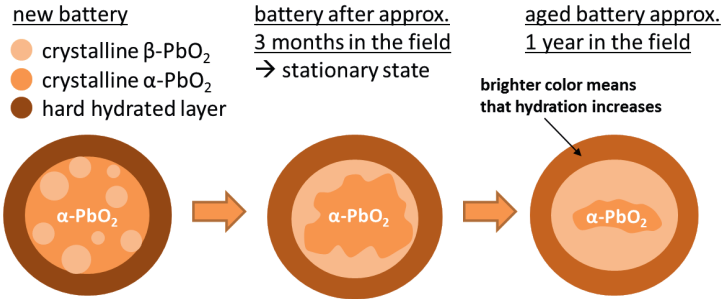

Fig. 91. Transformation of α-PbO_2 into β-PbO_2 presented using DLGCM.

At the beginning of battery life hard hydrated layer is relatively less distorted (hydrated) and crystalline material composition is characterized by high amount of α-PbO_2. According to Pavlov [18] α-PbO2 has much lower electrochemical activity than β-PbO_2. Additionally, it does not adsorb H_2SO_4 (also hydrogen species and OH^- groups) on its surface. It means that it is significantly less prone to hydration than β-PbO_2 and is able to preserve high part of its crystalline structure during operation. It explains why tested brand new batteries showed much lower t_{relax} and η_{relax} in comparison to those that reached a stationary state concerning relaxation (β-PbO_2 covers significantly greater part of PAM surface). Furthermore, qualitative evolution of these parameters is also the same. It shows a sharp increase of β-PbO_2 content and t_{relax} as well as η_{relax}. However, not always such a behaviour can be observed in the commercial batteries. This issue is strongly connected to the used formation [122] procedure and density of a paste as observed by Dodson in [123]. Wide range of initial α-PbO_2/β-PbO_2 ratios is possible due to the fact that there is no fixed or normalized mixture of positive paste and each battery manufacturer can choose it freely. On the one hand, it may happen that directly after assembling in the vehicle a brand-new battery reaches promptly the stationary state. On the other hand, a case when extended transient time (more than expected 3 months) to reach a stationary state, must be also considered.

Meissner et al. [104] found that maximum possible distortion of PAM regardless of α-PbO_2/β-PbO_2 ratio equals $\delta = 0.016$. It indicates that potential shift analytically described by (36) should saturate when this value of δ is reached. This statement is in full agreement with test results presented in 5.3. If hydration level of hard hydrated layer determines the minimal (basis) distortion of the soft hydrated layer, the hydration range (width between minimum and maximum value) of the latter one will continuously decrease during battery life. It explains why t_{relax} and η_{relax} measured at the same conditions, which are proportional to initial hydration of soft layer, grow with battery ageing.

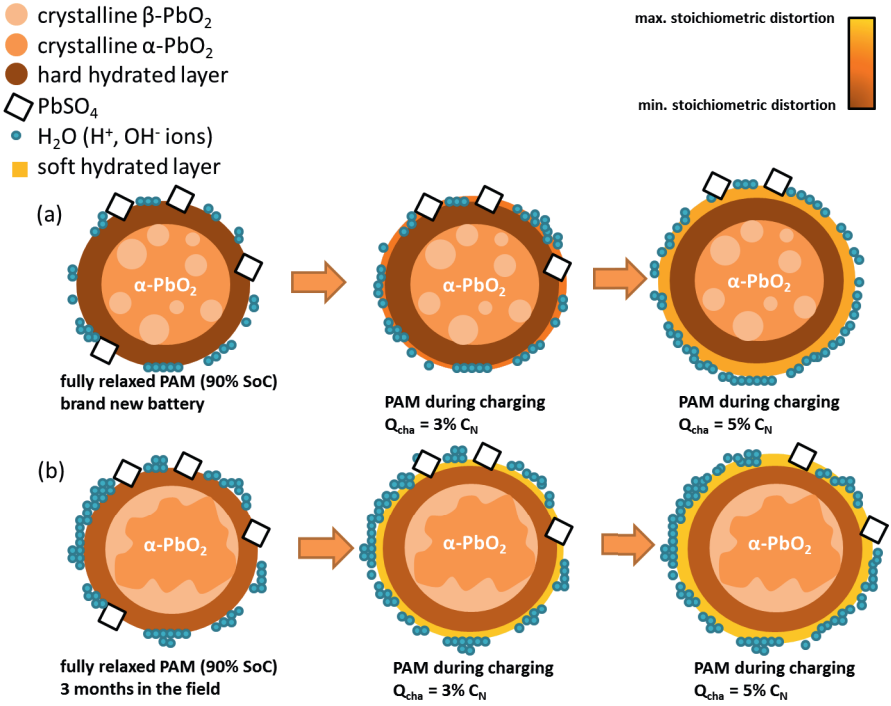

Fig. 92. DLGCM describing processes that occur on the surface of PAM in case of charging of (a) brand new battery and (b) new battery that have already reached a stationary state concerning relaxation behaviour. In case (b) maximal non-stoichiometry is reached at much lower Q_{cha}, which explains emergence of saturation effect that is only relevant for η_{relax}.

Moreover, it also clarifies why saturation behaviour was observed only for η_{relax} and not for t_{relax}. It refers to the fact that during charging of aged or new battery with stabilized relaxation behaviour δ is reached at a given time point but the width of soft hydration layer continuously grows. The value of δ is decisive for η_{relax} and the width of $PbO(OH)_2$ determines t_{relax}. These processes have been illustrated in Fig. 92. During rest periods soft hydrated layer generated during preceding charging is being transformed into crystalline by means of both recrystallization reaction progressing with time and discharging linked to self-discharge and $I_{quiescent}$. Dehydration obeys well-known Arrhenius relation. Its rate significantly decreases at low temperatures, which have been also observed in the carried out experimental study. Illustration of this phenomenon can be found in Fig. 93.

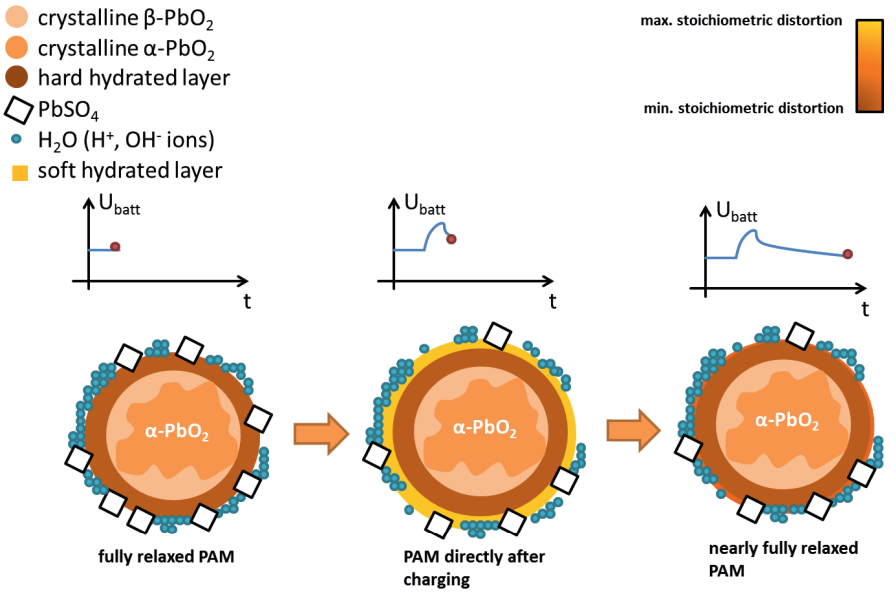

Fig. 93. DLGCM describing recrystallization processes that occur on the surface of PAM in case of resting after preceding charging.

Ruetschi et al. [124] discovered that the amount of oxygen evolved from PbO_2 samples immersed in electrolyte with various densities significantly increases with higher ρ_{acid}. It can be directly linked with SoC dependency obtained from SRT results, which is proportional to ρ_{acid}. The higher the SoC or electrode potential, the more prone to hydration active material will be and also the higher t_{relax} and η_{solid} becomes.

Presented concept of DLGCM fully complies with all identified relationships and observed PbA relaxation behaviour. It does not only explain how the short-term charge history forces increased overvoltage and extended rest periods but also clarifies the impact of ageing necessary to get U_{00} value. Furthermore, it gives an insight why additional overvoltage originating from unfinished relaxation process is still present in the battery voltage during subsequent discharging phases. Characteristic voltage step demonstrated in chapter 5.3.7 occurring when the exact number of amp-hours is firstly charged and discharged afterwards, indicates that soft hydrated layer has been fully removed. It means that open-circuit potential, which is directly related to characteristics of materials present in the active material/electrolyte interface, is back again determined by significantly increased crystallinity of PAM. The only factor, which alters this relation, is advancing time at rest. Thus, the more time at rest is given the higher amount of hydrated PAM will recrystallize so that lower Q_{dch} is needed for full removal of η_{solid}.

Described novel DLGCM fully complies with all conducted measurements and literature survey. Presented approach is based on the new theory that is based on the described observations. It has been developed considering known scientific evidence as well as current theories, which have been shown and discussed throughout this chapter. It complements understanding of PbA, especially processes happening during relaxation events. Furthermore, it provides a solid basis for development of reliable U_{00} estimation algorithms, which should be able to accurately calculate η_{relax} and subtract it from measured U_{batt} to get the value of a fully equilibrated U_{00}. In the end the more accurate U_{00} estimation is, the more precise final SoC prediction will be.

5.5 Online prediction of open-circuit voltage based on thorough understanding gained from carried out study

In the following subchapters two U_{00} estimation approaches are described, which have been developed. Their simplicity and promising improved accuracy make them suitable for final implementation in EBS. It was also found that smart combination of both called a hybrid U_{00} estimation model (HOCVM) can be efficiently used to provide even higher accuracy and adaptivity in all considered conditions, which is necessary to avoid deterioration of accuracy with battery ageing and adjustment to different PbA products. They are based on scaling approach, which has been already applied for quantification of carried out experimental study. According to carried out tests this method allows using just one normalized initial value that can be obtained by means of simplified parametrization test. In the next step this value is weighted with scaling factors concerning current operation conditions. Standardized value can be found by means of both laboratory tests and online adaptation algorithms. Although ASSF is switched-off in the most of commercial μH vehicles when the ambient temperature drops below 0°C, developed algorithms can efficiently operate with batteries conditioned to both low and elevated temperatures. It provides a higher degree of freedom for each automotive engineer that is reconsidering altering the mentioned temperature limit due to introduction of new PbA products with improved performance and dynamic charge acceptance (see [25]). The only issue, which remains unsolved, is a proper calculation of Q_{cha}, which is needed as an input of each model. In the field conditions hardly any rest period is long enough for a full removal of η_{relax}, which means that Q_{cha} cannot be reset after each resting and has to be cumulated over time according to the current state of Ah counter and set to 0 when a rest period longer than at least one week occurs. However, within the frame of this work this methodology has been neither implemented nor tested and can be considered as crucial part of a future work.

5.5.1 Equivalent electrical circuit model with arbitrary number of RC elements

Battery voltage measured over time during relaxation behaviour excited with charge short-term history is equivalent to discharging process of a RC element. It refers to a case when fully charged capacity discharges itself through resistance in open-circuit conditions. Following this observation and using the developed DLGCM as a basis, an algorithm concept has been created. A schematic representation is depicted in Fig. 94. It is based on EEC modelling methodology and assumes that the longer expected t_{relax} is, the more RC elements are needed to accurately

model considered phenomena. Each RC element can be associated with number of soft hydrated layers with its own time constant ($\tau_{soft,i}$). The identified and considered parameters that influence expected t_{relax} and η_{relax} are Q_{cha}, T, SoC and $I_{quiescent}$. Additionally, ageing that mostly influences crystalline material and hard hydrated layer needs to be also taken into account. It can be addressed by smart online adaptation algorithm that will alter standardized values used for scaling. However, development of such adaptation method was not in the scope of this work. Mentioned factors have to be considered for an accurate prediction of η_{relax} at a given time point, which will be subsequently used for U_{00} estimation according to (37). Major requirement is that the maximal time interval between the beginning of the relaxation and an accurate U_{00} estimation should be not higher than 4 h.

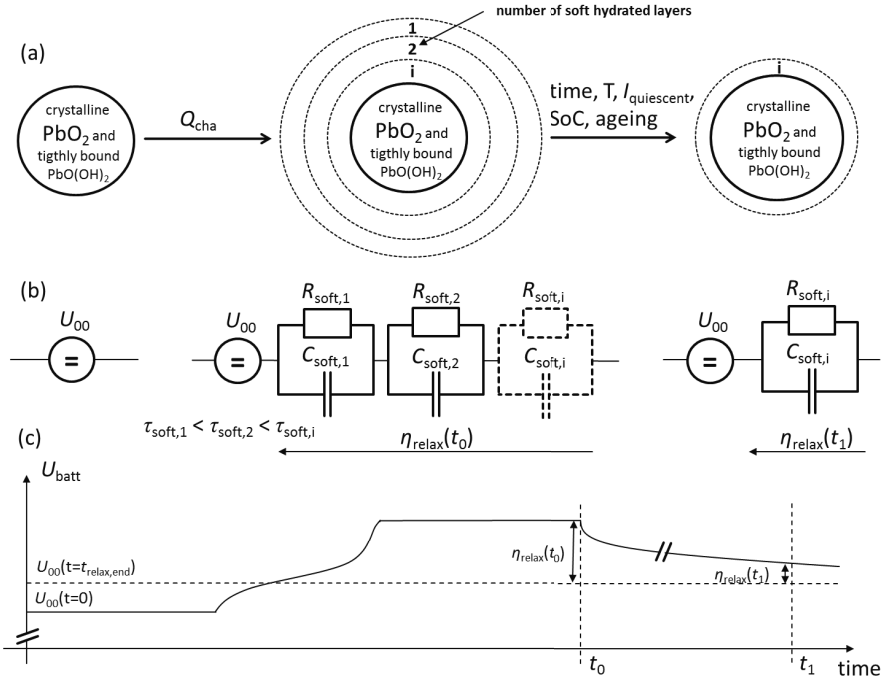

Fig. 94. Concept of EEC model with arbitrary number of RC elements (OCVFIT): (a) physico-chemical background originating from DLGCM, (b) implementation in form of EEC model, (c) voltage profile during relaxation, which illustrates how EEC model covers considered relaxation behaviour and calculates current value of η_{relax}.

$$\boldsymbol{U_{00}}^{\text{predicted}} = \boldsymbol{U}_{\text{batt}}(\text{t}) - \boldsymbol{\eta}_{\text{relax}}(\text{t})^{\text{predicted}} \tag{37}$$

In order to find how many RC elements are necessary to properly fit obtained relaxation curve (voltage over time recorded during relaxation with charge short-term history) all available test results have been fitted. It was found that relatively short relaxation with t_{relax} lower than approx.

10-20 h can be modelled accurately with one RC element, whereby two and three RC elements are needed for U_{00} estimation with relaxation characterized by t_{relax} up and above 100 h. Reduced gradient method was a fitting algorithm of choice. Its implementation resulted in the most stable and reproducible fitting results. They were achieved by means of fitting the mathematical relation presented in (38), whereby presented summation corresponds to η_{relax} at particular time point, t. Error definition used throughout all fittings was cumulated weighted absolute error, whereby the first hour of relaxation was neglected in the final implementation. It refers to assumption, which states that during first hour of relaxation η_{con} and η_{act} contribute the most to the overall overvoltage directly measurable as increased U_{batt}. They are not considered in this work and therefore a fitting process in this time range is not feasible. For the sake of better fitting quality U_{00} was exchanged with measured $U_{00,ref}$ and measured U_{batt} at the end of relaxation step was weighted higher than at the beginning.

$$\boldsymbol{U}_{\mathrm{batt}}(\mathrm{t}) = \boldsymbol{U}_{00,\mathrm{ref}} + \sum_{\boldsymbol{i}=1}^{\boldsymbol{n}_{\mathrm{RC}}} \boldsymbol{A}_{\mathrm{RC,i}} \cdot \boldsymbol{e}^{\left(\frac{-\mathrm{t}}{\boldsymbol{\tau}_{\mathrm{RC,i}}}\right)} \tag{38}$$

In equation (38) $A_{RC,i}$ and $\tau_{RC,i}$ refer to maximal voltage and time constant of each RC element respectively. n_{RC} refers to a number of RC elements estimated using mentioned criteria based on expected value of t_{relax}. Extracted $A_{RC,i}$ and $\tau_{RC,i}$ values are scaled using standardized values (T = 25 °C, 90% SoC, Q_{cha} = 1% DoD and $I_{quiescent}$ = 20 mA) as a function of all considered operation conditions (T, Q_{cha}, SoC, $I_{quiescent}$). These are then used for creating final U_{00} estimation algorithm concept which has been depicted in Fig. 95.

As the figure shows, the developed approach significantly simplifies fitting of the employed EEC. This has been achieved by means of implementation of the already known relaxation behaviour in form of relations and factors extracted from parameterization tests so that there are only two fitted parameters online, namely U_{00} and k. The latter one is used to compensate possible deviations of the model caused by ageing or modelling noise. It can be also employed for adaptation of the standardized values and calculation of the expected error range. Presence of only two parameters is of high significance for reduction of necessary computational power, reproducibility of fitting results and robustness. Over the course of its development and parametrization it was found that implementation of the most optimal online fitting algorithm is as important as high accuracy of the relaxation model itself, especially for operation at low temperatures. Exemplary algorithm, which has been used in this work, is recursive least square (RLS) fitting. More information about its features can be found in [62].

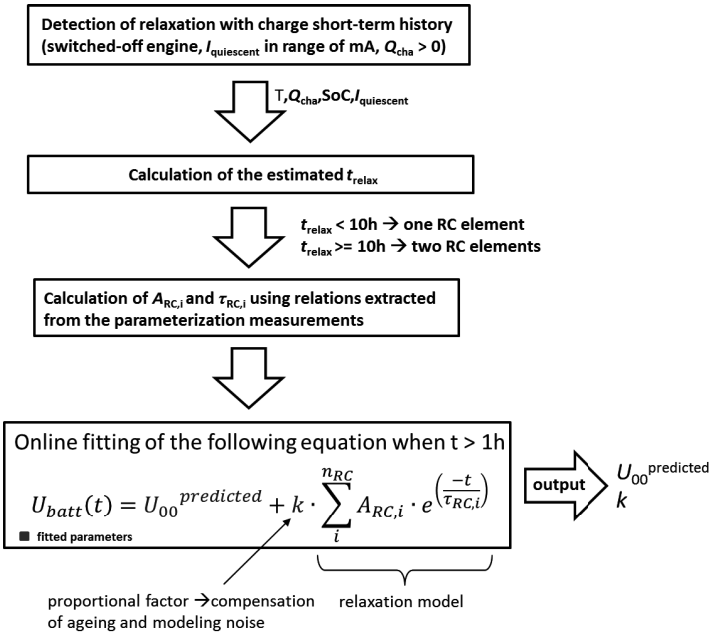

Fig. 95. Concept of U_{00} estimation algorithm based on EEC with arbitrary number of RC elements.

Summarizing, on the one hand the developed model is characterized by excellent robustness against measurement and modelling noise as well as adaptivity to battery ageing via employed proportional factor, k. It is fitted online every time a relaxation phase with charge short-time history is detected. On the other hand, it required long and comprehensive parametrization with experimental data, but, on the other hand obtained qualitative relations can be used throughout the battery life and do not have to be adapted. Final accuracy of U_{00} estimation strongly depends on the employed fitting algorithm, which in worst case scenario can get unstable and, the output would result in poor values.

5.5.2 Shifting of the characteristic curve approach

Shifting of the characteristic curve (SCC) originates from finding that differentiation of each recorded relaxation curve regardless of the current operation conditions leads to nearly the same relation with different constant coefficient. This coefficient shifts obtained relationship between η_{relax} and ΔU_{batt} depending on the factors representing current operating conditions. This observation is valid for every analysed measurement regardless of the employed testing specification. Using such approach allows observation of the current ΔU_{batt} over given time step and calculation of η_{relax} that can be directly subtracted from U_{batt} providing U_{00} value according to (37). Exemplary results of the mentioned differentiation as well as shifting procedure have been depicted in Fig. 96. It can be seen that the shape of resulting curves negligibly deviate

from each other so that just one characteristic or standardized curve can be implemented and shifted with known factors depending on the given operating conditions. Chosen differentiation time step of 2h is a trade-off between two requirements. The first one is related to maximum relaxation time interval of 4h after with an accurate U_{00} estimation must be available. The second on refers to simplicity of the developed approach, which is required for implementation in the low-cost hardware. At the beginning of relaxation the voltage decays very fast with η_{relax} staying high and not changing significantly. In this region obtained characteristic curve can be modelled by a simple linear curve.

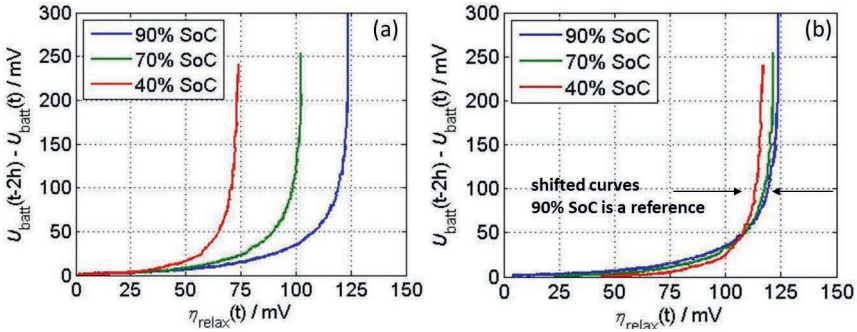

Fig. 96. Differentiation of relaxation curves obtained from testing of 74 Ah standard flooded battery subjected to SRT, excited with Q_{cha} = 5% DoD and conditioned to 25 °C and 90% SoC, $I_{quiescent}$ = 0: (a) original curves differentiated with time step of 2 h, (b) shifting of obtained characteristic curves towards reference.

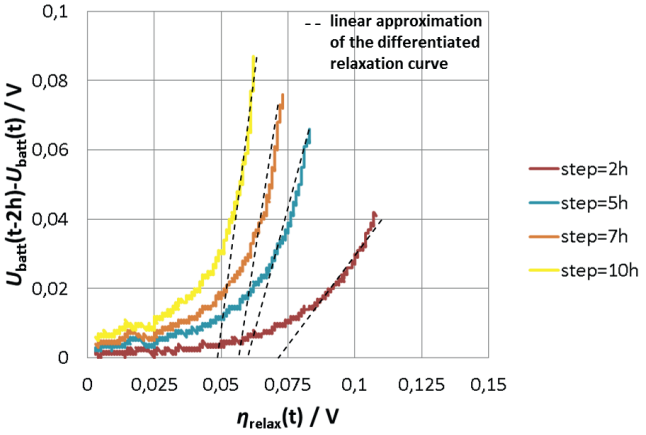

Fig. 97. Differentiation of the relaxation curves with different time steps performed using SRT results from 74 Ah standard flooded battery conditioned to 25 °C, 90% SoC and excited with Q_{cha} = 5% DoD, $I_{quiescent}$ = 0.

Working in range characterized by low η_{relax} is not feasible. This is due to the fact that η_{relax} alters relatively fast with very limited change of ΔU_{batt} in this area, which causes an unacceptably high sensitivity to measurement noise. On the one hand the higher the differentiation time step is the steeper resulting linear approximation will be. It is demonstrated in Fig. 97 (more steepness means less error caused by modelling noise of the slope). On the other hand longer working with time step causes a direct extension of required relaxation time to output first estimated U_{00}. Employment of two-hour differentiation step allows acceptable linear approximation and U_{00} estimation between 3rd and 4th hour (1st hour is fully neglected). Continuous U_{00} estimation for a given time is of high importance because a situation when only two measurement points are available for final U_{00} calculation has to be avoided. It is due to possible measurement noise, which can lead to emergence of transient error peaks that are fully removable applying low-pass filter on one-hour vector. Considering mentioned findings and simplifications, a second concept of U_{00} estimation algorithm using SCC approach has been created. Graphical explanation of its working principle can be found in Fig. 98.

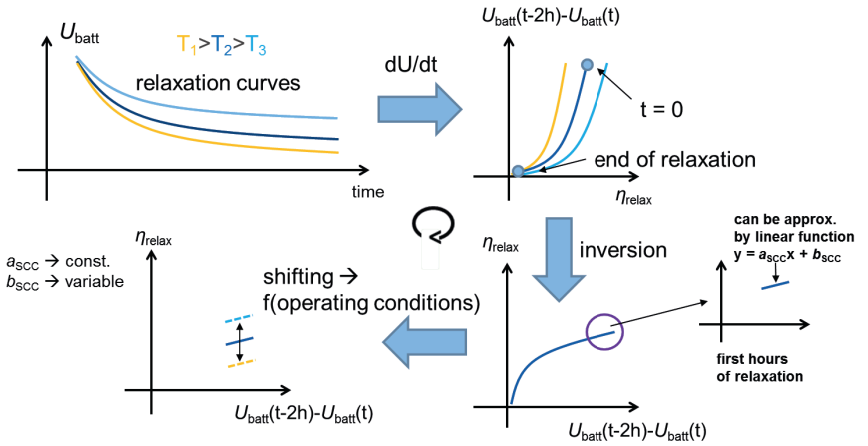

Fig. 98. Graphical description of U_{00} estimation algorithm based on SCC concept.

Final U_{00} calculation can be carried out using (39).

$$\boldsymbol{U_{00}}^{\text{predicted}} = \boldsymbol{U}_{\text{batt}}(\text{t}) - (\boldsymbol{a}_{\text{SCC}}(\boldsymbol{U}_{\text{batt}}(\text{t-2h}) - \boldsymbol{U}_{\text{batt}}) + \boldsymbol{b}_{\text{SCC}}) \tag{39}$$

where a_{SCC} is the constant slope of the employed linear approximation. b_{SCC} is a shifting coefficient and changes with varying operation conditions. The biggest advantage of using a linear function is its straightforward implementation in the low-cost hardware and low computational power required. Operation of the described algorithm has been illustrated in Fig. 99. Introduced linear approximation of the characteristic curve that describes identified relationship between differentiated U_{batt} and η_{relax} is only valid up to 4th hour of relaxation. After reaching this limit, the emergence of a significant modelling error can be expected.

Concluding, introduced SCC approach is characterized by significantly reduced complexity that is directly related to employment of linear relation between ΔU_{batt} and η_{relax}. It has been designed in a scalable way, which allows using of the known and non-adaptable scaling factors. It means that only single normalized value (e.g. 25 Ć, 90% SoC, $I_{quiescent}$ = 20mA), which alters with battery ageing, C_N or technology needs to be adapted. Developed SCC algorithm has a potential to provide accurately estimated value of U_{00} already after 3h of relaxation.

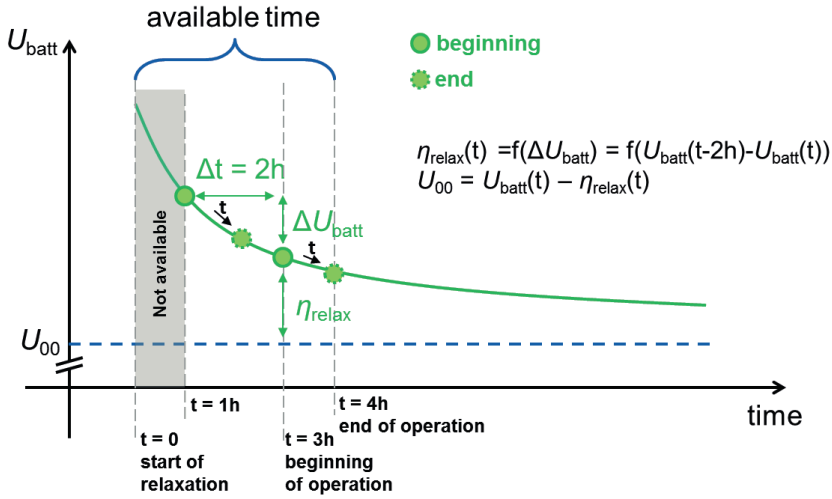

Fig. 99. Operation of the developed SCC algorithm for U_{00} estimation.

However, main disadvantage of SCC is lack of any direct possibility for adaptation that causes high sensitivity to changes in battery behaviour, which can be understood as modelling noise. This issue can be addressed either by implementation of both OCVFIT and SCC algorithm together and adaptation of the latter one with the fitting results of the former one. Another possibility of adaptation is related to observation of discharging behaviour recorded after unfinished relaxation, which has been shown and discussed in chapter 5.3.7. These two possibilities may have a high potential for a correct and accurate adaptation. However, they have not been developed in the frame of this work and can be analysed in the future research.

5.6 Calibration and validation

Calibration of the presented approaches has been carried out by means of fitting of extended number of relaxation curves collected from conducted experimental investigations described in chapter 5.3. They correspond to operation with both brand new and aged batteries at the following conditions:

- Temperature: -20 – 50 °C
- SoC: 40 – 90%
- Q_{cha}: 1 – 20% DoD
- $I_{quiescent}$: 20 – 102 mA

During initial tests it was found that OCVFIT shows excellent accuracy during operation at high temperatures and SCC at low temperatures. Because of that already mentioned HOCVM concept has been developed. It combines two described models so that adaptation is also possible. HOCVM utilizes strengths and limits weaknesses of SCC and OCVFIT and it is illustrated in Fig. 82.

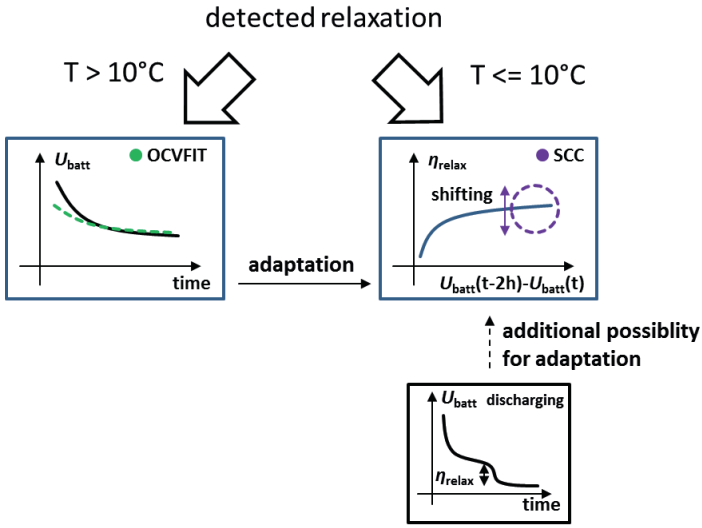

Fig. 100. Concept of hybrid U_{00} estimation model (HOCVM).

Additionally, standardized values of OCVFIT should also be adapted within the battery life to keep the expected the error as low as possible. Periodically executed refresh charging can be used to accomplish this task. Schaeck et al. [37] mentioned the timespan between successive refresh charging that is equivalent to 6 equivalent full capacity cycles. It can be considered as sufficient to register significant changes in the relaxation behaviour. After each refresh charging and at the beginning of following operation SLI battery is fully charged and it gets deliberately discharged by EMS to target SoC level, which usually lays around 80% SoC. In this case SoC

of the battery calculated using Ah counter can be considered as relatively accurate. Additionally, calculation of Q_{cha} should not be an issue in this case because all the charge from unfinished relaxation is being discharged. These are favourable conditions for special online fitting of the standardized parameters. However, development of such an approach was not in the scope of the presented work. This suggestion can be considered as a vital part of the future work. Achieved average absolute error using HOCVM on all collected 158 relaxation curves equals 23 mV, which refers to approx. 2% SoC.

Validation of introduced U_{00} estimation algorithms has been carried out using specially designed validation test (VAL) presented in Fig. 101 and described in detail in Table VII. VAL is based on a limited DCA of PbA, which will lead to a gradual decay of SoC if the battery is operated at high SoC. It is only valid if charging phases are time limited, which is the reproduced case. Such test specification resulted in observed relaxation with varying Q_{cha} and SoC that were set by the tested battery itself.

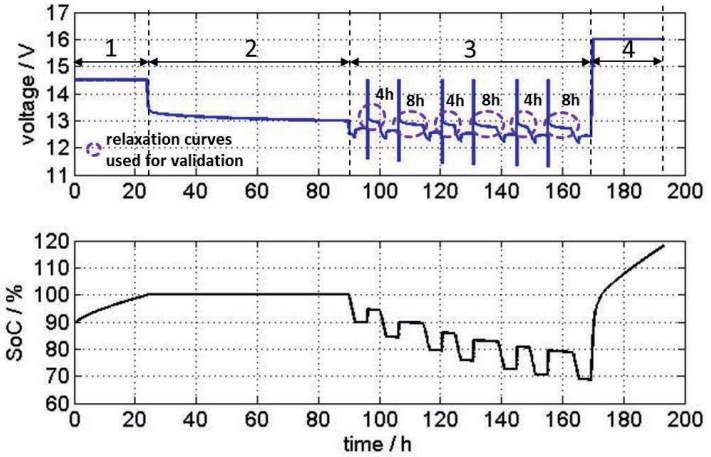

Fig. 101. Specification of the designed validation test (VAL) for U_{00} estimation algorithms using an example of U_{batt} and SoC measured during testing of 60 Ah EFB battery conditioned to 25 °C. Time indicated in phase 3 refers to the length of relaxation phases. Detailed explanation of each phase can be found in Table XIX.

Maximal current value during quasi cranking events of 100 A is the maximal current rate of the used automatic battery tester delivered by Digatron Power Electronics GmbH. 10% DoD discharge phases imposed after each relaxation were used for both collecting of $U_{00,ref}$ and full removal of imposed Q_{cha} so that the latter one was exactly known (calculated using Ah counter) for each collected relaxation curve. Even though that such discharging is not field-relevant, its implementation was necessary for reasonable evaluation of the developed U_{00} estimation algorithms, which could not be performed without $U_{00,ref}$ values and unknown Q_{cha}.

Validation of the developed U_{00} estimation algorithms employing VAL testing procedure was conducted using four different batteries, which were not brand new. None of them was used for preceding parametrization. Tested specimens are 60 Ah AGM, 60 Ah EFB, 74 Ah and 95 Ah standard flooded batteries. The former and latter one are the same type, which was used throughout experimental study of relaxation behaviour described in chapter 5.3. Before VAL started all of tested specimen had already reached stationary state concerning relaxation. Furthermore, used 60 Ah EFB battery can be considered as significantly aged. Before phase 1 of VAL took place, it experienced approx. four years of calendar ageing.

phase	description	comments
1	full charging	-
2	preconditioning needed for removal of residual acid stratification and relaxation from preceding charging	It consisted of rest period at 25 °C followed by temperature setup (valid for all tests performed at T < 25 °C). All tested batteries had initial SoC > 80% SoC. For deeply discharged ones significantly longer initial rest period is recommended.
3	driving profile with rest periods	Begins with 10% SoC discharging applying I_{20} that is followed by several hour long rest period. Rest period ends with a short discharging phase with given $I_{quiescent}$ at the end of which $U_{00,ref}$ is collected. Driving phases consist of synthetic operation with ASSF and BER: 1) DCH with $2I_{20}$ for 10 sec. 2) DCH with 100 A for 1 sec 3) CHA for 2 min. with $20I_{20}$ and 14.5 V 4) DCH with $10I_{20}$ for 1 min. 5) DCH with 100 A for 1 sec. 6) CHA for 2 min. with $20I_{20}$ and 14.5 V 7) repetition of steps 4-6 for 5 times There are 6 driving phases altogether. Each one lasts 30 min. and it is followed by alternatively positioned 4 h and 8 h relaxation phases with subsequent 10% DoD discharging with I_{20}. Subsequently, $U_{00,ref}$ is extracted in the same way as after initial discharging. $I_{quiescent}$ during 1-2, 3-4 and 5-6 relaxation phases is in range 20-30, 30-40 and 40-50 mA.
4	full charging	-

Table VII. Detailed specification of VAL testing procedure.

Performing validation with various battery sizes and types at entirely different states gives an opportunity to see whether previously reported accuracy can be assumed as valid regardless of battery product and its current progress of ageing. To get a good insight how the temperature influence expected accuracy, chosen tested batteries have been tested at various temperatures. Table VIII illustrates final assignment of particular batteries to chosen temperatures.

60 Ah AGM	60 Ah EFB	74 Ah flooded	95 Ah flooded
-	25 °C	-	25 °C
15 °C	-	15 °C	-
-5 °C	-5 °C	-5 °C	-5 °C
-18 °C	-	-	-18 °C

Table VIII. Assignment of temperatures for VAL testing of particular batteries under test.

For the sake of reducing the duration of the battery testing none of tested specimen were tested at all chosen temperatures. Relaxation behaviour of both 60 Ah AGM and 74 Ah standard flooded at 25 °C had been deeply studied during the described experimental study and that is why they were not subjected to the same conditions throughout the validation tests as used in the previous investigations (chapter 5.3). $U_{00,ref}$ recorded during rest periods succeeding driving phases were modified in a way that allows using their values for determination of the U_{00} estimation accuracy. It was done employing assumption that 1% SoC = 11 mV. Thus, 10% of SoC deviation results in necessary addition of 110 mV to the measured value. Description of all collected relaxation curves can be found in appendix (chapter 9.4).

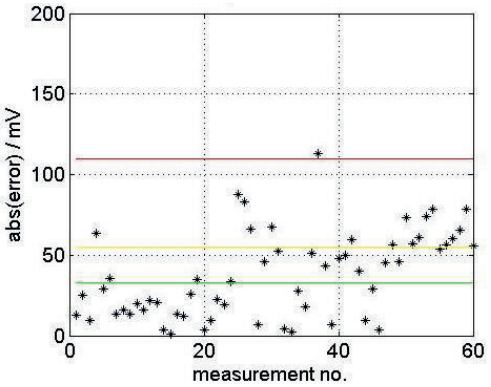

Fig. 102. Validation of the HOCVM algorithm obtained using relaxation curves described in chapter 9.4. Excellent, good and acceptable estimation refers to absolute error values of 33, 55 and 110 mV respectively. Obtained error has been recorded after 4 h of relaxation.

All relaxation curves obtained from VAL tests fully correspond to field conditions and can be considered as suitable for validation of the developed U_{00} estimation algorithms. Applying

hybrid HOCVM approach gives the best results and the lowest expected value of error. It indicates advantages provided by smart combination of OCVFIT and SCC as demonstrated in Fig. 102. It should be noted that standardized values needed for operation of each model have not been adjusted before the simulation so that presented results correspond to operation with unknown batteries, which type and current state is not known.

Summarizing, the developed HOCVM approach shows a superior performance and provides +/- 3% SoC and +/-7 % SoC accuracy of U_{00} estimation regarding operation at high and low temperatures respectively.

5.7 Summary

Estimation of fully equilibrated U_{00} is a challenging task in field relevant conditions characterized by limited duration of rest periods. Results of the experimental study presented in this work are in full agreement with this statement. They indicate that applying any purely mathematical approach will lead to substantial SoC estimation error, especially in case of operation at low temperatures. Furthermore, other crucial factors that have to be considered for the final calculation of the expected SoC estimation error have been also found and discussed, such as:

- wide manufacturing tolerances
- limited accuracy of voltage drop estimation caused by quiescent current
- altering relationship between SoC and U_{00} imposed by ageing

Deep understanding of relaxation behaviour that resulted from the carried out analysis allowed the creation of phenomenological double-layer gel-crystal one particle model of positive electrode, which complements the already known single layer gel-crystal theory and fully explains observed phenomena. It provided a good basis for the development of a novel hybrid U_{00} estimation algorithm, which allowed addressing the most substantial influence factors, namely temperature, charge short-term history represented by cumulated amount of charged amp-hours, SoC and quiescent current rate. It also proves that extrapolation of the obtained parameterization is correct and can be modelled in the presented way. Developed phenomenological model allowed identification of operation modes and other conditions when a reasonable adaptation could be executed. It points out that resulting know-how is not only applicable to battery behaviour in rest periods but also far beyond them. This study led to discovering significant impact of unfinished relaxation on the following discharging (vital for SoF estimation and cranking capability prediction in case of immediate cranking preceded by charging).

Developed novel hybrid approach allows the best utilization of the advantages of the two created U_{00} estimation algorithms. Suggested implementation offers a possibility to adapt one with the output of the other one, whereby it would not be possible if a single-approach solution was chosen. It is also relatively robust against measurement and modelling noise, insensitive to variation of the input parameters and universal for different battery types and sizes. All extracted relations have been implemented using scaling concept, which does not require

repetition of all conducted measurements for each battery type. The only necessary calibration test used for extraction of the standardized parameter values takes only two weeks and is carried out at easily obtainable temperature of 25 °C. The architecture of developed method has been designed in a way that allows direct implementation in battery state detection algorithms being a part of electronic battery sensor. It does not require greater amount of storage space and consists of easily implementable exponential and linear functions. Achieved excellent performance is superior in comparison to the known state-of-the-art algorithms [125][126][127][128]. SoC estimation accuracy using estimated U_{00} does not exceed ± 5% SoC (average expected error value was even below ± 3% SoC) regardless of the current operating conditions. This value is valid if parametrization results are available. Otherwise, error of ± 3% SoC and ± 7% SoC applies for temperatures below and above 10 °C respectively. All mentioned values of error correspond exclusively to U_{00} estimation. It has to be emphasized that specifying of the final SoC estimation error requires also considering of accuracy of the mentioned integral factors, which have not been taken into account in this study.

6 Online internal failure detection

EMS and BSD are essential for the optimization of the battery life time, maximization of the fuel savings and reduction of the CO_2 emissions provided by the additional micro-hybrid functionality. Furthermore, in the near future this functionality will be extended by new solutions aiming to further reduce the adverse environmental impact. Of what one of them is the enhancement of ASSF with the coasting (also called stop-in-motion) function. It switches off the combustion engine not only during standstill phases but also during driving when a deceleration is detected.

Frequently used "coasting mode" has a high potential to significantly improve the fuel economy of future µH vehicles. However, it requires additional consideration of safety related aspects which are connected to possible battery failure not only during standstill phase but also while driving. Development of battery internal failure detection (IFD) algorithm is an absolutely essential feature for this application and for energy management in general. Its main goal is to detect internal failure in form of macro or micro short-circuits using the measured physical values and internal parameters calculated by the BMS. Detecting battery failure accurately prohibits switching off the engine and thus risking power-down of the entire power net with its safety-critical loads. Even though the future generations of µH vehicles with coasting functionality will be probably equipped with two battery storage systems to provide necessary redundancy, still unexpected failure of one of them may lead to unwanted states in the power net.

This chapter provides an insight into the possible internal failure mechanisms for both AGM and EFB batteries. It describes a carried out systematic and reproducible investigation based on practical tests which allows understanding the behaviour of a PbA under conditions typical for µH vehicles with existing internal failure. Mentioned study also provided enough information for development and validation of an IFD algorithm able to detect internal short-circuits and unwanted imbalance between cells caused by sudden capacity losses at an early stage of their existence. This can significantly improve the safety and reliability of the power net for both present and future generations of µH vehicles.

6.1 Internal failure mechanisms

Failure detection of PbA operated in the field is a challenging task, whereby a clear differentiation between failure and ageing is necessary. For a good failure detection algorithm an aged battery is still a healthy battery. There is no reference value of a considered parameter because it will definitely change due to ageing and taking its absolute value for a new battery will not be reasonable anymore. Internal failure is a process, which causes unexpected loss of the batteries performance in both slow and fast pace. It cannot be derived directly from SoH of

the battery because internal failures may emerge for new and for aged batteries as well. However, the more aged the battery is the higher the probability of internal failure occurrence will be. An example of such clear difference between these two phenomena can be described in the following manner. A few percent of capacity loss normalized to the C_N after a couple of months of operation have to be considered as normal, whilst the increase of normalized ohmic internal resistance of 20% after one week of a rest period is already an indication of the internal failure. For the sake of simplicity in this work the significant battery performance loss leading to failed cranking within the time considerably longer than 1 month is considered as ageing, whilst every other effect that causes faster deterioration will be classified as internal failure.

Mechanisms that can cause unexpected internal failure of the SLI battery are strongly connected to the ageing phenomena described in chapter 3.1.2. However, they cause much faster degradation of the battery, have more random nature and end up with either internal short-circuits that cause significantly increased self-discharge rate or open-circuit conditions. A possibility exists to calculate on-line the probability of occurrence of internal failure, which will definitely grow with ageing. However, such a probability factor is not sufficient for a proper detection because of randomness of such effects that cannot be neglected. This chapter explains the possible mechanisms of internal failures and the conditions which can favor their emergence. They cause failures in form of micro and macro short-circuits as well as sudden contact and capacity loss.

6.1.1 Corrosion

Corrosion causes a consumption of the positive grid as well as positive top lead (all lead components located in the top part of each cell which are in a direct contact to the positive plates including their lugs and straps), which leads to increase of R_{ohmic} and possible contact loss between positive active material and the grid. This causes capacity loss and expansion of the positive electrode. Additionally, it may also cause peeling off of the top lead (COS, terminals and lead connection between them), as demonstrated in Fig. 103.

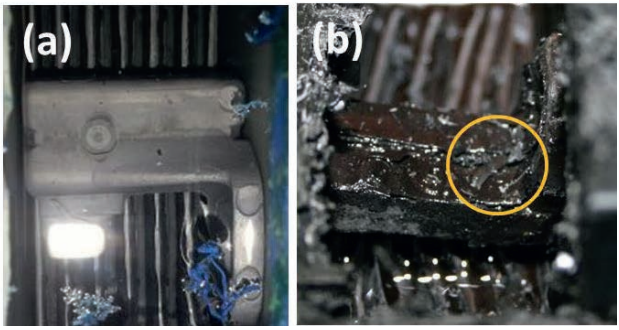

Fig. 103. Peeling off (highlighted) of the top lead caused by the corrosion in a commercial SLI flooded lead-acid battery, (a) brand new battery, (b) aged but still fully functional battery.

If the small pieces of the peeled off material fall down on the electrodes they may create a metallic connection between differently polarized plates and in the end, cause an internal short-circuit. The mentioned expansion of the positive plates causes their growth mainly towards the top of the cell. This exerts an additional force on separator and COS. An example of bending of the latter has been depicted in Fig. 104. If the force is considerably high the COS may get fractured, which will cause a sudden capacity loss (SCL) because at least one plate will get disconnected from the stack.

Fig. 104. Bending (highlighted) of the positive COS due to excessive corrosion (grid growth) in a commercial flooded SLI battery.

Expansion of PAM also brings a risk of short-circuit between positive and negative COS. This case has been illustrated in Fig. 105. It is clearly visible that the positive plates grow and expand within each cell, which can end up with establishing an electric contact between two COS of the different polarity via one or multiple positive plates.

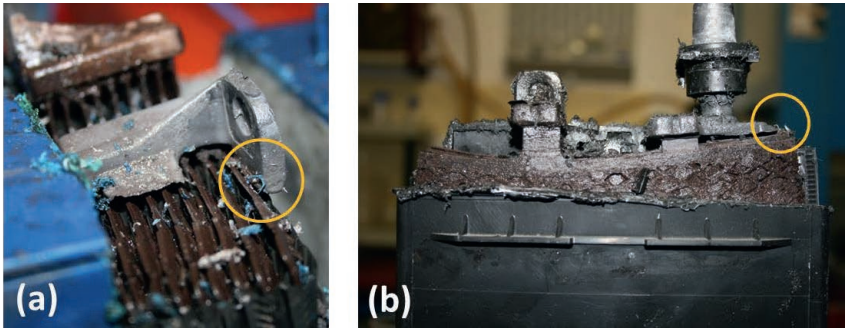

Fig. 105. Short-circuit between the positive and negative COS (highlighted) caused by extensive corrosion of the positive electrode in a commercial SLI flooded batteries: (a) failure after laboratory testing, (b) failure occurred in the field.

The rate of grid corrosion increases exponentially with the increase of average battery voltage and temperature, which means the presented failure mechanisms are more likely to occur when

the battery is operated at elevated temperatures. It is not only related to the country where the automobile is being driven but also to the positioning of the battery within the vehicle, e.g. the battery which is located in engine compartment very close to heat generating appliance will suffer from much higher degradation due to corrosion than the one located in the trunk. Additionally, too frequent and not optimized refresh charging of the battery, which is being implemented in EMS of modern μH vehicles [37], will also accelerate its rate.

Worth mentioning is also corrosion of the negative COS that emerges only in AGM batteries that are constantly overcharged. It is caused by loss of cathodic protection during charging of negative top lead, which is in contact with the electrolyte through a thin acid film. It has been deeply studied by Vaccaro et al. in [129]. Corroded negative COS may lead to SCL through loss of contact between single electrodes or whole stack of plates. This effect is only relevant to PbA operated in electric and plug-in hybrid vehicles where 12 V battery experiences long overcharging phases that are connected to charging the vehicle from the grid.

6.1.2 Dendrite growth (metallization of separator)

Dendrites are "club-shaped" needles of lead that are characterized by the diameter of less than 10μm. Their growth in PbA mainly occurs if the battery was deeply discharged and stored in such state for a considerable time. Furthermore, elevated temperatures accelerate this process due to the very low acid density of the battery at low SoC (below 1.10 $kg \cdot l^{-1}$), which promotes the recrystallization processes, as explained in detail by Yamaguchi et al. in [130]. In this study it was found that new lead sulfate crystals are formed on the old ones with preservation of the volume but with a significantly reduced surface as presented in Fig. 106.

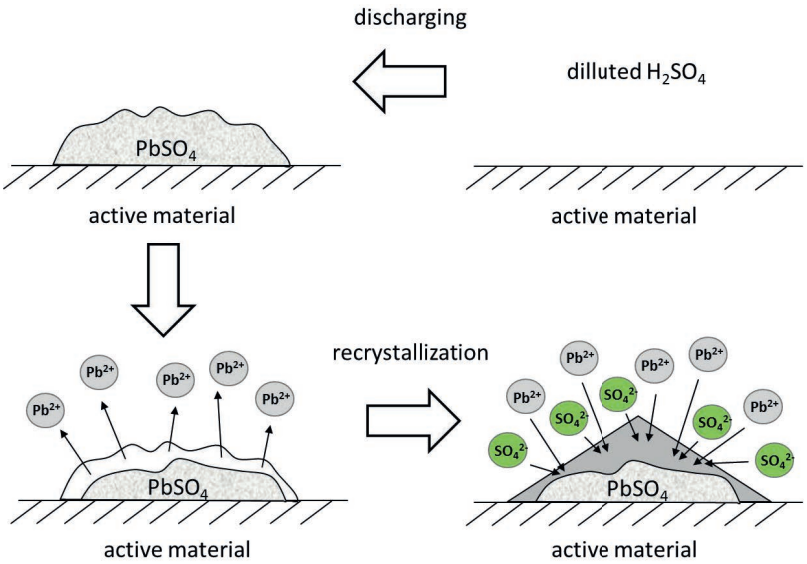

Fig. 106. Recrystallization caused by dissolution and re-precipitation of lead sulfate.

This effect may lead to bridging of the NAM and PAM and forming an internal short-circuit if the lead sulfate crystals are converted back into lead again during charging. It is because $PbSO_4$ is characterized by high specific resistivity, which makes it an electrical insulator and does not lead to a noticeable current flow in the very first moment after connection between two electrodes was established. In standard flooded and EFB batteries separator metallization is less likely because the dendrites are very thin so that any mechanical stress, caused for example by vibration while driving, will make them break apart. However, in case of AGM batteries the AGM separator provides a mechanically stable medium that let the dendrites grow in undisturbed manner. This could be avoided by employing an AGM separator with many very thin glass fibres and reduced pore size [22]. However, starter batteries are a low-cost product, i.e. such separators are not used due to their significantly higher cost. Results of the post-mortem-analysis on a AGM battery clearly show the presence of dendrites in the AGM separator as illustrated in Fig. 107.

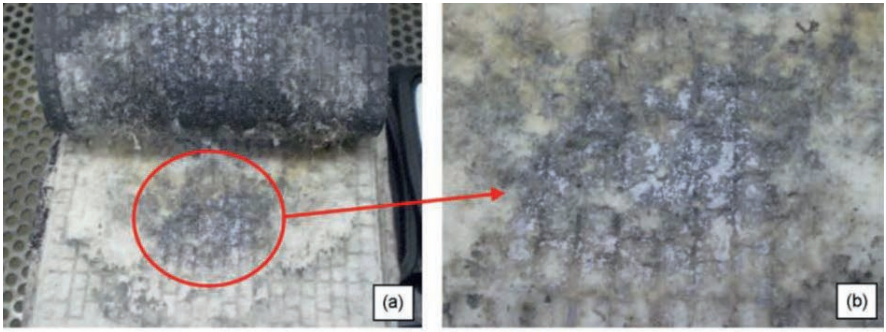

Fig. 107. Tear-down analysis results of the SLI AGM battery that has been overdischarged a multiple times presented by Schaeck et al. in [26]. Lead dendrites (highlighted) are clearly visible and mostly present in the middle of the plate (a and b) where acid density tends to be the lowest.

Dendrites do not have to be necessarily associated with the aged batteries from the field. They can be also present in the brand new battery, which were either stored without recharging for a relatively long time or improperly manufactured. The latter one can be a result of too long soaking time than recommended at higher temperature [122] and carrying out of the formation process at significantly lower acid density than the nominal one [18]. A detailed study of these effects has already been published for batteries operating in electric bike (scooter) applications [131], where the authors reported that the dendrite growth is responsible for about 20-30% of the battery failures in the warranty period.

6.1.3 Oxidation or mechanical damage to the separator

The main functions of the separator in lead-acid batteries are:

- Electrical and mechanical insulation of the NAM and PAM from each other, whilst providing excellent ion conductivity and acid diffusion through the pores. This requires high oxidation resistance and high chemical stability in the strongly acidic environment.

- Separator should block the passage of metal particles from the positive (e.g. Sb^{2+} or Cu^{+}) to the negative electrode, which cause increased water loss.

- Resistance to mechanical vibration is also required, especially at higher temperatures.

- Holding PAM to same degree to prevent shedding and falling of the active material.

Additionally, the separator should be also as thin as possible in order to reduce the R_{ohmic} of the battery. Currently used PE pocket separators (flooded and EFB batteries) fully meet these requirements. However, PE separators are also experiencing ageing during operation and their oxidation resistance and mechanical strength are being significantly deteriorated, which is mainly accelerated by the operation at elevated temperatures.

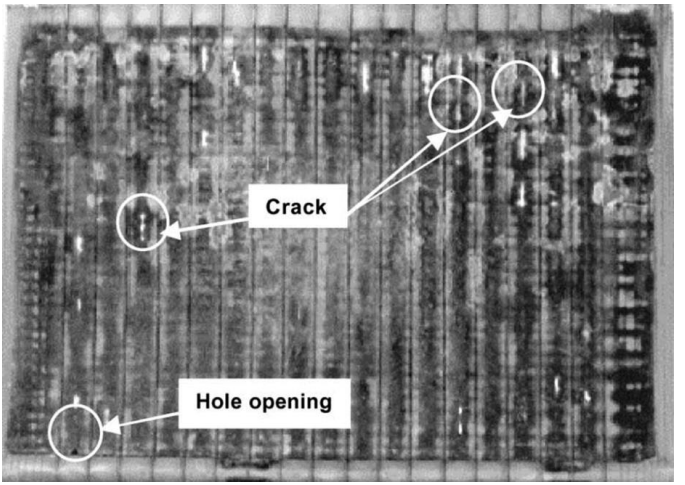

Fig. 108. Deteriorated PE socket separator withdrawn from the commercial SLI battery presented by Wada et al. in [132].

Fig. 108 illustrates a deteriorated PE separator. Since PE is an organic material it decomposes in the strongly oxidative atmosphere and forms water and carbon dioxide. The results of this process are cracks and holes that may appear on its surface. Consequently, the whole area of the electrodes is no longer protected and internal short-circuits are likely to take place. Furthermore, expanded and punched grids have sharp edges, which in case of mechanical stress

caused by vibration or positive grid expansion can also lead to cracking of the separator. This effect is even more likely in the aged batteries due to the shrinking of the separator (often called a "t-shirt effect"), which has been kept considerably long in low density sulfuric acid (especially at elevated temperatures). It occurs when battery is deeply discharged or when a significant acid stratification is present. The latter one leads to much lower acid density in the top of the battery that results in separator shrinking. Moreover, a considerable risk of separator breaking in its very bottom is also possible due to mechanical stress caused by its bending during manufacturing. This can lead to a significant weakening of the PE material in this area.

6.1.4 Short-circuits through disintegrated active material

Throughout the life-time the battery active material can get disintegrated from both electrodes. This exhausted material falls down to the bottom of the cell or stay attached to the electrode in a very soft form and does not take part in the main reaction anymore. The reason for this process on the positive side is mainly the mechanical stress caused by volume change of the active material during charging and discharging as already described in chapter 3.1.2.2. It can be assumed that there is very little lead sulfate in the disintegrated PAM accumulated in the bottom of the cell [104], which makes the sludge a good conductive material. In case of the NAM the mentioned "breathing effect" usually does not cause any disintegration but it is possible that the adhesion of active material to the grid is relatively poor due to many savings in the manufacturing process. This case has been illustrated in Fig. 109.

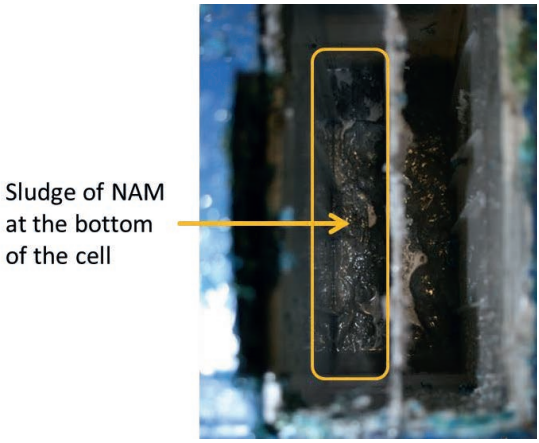

Fig. 109. Disintegrated negative active material (highlighted) accumulated on the bottom of two cells of an aftermarket flooded battery.

Concerning possible internal failures, the accumulated active mass on the bottom of the cell may short-circuit the two electrodes through a hole in the separator. Such a hole can be seen in the Fig. 108.

6.1.5 Loss of contact between cells

In the starter battery, the contact between cells can get lost due to cracks and corrosion of the weld that connects two COS [133]. In case when the contact gets lost or becomes very weak the R_{ohmic} increases dramatically so that the vehicle cannot be started anymore. However, this effect is very random and it is challenging to predict its occurrence in advance. In comparison to the internal short-circuits such failures are rather rare but they cannot be entirely neglected. Fig. 15 presents a negative COS of a commercial field-aged flooded SLI battery where the connection between two cells went missing. In this case, it was possible to pull up the COS without exerting any force. The possible explanation is weld cracking due to formation of a corrosion layer, which mainly consists of lead sulfate and causes a build-up of cracks and their gradual growth with time until the final disconnection. A cross-section of a tombstone, which shows the possible position of cracks, has also been shown in Fig. 15.

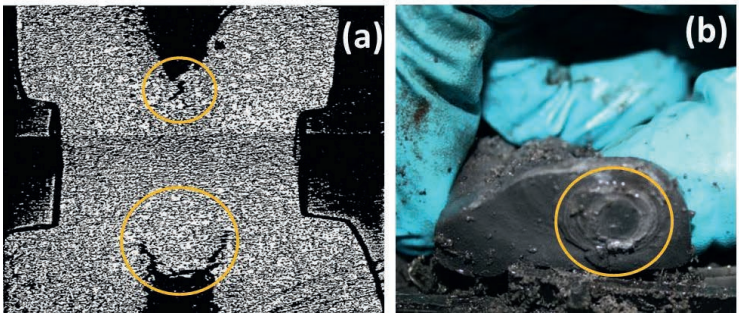

Fig. 110. Negative COS of the commercial flooded SLI lead-acid battery that got disconnected from the neighbouring cell (highlighted), (a) cross-section of a tombstone with cracks in weld according to [133], (b) disconnected COS observed in the post-mortem-analysis.

6.2 Theoretical estimation of short-circuit resistance

In the previous chapters the nature and mechanisms that may cause an internal failure have been described in detail. However, a few additional questions considering internal short-circuits may arise:

- Is the value of the short-circuit resistance constant from the time point of its occurrence up to the final breakdown or does it change?

- What is the expected value range of the short-circuit resistance? Is it high ohmic or low ohmic? If the range is relatively high, which mechanisms cause so called micro short-circuits and which are responsible for so called macro short-circuits?

- Is the behaviour of various SLI lead-acid battery technologies (standard flooded, EFB or AGM) after the occurrence of an internal short-circuit similar?

- What is the probability that in future starter lead-acid batteries the issue of internal short-circuits gets even more pronounced?

In order to answer these questions the specific electric resistivity of all components, which may be a part of the additional current conducting path creating short-circuit, has to be known. They have been reported in Table IX. For the sake of simplicity, it has been assumed that the grids are made of pure lead. In fact, the majority of lead-acid batteries used in automotive applications consists of plates manufactured from lead-calcium based alloys [34]. However, the dosage of all additives is relatively low, which allows making such assumption without inflicting a considerable error.

If the current path only consisted of active material (lead and lead dioxide) the value of the short-circuit resistance (R_{SC}) would be very low and the battery or one particular cell will get fully discharged within a couple of minutes.

Material	**Specific electric resistivity at 20 °C (ρ) [Ωm]**
Pb	$2.1 \cdot 10^{-7}$ [88]
α-PbO_2	10^{-5} [88]
β-PbO_2	$4 \cdot 10^{-5}$ [88]
$PbSO_4$	$3 \cdot 10^{11}$ [134]
PbO	10^{12} [88]

Table IX. Specific resistivity of components taking part in the electrochemical reactions in lead-acid battery chemistry.

However, in case of existence of a very thin layer of lead oxide or lead sulfate, the overall value of R_{SC} may be very high, so that the battery will lose performance very gradually. Furthermore, not only the specific resistance of the current conducting path has to be taken into account. Other parameters such as the force that is exerted on the contact that forms short-circuit and its surface are also necessary for good estimation of the R_{SC}.

$$\boldsymbol{R}_{\mathrm{SC}} = \boldsymbol{R}_{\mathrm{path}} + \boldsymbol{R}_{\mathrm{constriction}} + \boldsymbol{R}_{\mathrm{film}} \tag{40}$$

(40) shows all relevant components for the calculation of R_{SC}, where R_{path} means a resistance of the conducting path, $R_{constriction}$ is a contact resistance that depends on the force and surface of contact. The stronger the two bodies, which form the contact, touch themselves and the bigger the surface area where they meet is, the lower the value of $R_{constriction}$ will be. R_{film} is a resistance of the pollution film that can appear on the surface of the contact.

$$\boldsymbol{R}_{\mathrm{path}} \text{ and } \boldsymbol{R}_{\mathrm{film}} = \frac{\boldsymbol{\rho l}}{\boldsymbol{s}} \tag{41}$$

$$\boldsymbol{R}_{\text{constriction}} = \frac{\boldsymbol{\rho}}{\mathbf{2}}\sqrt{\frac{\boldsymbol{\pi H}}{\boldsymbol{F}_{\text{N}}}} \tag{42}$$

R_{path} and R_{film} can be calculated using well-known relations from the fundamentals of electrical engineering presented in (41), where l means length and thickness of the conducting path and pollution layer respectively, ρ is an electrical resistivity and s is their surface. Read et al. in [135] derived a formula depicted in (42), which allows calculation of $R_{constriction}$ using just an applied force (F_N), hardness of the material (H) and ρ. $R_{constriction}$ concerning different forces is demonstrated in Table X.

Force (F_N) [N]	**$R_{constriction}$ [mΩ]**	**comments**
0.2	2.632	just touching
7	0.449	noticeable force
200	0.0832	substantial force

Table X. Values of $R_{constriction}$ calculated using (42) and assuming the hardness of lead as 40MPa [35] and its specific resistivity (ρ_{Pb}) according to Table IX.

For the calculation of further R_{SC} components an example of the internal short-circuit caused by the expansion of the positive grid and forming short-circuit through a contact with the negative COS (Fig. 105) was adapted. The necessary geometry was taken from a 74 Ah standard flooded battery that failed due to the described effect. Visualization of the all considered resistances can be found in Fig. 111.

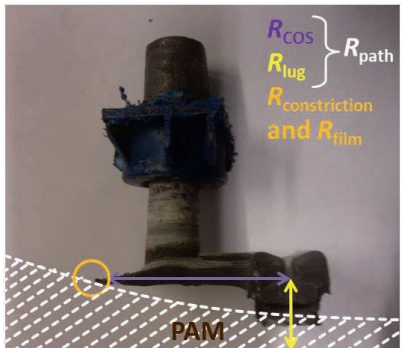

Fig. 111. Visualization of the R_{SC} components in case of internal short-circuit formed by the excessively expanded positive plate and the negative COS.

Estimated values of R_{COS}, R_{lug} and R_{path} equal 0.0472, 0.212 and 0.259 mΩ respectively. It can be clearly seen that the estimated value of all mentioned resistances is negligibly low in

comparison to $R_{constriction}$ calculated using a contact force that corresponds to very gentle touching of the contacts. The last component of R_{SC}, which is necessary for an accurate estimation of the short-circuit strength, is R_{film}. In order to calculate the value of the R_{film} the type of material which can deposit on the surface of both positive grid and negative COS has to be known.

In case of the negative COS it can be assumed that there is just pure lead on the contact due to cathodic protection of the negative electrode resulting from its negative potential. However, on the positive electrode there are corrosion products that are always present and cannot be neglected as already described in 3.1.2.1.

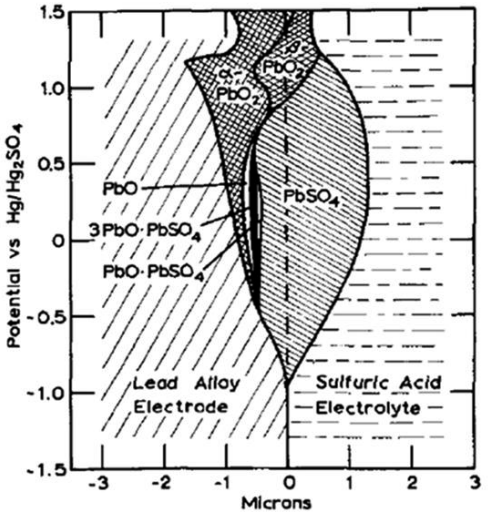

Fig. 112. Schematic diagram of the composition of the corrosion film as a function of potential according Ruetschi et al. [32]. Microns are micrometers.

According to the work of Ruetschi et al. [32] a corrosion layer may consist of many different materials. Their occurrence strongly depends on the potential of the positive plates during operation, which has been presented in Fig. 112. Usually, the potential of the positive electrode during charging applying constant-voltage and 25 °C is not higher than 1.27 V vs. Hg/Hg_2SO_4 reference electrode, whilst at the end of capacity test at the same conditions with twenty-hour current rate is not lower than 0.87 V. It means that if the battery is constantly overcharged and hardly ever experiences any discharging as it is the case of UPS (uninterruptable power supply), the corrosion film will consists of only well conductive PbO_2. However, in the case of the automotive applications, especially µH vehicles the battery is being operated at lower SoCs, usually in the range of 75-85% [102], although it is also possible that it gets even more discharged (heavy traffic or during relatively long parking period). Furthermore, in case of EFB and flooded batteries additional cycling triggers evolution of the acid stratification that causes inhomogeneous acid distribution within the cell. Heavy and more dense acid falls down and

light less concentrated acid stays on top of the cell [44]. Due to this effect the potential of PAM is even lower in this area and the probability of formation of lead sulfate crystals in the corrosion layer is significantly increased. Presented consideration makes it clear that lead sulfate has to be expected as part of the film on the contact surface. Other materials such as lead oxide are less likely. Assuming that the thickness of the corrosion film equals 0.1 mm and its surface is 1 mm^2. It is homogeneous and consists of 0.1 µm of the lead sulfate and 99.9 µm of β-PbO_2 just below it. Resulting value of R_{film} would equal approx. 30 GΩ. Thus, it becomes evident that the presence of even a very thin layer of lead sulfate will drastically increase the value of R_{SC}.

It can be concluded that R_{film} is decisive in the proper estimation of the overall short-circuit strength. However, the exact contact surface is unknown, which makes an accurate R_{SC} estimation a challenging task. Fig. 113 depicts a schematic illustration of the expected contact surface. Because the exact distribution of the contacts and involved materials is not known the value of R_{SC} can be in the range of several mΩ up to TΩ.

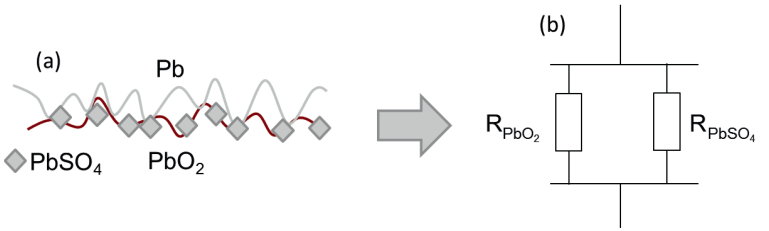

Fig. 113. Schematic illustration of the expected contact surface forming short-circuits between positive electrode and negative COS: (a) schematic visualization of the expected contact surface, (b) equivalent electrical circuit of R_{film}.

The probability of high values of R_{SC} is much higher than low values. It is because of the relatively low contact force that is expected at the very beginning of the operation in a short-circuited state. Additionally, as explained before the presence of lead sulfate on the contact surface is also most likely. Nevertheless, a very high R_{SC} may decrease within a given time to a more considerable level due to further expansion of PAM, which results in higher contact force. Furthermore, if the lead-sulfate layer is very thin it can also get penetrated. In case of dendrites the contact surface can be various as well. As explained in [136], appearance of a thin but dense lead-sulfate layer is highly probable in the HRPSoC operation regime typical for µH vehicles. Concerning dislodged material that accumulates in the bottom of the cell the conducting path will be rather low ohmic. This is due to the fact that the sludge comprises very little lead-sulfate particles. However, the absolute hardness of the PbO_2 is approx. factor 60 [137] higher than that of pure lead, which significantly increases $R_{constriction}$. Furthermore, mostly due to acid stratification a heavy sulfation is being found in the bottom of the plates [39], which also increases the probability of rather high ohmic R_{SC} after establishing an internal short-circuit.

6.2.1 Short-circuit resistance obtained from post-mortem analysis

In order to experimentally determine the value of R_{SC} and compare it with the theory explained in the previous chapter a 74 Ah standard flooded SLI battery that experienced an internal short-circuit was subjected to a tear-down analysis (TDA). Identification of short-circuited cells was relatively straightforward because their electrolyte density was very close to that of distilled water, namely 1 $kg \cdot l^{-1}$, which means that they were completely discharged.

Fig. 114 shows two cells which experienced an internal short-circuit caused by excessive expansion of the positive plate, which reached the negative COS (Fig. 116). Significantly progressed ageing in the form of low electrolyte level is also visible in the picture. It can be noticed by the low electrolyte level and is highlighted by bending of the positive lugs resulting from considerable grid expansion. This can also be observed during optical examination of the withdrawn plates as presented in Fig. 115.

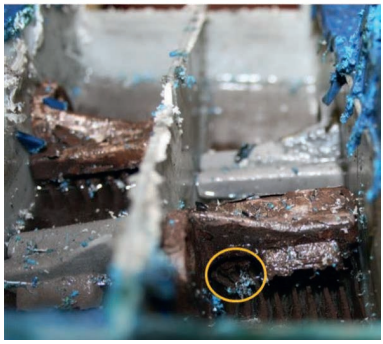

Fig. 114. Two short-circuited cells of the failed 74 Ah standard flooded SLI battery.

Fig. 115. Considerably corroded positive plate withdrawn from the short-circuited cell of a failed 74 Ah standard flooded SLI battery.

Fig. 116 illustrates the exact place, where short-circuit occurred. The positive plates not only established a contact with the negative COS but also a noticeable bending contact force was present. Both failed cells of the investigated battery were short-circuited in the same way.

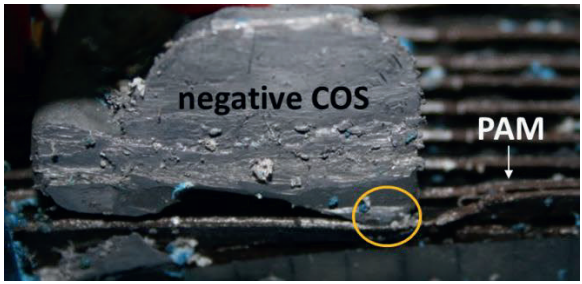

Fig. 116. Position of short-circuit occurrence in one of two failed cells in 74 Ah standard flooded SLI battery.

Short-circuit occurred within the third and fourth cell counting from the negative pole. R_{SC} was measured using Keithley 2000 laboratory multimeter and 4 point resistance measurement technique. Its value was in the range of 6-7 mΩ and 2-3 Ω respectively, which correspond to discharging with 300-350 A and 0.7-1.05 A respectively. This indicates a relatively fast decay of performance (see Table XI). It should be noted that the TDA was carried out after nearly two months of resting time after the failure occurred, which means that the further expansion of PAM took place and the measured value of R_{SC} is expected to be lower than directly after the failure occurred.

measurement	R_{SC} **[Ω]**	I_{SC} **[A]**	$t_{full\ discharge}$ **[h]**
3rd cell	$6\text{-}7\cdot10^{-3}$	300 - 350	0.247 - 0.211
4th cell	2 - 3	0.7 - 1.05	106 – 70.5
manual R_{SC} meas. - just touching	$40\cdot10^{3}$	$52.5\cdot10^{-6}$	$1.41\cdot10^{6}$
manual R_{SC} meas. - noticeable force	$20\cdot10^{3}$	$105\cdot10^{-6}$	$0.705\cdot10^{6}$
manual R_{SC} meas. - substantial force	400	$5.3\cdot10^{-3}$	$14\cdot10^{3}$

Table XI. Resulting R_{SC} values from post-mortem-analysis of failed 74 Ah standard flooded SLI battery, $t_{full\ discharge}$ refers to full discharge time employing I_{SC} and has been calculated using C_N without concerning current dependency of the available capacity.

Table XI provides an overview of measured R_{SC} values. It must be noted that $t_{full\ discharge}$ is a first order approximation which does not consider current dependency of the available capacity. However, this is sufficient for a general comparison between different short-circuits. In order to estimate its value more accurately the Peukert relation has to be taken into account. Its detailed explanation and implementation details can be found in [14]. It can be concluded that

the measured values match with the reasoning presented in previous chapter very well. They also represent a very wide range of R_{SC} values, which may occur in the field.

6.3 Influence of internal short-circuits on battery behaviour during operation

The identification of the failure mode for a given application has already been a topic of many publications e.g. [39][119][136][138]. However, the focus was laid more on finding and analysis of the decisive ageing mechanism (see chapter 3.1.2) rather than on battery behaviour after an internal failure emerged. Knowing and understanding this behaviour is absolutely necessary for the development of internal failure detection. Ruetschi in [33] categorized internal short-circuits as one of the major ageing effects of PbA. However, no information about short-circuited battery behaviour in practical applications was presented in this publication. Schaeck et al. in [26] studied formation of dendrites by means of repetitive overdischarging and showed a charging current behaviour during full charging under laboratory conditions of a healthy and short-circuited battery, but did not present any results relevant to the field conditions. Lack of necessary information in the former literature about the way how battery behaves in the field when a particular internal failure mechanism (see chapter 6.1) occurs is the reason behind the comprehensive experimental study presented in this work.

In order to carry out a systematic and reproducible investigation of the impact of internal short-circuits on battery behaviour during operation two requirements are necessary. On the one hand the tested batteries have to be in the same initial state. On the other hand the short-circuit parameters need to be controlled. However, it is very challenging to obtain such specimens from the field because failed batteries are usually directly exchanged with new ones and returned back for recycling, so that they are not accessible for further investigations. Furthermore, purposeful ageing in the laboratory conditions is also not sufficient enough. It is due to the random nature of the considered mechanisms, which makes it hardly possible to estimate accurately how many given cycles or how much time at constant overcharging at elevated temperatures is necessary to obtain a given internal short-circuit characteristics. Because of this targeted intrusive modification of tested batteries has been chosen as the most feasible option. Its main aim was to provide a possibility to connect one cell out of six to external testing equipment, which simulates an operation with an internal short-circuit by means of constant resistance discharging while the whole battery is subjected to a different load profiles. A schematic illustration of the employed test setup has been depicted in Fig. 117.

For experimental investigation two types of the batteries most relevant for state-of-the-art µH vehicles have been chosen, namely 60 Ah AGM and 60 Ah EFB battery. Before a proper testing started each brand new battery was subjected to a two-week run-in procedure, which aimed to bring them to the so called “field-relevant” state. It is well-known that the brand new PbA have a very high DCA that deteriorates to a relatively low stationary value after approx. four months in the field [25]. Both active materials are not entirely formed and in case of AGM batteries the COC is not fully developed [22].

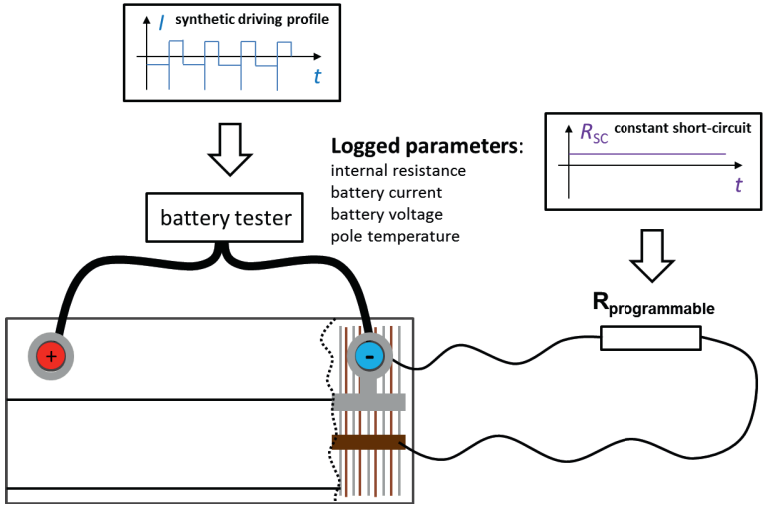

Fig. 117. Test setup used for testing battery behaviour with typical µH load profile while simultaneously discharging one cell with constant resistance emulating an internal short-circuit.

Employed run-in testing routine has been partly developed by ISEA [139] for fast ranking of the SLI batteries focusing mainly on their DCA. As the last step, batteries under test were intrusively modified so that one cell could be independently connected to the testing equipment.

The intrusive connection of the outermost (negative terminal) was done by means of welding five bundles of five thin lead wires with a diameter of 1mm to the positive COS which has been illustrated in Fig. 118. The number of wires has been determined experimentally. The maximal experimentally examined short-circuit current equalled 60 A. Single 100 A, 18 V battery tester manufactured by Digatron Power Electronics GmbH was used for both realization of the µH load profile and simulation of internal short-circuits. The potential at the two negative terminals of used testing channels had to be the same which is related to the lack of galvanic separation between them. This was the reason why the most outermost cell was chosen. To measure a voltage of the contacted cell a smaller bundle of three wires has also been welded to the other end of the positive COS and made available for picking off on the side of battery cover. After electric contacting the opened cell was sealed back again using hot glue and connected to the battery tester.

The main difference between modification procedure of the two chosen technologies laid in the necessity of removal of electrolyte before welding for the EFB batteries. It was carried out using a syringe and a glass where the acid was shortly stored and placed back again in the cell afterwards. Finished test setup has been depicted in Fig. 119.

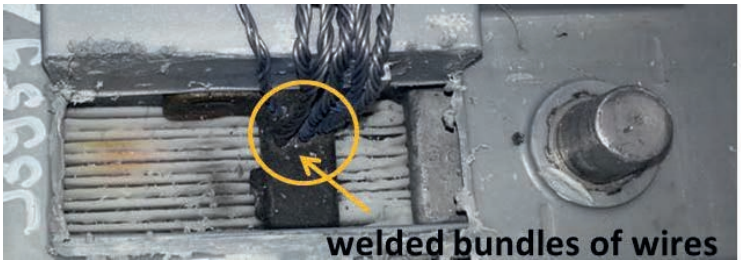

Fig. 118. Intrusive contacting of the narrowest cell of tested battery for simulating of the internal short-circuits (60 Ah AGM battery).

In order to cover a relatively wide range of internal short-circuits a test matrix comprising 8 possible R_{SC} values has been employed for both battery types: the values of R_{SC} are the one which fully discharge a short-circuited cell within: 1, 3, 6, 12 h and 1, 3, 7, 14 days. In further part of this work they will be called *RIcxh* or *RIcxd* (or macro and micro short-circuits) respectively.

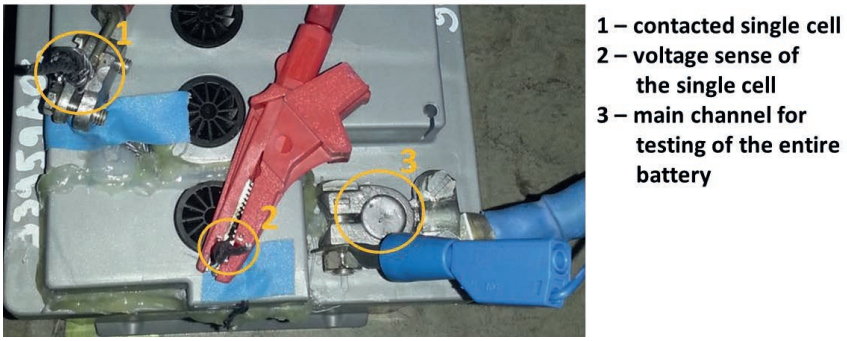

Fig. 119. Finished test setup for testing with emulated internal short-circuits (60 Ah AGM battery).

Their value has been calculated according to simplified relation presented in (43), whereby 2.1 V is an approximate of cell open-circuit voltage at full SoC and multiplication of I_{20} refers to assumed linear relation between discharge current rate and time until C_N is being discharged.

$$\boldsymbol{R_{SC}} = \frac{\boldsymbol{2.1V}}{\text{multiplication of } \boldsymbol{I_{20}}} \tag{43}$$

As an example of such calculation the value of *RIc1h* for 60 Ah battery equals 2.1/60 = 35 mΩ. Table IV provides an overview of all used R_{SC} values. All tests have been carried out in water bath conditioned to 25 °C.

name	R_{SC} **[Ω]**
RIc1h	0.035
RIc3h	0.105
RIc6h	0.210
RIc12h	0.420
RIc1d	0.840
RIc3d	2.52
RIc7d	5.88
RIc14d	11.76

Table XII. Overview of all carried out tests with different R_{SC} values.

To check the behaviour of the battery experiencing an internal short-circuit in field-relevant conditions a simplified load profile has been developed as depicted in Fig. 120. The developed profile is characterized by a relatively high number of cranking events, which in this case had to be realized by significantly reduced discharging current of 100 A. The reason for this limitation was the maximal allowed current rate of the used battery tester. Another important aspect is its strongly positive Ah balance, to investigate if there is any possibility to compensate the lost energy due to increased self-discharge rate that refers to the constant discharging through the short-circuit resistance of a one cell. It should be noticed that the maximal charging voltage equals 14.5 V.

Due to limited DCA of lead-acid batteries the actual measured charging current differed significantly from the values presented in Fig. 120. Different length of rest periods originates from a need to keep the overall time of 24 h for one day of driving. The value of R_{SC} is constant and it neither changes nor is interrupted within the entire test. Before 1 h charging event, which simulates driving through motorway, six ASSF events have been designed. After the charging event, eight ASSF events have been added. Voltage and current of both battery and cell as well as battery internal resistance were logged during each test. The latter one was measured using portable internal resistance measuring device Hioki 3554 [140]. It corresponds to the real part of the complex impedance at 1 kHz and its value can be assumed as the ohmic resistance, R_{ohmic}. Furthermore, the temperature of the negative terminal has also been recorded.

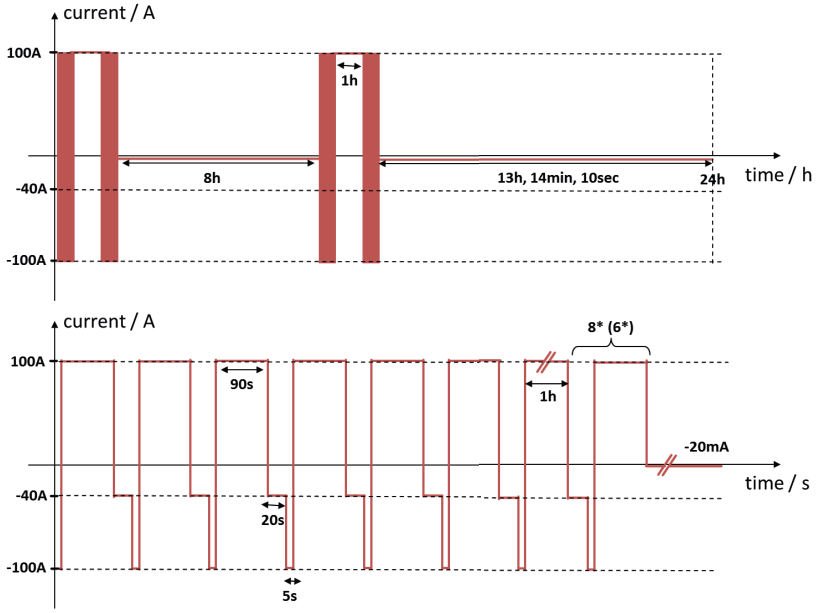

Fig. 120. Current profile of the developed simplified test that simulates conditions typical for µH applications (µHRSC Test): (a) overview of one day driving cycle consisting of two driving phases including motorway trip, (b) zoom into one driving phase.

Ten 60 Ah AGM and EFB batteries were taken to carry out introduced µHRSC test with varying short-circuit resistance. One of them was internally modified without connecting the contacted cell to the battery tester and another one was only subjected to the µHRSC test without any intrusion in its interior. The reason for that was the necessity of checking the impact of invasive modification on the battery behaviour, so that distinguishing between effects originating from imposed internal short-circuits and modification itself could be possible. The latter one cannot be neglected mostly due to the risk of additional oxidation of the negative electrode caused by intake of oxygen, which has been studied in detail by Berndt in [12]. The oxygen intake is likely due to relatively poor sealing characteristics of the applied hot glue method, which makes probability of oxygen leakage relatively high. The order of testing was: firstly, two reference batteries; secondly, four macro short-circuits (*RIcxh*) and lastly, four micro short circuits (*RIcxd*).

Test results of a *RIc1d* and *RI14d* with AGM batteries have been illustrated in Fig. 121. The following conclusion can be drawn. Even though that the Ah balance of the µHRSC test is strongly positive the significantly higher self-discharge rate caused by imposed R_{SC} could not be compensated. At the beginning of the test the battery was conditioned to 80% SoC by discharging with I_{20} followed by 4 h of rest period.

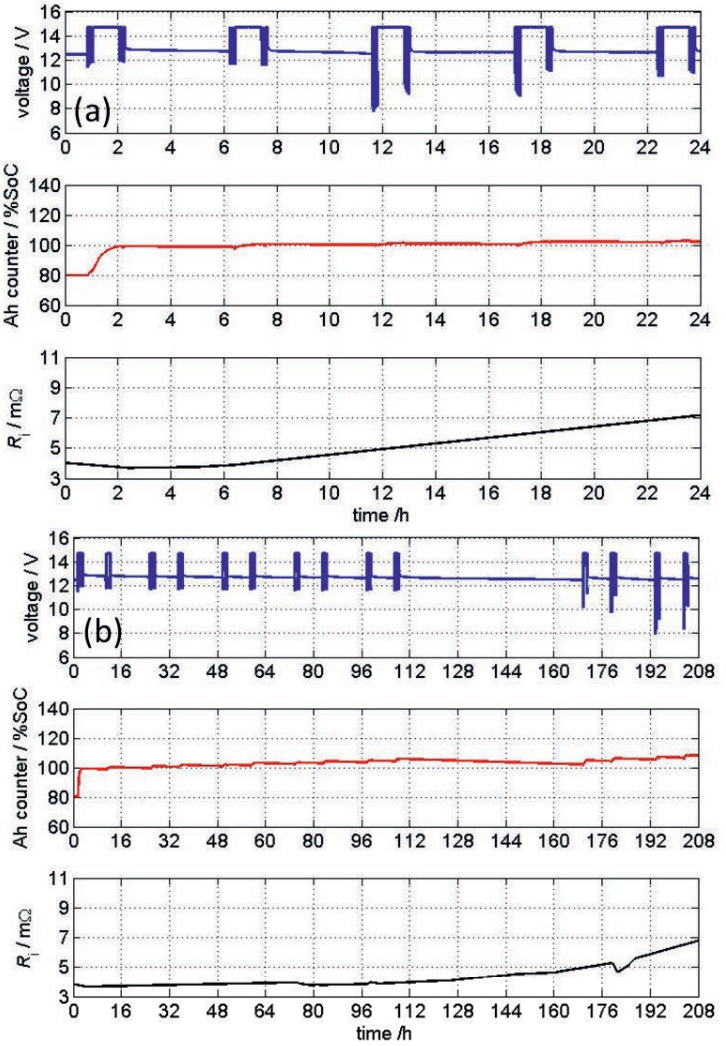

Fig. 121. Test results of the *RIc1d* (a) and *RIc14d* (b) test on the 60 Ah AGM batteries. Even though that the Ah balance of the µHRSC test is strongly positive the significantly higher self-discharge rate caused by imposed R_{SC} could not be compensated. Initial SoC equals 80% in both cases. The test has been carried out at 25 °C.

Shortly after testing with a developed synthetic driving profile started, the battery seemed to reach a fully charged state and according to Ah counting the state is maintained until the end of test. However, the exponential increase of measured R_{ohmic} and overvoltage caused by 100 A quasi-cranking pulses shows a considerable decrease of battery performance, which will

eventually lead to failed cranking in the field. As it was expected the *RIc1d* battery reaches a significantly lower voltage during discharge phases than *RIc14d*. Although two weeks of operation equal to 336 h and taking Peukert factor into account the expected discharging of a one cell should have lasted longer than 400 h, the *RIc14d* battery failed already after 200 h of testing. It can be related to the mentioned oxygen intake that discharged the negative electrode of the tested battery together with the fact that it has been tested as the last one and there was a significant standing time after run-in procedure and beginning of the µHRSC test. The behaviour of all other tested batteries was similar.

Moreover, there is no significant difference between reference and modified reference battery. Their behaviour remained stable and no significant voltage breakdown occurred as it was the case for the batteries with imposed R_{SC}, whereby it should be emphasized that they were tested as the first ones without any considerable rest period in-between. The comparison of Ah balance of the reference and *RIc1d* battery has been illustrated in Fig. 122. SoC calculation has been normalized to C_N of 60 Ah. Due to this the SoC values are exceeding 100% at the end of test, which is physically caused by the presence of side reactions. The Ah balance for the short-circuited battery is slightly higher than for the reference one. It originates from a considerable imbalance, which is imposed by discharging of one cell with R_{SC}. Its voltage level gets lower, which means that the voltage of the other healthy cells can reach higher values and thus causing a flow of higher charging current. It is known that the presence of side reactions in PbA can be used for balancing of such an imbalanced system and long charging at higher charging voltage could eventually lead to at least partial compensation of the energy lost due to the presence of the internal short-circuit. However, in the automotive applications the most of vehicles are predominantly standing and not being driven which is the reason why such compensation is not expected in the present study.

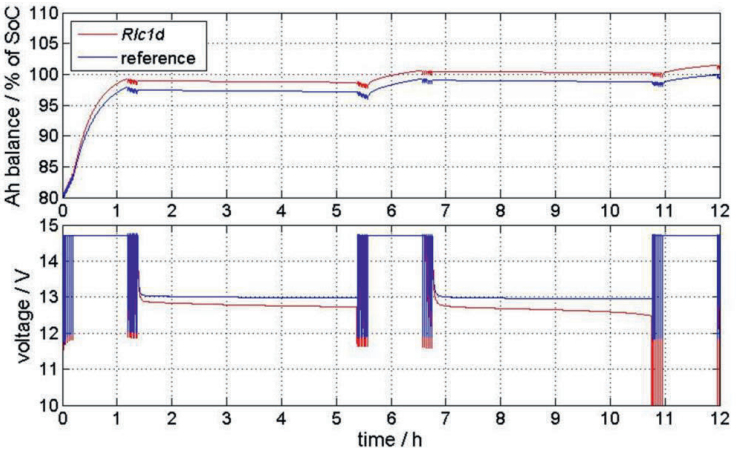

Fig. 122. Comparison between *RIc1d* and reference battery subjected to µHRSC test with the focus on the Ah balance and terminal voltage (60 Ah AGM batteries).

Fig. 123a illustrates the course of minimal voltage measured during quasi cranking phases for each tested battery (see Fig. 120), while Fig 123b focuses on idle-stop phases.

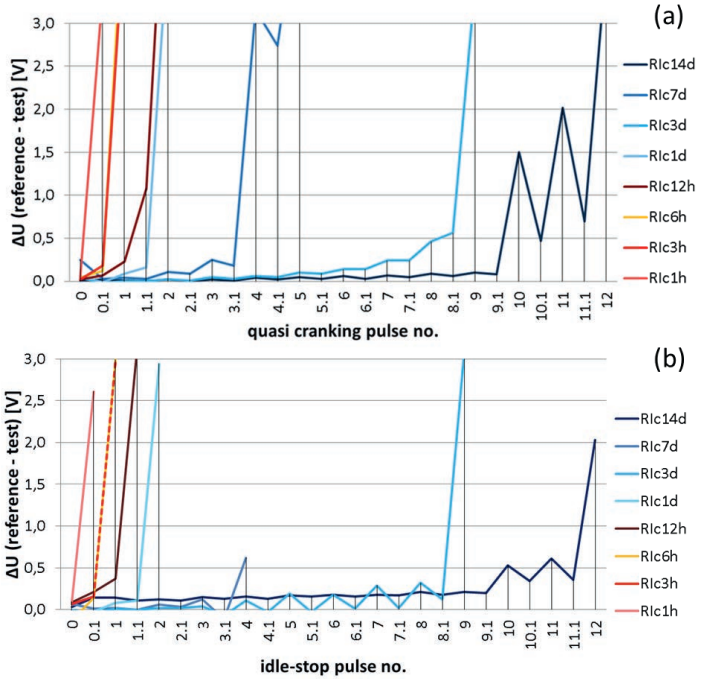

Fig. 123. Minimal voltage measured during quasi cranking phases (a) and after 10 seconds of idle-stop phases (b) for each tested battery according to µHRSC test for 60 Ah AGM batteries. Numbers on x-axis describe the time order of the given driving block. A quasi cranking pulse no. with and without comma indicates the deepest voltage drop of cranking event after and before 1h overcharging phase respectively.

Numbers without comma are related to the cranking event which gave the deepest voltage drop in the given driving block with ASSF functionality before 1 h overcharging phase as demonstrated in Fig. 120, whereby number with comma considers the driving block after 1h overcharging phase. Presented results in all concerned cases show exponential behaviour (deterioration) as mentioned before. The same characteristics were also observed in the ASSF phases during discharging with current rate of 40 A (Fig. 123b). The visible fluctuation, especially in case of macro short-circuits, is related to the fact that 1h overcharging phases were always slightly compensating the SoC decay of the modified cell and therefore decreasing its overall internal resistance.

Fig. 124 shows a measured temperature profile of a reference battery and specimen subjected to the highest considered short-circuit value, namely *RIc1h*. The imposed I_{SC} flowing through battery was in the first stage as high as 60 A, which could lead to noticeable heat generation

due to Joule heating. It can be clearly seen that even in case of highest considered I_{SC} the difference between these two batteries does not exceed 1.5 °C and therefore it can be considered as negligible in automotive applications. Such relatively small temperature deviations cannot be used for internal failure detection. This is due to the following factors: limited accuracy of temperature sensor installed in the EBS, not homogeneously distributed sources of heat in battery's environment (possible temperature differences between cells) and lack of sophisticated and highly accurate thermal model, which should be able to readapt itself constantly in operation. The latter one could be used to compare the steepness of the temperature increase during active charging, which may have a much higher potential as a parameter for internal failure detection. Nevertheless, it is not considered in the presented work.

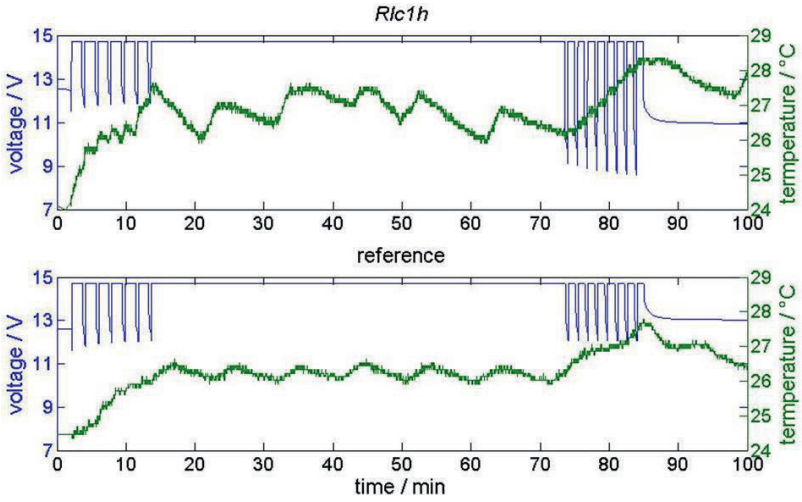

Fig. 124. Battery temperature measured on the negative terminal during µHRSC (*RIc1h*) test conducted using 60 Ah AGM batteries.

The comparison of charging currents obtained during 1 h overcharging phases did not provide any functional relation. It is due to the relatively complex charging behaviour of lead-acid batteries and their limited charge acceptance that has been discussed by several authors [26][35][76]. Because of that the charging current in the pure measured form cannot be simply used as indicator of presence of the internal short-circuits. Another parameter which cannot be used for straightforward detection of failures is the open-circuit voltage or generally voltage during rest periods. It is referred to complex relaxation behaviour of PbA (see chapter 5) and presence of the additional relaxation overvoltage that could remain visible for even hundreds of hours, especially at low temperatures.

The qualitative behaviour of the tested EFB batteries was exactly the same as in case of AGM batteries concerning comparison between healthy reference and batteries with emulated short-circuits. The occurrence of internal short-circuit could not be compensated by charging during

driving phases and the batteries experienced exponential growth of both internal resistance and voltage drop during discharge events. Calculated Ah balance through simple integration of the measured battery current was also positive which directly indicated the presence of internal failure.

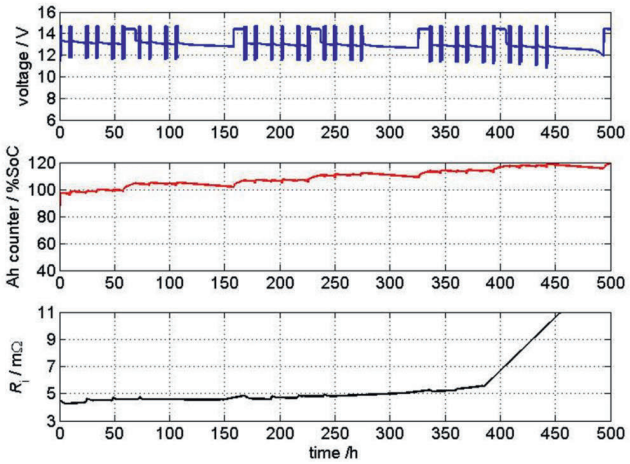

Fig. 125. Test results of the *RIc14d* µHRSC test using 60 Ah EFB battery carried out at 25°C. The initial SoC equals 80%.

Fig. 125 presents test results of performed *RIc14d* test. It can be seen that its duration is significantly longer than using AGM batteries with the equivalent short-circuit (Fig. 121). It is believed that the main reasons for this difference are lack of oxygen intake issue and considerable higher oversizing of tested EFB batteries (actual capacity of 60 Ah EFB was noticeably higher than 60 Ah AGM). Additional cause for such behaviour is the presence of added ten hour long overcharging phases. Main reason behind introduction of these phases is to check if in case of plug-in hybrid electric vehicles (PHEV), which are being often charged in the close environment for a longer time, the charging current can be used to detect battery failure. They lead to a partial compensation of the discharged Ah caused by the imposed R_{SC} that could be also noticed by comparing the Ah counter results during testing of both considered technologies. Usually the flooded batteries are being used in such applications and this is the reason why it has been applied only for testing of the EFB technology. Nevertheless, even with the additional ten hour long overcharging periods the battery eventually experience a breakdown, which got just postponed in time. For the sake of comparison between µHRSC test results of AGM batteries presented in the previous chapter and EFB batteries, observed behaviour of the latter ones in two chosen cases is illustrated in Fig. 126. Their behaviour is the same.

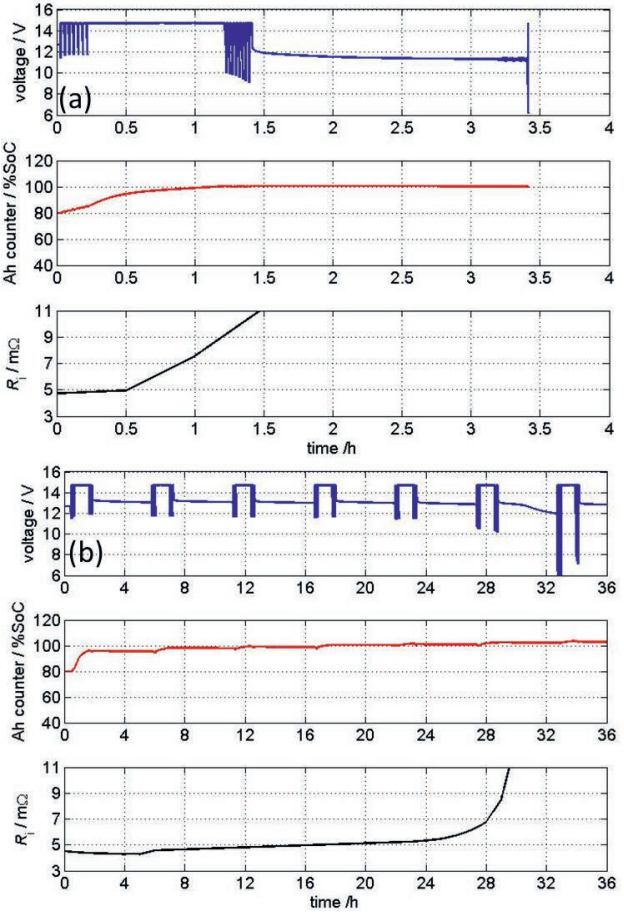

Fig. 126. Test results of the *RIc1h* (a) and *RIc1d* (b) test on the 60 Ah EFB batteries. Initial SoC equals 80% in both cases. The test has been carried out at 25 °C.

Observed overcharging currents measured at the end of each μHRSC test with different macro short-circuits (*RIcxd*) signalized that the lower the R_{SC} is the higher measured overcharging current will be. However, at relatively high values of R_{SC} (e.g. *RIc14d*) the difference between its value and reference taken at the end of charging was relatively low (approx. 20 mA). It indicates that internal failure detection using long overcharging periods should be carried out by using an accurate and self-adapting model that estimates the current, which is flowing into side reactions. It allows a direct comparison and calculation of deviation between the measured and estimated charging current rate that can be directly linked to the presence of internal failure.

From the presented discussion, it can be concluded that observation of the battery voltage during discharging (i.e. cranking phases) and internal resistance can be efficiently used for

detection of internal short-circuits. In case when these two parameters normalized to standard conditions (i.e. 25°C, 100% SoC, CCA) show an exponential growth, whereby the Ah balance of the battery is positive, deterioration of the battery performance can be directly linked to presence of the internal failure mechanisms.

6.4 Impact of sudden capacity loss on the battery behaviour during operation

The term of sudden capacity loss (SCL) in the internal failure detection context refers to a case when a contact between one or multiple plates and the COS is being lost. If it happens the full capacity of affected electrodes is in a very short time no longer available. It can be caused by:

- excessive corrosion of positive lugs (see chapter 3.1.2.1)
- mechanical force exerted by expanded positive electrode (Fig. 104), which may result in a COS fracture.
- corrosion of the negative lugs, which is known as lug thinning and has been deeply studied in [100]

However, only the first and second mechanism is considered as relevant for automotive applications, since lug thinning has only been observed after performing a SBA S0101 test [100], which consists of constant micro cycling without any rest periods. Although the micro cycling itself is present in the field, most vehicles are being driven for only approximately 2 hours per day, which means that majority of automobiles are mainly standing still. It is one of the main reasons why this effect has not been observed in the batteries operated in the field yet. Furthermore, other reasons for that are also possible including much lower discharging current rate of only 300 A during cranking in SBA test and modified grid alloys in the most recent generations of SLI batteries. To conduct a systematic and reproducible study of impact of these events a similar approach has been adapted as it was the case for the investigation of internal short-circuits (chapter 6.3). Firstly, the batteries were subjected to an already presented run-in procedure and secondly tested using µHRSC test profile, whereby a positive COS fracture was manually imposed at the beginning of each test. Fig. 127 shows two cases that have been investigated.

Two AGM and EFB batteries were needed to perform the described tests. It was not necessary to take additional reference batteries because the specification of the used µHRSC test profile remained unchanged and the test data obtained from the internal short-circuit test could also be used in this case. In the following description, the case of disconnecting three plates at once and one plate one after another with two days of testing time in between the subsequent cuts will be called *SCL3* and *SCL123* respectively.

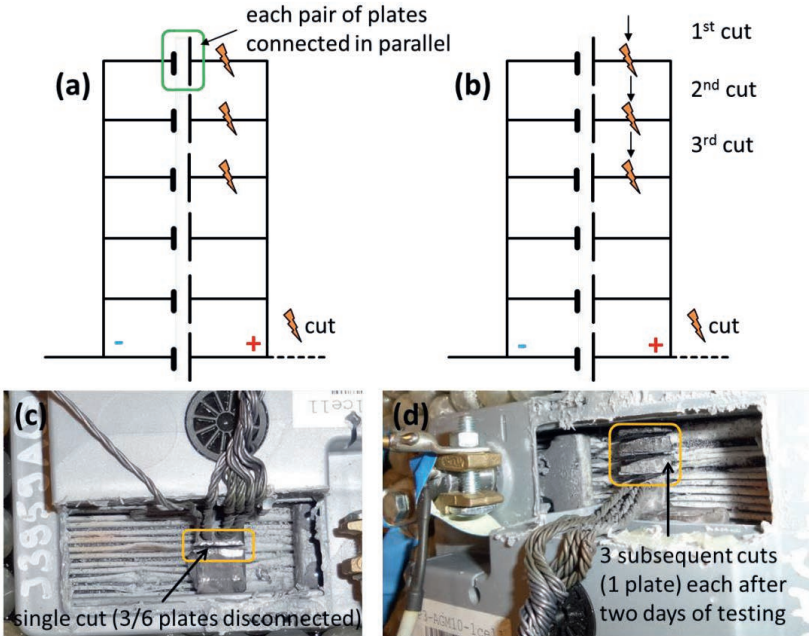

Fig. 127. Two considered failure modes that have been investigated in the SCL study: (a and c) forced manual fracturing of the positive COS where 3 out of 6 plates were disconnected at once, (b and d) detaching 3 single plates one by one each after 2 days of testing.

Fig. 128 presents µHRSC test results with SCL123 for both EFB and AGM battery. Especially in case of the AGM battery the internal resistance slightly increased and also the voltage drop during the quasi cranking phase got lower, namely approx. 500 mV. The EFB battery has not experienced such noticeable performance deterioration. However, the difference between minimal voltage from quasi cranking phase at the beginning and the end was still 270 mV. These values dramatically increased during SCL3 test, especially for AGM battery as illustrated in Fig. 129 and exceeded 3 V.

The presented results indicate that the imbalanced state caused by SCL cannot be compensated in the field as in case of internal short-circuits. Directly after occurrence of the failure, the affected cell is being cycled deeper in comparison to the other cells because its C_N decreased and therefore the discharging current is distributed among smaller number of electrodes (see Fig. 127). This brings them to lower SoC. Additionally, while charging, other cells with higher SoC reach a strong polarization (due to the limited DCA of PbA) much faster than the one with the failure (it stays at the lower voltage), which leads to gradual decay of its SoC and entire battery failure. The lower the number of affected plates, the slower the degradation will be.

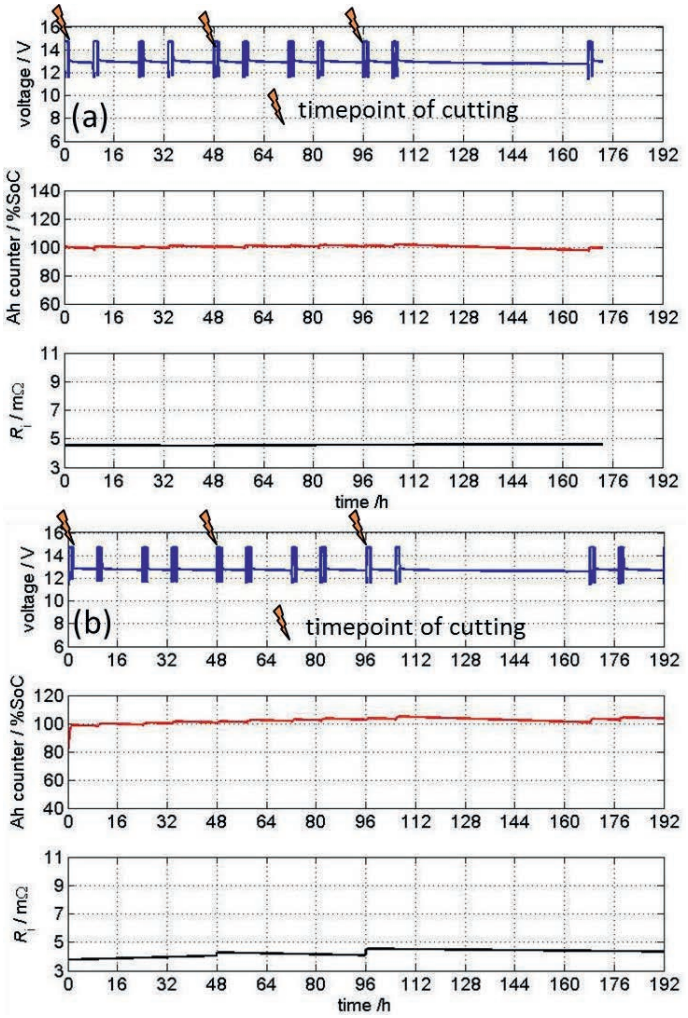

Fig. 128. µHRSC test results with SCL123 for: (top) EFB battery, (bottom) AGM battery. Initial SoC equals 80% in both cases. Tests have been carried out at 25 °C.

It is believed that the main reason for a significant difference between EFB and AGM battery behaviour was caused by the fact that for the latter one its electrolyte is immobilized in the AGM separators. This means that the electrolyte in one separator is only available to the plates which are in a direct contact with it (Fig. 11) and does not have access to the other ones. It is well-known that the electrolyte in PbA is not only a medium for ion conduction but it is also considered as an active material.

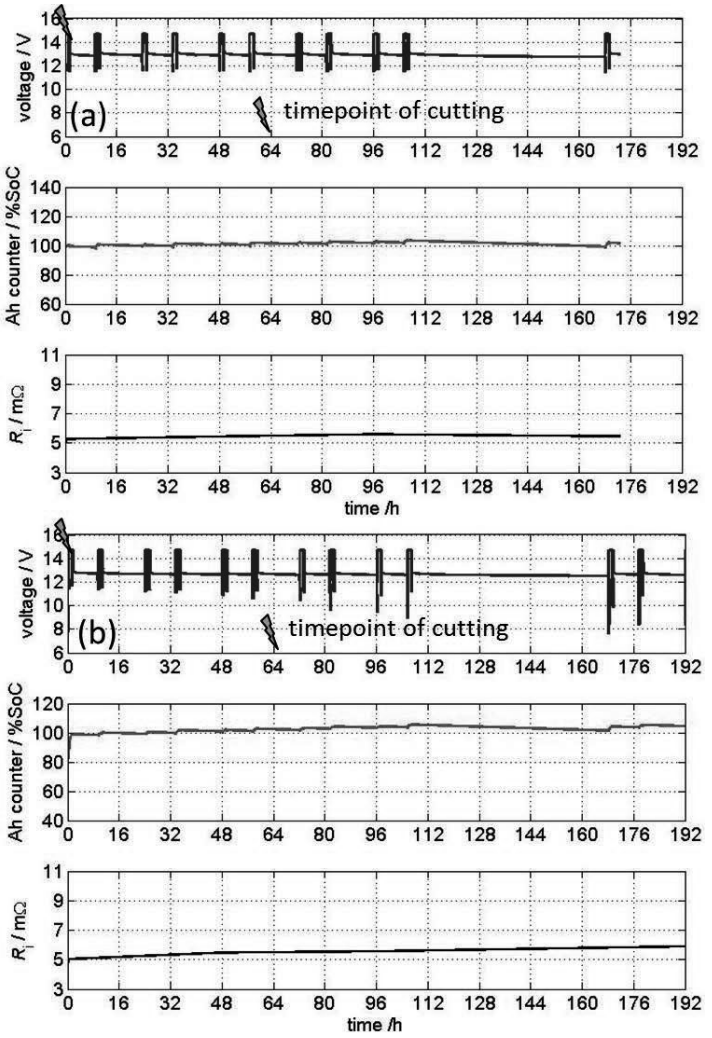

Fig. 129. µHRSC test results with SCL3 for: (top) EFB battery, (bottom) AGM battery. Initial SoC equals 80% in both cases. Tests have been carried out at 25 °C.

Therefore, loss of contact between one lug and the rest of plates means not only a loss of capacity (active material) in the plates themselves but also concerning the acid. Regarding EFB batteries the PAM of one or multiple electrodes gets lost but the acid is still available to the other components. It results in considerably higher density of the electrolyte in the failed cell than for AGM batteries. Higher density means a higher capacity and average voltage level. Therefore, it can be concluded that in such conditions imbalance caused by SCL leads to much faster deterioration of AGM battery performance in comparison to the EFB. However, it must

be mentioned that the tested AGM batteries were intrusively modified before the test started which means that issues such as considerable oxygen intake also contributed to their faster deterioration. That is why it is expected that observed performance deterioration in case of AGM batteries will be still faster than that of EFB batteries in the field, but not as fast as observed in the presented work.

Summarizing, SCL effects caused the same behaviour and gradual considerable performance deterioration as internal short-circuits described in the previous chapters. It means that the parameters, which can be used for internal failure detection caused by internal short-circuits, are also valid for sudden capacity loss issues.

6.5 Development of internal failure detection model

The development of failure detection algorithms which are suitable for implementation in EBS requires fulfilment of the criteria mentioned in chapter 3.2. Furthermore, time span from the occurrence of the internal failure until it gets detected should be as short as possible, while misleading failure detection of a healthy battery must be surely avoided. This means that the implemented thresholds and detection speed must be smartly optimized. Fast and correct failure detection is only useful when the risk of mistake is limited.

Internal failure must be also distinguished from ageing so that using reference value of any parameter is not feasible. Results of the carried out experiments showed that working with a trend of a given parameter is sufficient for accurate failure detection. Additionally, it is also important to have access to Ah counter that is not recalibrated too frequently, i.e. time span between two recalibrations should be higher than two weeks. It is known that in automotive applications the integration of current should be periodically recalibrated and set to a given point. This functionality is usually realized by means of open-circuit voltage (U_{00}) determination in the rest periods. However, obtained test results showed that internal failure mechanisms also cause a decrease of U_{00}. If the Ah counter is recalibrated or reset using this parameter, this will cause a false recalibration which affects the normalization algorithms that recalculate the values of the measured parameters to a given conditions (e.g. 100% SoC, 25 °C). This makes accurate internal failure detection not possible. The application of this procedure is necessary and cannot be neglected. Nonetheless, observation of the SoC recalibration using U_{00} can also provide vital information about existence of the internal short-circuit. In case of positive Ah balance consequent three or more recalibrations to the lower SoC values with imposed SoC change of more than -10% could be interpreted as probable internal failure. Moreover, accuracy of the failure detection algorithm that works together with less often recalibrated Ah counter can be significantly increased by means of incorporating a smart and adaptable gassing model. Exemplary implementations can be found in [31] and [53]. The authors found that in case of photovoltaic applications with battery storage systems, after 112 days of operation the deviation between real and calculated SoC without compensation of side reaction equalled 16%. Implementation of an advanced gassing model reduced this value to 6%, which can be considered as significant improvement.

Regarding modelling and measurement noise, the high complexity and non-linearity of PbA does not allow development of simple battery state detection algorithms, which cover all observed effects and could be relatively easily implemented in EBS. Examples of such effects are: acid stratification, DCA and impact of the short-term history on the overall internal resistance. The latter one causes a noticeable fluctuation of the internal resistance depending whether the battery was charged, discharged or idling before the measurement. As an example, at 25 °C such fluctuation of pure R_{ohmic} in most cases does not exceed the value of ± 0.2 mΩ. Furthermore, each cell of the battery can be heated in a different way due to inhomogeneous distribution of the sources of heat in the vehicle, which could cause significant temperature gradients within the battery. These factors have to be considered for careful choosing of the thresholds that will be used by the trend observing algorithms. Graphical illustration describing the trend observation concept has been depicted in Fig. 130.

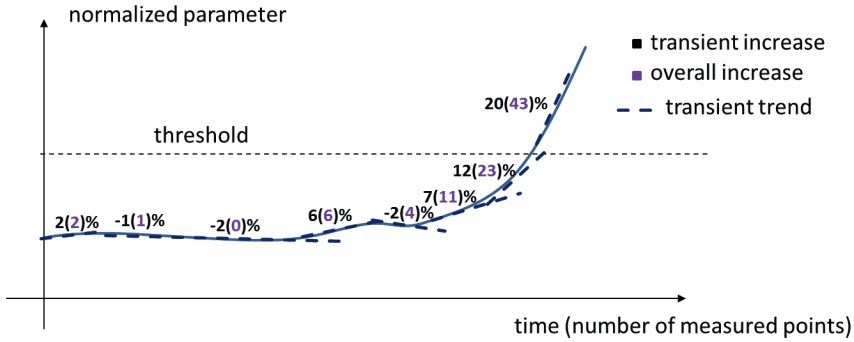

Fig. 130. Trend observation concept for realization of the internal failure detection.

Although the absolute value of any considered parameter cannot be directly taken for the accurate IFD, observation of its trend (in this case increase) is suitable for this task. It can be realized by either interpreting of only transient increase or collecting information about the past behaviour and forgetting it with time so that the amount of necessary memory is limited. On the one hand the first approach is very simple and requires limited amount of memory, but, on the other hand in case of relatively slow deterioration caused by e.g. internal short-circuits with high R_{SC}, internal failure cannot be detected at an early stage of its presence. This issue is fully solved by the second approach but the size of dedicated memory increases. It also has to be mentioned that the threshold for the first approach does not have to be necessarily the same as for the second one. Reducing its value could lead to the earlier failure recognition. However, sensitivity to measurement and modelling noise of such algorithm also increases dramatically. It has to be added that for the sake of robustness and reduction of the possibility of false IFD at least two parameters should be observed in parallel, which provides necessary redundancy. Regarding to the results of experimental investigation described in chapter 6.3 and 6.4 and considerations presented in this chapter a main concept for the internal failure detection has been developed and depicted in Fig. 131.

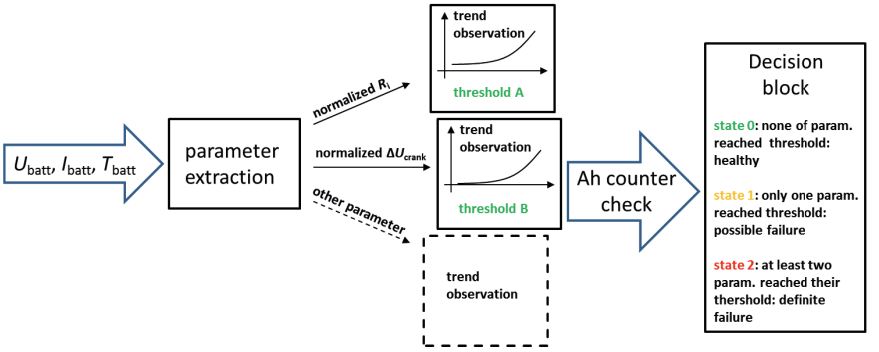

Fig. 131. Main concept of the developed internal failure detection algorithm.

In the next chapter, all the mentioned requirements are addressed. Two algorithms with a high potential to provide accurate and reliable internal failure detection are described. Their disadvantages and advantages are also discussed and the most suitable approach is determined.

6.5.1 Moving window concept

The main idea standing behind the moving window concept is observing trends of given parameters in a limited range so that the necessary amount of memory is significantly reduced and battery ageing does not have to be taken into account. It is assumed that performance degradation caused by the latter is much slower than in case of internal failures and that is why implementation of larger operation time window then one month, is concerned as not feasible. Main advantage of moving window concept is its stability, which is a critical parameter for IFD. However, it requires storing measured data in the memory. It is also sensitive to measurement noise, which can be only filtered out by implementation of the special filters that further increase its complexity.

The developed approach has been divided into three steps. Firstly, the values of the observed normalized parameter are being saved in the memory followed by determination of their mean value. Secondly, the collected mean values are used for fitting of the linear function demonstrated in (44).

$$\boldsymbol{f}_{\mathrm{inc}}(\boldsymbol{p_i}) = \boldsymbol{m} * \mathrm{t}(\mathrm{or}\ \boldsymbol{n}) \tag{44}$$

As the last step, the steepness is calculated by means of dividing f_{inc} with time or sample number. This is performed each time the chosen data length is reached, e.g. one hour of operation or 6 samples (n). Determined steepness (m) is then saved in memory and added to other available values. Obtained cumulative m or increase is outputted from the model and further evaluated. If its value reaches a given threshold an internal failure is being detected. Determination of the cumulative m is being carried out in a moving window. It means that there is a matrix with fixed size, which deletes in each simulation step the oldest available m value, moves all others to the next position and saves the most recent value in the first cell.

Visualization of the described approach can be found in Fig. 132, whereby it assumes the case of operation with internal failure. If the battery is healthy, the value of cumulative steepness of the charge in the slope will be close or equal 0.

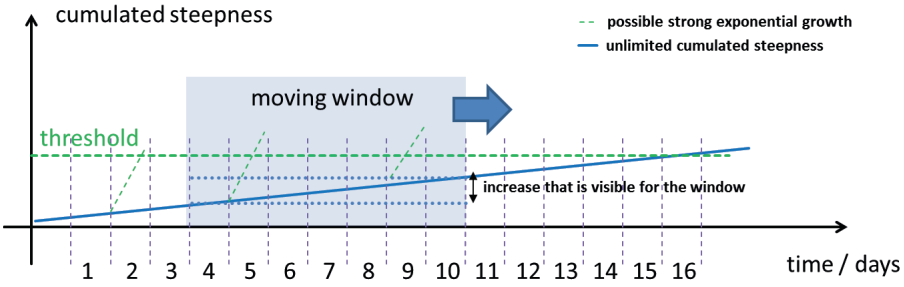

Fig. 132. Visualization of the moving window concept.

The width of the implemented window is critical, especially for the early failure detection capability. However, increasing its size is also associated with the higher need of dedicated memory, which also has to be optimized. This issue has been depicted in Fig. 133 using an example of internal resistance parameter that is being frequently measured so that rather time domain instead of sample number has been considered.

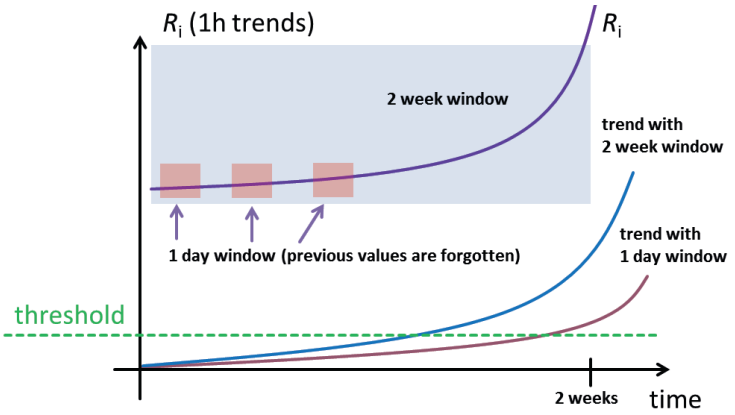

Fig. 133. Difference between failure detection of 1 day and 2 week window based on cumulating 1h steepness using an example of internal resistance parameter.

It can be clearly seen that using moving window approach internal failure can be always detected. Nevertheless, very narrow window will lead to relatively late detection. In order to use the advantages of both wide and narrow moving windows a hybrid window algorithm has also been developed. The first, shorter window operates within 1 day and uses 1 h *m* values, whereas the longer 2 week window is delayed by 1 day and determines 1 day *m*. Both cumulated

m values are being added and overall *m* is being evaluated for the internal failure detection. It means that in case of a sudden sharp increase of the considered parameter 1 day window will be able to react fast enough and wide window will deliver enough information about the past. It combines the main advantages of the both widths and offers relatively early internal failure detection with reduced amount of the data that has to be saved in the internal memory.

6.5.2 Recursive online trend fitting

Recursive online trend fitting (ROTF) approach is based on RLS filter described by Waag et al. [62]. It considers input signals as deterministic and does not require computationally intensive matrix operations such as inversion, which makes it suitable for implementation in EBS. Furthermore, it can be implemented in a way that does not require usage of any dedicated memory, which originates from complete avoidance of redoing least squares fit as time or sample number evolves. It is a big advantage considering IFD application. Its main disadvantages are high sensitivity to modeling noise, especially when the considered plant is highly non-linear, and possible divergence problems or instabilities.

Trend fitting of a given parameter, which is expected to grow exponentially as explained in the previous chapters, can be realized by applying linear function as demonstrated in Fig. 134.

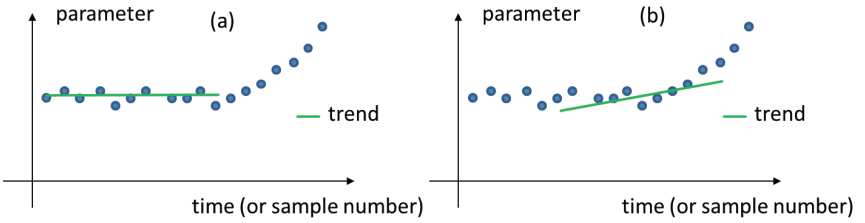

Fig. 134. Linear trend fitting of an exponentially growing parameter: (a) early stage of growth where m_{slope} of the exponential curve is negligible, (b) significant growth of the parameter contributes to considerable increase of m_{slope}.

Assuming that the considered parameter is normalized R_{ohmic}, at the beginning of exponential growth or during a normal operation the value of m_{slope} will be very close to 0 so that time dependent term of the linear function can be fully neglected. This case has been depicted in (45).

$$\boldsymbol{R}_{\text{ohmic}} = \boldsymbol{R}_{\text{ohmic,healthy}} + \boldsymbol{m}_{\textbf{slope}} * \text{t(or } \boldsymbol{n}) \tag{45}$$

Unless an internal failure is present the value of the fitted R_{ohmic} or other parameter should equal $R_{ohmic,healthy}$. In the opposite case, m_{slope} of a fitted curve starts increasing and when it reaches a given threshold it can be considered as detected failure as demonstrated in (46). Alternatively, if a direct value (not a percental one) of increase is being considered as it is the case for U_{crank} only multiplication of m_{slope}·t(or *n*) is used for a comparison, without the need of dividing the value by a constant coefficient, whereby the threshold has to be also specified as absolute value.

$$\text{threshold} < \frac{m_{slope} \cdot \text{t(or } \boldsymbol{n})}{\boldsymbol{R}_{\text{i,healthy}}} \rightarrow \text{failure} \tag{46}$$

RLS algorithm updates itself constantly during operation and outputs necessary values that can be used for internal failure detection according to (46). Furthermore, information about the past is hidden in the parameter values from the previous step so that no memory is needed.

6.6 Simulation results

In order to study the accuracy of the developed IFD algorithms and choose the most promising one for the implementation in the EBS, a simulation with the data recorded from the experimental study presented in chapter 6.3 and 6.4 has been carried out. Fig. 135 presents battery voltage and R_{ohmic} values recorded during µHRSC test with *RIc12h*. As expected the observed voltage drop and R_{ohmic} increases exponentially and after a short-time causes significant battery performance deterioration, which in the field would lead to a failed cranking.

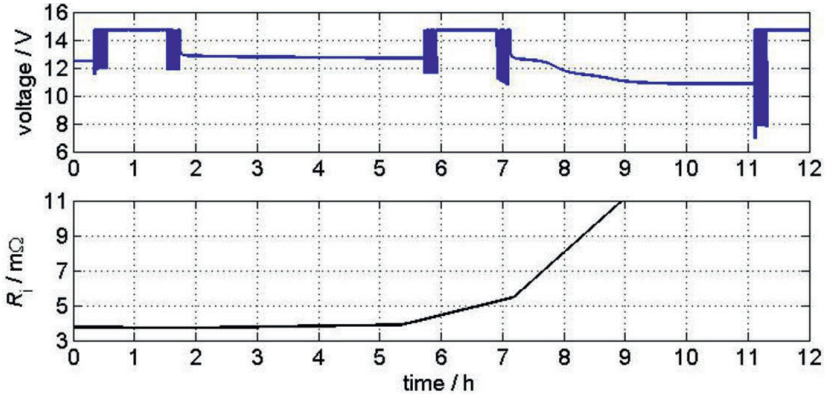

Fig. 135. µHRSC test results carried out with *RIc12h* of 60 Ah AGM battery conditioned to 25 °C. Initial SoC equals 80%.

Fig. 136 presents simulation results of µHRSC test on 60 Ah AGM battery with *RIc12h*. Both considered algorithms detected the failure just in time, namely before the sharp voltage drop in the rest period at 11$^{\text{th}}$ hour of test occurred. Fig. 137 depicts simulation results of µHRSC test on 60 Ah AGM battery with *RIc14d* (Fig. 121). It can be seen that hybrid window approach successfully combined the reduced amount of dedicated memory and fast reaction speed during last stage of discharging with short-circuit when the battery performance sharply decreases.

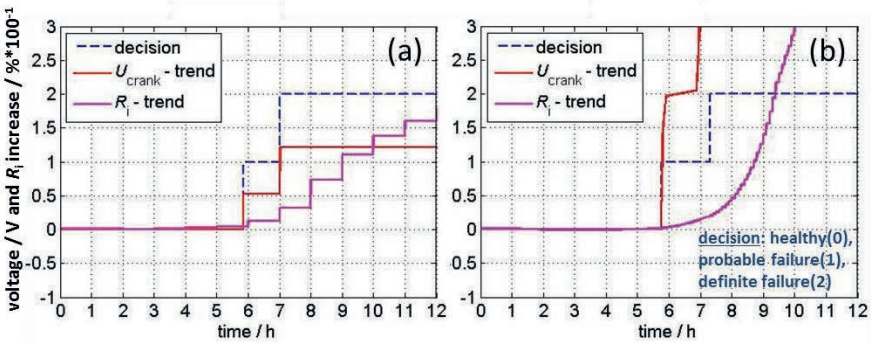

Fig. 136. Simulation results using µHRSC test data on 60 Ah AGM battery with *RIc12h* according to Fig. 131. Observed parameters are R_{ohmic}(t) and U_{crank}(n): (a) hybrid window comprising 1 day and modified 2 weeks window with 1 day of delay, (b) ROTF algorithm.

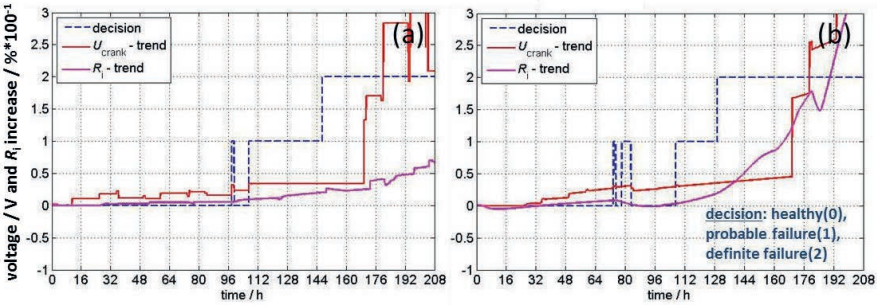

Fig. 137. Simulation results using µHRSC test data on 60 Ah AGM battery with *RIc14d* according to Fig. 131. Observed parameters are R_{ohmic}(t) and U_{crank}(n): (a) hybrid window comprising 1 day and modified 2 weeks' window with 1 day of delay, (d) ROTF algorithm.

ROTF algorithm showed the fastest detection speed, which proved the validity of a concept presented in Fig. 134. It refers to slightly reduced value of fitted constant coefficient (see (45)) while entering the area of sharp increase of the considered parameter. Worth mentioning is also presence of visible fluctuations between healthy and probable failure state. This fact emphasizes a need to interpret stationary state values and not transients, which can be misleading as shown in this case. Stationary value means a recognized failure that stays present for at least one trip. However, state transition from probable to definite failure showed no oscillation, which shows that making final decision about the presence of internal failure is not affected by this issue. Nevertheless, implementation of a saturation function that controls transition from any upper to lower state could significantly reduce this issue. Trend detection using minimal voltage during ASSF phases (not cranking) has not been considered, due to the fact that in the

application it is very challenging to perform an accurate normalization of this parameter due to presence of several complex phenomena like diffusion, relaxation and dynamic overvoltage of both PAM and NAM, which makes it not suitable for IFD. This can be furthermore related to the considerable and not negligible modelling noise, which poses a high risk of triggering false internal failure detection.

Simulation results of all collected test data and considerations presented in this subchapter lead to the following conclusions:

- The developed concept of trend following shows a high potential for realizing an accurate and early internal failure detection in the field.

- For the implementation in EBS the most proper is ROTF algorithm, due to its low memory requirements and easy implementation. However, its stability should be confirmed by means of comprehensive analysis and simulation with the real field data recorded from different vehicles that were operated in various conditions.

- Internal failure detection in case of failures with relatively low R_{SC} is more challenging due to possible lack of necessary information in a short time, e.g. it may happen that the vehicle is standing unused for a long time and no voltage drop during cranking is available. In this case an observed relaxation behaviour could be compared with the predicted one from a novel approach described in chapter 5. In case of significantly lower measured voltage a probable failure could be recognized.

- Recognition of a failure using a charging current value during long charging phases typical for PHEV should be realized by means of comparison with an adaptable gassing model. Such approach provides acceptable results for all mechanisms that degrade the battery in both very gradual and fast pace.

6.7 Summary

In this subchapter, an approach for internal failure detection of 12 V power net lead-acid batteries has been developed. It is based on the recursive least-square filter that observes the battery behaviour and has been optimized in a way that makes it suitable for implementation in electronic battery sensor or energy management system operating in the modern conventional, hybrid and electric vehicles. Considered parameters are internal resistance and minimal cranking voltage that should be normalized to the standard conditions (typically are 100% SoC, 25 °C and given maximal cranking current e.g. 700 A or CCA). Theoretically only one parameter is necessary to perform accurate failure recognition. However, second parameter is needed to provide necessary redundancy with significant reduction of the risk of wrong internal failure detection. Its demand for dedicated internal memory, required computational power, robustness against noise and stability has been successfully tested. Required performance has been proven by comprehensive reproducible and systematic investigation that provided information about the battery behaviour during operation with imposed presence of internal failure. It was found that even in case when batteries with internal failure were frequently fully

charged or even significantly overcharged for a longer time, their performance worsening impact could not be compensated. Macro short-circuits that cause battery breakdown within significantly shorter time than one hour has not been considered in the presented study. They are relatively easily detectable using actual value of current rate and voltage.

7 Conclusions and future work

This study shows advances in the field of battery monitoring of PbA in µH vehicles. They lead to the further improvements of fuel economy and reduction of CO_2 emissions through improved accuracy that guarantee significant reduction of missed ASSF opportunities and premature engine restarts. Additionally, improved BSD is also used for development of novel operation strategies, which could help to further optimize mentioned aspects. Reduced error in comparison to the state-of-the-art algorithms has been achieved by means of thorough understanding of modelled processes and specification of the application, which lead to highly adaptable heuristic solutions. Furthermore, their complexity and accuracy has been optimized in a way that allows implementation on the low-cost EBS and reaching excellent performance that has been confirmed through carried out verification tests. Following aspects have been addressed in this study:

BDR estimation using BVE based concept that considers SoC, remaining capacity (or different battery sizes) and current rate. The latter dependency has been neglected in the most of contemporary algorithms. It has been thoroughly analysed in this work and provides one of the main advantages of the presented method. Developed approach is used for accurate prediction of the minimal voltage during cranking or any arbitrary dynamic load as well as supporting tool for SoH estimation. Its simplified implementation allows working with one variable that can be easily adapted in the field conditions. Achieved accuracy is as low as ± 200 mV for cranking currents, which is considered as excellent result concerning pronounced non-linearity of PbA and two times lower precision of the state-of-the-art solutions. On the one hand presented implementation focuses only on NAM, but, on the other hand the same methodology also applies for modelling of PAM and developing a highly accurate voltage response prediction in a wide range of parameters including discharging time. Suggested future work should consider extensive testing with possibly high number of vehicles and different batteries, which will provide a further insight into the validity of applied assumptions as well as scalability of the model. Additionally, implementation of the whole model together with double-layer capacity and improvements, which extend validity of presented solution to charging current range, should be also analysed.

U_{00} estimation (needed for SoC calculation using linear relation between these two parameters) applying algorithm based on the presented novel phenomenological double-layer gel-crystal model. It has been developed using results of the comprehensive experimental study, which revealed significantly different relaxation behaviour of PbA during relaxation excited with charge and discharge short-term history. The former one causes significantly longer relaxation with increased overvoltage that has to be compensated for accurate calculation of U_{00}. Findings shown in this thesis are unique. They proved that widely used assumption, which links long

relaxation with concentration gradients, is incorrect. Furthermore, they delivered necessary understanding necessary for the development of accurate BSD algorithms, which was not available before. Identified parameters, which mostly influence relaxation, are temperature, SoC, Q_{cha} and $I_{quiescent}$. Developed approaches are characterized by improved adaptivity, low complexity and excellent accuracy that is most pronounced for operation at low temperatures. In case of parametrized batteries regardless of size type and technology it should be not lower than ± 5% SoC, which is significantly less than in case of state-of-the-art solutions that cannot guarantee precision of even ± 10% SoC at low temperatures and short rest periods. Lack of calibration results in slightly increased accuracy of ± 7 % SoC. Furthermore, conducted validation showed accuracy lower than ± 3% SoC for U_{00} estimation for temperatures higher than 10 °C. Future work should be involved in the development of smart approaches that will estimate cumulated value of Q_{cha} which is a vital parameter influencing final accuracy. It was found that after unfinished relaxation typical for field conditions, imposed value of Q_{cha} does not get fully removed from the battery. On the one hand, simple Ah counting should provide good results, but, on the other hand duration between two rest periods has to be also considered. Another aspect, which is worth investigating, is optimization of HOCVM that chooses between two developed approaches. It is believed that further increase of accuracy could be achieved by means of collecting and evaluation bigger set of field data. The last suggested analysis focuses on further evidence that could prove the validity of developed double-layer gel-crystal model. Firstly, probe preparation technique that allows preservation of the soft hydrated layer should be developed to conduct feasible and reproducible study. It should consist of relatively limited washing and drying procedures as well as storage and probe extraction at low temperatures. Alternatively, in-situ observation technique of the positive electrode could be also applied. Such investigation could show the state of the active materials surface directly after finished charging and deliver information about how it changes during rest periods. Next step is the chemical analysis using following methods: X-ray diffraction, microscopy or thermogravimetric analysis. The most promising results could be obtained by the former one, which shows exactly how much of the material in the probe can be categorized as crystalline. It means that extracted probes without any charging short-term history could be compared with the ones shaped by given time intervals at rest.

IFD using developed trend observation technique, makes possible to detect whether a given battery experiences performance deterioration caused by internal failure mechanisms and distinguish them from ageing. Applied experimental emulation of internal short-circuits and sudden capacity loss provided a crucial information for systematic analysis of battery behaviour in the considered states. Until now no such data was available due to lack of access to batteries with internal failure, which are simply directly recycled. Furthermore, no analytic relations are known, which allow estimation of the investigated parameters, e.g. value of short-circuit resistance, as a function of the applied ageing. It was shown that relatively easy implementation of the developed method with reduced amount of dedicated memory can provide satisfactory results and relatively fast detection speed. Additionally, presented approach is characterized by improved robustness and redundancy that significantly reduces probability of wrong failure detection that must be avoided. The main part of the future work should focus on simulation

that will be carried out with data coming from possibly high number of conditions and test vehicles, which will allow finding of the most optimized thresholds. Furthermore, operation of the developed algorithms with heavily stratified flooded battery could be also investigated. It is known that average voltage of such battery will gradually fall down due to diffusion that will eventually remove the stratification. However, such behaviour could be wrongly interpreted by IFD as a failure. Furthermore, testing of the modified battery with emulated short-circuits should also be carried out. The battery should be installed in a vehicle so that a final validation with the closest possible conditions to the field could be achieved. Modified battery could be also equipped with a controllable switch to allow investigating further aspects e.g. loose short-circuit.

Future study should also include determination of the BSD accuracy with the developed methods during operation of PbA as a part of "dual" storage systems, which consist of PbA and another advanced battery technology (e.g. li-ion battery or electrochemical double-layer capacitor bank) connected in parallel. Usually, in this kind of storage systems PbA has significantly higher C_N than the considered second energy storage system. In this case BVE and IFD algorithms are directly applicable with some limited tuning of the thresholds used by the latter one. However, in case of HOCVM redesigning of the whole method is necessary. It is because in most cases PbA is not going to be discharged during rest periods as it is the case in the current generation of μH, but rather charged by the second battery connected in parallel. It means that there is no longer a quasi-unconstrained decay of the battery voltage during relaxation. Voltage of the whole system is directly related to the actual voltage of the advanced battery solution, which can be considered as the voltage source. On this wise PbA behaves like a load and determine transient behaviour and stead-state of the current that flow between two batteries. This indicates significant changes in the PbA behaviour during rest periods.

8 Bibliography

[1] C. Pillot, Avicenne Energy, *Lithium-Ion Battery Market Expansion Beyond Consumer and Automotive*, AABC Eur. January (2015).

[2] L. Gaines, *The future of automotive lithium-ion battery recycling: Charting a sustainable course*, J Sus Mat. 1-2 (2014) 2–7.

[3] J. Garche, *Encyclopedia of electrochemical power sources*, Elsevier, Spain, 2009.

[4] P. Kurzweil, *Gaston Plante and his invention of the lead-acid battery - The genesis of the first practical rechargeable battery*, J Power Sources. 195 (2010) 4424–4434.

[5] E. Meissner, J. Albers, S. Shirazi, R. Xie, *Impact of Battery Type and Design on Availability of Engine Start-Stop Systems and on Fuel Efficiency on the Road*, 14th ELBC. Edinburgh, Scotland, UK (2014).

[6] The World Bank, *World Development Indicators: Traffic and congestion*, (2015). http://web.archive.org/web/20140408034906/http://wdi.worldbank.org/table/3.13.

[7] D. Benchentrite, *2013 Valeo Powertrain Forecast*, EEHE Meet. Bamberg, Germany (2014).

[8] S. Peng, *Lead Acid Batteries for Stop-Start Application in China*, 14th ELBC. Edinburgh, Scotland, UK (2014).

[9] HELLA KGaA Hueck & Co., http://www.hella.com/microsite-electronics/154.html, HELLA KGaA Hueck & Co., (2014). http://www.hella.com/microsite-electronics/154.html.

[10] E. Meissner, G. Richter, *The challange to the automotive battery industry: the battery has to become an increasingly integrated component within the vehicle electric power system*, J Power Sources. 144 (2005) 438–460.

[11] J. Valenciano, M. Fernandez, F. Trinidad, L. Sanz, *Lead-acid batteries for micro- and mild-hybrid applications*, J Power Sources. 187 (2009) 599–604.

[12] D. Berndt, *Valve-regulated lead-acid batteries*, J Power Sources. 100 (2001) 29–46.

[13] E. Meissner, G. Richter, *Battery Monitoring and Electrical Energy Management Precondition for future vehicle electric power systems*, J Power Sources. 116 (2003) 79–98.

[14] G. Pilatowicz, H. Budde-Meiwes, D. Schulte, J. Kowal, Y. Zhang, X. Du, M. Salman, D. Gonzales, J. Alden, D. U. Sauer, *Simulation of SLI Lead-Acid Batteries for SoC, Aging and Cranking Capability Prediction in Automotive Applications*, J Electrochem Soc. 159 (2012) A1410–A1419.

[15] Bosch Automotive Products (Suzhou) Co., Ltd., Electronic Battery Sensor (EBS), (2015). http://microsite.bosch.com.cn/ebrochures2015/energizing_powertrain/electronica_battery_sensor_en.pdf.

[16] J. L. Weininger, J. L. Briant, *State-of-Charge Indicator for Lead-Acid Batteries*, J Electrochem Soc. 129 (1982) 2409–2412.

[17] D.U. Sauer, *Optimierung des Einsatzes von Blei-Säure-Akkumulatoren in Photovoltaik-Hybrid-Systemen unter spezieller Berücksichtigung der Batteriealterung*, PhD Thesis, Ulm University, Ulm, Germany, 2003.

[18] D. Pavlov, *Lead-Acid Batteries Science and Technology*, 1st edition, Elsevier, 2011.

[19] A. Jossen, W. Weydanz, *Moderne Akkumulatoren richtig einsetzen*, Andreas Jossen und Wolfgang Weydanz, Leipheim und München, 2006.

[20] D. Berndt, *Maintenance- Free Batteries Based on Aqueous Electrolyte*, Research Studies Press LTD., 2003.

[21] Y. Shi, C. A. Ferone, C. D. Rahn, *Identification and remediation of sulfation in lead-acid batteries using cell voltage and pressure sensing*, J Power Sources. 221 (2013) 177–185.

[22] D. A. J. Rand, P. T. Moseley, J. Garche, C. D. Parker, *Valve-Regulated Lead-Acid Batteries*, Elsevier B.V., 2004.

[23] D. Pavlov, A. Kirchev, B. Monahov, *Mechanism of the oxygen cycle reactions proceeding at the negative plates of VRLA batteries*, J Power Sources. 144 (2005) 521–527.

[24] N.E. Bagshaw, *Lead/Acid recombination batteries: principles and applications*, J Power Sources. 31 (1990) 23–33.

[25] H. Budde-Meiwes, D. Schulte, J. Kowal, D. U. Sauer, R. Hecke, E. Karden, *Dynamic charge acceptance of lead-acid batteries: Comparison of methods for conditioning and testing*, J Power Sources. 207 (2012) 30–36.

[26] S. Schaeck, A. O. Stoermer, F. Kaiser, L. Koehler, J. Albers, H. Kabza, *Lead-acid batteries in micro-hybrid applications. Part I. Selected key parameters*, J Power Sources. 196 (2011) 1541–1554.

[27] R. Wagner, M. Gelbke, *Charge / Discharge Behaviour of positive and negative Plates under different Cycling Conditions*, 13th ELBC. Paris, France (2012).

[28] J. Valenciano, I. Torija, F. Trinidad, *Improvements in Flooded Lead-Acid Batteries for a Better Cycling Life Performance under Different Surrounding and PSOC Conditions. Closing the Gap with AGM Batteries for Micro-hybrid Applications*, 14th ELBC. Edinburgh, Scotland, UK (2014).

[29] M. Schindler, *Mehr-Batterie-System für Mikro-Hybrid-Fahrzeuge auf Basis von Blei-Säure- und Lithium-Ionen-Technologie*, PhD Thesis, RWTH Aachen University, Aachen, Germany, 2014.

[30] J. J. Lander, *Further Studies on the Anodic Corrosion of Lead in H2SO4 Solutions*, J Electrochem Soc. 103 (1956) 1–8.

[31] J. Schiffer, D. U. Sauer, H. Bindner, T. Cronin, P. Lundsager, R. Kaiser, *Model prediction for ranking lead-acid batteries according to expected lifetime in renewable energy systems and autonomous power-supply systems*, J Power Sources. 168 (2007) 66–78.

[32] P. Ruetschi, R. T. Angstadt, *Anodic Oxidation of Lead at Constant Potential*, J Electrochem Soc. 111 (1964) 1323–1330.

[33] P. Ruetschi, *Aging mechanisms and service life of lead-acid batteries*, J Power Sources. 127 (2004) 33–44.

[34] R. D. Prengaman, *Challanges from corrosion-resistance grid alloys in lead-acid battery manufacturing*, J Power Sources. 95 (2001) 224–233.

[35] D. U. Sauer, E. Karden, B. Fricke, H. Blanke, M. Thele, O. Bohlen, J. Schiffer, J. B. Gerschler, R. Kaiser, *Charging performance of automotive batteries - An underestimated factor influencing lifetime and reliable battery operation*, J Power Sources. 168 (2007) 22–30.

[36] M. Fernandez, P.G. Gracia, F. Trinidad, J. Valenciano, *VRLA batteries electrochemical factors affecting life*, J Power Sources. 113 (2003) 233–240.

[37] S. Schaeck, A. O. Stoermer, E. Hockgeiger, *Micro-hybrid electric vehicle application of valve-regulated lead–acid batteries in absorbent glass mat technology: Testing a partial-state-of-charge operation strategy*, J Power Sources. 190 (2009) 173–183.

[38] H. A. Catharino, F. F. Feres, F. Trinidad, *Sulfation in lead-acid batteries*, J Power Sources. (2004) 113–120.

[39] J. Albers, E. Meissner, S. Shirazi, *Lead-acid batteries in micro-hybrid vehicles*, J Power Sources. 196 (2011) 3993–4002.

[40] E. Karden, *Using low-frequency impedance spectroscopy for characterization, monitoring, and modeling of industrial batteries*, PhD Thesis, RWTH Aachen University, Aachen, Germany, 2001.

[41] T. Ohmae, K. Sawai, M. Shiomi, S. Osumi, *Advanced technologies in VRLA batteries for automotive applications*, J Power Sources. 154 (2006) 523–529.

[42] K. Sawai, T. Ohmae, H. Suwaki, M. Shiomi, S. Osumi, *Idling-stop vehicle road tests of advanced valve-regulated lead-acid (VRLA) battery*, J Power Sources. 174 (2007) 54–60.

[43] D. Schulte, T. Sanders, W. Waag, J. Kowal, D. U. Sauer, E. Karden, *Automatic device for continuous measurement of potential distribution and acid stratification in flooded lead-acid batteries*, J Power Sources. 221 (2013) 114–121.

[44] D. Schulte, D. U. Sauer, E. Ebner, A. Börger, S. Gose, H. Wenzl, *"Stratifiability index" – A quantitative assessment of acid stratification in flooded lead acid batteries*, J Power Sources. 269 (2014) 704–715.

[45] J. Kowal, D. Schulte, D. U. Sauer, E. Karden, *Simulation of the current distribution in lead-acid batteries to investigate the dynamic charge acceptance on flooded SLI batteries, J Power Sources*. 191 (2009) 42–50.

[46] P. T. Moseley, D. A. J. Rand, B. Monahov, *Designing lead-acid batteries to meet energy and power requirenments of future automobiles*, J Power Sources. 219 (2012) 75–79.

[47] A. C. Zachlin, *Self-discharge in lead-acid storage batteries*, J Electrochem Soc. 92 (1947) 259–279.

[48] N. Clement, *How important is the Absorbent Glass Mat separator in VRLA automated assembly line?*, in: 15th ABC, Singapore, 2013.

[49] Varta-Batterie-AG, *Bleiakkumulatoren*, VDI-Verlag, Düsseldorf, 1986.

[50] L.T. Lam, H. Ceylan, N.P. Haigh, T. Lwin, D. A. J. Rand, *Influence of residual elements in lead on oxygen- and hydrogen-gassing rates of lead-acid batteries*, J Power Sources. 195 (2010) 4494–4512.

[51] S. Nagashima, K. Takahashi, T. Yabumoto, S. Shiga, Y. Watabe, *Development and field experience of monitoring system for valve-regulated lead-acid batteries in stationary applications*, J Power Sources. 158 (2006) 1166–1172.

[52] R. Kaiser, *Optimized battery-management system to improve storage lifetime in renewable energy systems*, J Power Sources. 168 (2007) 58–65.

[53] M. Stoll, *Ein Schätzverfahren über den inneren Zustand geschlossener Bleiakkumulatoren*, VDI-Verlag, Düsseldorf, 1994.

[54] A. Lohner, *Batteriemanagement für verschlossene Blei-Batterien am Beispiel von Unterbrechungsfreien Stromversorgungen*, PhD Thesis, RWTH Aachen University, Aachen, Germany, 1998.

[55] O. Bohlen, *Impedance-based battery monitoring*, PhD Thesis, RWTH Aachen University, Aachen, Germany, 2008.

[56] D.U. Sauer, G. Bopp, A. Jossen, J. Garche, M. Rothert, Michael Wollny, *State of charge-What do we really speak about?*, in: Kopenhagen, Denmark, INTELEC, 1999: p. paper 31–32.

[57] DIN EN 50342-1, *Lead-acid starter batteries – Part 1: General requirements and methods of test*, EN 50342-1:2006 (2006).

[58] G. Pilatowicz, A. Marongiu, J. Drillkens, P. Sinhuber, D.U. Sauer, *A critical overview of definitions and determination techniques of the internal resistance using lithium-ion, lead-acid, nickel metal-hydride batteries and electrochemical double-layer capacitors as examples*, J Power Sources. 296 (2015) 365–376.

[59] Willi Steffens, *Verfahren zur Schätzung der inneren Größen von Starterbatterien*, PhD Thesis, RWTH Aachen University, Aachen, Germany, 1987.

[60] W. Waag, *Adaptive algorithms for monitoring of lithium-ion batteries in electric vehicles*, PhD Thesis, RWTH Aachen University, Aachen, Germany, 2014.

[61] M. Thele, O. Bohlen, D. U. Sauer, E. Karden, *Development of a voltage-behavior model for NiMH batteries using an impedance-based modeling concept*, J Power Sources. 175 (2008) 635–643.

[62] W. Waag, C. Fleischer, D. U. Sauer, *Critical review of the methods for monitoring of lithium-ion batteries in electric and hybrid vehicles*, J Power Sources. 258 (2014) 321–339.

[63] S. Piller, M. Perrin, A. Jossen, *Mothods for state-of-charge determination and their applications*, J Power Sources. 96 (2001) 113–120.

[64] H. Budde-Meiwes, J. Kowal, D.U. Sauer, E. Karden, *Influence of measurement procedure on quality of impedance spectra on lead-acid batteries*, J Power Sources. 196 (2011) 10415–10423.

[65] J. Kowal, *Spatially-resolved impedance of nonlinear inhomogeneous devices - using the example of lead-acid batteries*, PhD Thesis, RWTH Aachen University, Aachen, Germany, 2010.

[66] H. Blanke, O. Bohlen, S. Buller, R. W. De Doncker, B. Fricke, A. Hammouche, D. Linzen, M. Thele, D. U. Sauer, *Impedance measurements on lead-acid batteries for state-of-charge, state-of-health and cranking capability prognosis in electric and hybrid electric vehicles*, J Power Sources. 144 (2005) 418–425.

[67] M. Thele, *A contribution to the modelling of the charge acceptance of lead-acid batteries - using frequency domain based concepts*, PhD Thesis, RWTH Aachen University, Aachen, Germany, 2008.

[68] G. L. Plett, *Extended Kalman filtering for battery management systems of LiPB-based HEV battery packs Part 1. Background*, J Power Sources. 134 (2004) 252–261.

[69] G. L. Plett, *Extended Kalman filtering for battery management systems of LiPB-based HEV battery packs Part 2. Modeling and identification*, J Power Sources. 134 (2004) 262–276.

[70] G. L. Plett, *Extended Kalman filtering for battery management systems of LiPB-based HEV battery packs Part 3. State and parameter estimation*, J Power Sources. 134 (2004) 277–292.

[71] F. Huet, *A review of impedance measurements for determination of the state-of-charge or state-of-health of secondary batteries*, J Power Sources. 70 (1998) 59–69.

[72] W. Waag, C. Fleischer, D. U. Sauer, *Adaptive on-line prediction of the available power of lithium-ion batteries*, J Power Sources. 242 (2013) 548–559.

[73] E. Karden, S. Buller, R. W. De Doncker, *A method for measurement and interpretation of impedance spectra for industrial batteries*, J Power Sources. 85 (2000) 72–78.

[74] M. Thele, S. Buller, D. U. Sauer, R. W. De Doncker, E. Karden, *Hybrid modeling of lead-acid batteries in frequency and time domain*, J Power Sources. 144 (2005) 461–466.

[75] P. Mauracher, E. Karden, *Dynamic modelling of lead/acid batteries using impedance spectroscopy for parameter identification*, J Power Sources. 67 (1997) 69–84.

[76] M. Thele, J. Schiffer, E. Karden, E. Surewaard, D. U. Sauer, *Modeling of the charge acceptance of lead-acid batteries*, J Power Sources. 168 (2007) 31–39.

[77] A. Kirchev, N. Kircheva, M. Perrin, *Carbon honeycomb grids for advanced lead-acid batteries. Part I: Proof of concept*, J Power Sources. 196 (2011) 8773–8788.

[78] A. Kirchev, A. Delaille, M. Perrin, E. Lemaire, F. Mattera, *Studies of the pulse charge of lead-acid batteries for PV applications Part II. Impedance of the positive plate revisited*, J Power Sources. 170 (2007) 495–512.

[79] A. Kirchev, A. Delaille, F. Karoui, M. Perrin, E. Lemaire, F. Mattera, *Studies of the pulse charge of lead-acid batteries for PV applications Part III. Electrolyte concentration effects on the electrochemical performance of the positive plate*, J Power Sources. 179 (2008) 808–818.

[80] A. Kirchev, F. Mattera, E. Lemaire, K. Dong, *Studies of the pulse charge of lead-acid batteries for photovoltaic applications Part IV. Pulse charge of the negative plate*, J Power Sources. 191 (2009) 82–90.

[81] K.J. Vetter, *Elektrochemische Kinetik*, Springer, Berlin, 1961.

[82] W. Waag, C. Fleischer, D. U. Sauer, *On-line estimation of lithium-ion battery impedance parameters using a novel varied-parameters approach*, J Power Sources. 237 (2013) 260–269.

[83] T. Erdey-Gruz, M. Volmer, *Zur Theorie der Wasserstoffüberspannung*, Z Phys Chem. A. 150 (1930) 203–213.

[84] M. Thele, E. Karden, E. Surewaard, D. U. Sauer, *Impedance-based overcharging and gassing model for VRLA/AGM batteries*, J Power Sources. 158 (2006) 953–963.

[85] W. Waag, S. Kaebitz, D. U. Sauer, *Experimental investigation of the lithium-ion battery impedance characteristic at various conditions and aging states and its influence on the application*, Appl. Energy. 102 (2013) 885–897.

[86] S. Buller, *Impedance-Based Simulation Models of Energy Storage Devices in Advanced Automotive Power Systems*, PhD Thesis, RWTH Aachen University, Aachen, Germany, 2003.

[87] T. Erdey-Gruz, *Kinetik der Elektrodenprozesse*, Akademiai Kiado, Budapest, 1975.

[88] H. Bode, *Lead- Acid Batteries*, John Wiley & Sons, Inc., 1977.

[89] G.T. Burstein, *A hundread years of Tafel's Equation*: 1905-2005, Corros. Sci. 47 (2005) 2858–2870.

[90] K.S. Champlin, K. Bertness, *Results of discrete frequency immitance spectroscopy (DFIS) measurements of lead acid batteries*, IEEE. (2001).

[91] A.J. Bard, G. Inzelt, F. Sholz, *Electrochemical dictionary*, Springer-Verlag, Berlin, Heidelberg, 2008.

[92] A.K. Shukla, V. Ganesh Kumar, N. Munichandraiah, T.S. Srinath, *A method to monitor valve-regulated lead acid cells*, J Power Sources. 74 (1998) 234–239.

[93] B. Hariprakash, S.K. Martha, A. Jaikumar, A.K. Shukla, *On-line monitoring of lead-acid batteries by galvanostatic non-destructive technique*, J Power Sources. 137 (2004) 128–133.

[94] J. Garche, A. Jossen, H. Doering, *The influence of different operating conditions, especially over-discharge, on the lifetime and performance of lead/acid batteries for photovoltaic systems*, J Power Sources. 67 (1997) 201–212.

[95] X. Zhang, R. Grube, K.-K. Shin, M. Salman, R. Conell, *Parity-relation-based state-of-health monitoring of lead acid batteries for automotive applications*, Control Eng. Pract. 19 (2011) 555–563.

[96] H. Karami, M. A. Karimi, M. Mahdipour, *ANN modeling of cold cranking test for sealed lead-acid batteries*, J Power Sources. 158 (2005) 936–943.

[97] M. Cugnet, S. Laruelle, S. Grugeon, B. Sahut, J. Sabatier, J. Tarascon, A. Oustaloup, *A Mathematical Model for the Simulation of New and Aged Automorive Lead-Acid Batteries*, J Electrochem Soc. 156 (2009) A974–A985.

[98] E. Meissner, *Phosphoric acid as an electrolyte additive for lead/acid batteries in electric-vehicle applications*, J Power Sources. 67 (1997) 135–150.

[99] G. Pasaoglu, D. Fiorello, A. Martino, G. Scarcella, A. Alemanno, A. Zubaryeva, C. Thiel, *Driving and parking patterns of European car drivers --- a mobility survey*, Eur. Comm. (2012). https://setis.ec.europa.eu/system/files/Driving_and_parking_patterns_of_European_car_drivers-a_mobility_survey.pdf.

[100] T. Takeuchi, K. Sawai, Y. Tsuboi, M. Shiota, S. Ishimoto, N. Hirai, S. Osumi, *The partial state-of-charge cycle performance of lead-acid batteries*, J Power Sources. 189 (2009) 1190–1198.

[101] T. Hildebrandt, J. Bauer, J. Albers, J. Douady, *TC21X Standardization Activities for Starter Batteries*, in: 14th ELBC, Edinburgh, Scotland, UK, 2014.
[102] H. Budde-Meiwes, J. Drillkens, B. Lunz, J. Muennix, S. Rothgang, J. Kowal, D. U. Sauer, *A Review of Current Automotive Battery Technology and Future Prospects*, IMechE Part J Automob. Eng. 227 (2013) 761–776.
[103] J. P. Carr, N. A. Hampson, *THE LEAD DIOXIDE ELECTRODE*, Chem Rev. 72 (1972) 680–703.
[104] E. Meissner, *How to understand the reversible capacity decay of the lead dioxide electrode*, J Power Sources. 78 (1999) 99–114.
[105] R. J. Hill, M. R. Houchin, *Incorporation of hydrogen into lead dioxide by a surface hydrolysis mechanism*, Electrochim Acta. 30 (1985) 559–561.
[106] S. M. Caulder, J. S. Murday, A. C. Simon, *The Hydrogen-Loss Concept of Battery Failure: The PbO2 Electrode*, J Electrochem Soc. 120 (1973) 1515–1516.
[107] D. Pavlov, I. Balkanov, *Hydration and Amorphization of Active Mass PbO2 Particles and Their Influence on the Electrical Properties of the Lead-Acid Battery Positive Plate*, J Electrochem Soc. 136 (1989) 3189–3197.
[108] A. Santoro, P. D'Antonio, S. M. Caulder, *A Neutron Powder Diffraction Study of and alpha- and beta-PbO2 in the Positive Electrode Material of Lead-Acid Batteries*, J Electrochem Soc. 130 (1983) 1451–1459.
[109] D. Pavlov, *The Lead-Acid Battery Lead Dioxide Active Mass:A Gel-Crystal System with Proton and Electron Conductivity*, J Electrochem Soc. 139 (1992) 3075–3080.
[110] P. T. Moseley, J. L. Hutchison, C. J. Wright, M. A. M. Bourke, R. I. Hill, V. S. Rainey, *Inelastic Neutron Scattering and Transmission Electron Microscope Studies of Lead Dioxide*, J Electrochem Soc. 130 (1983) 829–834.
[111] B. Monahov, D. Pavlov, *Hydrated structures in the anodic layer formed on lead electrodes in H2SO4 solution*, J Appl Electrochem. 23 (1993) 1244–1250.
[112] D. Pavlov, A. Kirchev, M. Stoycheva, B. Monahov, *Influence of H2SO4 concentration on the mechanism of the processes and on the electrochemical activity of the Pb/PbO2/PbSO4 electrode*, J Power Sources. 137 (2004) 288–308.
[113] D. Pavlov, I. Balkanov, *The PbO2 Particle: Exchange Reactions Between Ions of the Electrolyte and the PbO2 Particles of the Lead-Acid Battery Positive Active Mass*, J Electrochem Soc. 139 (1992) 1830–1835.
[114] J. P. Pohl, S. Atlung, *Gleichgewichtselektrodepotentiale von MeO2Hx(yH2O)-elektroden—I. Thermodynamik*, Electrochim Acta. 31 (1986) 391–397.
[115] S. Atlung, J. P. Pohl, *Gleichgewichtselektrodenpotentiale von MeO2Hx(yH2O) elektroden—II. Gleichgewichtseinstellung und pH-Abhänigigkeit des elektrodenpotentials*, Electrochim Acta. 31 (1986) 873–879.
[116] B. Bensmann, R. Hanke-Rauschenbach, E. Meissner, I. Koch, K. Sundmacher, *Model Simulation and Analysis of Proton Incorporation into the Positive Active Mass of a Lead/Acid Battery*, J Electrochem Soc. 157 (2010) A243–A253.
[117] D. Pavlov, B. Monahov, A. Kirchev, D. Valkovska, *Thermal runaway in VRLAB - Phenomena, reaction mechanisms and monitoring*, J Power Sources. 158 (2006) 689–704.
[118] D. Kordes, *Charakterisierung von Plusmassen aus Blei-Batterien durch Rontgenstrahlbeugung*, Chem Ing Tech. 38 (1966) 638–642.
[119] R. J. Ball, R. Kurian, R. Evans, R. Stevens, *Failure mechanisms in valve regulated lead/acid batteries for cyclic applications*, J Power Sources. 109 (2002) 189–202.
[120] I. M. Steele, J. J. Pluth, J. W. Richardson, *Progressive changes in positive active material over the lifetime of a lead–acid battery*, J Power Sources. 95 (2001) 79–84.
[121] T. G. Chang, D. M. Jochim, *Structural changes of active materials and failure mode of a valve-regulated lead-acid battery in rapid-charge and conventional-charge cycling*, J Power Sources. 91 (2000) 177–192.

[122] M.J. Weighall, *Techniques for jar formation of valve-regulated lead–acid batteries*, J Power Sources. 116 (2003) 219–231.
[123] V. H. Dodson, *Some Important Factors That Influence the Composition of the Positive Plate Material in the Lead-Acid Battery*, J Electrochem Soc. 108 (1961) 401–405.
[124] P. Ruetschi, J. Sklarchuk, R. T. Angstadt, *Stability and reactivity of lead oxides*, Electrochim Acta. 8 (1963) 333–342.
[125] V. Coroban, I. Boldea, F. Blaabjerg, *A novel on-line state-of-charge estimation algorithm for valve regulated lead-acid batteries used in hybrid electric vehicles*, in: IEEE, Bodrum, 2007: pp. 39–46.
[126] W. Waag, D. U. Sauer, *Adaptive estimation of the electromotive force of the lithium-ion battery after current interruption for an accurate state-of-charge and capacity determination*, Appl. Energy. 111 (2013) 416–427.
[127] C. Ehret, H. Laig-Hoerstebrock, L. Rauchfuss, *Process for the determination of the quiescent voltage of an storage battery*, 2005. https://www.google.com/patents/EP1589346A1?cl=en.
[128] H. Laig-Horstebrock, E. Meissner, *Method for predicting the equilibrated open-circuit voltage of an electrochemical energy store*, 2003. https://www.google.com/patents/US6653818.
[129] F.J. Vaccaro, J. Rhoades, R. Malley, B. Le, *Negative strap corrosion in valve-regulated lead acid batteries and its analysis by accelerated life testing*, in: INTELEC ’95, The Hague, Netherlands, 1995.
[130] Y. Yamaguchi, M. Shiota, Y. Nakayama, N. Hirai, S. Hara, *In situ analysis of electrochemical reactions at a lead surface in sulfuric acid solution*, J Power Sources. 85 (2000) 22–28.
[131] Y. Zeng, J. Hu, W. Ye, W. Zhao, G. Zhou, Y. Guo, *Investigation of lead dendrite growth in the formation of valveregulated lead-acid batteries for electric bicycle applications*, J Power Sources. 286 (2015) 182–192.
[132] T. Wada, T. Hirashima, *Progress in polyethylene separators for lead–acid batteries*, J Power Sources. 107 (2002) 201–210.
[133] R. D. Prengaman, *New low-antimony alloy for straps and cycling service in lead-acid batteries*, J Power Sources. 158 (2006) 1110–1116.
[134] M. Barak, *Electrochemical Power Sources*, Peter Peregrinus Ltd., Exeter, England, 1980.
[135] M.B. Read, J.H. Lang, A.H. Slocum, R. Martens, *Contact Resistance in Flat-on-Flat and Sphere-on-Flat Thin Films*, Proc. 56th Holm Conf. IEEE. (2010) 1–8.
[136] L.T. Lam, N.P. Haigh, C.G. Phyland, A.J. Urban, *Failure mode of valve-regulated lead-acid batteries under high-rate partial-state-of-charge operation*, J Power Sources. 133 (2004) 126–134.
[137] S. Mukherjee, *Applied Mineralogy: Applications in Industry and Environment*, Springer Science & Business Media, India, 2011.
[138] J.H. Yan, W.S. Li, Q.Y. Zhan, *Failure mechanism of valve-regulated lead–acid batteries under high-power cycling*, J Power Sources. 133 (2004) 135–140.
[139] E. Karden, *Dynamic Charge Acceptance (DCA) Test Method Development for EN 50342-6*, in: Würzburg, Germany, 2015.
[140] Hioki E.E. Corp., *Battery HiTESTER 3554*, Battery HiTESTER 3554. (2013). hioki.com/newproduct/3554/3554_e.html.

The student works listed below were guided during the research work for this thesis:

- A. BELEKE, *Parametrierungsmethodik für impedanzbasierte Modelle*, bachelor thesis, RWTH Aachen University, Institute for Power Electronics and Electrical Drives (ISEA), 2012.
- C. IRNICH, *Batterie-Zustandserkennung mit Hilfe des elektromagnetischen Feldes - am Beispiel der Bleibatterie*, master thesis, Institute for Power Electronics and Electrical Drives (ISEA), 2013.
- G. SEKULIC, *Untersuchung zur Ladezustandbestimmung anhand der Ruhespannung für Blei-Säure Starterbatterien*, seminar project, Institute for Power Electronics and Electrical Drives (ISEA), 2014.
- M. JANTOSCH, *Untersuchung zur Fehlererkennung für die Blei-Säure Starterbatterien*, master thesis, Institute for Power Electronics and Electrical Drives (ISEA), 2014.

9 Appendix

9.1 List of abbreviations

AC	alternative current
AGM	absorbent glass-mat
ASSF	automatic start and stop functionality
BDR	battery dynamic response
BER	brake energy regeneration
BMS	battery management system
BSD	battery state detection
BUT	battery under test
BVE	Butler-Volmer equation
CCA	cold cranking amps
CHA	charging
COC	closed oxygen cycle
COS	cast-on-straps
DCA	dynamic charge acceptance
DC	direct current
DCH	discharging
DLGCM	double-layer gel-crystal model
DoD	depths-of-discharge
EBS	electronic battery sensor
EEC	equivalent electrical circuit
EFB	enhanced flooded battery

EIS	electrochemical impedance spectroscopy
EMS	energy management system
EoL	end of life
ESP	electronic stability control
HOCVM	hybrid open-circuit voltage estimation model
HRPSoC	high-rate partial state-of-charge
ICE	internal combustion engine
IFD	internal failure detection
NAM	negative active material
OCVFIT	relaxation model based on equivalent electrical circuit approach with arbitrary number of RC elements
PAM	positive active material
PAU	rest period
PbA	lead-acid battery
PE	polyethylene
RLS	recursive least-square
PP	polypropylene
RIcxh	µHRSC test performed with macro short-circuit that will discharge contacted cell within 1, 3, 6 or 12 hours (x) as specified in text
RIcxd	µHRSC test performed with macro short-circuit that will discharge contacted cell within 1, 3, 7 or 14 days (x) as specified in text
RIRT	run-in relaxation test
ROTF	recursive online trend fitting
SCC	shifting of the characteristic curve
SCD	short-circuit detection
SCL	sudden capacity loss

SCL123	sudden capacity loss test with disconnecting three plats one by one with 2 days of testing in-between
SCL3	sudden capacity loss test with disconnecting three plates at once
SCTR	simplified calibration test for relaxation
SEM	scanning electron microscope
SLI	starting, lightning, ignition
SoF	state-of-function
SoF_{V1}	state-of-function related to a maximal cranking current
SoF_{V2}	state-of-function related to second part of cranking
SoC	normalized state-of-charge
SoC_{av}	available state-of-charge
$SoC_{av,noHi}$	available state-of-charge that distinguishes between capacity loss caused by various ageing phenomena
SoH	state-of-health related to available capacity
SoH_{Ri}	state-of-health related to current value of internal resistance
SRT	standardized relaxation test
TDA	tear-down analysis
TEM	transmission electron microscope
VAL	validation test for developed U00 estimation algorithms
VRLA	valve-regulated lead-acid battery
µH	micro-hybrid
µHRSC	micro-hybrid simplified test with parallel discharging of one cell with a emulated short-circuit resistance.

9.2 List of symbols

symbol	unit	description
a	[-]	empirical coefficient that corresponds to activation energy
a_{SCC}	[-]	constant slope of the approximation used by SCC algorithm
$a_{species}$	[-]	dimensionless chemical activity of a given species
b	[-]	Tafel slope
b_{SCC}	[V]	shifting coefficient of SCC algorithm
A	[m^2]	active surface area
A_{RC}	[V]	maximal voltage of RC element
$c_{Pb^{2+}}$	[mol·m^{-3}]	momentary concentration of the Pb^{2+} ions in the pores of the active material
$c_{SO_4^{2-}}$	[mol·m^{-3}]	momentary concentration of the SO_4^{2-} ions in the pores of the active material
$c^0_{Pb^{2+}}$	[mol·m^{-3}]	equilibrium concentration of the Pb^{2+} ions in the pores of the active material
$c^0_{SO_4^{2-}}$	[mol·m^{-3}]	equilibrium concentration of the SO_4^{2-} ions in the pores of the active material
C_N	[Ah]	rated capacity of SLI batteries obtained by discharging with I_{20} at 25°C until voltage limit of 10.5V
C_{dl}	[F]	double-layer capacity
$C_{dl,NAM}$	[F]	double-layer capacity of the negative electrode
$C_{dl,PAM}$	[F]	double-layer capacity of the positive electrode
$C_{eff,NAM}$	[F]	effective double-layer capacity of the negative electrode
C_{loss}	[-]	overall normalized capacity loss
C_{rem}	[Ah]	remaining capacity
E_0	[V]	concentration dependent potential of one cell that originates from Nernst equation
f_{inc}	[-]	increase function of a given parameter

F	[C·mol^{-1}]	Faraday constant that equals 96485
F_N	[N]	contact force
H	[MPa]	absolute hardness of the material
i	[A]	overall transient current rate
i_0	[A]	exchange current density
i_0'	[A·m^{-2}]	specific exchange current density
I_{20}	[A]	twenty-hour current rate that equals $C_N/20$ (nominal current in case of SLI batteries)
I_{batt}	[A]	battery current rate (negative value denotes discharging and positive value symbolizes charging)
$I_{crank,max}$	[A]	maximal current rate during cranking
I_{dc}	[A]	direct current rate
I_{gas}	[A]	part of the battery current that is consumed by water electrolysis
$I_{quiescent}$	[mA]	quiescent current rate
I_{SC}	[A]	short-circuit current rate
k	[-]	proportional factor used for online fitting of the OCVFIT relaxation model
L	[H]	inductance
m	[mol·kg^{-1}]	molality
m_{H2O}	[g]	mass of water
m_{slope}	[-]	steepness
M_{H2O}	[g·mol^{-1}]	molar mass of water that equals 18
n	[-]	number of electrons involved into electrochemical reaction
n_{plates}	[-]	number of plates in one stack
n_{RC}	[-]	estimated number of RC elements
Q_{cha}	[% DoD]	overall discharged or charged amp-hours before the beginning of relaxation (rest period).

Q_{dch}	[% DoD]	overall discharged amp-hours during relaxation (rest period).
Q_{gas}	[C]	energy consumed by water electrolysis
R	[J·mol^{-1}·K^{-1}]	universal gas constant that equals 8.314
R_{ct}	[Ω]	charge-transfer resistance
R_{con}	[Ω]	sum of the concentration related diffusion, migration, convection and chemical reaction resistances
$R_{constriction}$	[Ω]	constriction resistance
R_{COS}	[Ω]	resistance of the cast-on-straps
$R_{ct,NAM}$	[Ω]	charge-transfer resistance of the negative electrode
$R_{ct,PAM}$	[Ω]	charge-transfer resistance of the positive electrode
$R_{dynamic}$	[Ω]	dynamic internal resistance
R_{film}	[Ω]	resistance of the pollution film
R_{i}	[Ω]	generalized internal resistance
R_{large}	[Ω]	large-signal resistance
R_{lug}	[Ω]	resistance of the lug
R_{ohmic}	[Ω]	ohmic internal resistance
R_{path}	[Ω]	resistance of the current conducting path
R_{PbO2}	[Ω]	resistance of the lead dioxide
R_{PbSO4}	[Ω]	resistance of the lead sulfate
R_{SC}	[Ω]	overall short-circuit resistance
R_{small}	[Ω]	small-signal resistance
$R_{soft,i}$	[Ω]	resistance of *i*-th soft hydrated layer represented as a RC element
$t_{full\ discharge}$	[h]	full discharge time employing short-circuit current without concerning current dependency of available capacity
t_{relax}	[h]	overall duration of relaxation (it is assumed as completed at $U_{batt} = U_{00,ref} + 11mV$)

$t_{relax,ini}$	[h]	standardized initial value of t_{relax} referring to 90% SoC, 25°C and Q_{cha} = 1% DoD
T	[K]	temperature
T_{batt}	[K]	internal temperature of the battery
T_{pole}	[K]	temperature of the battery measured on the negative pole
U_{00}	[V]	fully equilibrated open-circuit voltage of 12V block
$U_{00,ref}$	[V]	reference open-circuit voltage of 12V block
U_{batt}	[V]	battery terminal voltage
U_{crank}	[V]	minimal voltage during cranking
U_{error}	[V]	voltage error
U_i	[V]	potential of *i*-th level of the electrode (bottom, middle, upper) considering vertical distribution
U_{neg}	[V]	potential of the negative electrode
U_{pos}	[V]	potential of the positive electrode
U_T	[V]	temperature voltage
x	[-]	distortion factor of PbO_2 according to the formula $PbO_{2-x}(OH)_y$
y	[-]	distortion factor of PbO_2 according to the formula $PbO_{2-x}(OH)_y$
$\underline{Z}_w$	[Ω]	Warburg impedance
α	[-]	symmetry coefficient
$\gamma_{Pb^{2+}}$	[-]	empirical coefficient for Pb^{2+} concentration term used for the calculation of the concentration related effects within Butler-Volmer equation
$\gamma_{SO_4^{2-}}$	[-]	empirical coefficient for SO_4^{2-} concentration term used for the calculation of the concentration related effects within Butler-Volmer equation
δ	[-]	distortion factor of PbO_2 according to the formula $PbO_{2-\delta}$
ε	[V]	electrode potential

η	[V]	overvoltage
η_{act}	[V]	activation overvoltage
$\eta_{act,NAM}$	[V]	activation overvoltage of the negative electrode
$\eta_{act,PAM}$	[V]	activation overvoltage of the positive electrode
η_{con}	[V]	sum of the concentration related diffusion, migration, convection and chemical reaction overvoltage
η_{cry}	[V]	sum of crystallization and nucleation overvoltage
η_{ohmic}	[V]	ohmic overvoltage
η_{relax}	[V]	sum of the η_{solid} and residual η_{con} during rest periods with charging short-term history
η_{SD}	[V]	voltage drop caused by self-discharge
η_{solid}	[V]	additional structural overvoltage appearing during rest periods with charging short-term history
η_{strat}	[V]	additional overvoltage caused by acid stratification (global vertical concentration gradient)
ξ_i	[-]	depression factor of *i*-th semicircle
ρ	[Ωm]	specific electrical conductivity
ρ_{acid}	[$kg \cdot l^{-1}$]	acid density of the electrolyte
$\rho_{acid,i}$	[$kg \cdot l^{-1}$]	acid density of electrolyte that is located on the *i*-th level (bottom, middle, upper) considering vertical distribution
τ	[s]	time constant
τ_{RC}	[h]	time constant of RC element
$\tau_{soft,i}$	[h]	time constant of *i*-th soft hydrated layer represented as a RC element

9.3 Battery testing protocols

9.3.1 Validation of Butler-Volmer Equation based approach with pulse tests

Step no.	procedure	setpoint	limit	comments
1	Charge	Setting climate chamber to 25°C, $5I_{20}$ or 16.0 V (flooded design) 14.7 V (AGM design)	24h or 120 % C_N	Full charging at 25°C (battery should be conditioned to at least room temperature)
2	Discharge	I_{20}	2h or 10.5 V	Discharge to 90% SoC
3	Rest period	-	1h	-
4	Ri test	1 kHz with max. 2 A or 18 mV	-	Measurement of AC internal resistance (R_{ohmic})
5	Rest period	-	1h	Short-term history with rest period
6	Discharge	200 A	100ms	Validation pulse with 200 A
7	Rest period	-	1s	-
8	Discharge	I_{20}	1h or 10.5 V	-
9	Charge	I_{20} or 16.0 V (flooded design) 14.7 V (AGM design)	5 % C_N	Short-term history with charging
10	Rest period	-	1s	-
11	Discharge	200 A	100ms	Validation pulse with 200 A

Step no.	procedure	setpoint	limit	comments
12	Rest period	-	1s	-
13	Charge	I_{20} or 16.0 V (flooded design) 14.7 V (AGM design)	5 % C_N	-
14	Discharge	I_{20}	1h or 10.5 V	Short-term history with discharging
15	Rest period	-	1s	-
16	Discharge	200 A	100ms	Validation pulse with 200 A
17	Rest period	-	1h	Short-term history with rest period
18	Discharge	700 A	100ms	Validation pulse with 700 A
19	Rest period	-	1s	
20	Discharge	I_{20}	1h or 10.5 V	-
21	Charge	I_{20} or 16.0 V (flooded design) 14.7 V (AGM design)	5 % C_N	Short-term history with charging
22	Rest period	-	1s	-
23	Discharge	700 A	100ms	Validation pulse with 700 A
24	Rest period	-	1s	-
25	Charge	I_{20} or 16.0 V (flooded design) 14.7 V (AGM design)	5 % C_N	-

Step no.	procedure	setpoint	limit	comments
26	Discharge	I_{20} or 10.5 V	1h	Short-term history with discharging
27	Rest period	-	1s	-
28	Discharge	700 A	100ms	Validation pulse with 700 A
29	Rest period	-	1s	-
30	Discharge	I_{20}	4h or 10.5 V	Discharge to 70% SoC
31	Repetition of the steps 3-30	1	-	-
32	Discharge	I_{20}	6h or 10.5 V	Discharge to 40% SoC (only for test at 25 and 0°C, otherwise steps 32-35 are skipped)
33	Repetition of the steps 3-30	1	-	-
34	Discharge	I_{20}	4h or 10.5 V	Discharge to 20% SoC (only for test at -20°C, otherwise steps 34-35 are skipped)
35	Repetition of the steps 3-30	1	-	-
36	Charge	Setting climate chamber to 25°C, $5I_{20}$ or 16.0 V (flooded design) 14.7 V (AGM design)	24h	Full charging at 25°C

Step no.	procedure	setpoint	limit	comments
37	Rest period	Setting climate chamber to 0°C	18h	Temperature setup
38	Repetition of the steps 2-36	1	-	-
39	Rest period	Setting climate chamber to -20°C	18h	Temperature setup
40	Repetition of the steps 2-36	1	-	-
41	End of test			

Table XIII. Detailed specification of the testing protocol used for pulse validation test for developed Butler-Volmer Equation based approach. Covered temperatures are 25, 0 and -20 °C. Covered SoC are 90, 70, 40 and 20%.

9.3.2 Validation of Butler-Volmer Equation based approach with synthetic driving profile

Step no.	procedure	setpoint	limit	comments
1	Rest periods	Setting climate chamber to 25°C	18h	-
2	Discharge	I_{20}	25h or 10.5 V	Capacity test
3	Charge	$5I_{20}$ or 16.0 V (flooded design) 14.7 V (AGM design)	24h	Full charging at 25°C
4	Repetition of the steps 2-3	2	-	Carried out only for the brand-new batteries (which were not cycled before), otherwise only step 2 and 4 should be skipped
5	Rest periods	Setting climate chamber to a target temperature	18h	-
6	Discharge	I_{20}	5h or 10.5 V	Discharge to 75% SoC (55% or 35% SoC with 9h and 13h of discharge respectively)
7	Charge	I_{20} or 16.0 V (flooded design) 14.7 V (AGM design)	5% C_N	Charge to 80% SoC (charge short-term history)
8	Rest period	-	10h	-
9	Ri test	1 kHz with max. 2 A or 18 mV	-	Measurement of AC internal resistance (R_{ohmic})

Step no.	procedure	setpoint	limit	comments
10	Rest period	-	1min	-
11	Discharge	50mA	10h	Rest period with key-off load
12	Rest period	-	10min	-
13	Ri test	1 kHz with max. 2 A or 18 mV	-	Measurement of AC internal resistance (R_{ohmic})
14	Rest period	-	1min	-
15	Discharge	$2I_{20}$	10sec.	-
16	Discharge	Max. current of the testbench	1s	Emulation of cranking
17	Charge	$20I_{20}$ or 14.5 V (flooded and AGM batteries)	5min.	Emulation of the field-oriented alternator charging
18	Discharge	$4I_{20}$	1min	Emulation of discharging during stop phase
19	Discharge	Max. current of the testbench	1s	Emulation of cranking
20	Charge	$20I_{20}$ or 14.5 V (flooded and AGM batteries)	5min.	Emulation of the field-oriented alternator charging
21	Repetition of the steps 18-20	4	-	Emulation of driving with ASSF and BER
22	Rest period	-	10min	-
23	Ri test	1 kHz with max. 2 A or 18 mV	-	Measurement of AC internal resistance (R_{ohmic})

Step no.	procedure	setpoint	limit	comments
24	Rest period	-	1min	-
25	Discharge	50mA	5.5h	Rest period with key-off load
26	Repetition of steps 13-25	3	-	one day of usage (2h of driving and 22h of rest period with key-off load)
27	Rest period	-	10min	-
28	Ri test	1 kHz with max. 2 A or 18 mV	-	Measurement of AC internal resistance (R_{ohmic})
29	Rest period	-	1min	-
30	Discharge	$2I_{20}$	10sec.	-
31	Discharge	Max. current of the testbench	1s	Emulation of cranking
32	Charge	$20I_{20}$ or 14.5 V (flooded and AGM batteries)	8h.	Emulation of the long freeway driving phase
33	Rest period	-	10min	-
34	Ri test	1 kHz with max. 2 A or 18 mV	-	Measurement of AC internal resistance (R_{ohmic})
35	Rest period	-	1min	-
36	Repetition of the steps 18-20	6	-	Emulation of driving with ASSF and BER
37	Rest period	-	10min	-

Step no.	procedure	setpoint	limit	comments
38	Ri test	1 kHz with max. 2 A or 18 mV	-	Measurement of AC internal resistance (R_{ohmic})
39	Rest period	-	1min	-
40	Discharge	50mA	100h	Rest period with key-off load
41	Rest period	-	10min	-
42	Ri test	1 kHz with max. 2 A or 18 mV	-	Measurement of AC internal resistance (R_{ohmic})
43	Rest period	-	1min	Beginning of driving with various current rates
44	Discharge	$2I_{20}$	10sec.	
45	Discharge	Max. current of the testbench	1s	Emulation of cranking
46	Charge	$40I_{20}$ or 14.5 V (flooded and AGM batteries)	5min.	Emulation of the field-oriented alternator charging
47	Discharge	80 A	1min	-
48	Discharge	Max. current of the testbench	1s	Emulation of cranking
49	Charge	$20I_{20}$ or 14.5 V (flooded and AGM batteries)	5min.	Emulation of the field-oriented alternator charging
50	Discharge	60 A	1min	-
51	Discharge	Max. current of the testbench	1s	Emulation of cranking

Step no.	procedure	setpoint	limit	comments
52	Charge	$10I_{20}$ or 14.5 V (flooded and AGM batteries)	5min.	Emulation of the field-oriented alternator charging
53	Discharge	50 A	1min	-
54	Discharge	Max. current of the testbench	1s	Emulation of cranking
55	Charge	$4I_{20}$ or 14.5 V (flooded and AGM batteries)	5min.	Emulation of the field-oriented alternator charging
56	Discharge	40 A	1min	-
57	Discharge	Max. current of the testbench	1s	Emulation of cranking
58	Charge	$8I_{20}$ or 14.5 V (flooded and AGM batteries)	5min.	Emulation of the field-oriented alternator charging
59	Discharge	20 A	1min	-
60	Discharge	Max. current of the testbench	1s	Emulation of cranking
61	Charge	$30I_{20}$ or 14.5 V (flooded and AGM batteries)	5min.	Emulation of the field-oriented alternator charging
62	Discharge	10 A	1min	-
63	Discharge	Max. current of the testbench	1s	Emulation of cranking
64	Charge	$20I_{20}$ or 14.5 V (flooded and AGM batteries)	5min.	Emulation of the field-oriented alternator charging

Step no.	procedure	setpoint	limit	comments
65	Rest period	-	10min	-
66	Ri test	1 kHz with max. 2 A or 18 mV	-	Measurement of AC internal resistance (R_{ohmic})
67	Rest period	-	1min	-
68	Discharge	50mA	5.5h	Rest period with key-off load
69	Repetition of the steps 37-68	3	-	Third day of the profile
70	Rest period	-	10min	-
71	Ri test	1 kHz with max. 2 A or 18 mV	-	Measurement of AC internal resistance (R_{ohmic})
72	Rest period	-	1min	Beginning of driving with various current rates
73	Discharge	$2I_{20}$	10sec.	
74	Discharge	Max. current of the testbench	1s	Emulation of cranking
75	Charge	$40I_{20}$ or 14.5 V (flooded and AGM batteries)	5min.	Emulation of the field-oriented alternator charging
76	Discharge	$20I_{20}$	1min	-

Step no.	procedure	setpoint	limit	comments
77	Discharge	Max. current of the testbench	1s	Emulation of cranking
78	Charge	$20I_{20}$ or 14.5 V (flooded and AGM batteries)	5min.	Emulation of the field-oriented alternator charging
79	Discharge	$15I_{20}$	1min	-
80	Discharge	Max. current of the testbench	1s	Emulation of cranking
81	Charge	$10I_{20}$ or 14.5 V (flooded and AGM batteries)	5min.	Emulation of the field-oriented alternator charging
82	Discharge	$12I_{20}$	1min	-
83	Discharge	Max. current of the testbench	1s	Emulation of cranking
84	Charge	$4I_{20}$ or 14.5 V (flooded and AGM batteries)	5min.	Emulation of the field-oriented alternator charging
85	Discharge	$10I_{20}$	1min	-
86	Discharge	Max. current of the testbench	1s	Emulation of cranking
87	Charge	$8I_{20}$ or 14.5 V (flooded and AGM batteries)	5min.	Emulation of the field-oriented alternator charging
88	Discharge	$8I_{20}$	1min	-
89	Discharge	Max. current of the testbench	1s	Emulation of cranking

Step no.	procedure	setpoint	limit	comments
90	Charge	$30I_{20}$ or 14.5 V (flooded and AGM batteries)	5min.	Emulation of the field-oriented alternator charging
91	Discharge	$6I_{20}$	1min	-
92	Discharge	Max. current of the testbench	1s	Emulation of cranking
93	Charge	$20I_{20}$ or 14.5 V (flooded and AGM batteries)	5min.	Emulation of the field-oriented alternator charging
94	Rest period	-	10min	-
95	Ri test	1 kHz with max. 2 A or 18 mV	-	Measurement of AC internal resistance (R_{ohmic})
96	Rest period	-	1min	-
97	Discharge	50mA	5.5h	Rest period with key-off load
98	Repetition of the steps 70-97	3	-	Fouth day of the profile
99	Rest period	-	10min	-
100	Ri test	1 kHz with max. 2 A or 18 mV	-	Measurement of AC internal resistance (R_{ohmic})
101	Rest period	-	1min	-
102	Discharge	50mA	10h	Rest period with key-off load

Step no.	procedure	setpoint	limit	comments
103	Rest period	-	10min	-
104	Ri test	1 kHz with max. 2 A or 18 mV	-	Measurement of AC internal resistance (R_{ohmic})
105	Rest period	-	1min	-
106	Discharge	$2I_{20}$	10sec.	-
107	Discharge	Max. current of the testbench	1s	Emulation of cranking
108	Charge	$20I_{20}$ or 14.5 V (flooded and AGM batteries)	5min.	Emulation of the field-oriented alternator charging
109	Repetition of the steps 18-20	5	-	Emulation of driving with ASSF and BER
110	Rest period	-	10min	-
111	Ri test	1 kHz with max. 2 A or 18 mV	-	Measurement of AC internal resistance (R_{ohmic})
112	Rest period	-	1min	-
113	Discharge	$6I_{20}$	30min or 10.5 V	-
114	Rest period	-	10min	-
115	Ri test	1 kHz with max. 2 A or 18 mV	-	Measurement of AC internal resistance (R_{ohmic})

Step no.	procedure	setpoint	limit	comments
116	Rest period	-	1min	-
117	Discharge	Max. current of the testbench	1s	Emulation of cranking
118	Discharge	$3I_{20}$	1h or 10.5 V	-
119	Rest period	-	10min	-
120	Ri test	1 kHz with max. 2 A or 18 mV	-	Measurement of AC internal resistance (R_{ohmic})
121	Rest period	-	1min	-
122	Discharge	Max. current of the testbench divided by 2	1s	Emulation of cranking
123	Discharge	$1.5I_{20}$	30min or 10.5 V	-
124	Rest period	-	10min	-
125	Ri test	1 kHz with max. 2 A or 18 mV	-	Measurement of AC internal resistance (R_{ohmic})
126	Rest period	-	1min	-
127	Discharge	Max. current of the testbench divided by 4	1s	Emulation of cranking
128	Rest period	-	10min	-
129	Ri test	1 kHz with max. 2 A or 18 mV	-	Measurement of AC internal resistance (R_{ohmic})

Step no.	procedure	setpoint	limit	comments
130	Rest period	-	1min	-
131	Discharge	$2I_{20}$	10sec.	-
132	Discharge	Max. current of the testbench	1s	Emulation of cranking
133	Charge	$20I_{20}$ or 14.5 V (flooded and AGM batteries)	5min.	Emulation of the field-oriented alternator charging
134	Repetition of the steps 18-20	5	-	Emulation of driving with ASSF and BER
135	Rest period	-	10min	-
136	Ri test	1 kHz with max. 2 A or 18 mV	-	Measurement of AC internal resistance (R_{ohmic})
137	Rest period	-	1min	-
138	Charge	Setting climate chamber to 25°C, $5I_{20}$ or 16.0 V (flooded design) 14.7 V (AGM design)	24h	Full charging at 25°C
139	End of test			

Table XIV. Detailed specification of the testing protocol used for validation test with synthetic driving profile for developed Butler-Volmer Equation based approach. Covered working points have been listed in Table IV.

9.3.3 Standardized relaxation test

Step no.	procedure	setpoint	limit	comments
1	Charge	Setting climate chamber to 25°C, $5I_{20}$ or 16.0 V (flooded design) 14.7 V (AGM design)	24h or 120 % C_N	Full charging at 25°C (battery should be conditioned to at least room temperature)
2	Rest period	25 °C (55 °C)	48h	SoC >= 70% (SoC < 70%)
3	Rest period	Setting climate chamber to the target temperature	18h	-
4	Discharge	I_{20}	2h or 10.5V	Discharging to 90% SoC or other target SoC (additional 2h of discharging per 10% SoC)
5	Rest period	-	4h (standard flooded battery at 25°C)	Obtaining reference U_{00}, this time strongly depends on the temperature and battery technology
6	Discharge	key-off load	3h	Additional rest period with key-off load is needed to get reference U_{00} with additional overvoltage (this step is skipped if the test does not consider the impact of key-off load)
7	Discharge	I_{20}	1% C_N	

Step no.	**procedure**	**setpoint**	**limit**	**comments**
8	Charge	$5I_{20}$ or 16.0 V (flooded design) 14.7 V (AGM design)	1% C_N	Imposing a given charge short-term history Q_{cha} (in this case 1% C_N)
9	Rest period	given key-off load (or no key-off load)	U_{batt} <= U_{00}+11mV	
10	Further steps	-	-	e.g. discharging to lower SoCs or imposing different value of Q_{cha}

Table XV. Detailed specification of the testing protocol used for standardized relaxation test

9.4 Laboratory tests

no.	battery	T [°C]	Q_{cha} [% DoD]	SoC [%]	$I_{quiescent}$ [mA]	state
1	60 Ah EFB	25	4.5	95	20	aged
2	60 Ah EFB	25	5.2	90	20	aged
3	60 Ah EFB	25	5.8	85	33	aged
4	60 Ah EFB	25	6.9	82	33	aged
5	60 Ah EFB	25	8.4	80	47	aged
6	60 Ah EFB	25	8.4	77	47	aged
7	95 Ah flooded	25	4.8	95	26	new, stationary state
8	95 Ah flooded	25	5.3	90	26	new, stationary state
9	95 Ah flooded	25	5.8	86	34	new, stationary state
10	95 Ah flooded	25	6.3	82	34	new, stationary state
11	95 Ah flooded	25	7.7	79	45	new, stationary state
12	95 Ah flooded	25	7.8	77	45	new, stationary state
13	60 Ah AGM	15	2.6	93	21	new, stationary state
14	60 Ah AGM	15	3.8	86	21	new, stationary state
15	60 Ah AGM	15	4.8	81	39	new, stationary state
16	60 Ah AGM	15	5.7	76	39	new, stationary state
17	60 Ah AGM	15	7	72	49	new, stationary state
18	60 Ah AGM	15	8	70	49	new, stationary state
19	74 Ah flooded	15	2.7	93	21	new, stationary state
20	74 Ah flooded	15	3.8	86	21	new, stationary state
21	74 Ah flooded	15	4.9	81	39	new, stationary state
22	74 Ah flooded	15	6.1	77	39	new, stationary state
23	74 Ah flooded	15	7	73	49	new, stationary state
24	74 Ah flooded	15	8.3	71	49	new, stationary state
25	60 Ah AGM	-5	0.8	91	20	new, stationary state
26	60 Ah AGM	-5	1.2	82	20	new, stationary state
27	60 Ah AGM	-5	1.3	77	39	new, stationary state
28	60 Ah AGM	-5	1.5	73	39	new, stationary state
29	60 Ah AGM	-5	1.7	69	49	new, stationary state
30	60 Ah AGM	-5	2.2	66	49	new, stationary state
31	60 Ah EFB	-5	1	91	23	aged
32	60 Ah EFB	-5	1.4	82	23	aged

33	60 Ah EFB	-5	1.5	78	34	aged
34	60 Ah EFB	-5	1.7	74	34	aged
35	60 Ah EFB	-5	2.4	71	49	aged
36	60 Ah EFB	-5	2.5	68	49	aged
37	74 Ah flooded	-5	1.1	91	27	new, stationary state
38	74 Ah flooded	-5	2	83	27	new, stationary state
39	74 Ah flooded	-5	1.7	79	37	new, stationary state
40	74 Ah flooded	-5	1.9	75	37	new, stationary state
41	74 Ah flooded	-5	2.6	72	47	new, stationary state
42	74 Ah flooded	-5	2.9	70	47	new, stationary state
43	95 Ah flooded	-5	0.9	91	23	new, stationary state
44	95 Ah flooded	-5	1.4	82	23	new, stationary state
45	95 Ah flooded	-5	1.4	78	31	new, stationary state
46	95 Ah flooded	-5	2.4	75	31	new, stationary state
47	95 Ah flooded	-5	1.9	72	45	new, stationary state
48	95 Ah flooded	-5	2.1	69	45	new, stationary state
49	60 Ah EFB	-18	0.3	90	27	aged
50	60 Ah EFB	-18	0.6	85	27	aged
51	60 Ah EFB	-18	0.4	83	37	aged
52	60 Ah EFB	-18	0.5	80	37	aged
53	60 Ah EFB	-18	0.6	77	47	aged
54	60 Ah EFB	-18	0.8	75	47	aged
55	95 Ah flooded	-18	0.3	90	24	new, stationary state
56	95 Ah flooded	-18	0.4	85	24	new, stationary state
57	95 Ah flooded	-18	0.4	82	34	new, stationary state
58	95 Ah flooded	-18	0.5	80	34	new, stationary state
59	95 Ah flooded	-18	0.6	78	44	new, stationary state
60	95 Ah flooded	-18	0.5	75	44	new, stationary state

Table XVI. Specification of all relaxation curves recorded during VAL testing and used for validation of the developed U_{00} estimation algorithms.

10 Curriculum Vitae

Personal Details:

Name	Grzegorz Piłatowicz
Date of birth	28.05.1986
Place of birth	Warsaw, Poland
Address	Chemin des Vassaux 6A, 1297 Founex, Suisse
	grzegorz.pilatowicz@rwth-aachen.de
Civil status	single

School education

2002 - 2005	XXII high school in Warsaw, Poland, degree: high-school diploma

University education

09/2005 - 09/2010	M.Sc.Eng. Electrical Engineering, Warsaw University of Technology, Major: Control and Computer Engineering
10/2009 – 09/2010	ERASMUS student exchange programme at RWTH Aachen University

Internships and student jobs

07/2008 - 09/2009	Student project work in Vattenfall Heat Poland (currently PGNiG Termika), Warsaw, Poland
03/2010 - 09/2010	Master thesis at E.ON ERC, Institute for Automation of Complex Power Systems, RWTH Aachen University

Work experience

10/2010 - 10/2015	Researcher Electrochemical Energy Conversion and Storage Systems, Institute for Power Electronics and Electrical Drives, RWTH Aachen University
01/2013 - 10/2015	Team leader of lead-acid battery research group, Institute for Power Electronics and Electrical Drives, RWTH Aachen University
10/2015 – 09/2016	Senior Engineer for battery storage systems, BatterieIngenieure GmbH
Since 10/2016	Technical Expert (Battery Management Systems), LEM Switzerland SA

Founex, September the 9th, 2017

ABISEA Band 1
Eßer, A.
Berührungslose, kombinierte Energie- und Informations-übertragung für bewegliche Systeme
1. Auflage 1992, 130 Seiten
ISBN 3-86073-046-0

ABISEA Band 2
Vogel, U.
Entwurf und Beurteilung von Verfahren zur Hochausnutzung des Rad-Schiene-Kraftschlusses durch Triebfahrzeuge
1. Auflage 1992, 130 Seiten
ISBN 3-86073-060-6

ABISEA Band 3
Redehorn, Th.
Stromeinprägendes Antriebssystem mit fremderregter Synchron-maschine
1. Auflage 1992, 130 Seiten
ISBN 3-86073-061-4

ABISEA Band 4
Ackva, A.
Spannungseinprägendes Antriebssystem mit Synchron-maschine und direkter Stromregelung
1. Auflage 1992, 135 Seiten
ISBN 3-86073-062-2

ABISEA Band 5
Mertens, A.
Analyse des Oberschwingungsverhaltens von taktsynchronen Delta - Modulationsverfahren zur Steuerung von Pulsstromrichtern bei hoher Taktzahl
1. Auflage 1992, 170 Seiten
ISBN 3-86073-069-X

ABISEA Band 6
Geuer, W.
Untersuchungen über das Alterungsverhalten von Bleiakkumulatoren
1. Auflage 1993, 100 Seiten
ISBN 3-86073-097-5

ABISEA Band 7
Langheim, J.
Einzelradantrieb für Elektrostraßenfahrzeuge
1. Auflage 1993, 215 Seiten
ISBN 3-86073-123-8
(vergriffen)

ABISEA Band 8
Fetz, J.
Fehlertolerante Regelung eines Asynchron-Doppelantriebes für ein Elektrospeicherfahrzeug
1. Auflage 1993, 136 Seiten
ISBN 3-86073-124-6
(vergriffen)

ABISEA Band 9
Schülting, L.
Optimierte Auslegung induktiver Bauelemente für den Mittelfrequenzbereich
1. Auflage 1993, 136 Seiten
ISBN 3-86073-174-2
(vergriffen)

ABISEA Band 10
Skudelny, H.-Ch.
Stromrichtertechnik
4. Auflage 1997, 259 Seiten
ISBN 3-86073-189-0

ABISEA Band 11
Skudelny, Ch.
Elektrische Antriebe
3. Auflage 1997, 124 Seiten
ISBN 3-86073-231-5

ABISEA Band 12
Schöpe, F.
Batterie-Management für Nickel-Cadmium Akkumulatoren
1. Auflage 1994, 156 Seiten
ISBN 3-86073-232-3
(vergriffen)

ABISEA Band 13
v. d. Weem, J.
Schmalbandige aktive Filter für Schienentriebfahrzeuge am Gleichspannungs-fahrdraht
1. Auflage 1995, 125 Seiten
ISBN 3-86073-233-1

ABISEA Band 14
Backhaus, K.
Spannungseinprägendes Direktantriebssystem mit schnelllaufender geschalteter Reluktanzmaschine
1. Auflage 1995, 156 Seiten
ISBN 3-86073-234-X
(vergriffen)

ABISEA Band 15
Reinold, H.
Optimierung dreiphasiger Pulsdauermodulations-verfahren
1. Auflage 1996, 116 Seiten
ISBN 3-86073-235-8

ABISEA Band 16
Köpken, H.-G.
Regelverfahren für Parallelschwingkreis-umrichter
1. Auflage 1996, 125 Seiten
ISBN 3-86073-236-6

ABISEA Band 17
Mauracher, P.
Modellbildung und Verbundoptimierung bei Elektrostraßenfahrzeugen
1. Auflage 1996, 192 Seiten
ISBN 3-86073-237-4

ABISEA Band 18
Protiwa, F.-F.
Vergleich dreiphasiger Resonanz-Wechselrichter in Simulation und Messung
1. Auflage 1997, 178 Seiten
ISBN 3-86073-238-2

ABISEA Band 19
Brockmeyer, A.
Dimensionierungswerkzeug für magnetische Bau-elemente in Stromrichter-anwendungen
1. Auflage 1997, 182 Seiten
ISBN 3-86073-239-0

ABISEA Band 20
Apeldoorn, 0.
Simulationsgestützte Bewer-tung von Steuerverfahren für netzgeführte Stromrichter mit verringerter Netzrück-wirkung
1. Auflage 1997, 132 Seiten
ISBN 3-86073-680-9

ABISEA Band 21
Lohner, A.
Batteriemanagement für verschlossene Blei-Batterien am Beispiel von Unterbrechungsfreien Stromversorgungen
1. Auflage 1998, 144 Seiten
ISBN 3-86073-681-7

ABISEA Band 22
Reinert, J.
Optimierung der Betriebseigenschaften von Antrieben mit geschalteter Reluktanzmaschine
1. Auflage 1998, 168 Seiten
ISBN 3-86073-682-5

ABISEA Band 23
Nagel, A.
Leitungsgebundene Störungen in der Leistungselektronik: Entstehung, Ausbreitung und Filterung
1. Auflage 1999, 160 Seiten
ISBN 3-86073-683-3

ABISEA Band 24
Menne, M.
Drehschwingungen im Antriebsstrang von Elektrostraßenfahrzeugen - Analyse und aktive Dämpfung
1. Auflage 2001, 192 Seiten
ISBN 3-86073-684-1

ABISEA Band 25
von Bloh, J.
Multilevel-Umrichter zum Einsatz in Mittelspannungs-Gleichspannungs-Übertragungen
1. Auflage 2001, 152 Seiten
ISBN 3-86073-685-X

ABISEA Band 26
Karden, E.
Using low-frequency impedance spectroscopy for characterization, monitoring, and modeling of industrial batteries
1. Auflage 2002, 154 Seiten
ISBN 3-8265-9766-4

ABISEA Band 27
Karipidis, C.-U.
A Versatile DSP/ FPGA Structure optimized for Rapid Prototyping and Digital Real-Time Simulation of Power Electronic and Electrical Drive Systems
1. Auflage 2001, 164 Seiten
ISBN 3-8265-9738-9

ABISEA Band 28
Kahlen, K.
Regelungsstrategien für permanentmagnetische Direktantriebe mit mehreren Freiheitsgraden
1. Auflage 2003, 158 Seiten
ISBN 3-8322-1222-1

ABISEA Band 29
Inderka, R.
Direkte Drehmomentregelung Geschalteter Reluktanzantriebe
1. Auflage 2003, 190 Seiten
ISBN 3-8322-1175-6

ABISEA Band 30
Schröder, S.
Circuit-Simulation Models of High-Power Devices Based on Semiconductor Physics
1. Auflage 2003, 124 Seiten
ISBN 3-8322-1250-7

ABISEA Band 31
Buller, S.
Impedance-Based Simulation Models for Energy Storage Devices in Advanced Automotive Power Systems
1. Auflage 2003, 136 Seiten
ISBN 3-8322-1225-6

ABISEA Band 32
Schönknecht, A.
Topologien und Regelungsstrategien für das induktive Erwärmen mit hohen Frequenz-Leistungsprodukten
1. Auflage 2004, 1 70 Seiten
ISBN 3-8322-2408-4

ABISEA Band 33
Tolle, T.
Konvertertopologien für ein aufwandsarmes, zweistufiges Schaltnetzteil zum Laden von Batterien aus dem Netz
1. Auflage 2004, 150 Seiten
ISBN 3-8322-2676-1

ABISEA Band 34
Götting, G.
Dynamische Antriebsregelung von Elektrostraßenfahrzeugen unter Berücksichtigung eines schwingungsfähigen Antriebsstrangs
1. Auflage 2004, 166 Seiten
ISBN 3-8322-2804-7

ABISEA Band 35
Dieckerhoff, S.
Transformatorlose Stromrichterschaltungen für Bahnfahrzeuge am 16 2/3Hz Netz
1. Auflage 2004, 158 Seiten
ISBN 3-8322-3094-7

ABISEA Band 36
Hu, J.
Bewertung von DC-DC-Topologien und Optimierung eines DC-DC-Leistungsmoduls für das 42-V-Kfz-Bordnetz
1. Auflage 2004, 156 Seiten
ISBN 3-8322-3201-X

ABISEA Band 37
Detjen, D.-0.
Characterization and Modeling of Si-Si Bonded Hydrophobie Interfaces for Novel High-Power BIMOS Devices
1. Auflage 2004, 146 Seiten
ISBN 3-8322-2963-9

ABISEA Band 38
Walter, J.
Simulationsbasierte Zuverlässigkeitsanalyse in der modernen Leistungselektronik
1. Auflage 2004, 134 Seiten
ISBN 3-8322-3481-0

ABISEA Band 39
Schwarzer, U.
IGBT versus GCT in der Mittelspannungsanwendung - ein experimenteller und simulativer Vergleich
1. Auflage 2005, 184 Seiten
ISBN 3-8322-4489-1

ABISEA Band 40
Bartram, M.
IGBT-Umrichtersysteme für Windkraftanlagen: Analyse der Zyklenbelastung, Modellbildung, Optimierung und Lebensdauervorhersage
1. Auflage 2006, 195 Seiten
ISBN 3-8322-5039-5

ABISEA Band 41
Ponnaluri, S.
Generalized Design, Analysis and Control of Grid side converters with integrated UPS or Islanding functionality
1. Auflage 2006, 163 Seiten
ISBN 3-8322-5281-9

ABISEA Band 42
Jacobs, J.
Multi-Phase Series Resonant DC-to-DC Converters
1. Auflage 2006, 185 Seiten
ISBN 3-8322-5532-X

ABISEA Band 43
Linzen, D.
Impedance-Based Loss Calculation and Thermal Modeling of Electrochemical Energy Storage Devices for Design Considerations of Automotive Power Systems
1. Auflage 2006, 150 Seiten
ISBN 3-8322-5706-3

ABISEA Band 44
Fiedler, J.
Design of Low-Noise Switched Reluctance Drives
1. Auflage 2007, 183 Seiten
ISBN 978-3-8322-5864-l

ABISEA Band 45
Fuengwarodsakul, N.
Predictive PWM-based Direct Instantaneous Torque Control for Switched Reluctance Machines
1. Auflage 2007, 150 Seiten
ISBN 978-3-8322-6210-5

ABISEA Band 46
Meyer, C.
Key Components for Future Offshore DC Grids
1. Auflage 2007, 196 Seiten
ISBN 978-3-8322-6571-7

ABISEA Band 47
Fujii, K.
Characterization and Optimization of Soft-Switched Multi-Level Converters for STATCOMs
1. Auflage 2008, 206 Seiten
ISBN 978-3-8322-6981-4

ABISEA Band 48
Carstensen, C.
Eddy Currents in Windings of Switched Reluctance Machines
1. Auflage 2008, 190 Seiten
ISBN 978-3-8322-7118-3

ABISEA Band 49
Bohlen, 0.
Impedance-based battery monitoring
1. Auflage 2008, 200 Seiten
ISBN 978-3-8322-7606-5

ABISEA Band 50
Thele, M.
A contribution to the modelling of the charge acceptance of lead-acid batteries - using frequency and time domain based concepts
1. Auflage 2008, 168 Seiten
ISBN 978-3-8322-7659-1

ABISEA Band 51
König, A.
High Temperature DC-to-DC Converters for Downhole Applications
1. Auflage 2009, 160 Seiten
ISBN 978-3-8322-8489-3

ABISEA Band 52
Dick, C. P.
Multi-Resonant Converters as Photovoltaic Module-Integrated Maximum Power Point Tracker
1. Auflage 2010, 192 Seiten
ISBN 978-3-8322-9199-0

ABISEA Band 53
Kowal, J.
Spatially-resolved impedance of nonlinear inhomogeneous devices - using the example of lead-acid batteries -
1. Auflage 2010, 214 Seiten
ISBN 978-3-8322-9483-0

ABISEA Band 54
Roscher, M.
Zustandserkennung von LiFeP04-Batterien für Hybrid- und Elektrofahrzeuge
1. Auflage 2011, 194 Seiten
ISBN 978-3-8322-9738-l

ABISEA Band 55
Hirschmann, D.
Highly Dynamic Piezoelectric Positioning
1. Auflage 2011, 156 Seiten
ISBN 978-3-8322-9746-6

ABISEA Band 56
Rigbers, K.
Highly Efficient Inverter Architectures for Three-Phase Grid Connection of Photovoltaic Generators
1. Auflage 2011, 254 Seiten
ISBN 978-3-8322-9816-9

ABISEA Band 57
Kasper, K.
Analysis and Control of the Acoustic Behavior of Switched Reluctance Drives
1. Auflage 2011, 214 Seiten
ISBN 978-3-8322-9869-2

ABISEA Band 58
Köllensperger, P.
The Internally Commutated Thyristor - Concept, Design and Application
1. Auflage 201 J, 212 Seiten
ISBN 978-3-8322-9909-5

ABISEA Band 59
Schoenen, T.
Einsatz eines DC/DC-Wandlers zur Spannungsanpassung zwischen Antrieb und Energiespeicher in Elektro-und Hybridfahrzeugen
1. Auflage 2011, 138 Seiten
ISBN 978-3-8440-0622-3

ABISEA Band 60
Hennen, M.
Switched Reluctance Direct Drive with Integrated Distributed Inverter
1. Auflage 2012, 150 Seiten
ISBN 978-3-8440-0731-2

ABISEA Band 61
van Treek, D.
Position Sensorless Torque Control of Switched Reluctance Machines
1. Auflage 2012, 144 Seiten
ISBN 978-3-8440-IO 14-5

ABISEA Band 62
Bragard, M.
Tue Integrated Emitter Turn-Off Thyristor. An Innovative MOS-Gated High-Power Device
1. Auflage 2012, 172 Seiten
ISBN 978-3-8440-1152-4

ABISEA Band 63
Gerschler, J. B.
Ortsaufgelöste Modellbildung von Lithium-Ionen-Systemen unter spezieller Berücksichtigung der Batteriealterung
1. Auflage 2012, 350 Seiten
ISBN 978-3-8440-1307-8

ABISEA Band 64
Neuhaus, C.
Schaltstrategien für Geschaltete Reluktanzantriebe mit kleinem Zwischenkreis
1. Auflage 2012, 144 Seiten
ISBN 978-3-8440-1487-7

ABISEA Band 65
Butschen, T.
Dual-ICT- A Clever Way to Unite Conduction and Switching Optimized Properties in a Single Wafer
1. Auflage 2012, 178 Seiten
ISBN 978-3-8440-1771-7

ABISEA Band 66
Plum, T.
Design and Realization of High-Power MOS Turn-Off Thyristors
1. Auflage 2013, 130 Seiten
ISBN 978-3-8440-1884-4

ABISEA Band 67
Kiel, M.
Impedanzspektroskopie an Batterien unter besonderer Berücksichtigung von Batteriesensoren für den Feldeinsatz
1. Auflage 2013, 232 Seiten
ISBN 978-3-8440-1973-5

ABISEA Band 68
Brauer, H.
Schnelldrehender Geschalteter Reluktanzantrieb mit extremem Längendurchmesserverhältnis
1. Auflage 2013, 202 Seiten
ISBN 978-3-8440-2345-9

ABISEA Band 69
Thomas, S.
A Medium-Voltage Multi-Level DC/DC Converter with High Voltage Transformation Ratio
1. Auflage 2014, 236 Seiten
ISBN 978-3-8440-2605-4

ABISEA Band 70
Richter, S.
Digitale Regelung von PWM Wechselrichtern mit niedrigen Trägerfrequenzen
1. Auflage 2014, 134 Seiten
ISBN 978-3-8440-2641-2

ABISEA Band 71
Bösing, M.
Acoustic Modeling of Electrical Drives - Noise and Vibration Synthesis based on Force Response Superposition
1. Auflage 2014, 208 Seiten
ISBN 978-3-8440-2752-5

ABISEA Band 72
Waag, W.
Adaptive algorithms for monitoring of lithium-ion batteries in electric vehicles
1. Auflage 2014, 242 Seiten
ISBN 978-3-8440-2976-5

ABISEA Band 73
Sanders, T.
Spatially Resolved Electrical In-Situ Measurement Techniques for Fuel Cells
1. Auflage 2014, 138 Seiten
ISBN 978-3-8440-3121-8

ABISEA Band 74
Baumhöfer, T.
Statistische Betrachtung experimenteller Alterungsuntersuchungen an Lithium-Ionen Batterien
1. Auflage 2015, 174 Seiten
ISBN 978-3-8440-3423-3

ABISEA Band 75
Andre, D.
Systematic Characterization of Ageing Factors for High-Energy Lithium-Ion Cells and Approaches for Lifetime Modelling Regarding an Optimized Operating Strategy in Automotive Applications
1. Auflage 2015, 210 Seiten
ISBN 978-3-8440-3587-2

ABISEA Band 76
Merei, G.
Optimization of off-grid hybrid PV-wind-diesel power supplies with multi-technology battery systems taking into account battery aging
1. Auflage 2015, 194 Seiten
ISBN 978-3-8440-4148-4

ABISEA Band 77
Schulte, D.
Modellierung und experimentelle Validierung der Alterung von Blei-Säure Batterien durch inhomogene Stromverteilung und Säureschichtung
1. Auflage 2016, 168 Seiten
ISBN 978-3-8440-4216-0

ABISEA Band 78
Schenk, M.
Simulative Untersuchung der Wicklungsverluste in Geschalteten Reluktanzmaschinen
1. Auflage 2016, 142 Seiten
ISBN 978-3-8440-4282-5

ABISEA Band 79
Wang, Y.
Development of Dynamic Models with Spatial Resolution for Electrochemical Energy Converters as Basis for Control and Management Strategies
1. Auflage 2016, 198 Seiten
ISBN 978-3-8440-4303-7

ABISEA Band 80
Ecker, M.
Lithium Plating in Lithium-Ion Batteries: An Experimental and Simulation Approach
1. Auflage 2016, 170 Seiten
ISBN 978-3-8440-4525-3

ABISEA Band 81
Zhou, W.
Modellbasierte Auslegungsmethode von Temperierungssystemen für Hochvolt-Batterien in Personenkraftfahrzeugen
1. Auflage 2016, 192 Seiten
ISBN 978-3-8440-4589-5

ABISEA Band 82
Lunz, B.
Deutschlands Stromversorgung im Jahr 2050
Ein szenariobasiertes Verfahren zur vergleichenden Bewertung von Systemvarianten und Flexibilitätsoptionen
1. Auflage 2016, 196 Seiten
ISBN 978-3-8440-4627-4

ABISEA Band 83
Hofmann, A.
Direct Instantaneous Force Control Key to Low-Noise Switched Reluctance Traction Drives
1. Auflage 2016, 244 Seiten
ISBN 978-3-8440-4715-8

ABISEA Band 84
Budde-Meiwes, H.
Dynamic Charge Acceptance of Lead-Acid Batteries for Micro-Hybrid Automotive Applications
1. Auflage 2016, 168 Seiten
ISBN 978-3-8440-4733-2

ABISEA Band 85
Engel, S. P.
Thyristor-Based High-Power On-Load Tap Changers Control under Harsh Load Conditions
1. Auflage 2016, 170 Seiten
ISBN 978-3-8440-4986-2

ABISEA Band 86
VanHoek, H.
Design and Operation Considerations of Three-Phase Dual Active Bridge Converters for Low-Power Applications with Wide Voltage Ranges
1. Auflage 2017, 242 Seiten
ISBN 978-3-8440-5011-0

ABISEA Band 87
Diekhans, T.
Wireless Charging of Electric Vehicles - a Pareto-Based Comparison of Power Electronic Topologies
1. Auflage 2017, 156 Seiten
ISBN 978-3-8440-5048-6

ABISEA Band 88
Lehner, S.
Reliability Assessment of Lithium-Ion Battery Systems with Special Emphasis on Cell Performance Distribution
1. Auflage 2017, 202 Seiten
ISBN 978-3-8440-5090-5

ABISEA Band 89
Käbitz, S.
Untersuchung der Alterung von Lithium-Ionen-Batterien mittels Elektroanalytik und elektrochemischer Impedanzspektroskopie
1. Auflage 2017, 257 Seiten
urn:nbn:de:hbz:82-rwth-2016-120944

ABISEA Band 90
Witzenhausen, H.
Elektrische Batteriespeichermodelle: Modellbildung, Parameteridentifikation und Modellreduktion
1. Auflage 2017, 286 Seiten
urn:nbn:de:hbz:82-rwth-2017-034373

ABISEA Band 91
Münnix, J.
Einfluss von Stromstärke und Zyklentiefe auf graphtitische Anoden
1. Auflage 2017, 178 Seiten
DOI: 10.18154/RWTH-2017-01915